12-2006

INVESTIGATION OF FLOW AND MICROSTRUCTURE IN RHEOMETRIC AND PROCESSING FLOW CONDITIONS FOR LIQUID CRYSTALLINE PITCH

Santanu Kundu
Clemson University, santanukundu@gmail.com

INVESTIGATION OF FLOW AND MICROSTRUCTURE IN RHEOMETRIC AND PROCESSING FLOW CONDITIONS FOR LIQUID CRYSTALLINE PITCH

A Dissertation
Presented to
the Graduate School of
Clemson University

In Partial Fulfillment
of the Requirements for the Degree
Doctor of Philosophy
Chemical Engineering

---

by
Santanu Kundu
December 2006

Accepted by:
Dr. Amod A Ogale, Committee Chair
Dr. Mark C Thies
Dr. Alejandro D Rey
Dr. Christopher L Cox

ABSTRACT

The microstructure development within mesophase pitch-based carbon materials depends on the flow history that the pitch is subjected to. Therefore, a fundamental understanding of flow and its influence on the microstructure is required to obtain carbon materials with desired properties. The objective of this research was to investigate the flow and microstructural behavior of a synthetic mesophase pitch (AR-HP) in rheometric and processing flow conditions. In addition, simulation studies were performed to establish a frame work for modeling the flow behavior of this complex material in different flow situations.

The steady-shear viscosities obtained from a cone-plate rheometer during increasing rate-sweep experiments exhibited shear-thinning (Region I) and plateau (Region II) responses. However, the slope of the shear-thinning region was only about -0.2, much lower than -0.5 observed in some pitches and liquid-crystalline polymers. This difference could arise from the different molecular constituents of pitches. At higher shear rates, as measured from capillary rheometers, the viscosity values remained almost constant. The transient shear stress responses, as measured from cone-plate rheometer, exhibited nonmonotonic behavior as a function of applied strain at all shear rates and temperatures tested. After rheological experiments, the samples were collected by developing a new experimental protocol for preservation of the sample for microstructural analysis. Microstructural observations obtained from three orthogonal sections, reported for the first time in the literature, indicate that the local maximum in

shear stress was due to yielding of initial microstructure. The microstructure became flow oriented with further shearing, and the structure size decreased with increasing shear rates.

In addition to high-strain experiments, dynamic experiments were also performed in the linear viscoelastic region where no significant deformation of fluid takes place. The elastic response was found to be strongly dependent on the microstructure, and a lower slope of 0.8 for the elastic modulus in the low-frequency terminal region was observed as compared to 2 observed for flexible chain polymers. Relaxation of microstructure resulted in an increase of storage moduli. However, the relaxation time did not follow the scaling argument, $\tau \sim \eta a^2/K$. It is postulated that the relaxation process is influenced not only by the textural size, but also by layer-plane orientation.

The flow-microstructural study was extended to the processing flow conditions and in this case AR-HP mesophase pitch was extruded through custom-made dies using a single-screw extruder. Due to changing dimensions of these dies, the mesophase pitch was subjected to varying shear rates. Microstructural observations suggest that in the capillary region of these dies, the orientation of the layer-plane was approximately radial near the wall. Away from the wall, the deviation of orientation of the layer-planes from the radial direction was significant and some layer-planes were oriented tangentially. In the core, the microstructure was coarse and no preferred orientation of mesophase layer-planes was observed.

Simulation studies were performed using constitutive equations for discotic liquid-crystalline materials in simple shear flow, corresponding with the experimental studies. The simulation studies were performed for two different initial conditions that

resemble the experimental results. At steady state, the bulk of the discs were found to be oriented at a flow-aligned angle of -64.1°, which is consistent with the theoretical predictions. Although, the simulation studies could not capture the complex microstructure observed experimentally, similarities in flow-aligned domains were observed. This study establishes a frame work to simulate the flow dynamics of complex mesophase pitch in multiscale-mulidimensional problems using the computational facility and expertise of the Center for Advanced Engineering Fibers and Films (CAEFF).

DEDICATION

I dedicate this work to my parents, Mr. Nimai Charan Kundu and Mrs. Laxmi Kundu.

ACKNOWLEDGMENTS

I would like to thank the following individuals, without whose support the completion of this work would not have been possible:

Dr. Amod A Ogale, my research advisor, for motivating and guiding me towards the successful completion of this work. I thank him for the invaluable support he has provided during my research. I am also thankful to him and Mrs. Ogale, for their kind hospitality during the numerous dinners they have hosted over the years.

Dr. Alejandro D Rey, Dr. Mark C Thies, and Dr. Christopher L Cox, for their helpful suggestions during the course of this research and for serving on my dissertation committee.

Dr. Amit K Naskar, for his help during the X-ray experiments. I also appreciate his friendship over the last few years.

Dr. J vonOhesen and Mr. Edward Duffy, for their help during the simulation studies. Dr. Dana Grecov and Dr. L.R.P. de Andrade Lima, for helping me to understand the complicated liquid-crystalline constitutive equations.

Mr. Bill Coburn, for assisting me to develop few experimental set up. Machining and technical Services of Clemson University for manufacturing the custom-made dies. Mr. Bobby Martin of Martin Microscope, Easley, for allowing me to use their facilities.

The Center for Advanced Engineering Fibers and Films for their financial support of this research work through the ERC Program of the National Science Foundation.

Dr. Amit Sankhe, Mr. Giriprasath Gururajan, Dr. Srinivas Cherukupalli, for their friendships and for helping to make Clemson a fun place.

Members of Dr. Ogale's research group, Dr. Tianren Guo, Mr. Sungho Lee, Mr. Dan Sweeney, Mr. Tad Cho for providing a stimulating research environment.

My parents, Nimai Charan Kundu and Laxmi Kundu, my sister MadhuChhanda Kundu, for their love and support during all these years. I never would have made it this far without their endless encouragement. My grandfather, Dr. Ramratan Kundu, for inspiring me through his values, discipline and hard-work. Finally, I thank my lovely wife Queenee, for being there for me anytime when I needed cheering up. All my love, Mou.

TABLE OF CONTENTS

Table of Contents (Continued) Page

LIST OF TABLES

LIST OF FIGURES

List of Figures (Continued)

List of Figures (Continued)

List of Figures (Continued)

List of Figures (Continued)

List of Figures (Continued)

List of Figures (Continued)

List of Figures (Continued)

List of Figures (Continued)

List of Figures (Continued)

List of Figures (Continued)

List of Figures (Continued)

List of Figures (Continued)

CHAPTER 1

INTRODUCTION

1.1 Background

Carbon products are widely used as structural materials in aerospace and sporting goods industries, as thermal management materials in high performance microelectronics, and as electrical by conducting materials in industrial equipment [Edie, 2003; Zweben, 2005]. Carbon products are also believed to have a great potential as structural materials in automobile industries and even in energy storage applications [Paulauskas 2004; Sröbel et al., 2006]. Of these products, the ones that possess high thermal/electrical conductivity are derived from mesophase pitch precursors.

Mesophase pitches are typically produced by catalytic polymerization of aromatic compounds such as naphthalene, methyl naphthalene, or by heat soaking (thermal-polymerization) of petroleum/coal-tar pitches. Mesophase pitch possesses discotic liquid crystalline nature and the ordered liquid crystalline state results in preferred orientation of mesophase molecules during processing. The ordered structure is retained during stabilization and graphitization, and as a result excellent lattice-dependent properties, such as thermal conductivity and modulus, are obtained in final products. Since the development of orientation for these types of structured fluids depends on the flow, a fundamental understanding of flow and its influence on microstructure is required to obtain carbon materials with desired properties.

Several studies have been performed in the past to understand the flow-microstructural behavior for different grades of mesophase pitch from experimental and modeling perspectives [Edie, 2003; Fathollahai and White, 1994; Grecov and Rey, 2003a & 2003b]. This chapter summarizes such results that motivated us to further investigate the flow-microstructure relationships.

1.2 Production of Mesophase Pitch

Mesophase pitch is a thermotropic liquid crystalline material consisting of high molecular weight poly-nuclear aromatic compounds. It was first observed by Brooks and Taylor [1965] during heat treatment of coal tar pitch, petroleum residue and pure aromatic compounds such as naphthacene, polyvinyl chloride, and dibenzanthrone. During heat-treatment, due to polymerization reactions, molecular weight increases and the planar aromatic molecules stack/assemble in nearly parallel arrays to form a liquid crystalline material. Stacking leads to the formation of spherules, which are then precipitated due to their higher density. Brooks and Taylor observed the precipitation of these spherules, also known as Brooks-Taylor spherule, in the temperature range of 400-500°C.

During 1970s, researchers at Union Carbide heat soaked coal-tar, petroleum residues and acenaphthylene in the temperature range of 350-500°C for an extended period (from few hours to a week) to produce mesophase pitch [Singer, 1977; Lewis, 1977]. It was also observed that the continuation of heat soaking, mesophase spherules grew and coalesced into a continuous phase [Singer, 1977; Lewis, 1977; Rand, 1985].

In a different approach, solvent extraction technique was used to separate the heavy mesophase forming molecules from aromatic-lean compounds [Diefendorf and Riggs, 1980]. The heavy fraction was then heat-treated for ~10 mins to obtain mesophase pitch. The problem with this technique was the difficulty of removal of residual solvent, which, caused difficulty in spinning/processing of this pitch. In another solvent-based process, Thies and co-workers [Bolaños et al., 1993; Dauché et al., 1998; Edwards 2005] have used a dense gas extraction technique for selectively separating desired molecular weights from isotropic pitch. Mesophase pitch produced by this technique resulted in narrower molecular weight distribution [Edwards, 2005].

The present commercial grades of mesophase pitches are synthetically prepared from catalytic polymerization of aromatic monomers. Mochida and coworkers [Mochida et al., 1975; Mochida et al., 1985; Mochida et al., 2000] used $AlCl_3$ catalyst for non-dehydrogenative polymerization of naphthalene and ethylene tar into mesophase. The problem with this technique was the incomplete removal of aluminium chloride from the pitch; presence of small amount of aluminium chloride (<10 ppm) resulted in carbon fibers of inferior quality [Mochida et al., 2000]. However, in a recent study, Chioujones et al. [2006] used this technique for *in situ* transformation of naphthalene into mesophase pitch for fabrication of carbon-carbon composites.

To circumvent the problem with $AlCl_3$, $HF\text{-}BF_3$, a super-acid Friedel-Craft type catalyst has been used in production of synthetic mesophase pitch [Mochida et al., 1985]. Mitsubishi Gas Chemical Corporation uses this method on an industrial scale to manufacture synthetic mesophase pitch commercially [Mochida et al., 1985; Mochida et al., 2000]. Naphthalene is typically used as the starting material to produce mesophase

pitch commercially because the presence of naphthanic and short alkyl groups in pitch is essential for low softening point [Mochida et al., 2000]. The low softening point is necessary for stable spinning and reasonable stabilization reactivity.

Various techniques such as vapor-pressure osmometry, gel-permeation chromatography (GPC), field desorption mass spectrometry (FD-MS), Matrix-assisted laser desorption/ionization time-of-flight mass spectrometry (MALDI) have been used to determine the molecular constituents and the molecular weight distribution of mesophase pitches [Singer, 1985; Rand, 1985; Edwards, 2005]. In vapor-pressure osmometry and GPC techniques, the sample must be dissolved in a solvent, but, it is hard to find a solvent that completely dissolves the mesophase pitch [Edwards, 2005]. Moreover, difficulty in finding suitable standard polynuclear aromatic molecules for calibration of GPC may result in inaccurate characterization of mesophase pitch. To overcome this problem, mass spectroscopy techniques such as MALDI was used and in this technique the characterization can be performed in solid state. No calibration is required for molecular weight (i.e., x-axis), which is a distinct advantage over GPC. However, calibration of the MALDI response (peak intensity *vs.* amount of the given fraction) needs further attention [Edward, 2005; Thies, 2006].

Despite the problems associated with the complete characterization of mesophase pitches, researchers have tried to identify the molecular constituents of mesophase pitches [Mochida et al., 2000; Mochida et al., 2002]. FD-MS and MALDI results show that the molecular weight distribution of naphthalene derived mesophase pitch varies from 150 to 1500 a.m.u.[Mochida et al., 2000; Mochida et al., 2002]. However, a long tail was observed (<5000 a.m.u.) for pyridine insoluble fraction. Based on the molecular weight

distribution curve, Mochida et al. [2002] suggested most probable mesogen molecules of mesophase pitches that were derived from different starting materials. Typical mesogen units for naphthalene derived mesophase pitch are shown in **Figure 1.1**.

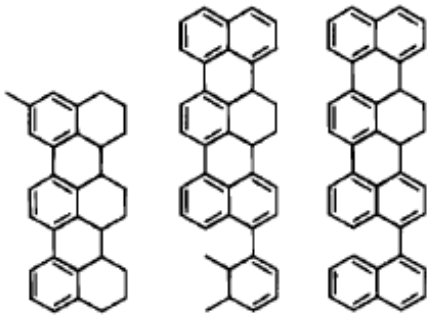

Figure 1.1: Typical mesogen units for naphthalene derived mesophase pitch [Mochida et al., 2002].

1.3 Liquid Crystalline Nature of Mesophase Pitch

Mesophase pitch is a discotic type of nematic liquid crystal, which possesses orientational order but no positional order. **Figure 1.2** represents a typical arrangement of discotic nematic liquid crystals. For discotic type liquid crystals, the unit normals to the constituent disk-like molecules are preferentially oriented along a common axis called director, **n**.

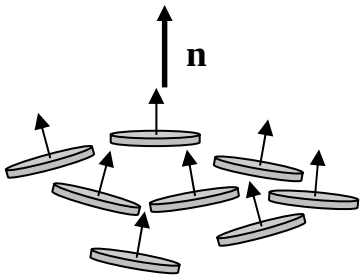

Figure 1.2: Schematic representation of discotic nematic liquid crystals, where **n** is the average preferred orientation of the unit normals to the disc-like molecules.

The average orientation (‹..›) of all unit normals along the director **n** can be represented by a scalar, known as scalar order parameter S:

$$S = \left\langle \frac{3}{2}\cos^2\theta - \frac{1}{2} \right\rangle$$

where, θ is the angle between the director, **n,** and the unit normal of each disc-like molecule. In an isotropic liquid, the order parameter S→0, whereas for a perfect crystal S→1. Typical values for the order parameter of liquid crystals range between 0.3 and 0.9, and are function of temperature [Singh, 2000].

Mesophase pitch is considered to be thermotropic liquid crystalline, i.e., the material becomes liquid crystalline below the isotropic-nematic transition temperature. **Figure 1.3** shows the transition of scalar order parameter from liquid crystalline state to isotropic state [Singh, 2000]. Above nematic-isostropic transition temperature (T_{NI}), the scalar order parameter drops to zero. Unfortunately, the nematic-isotropic transition has rarely been observed for mesophase pitch since it thermally unstable nature of this material. The mesophase molecules thermally decompose into coke before nematic-isotropic transition takes place. However, in one study, a reversible isotropic-nematic

transition was reported for a naphthalene-derived mesophase pitch [Lewis, 1978]. It was observed that during heating mesophase regions completely changed to isotropic phase at 475°C and reappeared during cooling.

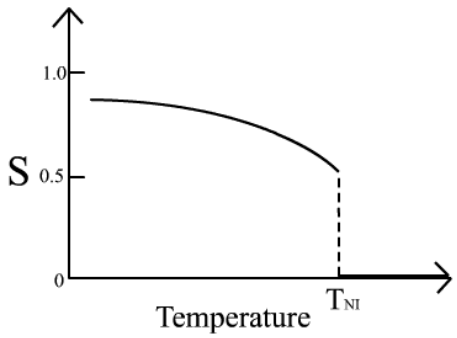

Figure 1.3: Transition of scalar order parameter, S of a thermotropic liquid crystalline polymer. T_{NI} is the nematic-isotropic transition temperature [Singh, 2000].

In some cases, mesophase pitches have also been reported to exhibit lyotropic liquid crystalline behavior. The low-molecular weight species act as mobilizing agent (similar to a solvent in lyotropic liquid crystals) in these systems. Vaporization, polymerization or solvent extraction of low-molecular weight species resulted in increase of concentration of high-molecular weight species and at a certain concentration the system behaves like liquid crystals [Rand, 1985; Hurt and Hu, 1999]. The phase behavior of polynuclear aromatic hydrocarbons and their transformation into mesophase has also been studied theoretically [Hurt and Hu, 1999; Zuang and Thies, 2000].

1.4 Flow and Microstructural behavior

The flow and microstructure behavior of a textured fluid, such as mesophase pitch, are interdependent. Different microstructures are a consequence of different flow fields encountered during melt-processing of mesophase pitch. For instance, during fiber spinning, the molten pitch is subjected to changing shear rates during the flow through the capillary. The shear rates and stresses vary across the capillary cross-section from a value of zero at the centerline to a maximum (~1000 s^{-1}) at the capillary wall. Also, during other steps of fiber spinning, such as the flow in bigger pipes and manifolds and spinneret counter-bores, the shear rates can be low to medium (of the order of 1-10 s^{-1}). There are also flow situations such as processing of carbon-carbon composites that utilize molten mesophase infiltration at low-medium pressures [Fathollahi et al., 2005]. The shear rates in such processes are expected to be in the medium range and the flow is transient. Such transient flow situation is experienced whenever there is change in cross-sectional area. To obtain the carbon products with desired properties, flow and microstructural characteristics of mesophase pitches have been of interest from experimental as well as modeling perspectives.

1.4.1 Flow Characteristics

1.4.1.1 Steady Shear Flow

Several experimental studies have described the rheological behavior of different mesophase pitches. In earlier studies, the change of rheological behavior coal-tar pitch

and petroleum pitches during mesophase transformation was reported [Rand, 1985; Balduhn and Fitzer, 1980; Collett and Rand, 1978a &1978b]. Above certain temperatures (≈380°C), coal tar pitches displayed a non-Newtonian flow behavior [Collett and Rand, 1978a]. Thixotropic flow characteristic was also observed for coal tar pitch [Collet and Rand, 1978b] and for a pitch of unspecified origin [Barr et al., 1976]. In another study, the steady shear viscosity at was reported to be pseudo-Newtonian for naphthalene-based pitch, whereas a non-Newtonian behavior was observed for dimethylnapthalene-based pitch [Nazem, 1980; 1982]. Also, viscosity was found to be independent of shear rates over the tested range for an alkylbenzene based mesophase pitch [Fathollahai and White, 1994]

In a recent study, as shown in **Figure 1.4**, a two-region steady shear viscosity behavior was reported for a naphthalene-derived ARA24R mesophase pitch [Cato et al., 2005]. A small negative first normal stress difference was also reported for that pitch under steady shear conditions [Cato et al., 2005]. Some mesophase pitches have exhibited the three-region viscosity behavior as measured from capillary [**Figure 1.5,** Yoon et al., 1994] and parallel plate experiments [Dumont et al., 2003], which has also been previously observed for liquid crystalline polymers [Onogi and Asada, 1980].

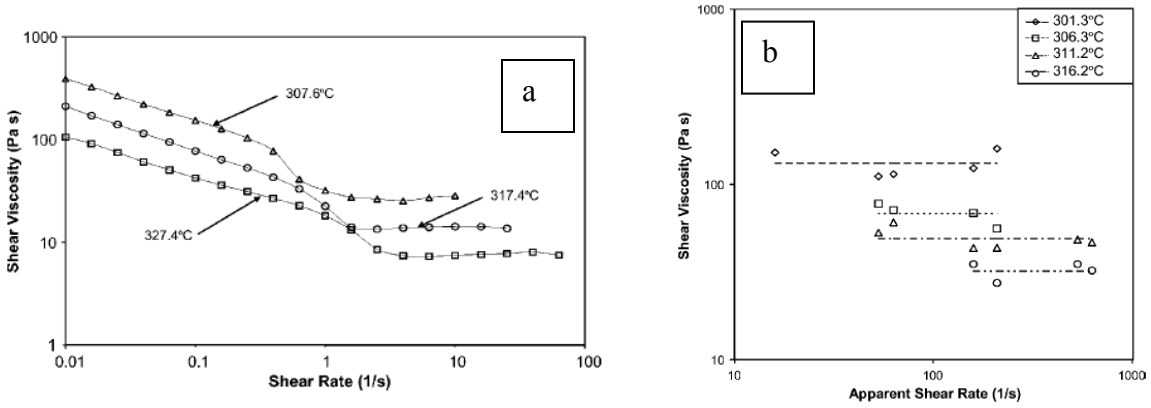

Figure 1.4: Two region viscosity behavior of ARA24R mesophase pitch. (a) Results from cone-plate rheometer, (b) Results from capillary rheometer [Cato et al., 2005].

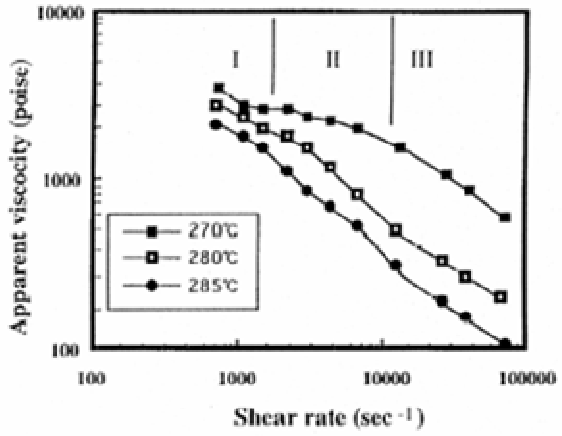

Figure 1.5: Three region viscosity behavior of a naphthalene derived mesophase pitch (NP1). Experiments were performed using capillary rheometer. [Yoon et al., 1994]

1.4.1.2 Transient Shear Flow

In addition to the steady-state response, the transient response also reveals structural features of a complex fluid. In some nematics, the startup response of shear flow displays pronounced oscillations in shear stress [Gu et al., 1993], which damps out to a steady value, can be interpreted as a manifestation of director tumbling. Other

thermotropic materials show a single transient shear stress [Viola and Baird, 1986; Guskey and Winter, 1991; Mather et al., 2000; Ugaz et al., 2001] and primary normal stress difference (N_1) overshoot peak [Guskey and Winter, 1991; Ugaz et al., 2001]. However, in some instances, major overshoot was followed by weaker damped oscillations that can persist for hundreds of strain units [Han and Kim, 1994; Mather et al., 2000]. In a few experiments, transient negative N_1 values have been observed [Moldenaers and Mewis, 1986; Guskey and Winter, 1991] and the magnitude of both shear stress and N_1 overshoots was found to depend on both temperature and shear rate [Han and Kim, 1994].

In contrast to rod-like thermotropic systems, pitch molecules are disk-like and much smaller in size, and can lead to different flow dynamics. However, the rheology of mesophase pitch under transient conditions has been reported only in limited literature studies. These studies on synthetic mesophase pitch (ARA24, Me-AR, ARA24R) and supercritically extracted mesophase pitches [Fleurot, 1998; Cato et al., 2005] showed that transient shear stress response exhibits an overshoot (**Figure 1.6**) and its magnitude depends on the previous flow-history. For the flow-cessation experiments, it was shown that the rest-period between two shearing experiments played an important role on the extent of shear-stress overshoot in the second shearing step [Fleurot, 1998; Cato et al., 2005].

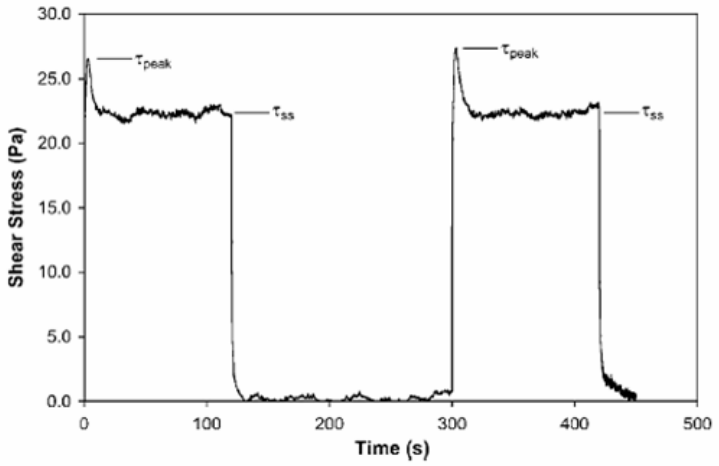

Figure 1.6: Transient shear stress responses of ARA24R mesophase pitch at 312.1°C and 0.5 s^{-1}. [Cato et al., 2005]

1.4.1.3 Dynamic Flow

In contrast to high-strain steady-shear experiments, dynamic experiments may be performed in the linear viscoelastic region where no significant deformation of fluid takes place. Such dynamic experiments can be used to investigate the structure of complex fluids [Romo-Uribe et al., 1997; Burghardt, 1998]. In some instances, dynamic studies on liquid crystalline polymers reported a smaller slope of low-frequency terminal zone of storage (G') and loss (G'') modulus as compared to that observed for conventional flexible chain polymers [Driscoll and Masuda, 1991; Guskey and Winter, 1991; Somma and Nobile, 2004]. The lower slope is likely caused by the textured nature of liquid-crystalline polymers. Effect of preshearing before dynamic experiments was studied for TLCPs, and it was shown that moduli/complex viscosity decreased with preshearing,

compared to that measured for unpresheared samples over the same frequency range [Wissbrun and Griffin, 1982; Kim and Han, 1994].

In addition to frequency-sweep experiments, dynamic time-sweep experiments have been performed to study the relaxation behavior of liquid crystalline polymers after cessation of shear flow. An increase of moduli after cessation of shear flow was reported for TLCPs [Han and Kim, 1994] and a lyotropic solution of HPC [Grizzuti et al., 1993; Burghardt, 1998]. The increase of moduli has been associated with the relaxation of microstructure. However, a decrease of complex modulus and complex viscosities was observed for a lyotropic solution of PBG in m-cresol during dynamic time-sweep experiments after cessation of shear flow [Moldenaers and Mewis, 1986].

In contrast to liquid crystalline polymers, the dynamic rheology of mesophase pitch has been reported only in limited literature studies. Previous studies show that for different grades of naphthalene based mesophase pitches, the loss modulus was higher than the storage modulus over the frequency range tested [Cato, 2002]. Also, no crossover frequency was observed. In another study, for gas-sparged mesophase pitch with different mesophase contents and for a naphthalene based mesophase pitch (AR824) cross-over was reported at higher frequency values [Cheung et al., 1996].

1.4.2 Microstructural observations

1.4.2.1 Steady & dynamic shear flow

To understand the microstructural evolution of complex fluids during different flow situations, i*n situ* studies have been performed using optical microscopy coupled

with a shearing (hot-) stage [Larson and Mead, 1992; Mather et al., 2000; Guo et al., 2005]. The transparent/translucent nature of the liquid crystalline polymers enables real-time measurement of evolution of domain structure and defect dynamics by optical microscopy in the transmission mode. During shearing experiments on the lyotropic PBG solutions, "stripe" (birefringent stripes parallel to the flow direction) microstructure was observed at steady state and this type of structure was suggested to be caused by 'roll cells'. Also, the "band" (birefringent bands perpendicular to the flow direction) patterned microstructures was observed during start-up and could be explained "by an instability of the director to a periodic out-of-plane director rotation" [Larson and Mead, 1992; Larson, 1999].

For thermotropic liquid crystalline polymers, microstructural change during heating has been reported in the literature [Shiwaku et al., 1990; Kim and Han, 1993]. It was shown that for X-7G (60 mol% p-oxybenzonate and 40 mol % ethylene terephthalate) the anisotropic microstructure disappeared after nematic-to-isotropic transition took place. Defect textures in shear flow were characterized by Graziano and Mackley [1984] for a small molecule nematic, MBBA and an increase of defect density with the increasing shear rates was reported. De'Neve et al. [1993] observed worm-like and flow-oriented textures during shear flow of Vectra B950 and reported that the transitions from one texture to another depend on both the shear rate and the shear strain.

Microstructural evolution during shear start-up and reversal flows have been reported in the literature for PSHQ10 [Mather et al., 2000] and Vectran V400P [Guo et al., 2005]. For PSHQ10, a single large overshoot was observed, which was shown to be attributed to the yielding of initial microstructure (**Figure 1.7**). "Band" microstructure

was also observed upon reversal of flow direction. For Vectran V400P, shear stress exhibited two maxima during transient shear experiments [Guo et al., 2005]. It was shown from *in situ* microstructural observation that the first peak was related to the textural evolution or yielding of initial domain structure; whereas WAXD studies suggested that the second peak was related to the refinement of molecular orientation [Guo et al., 2005; Guo et al., 2006].

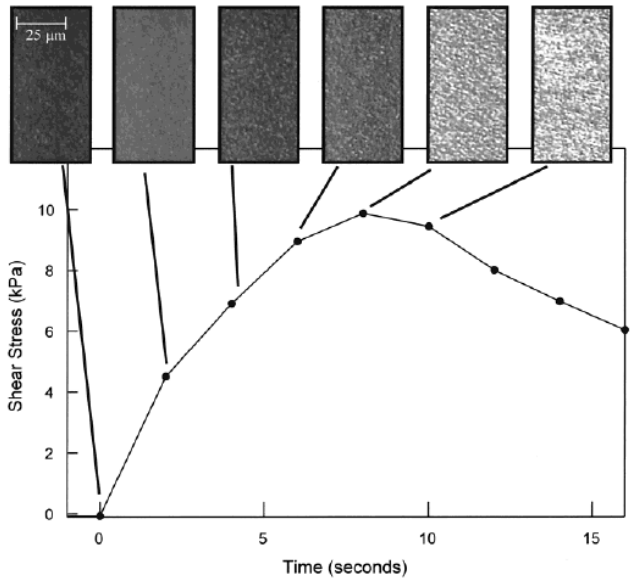

Figure 1.7: Transient shear stress response and corresponding microstructure evolution at $0.5s^{-1}$ and 160°C [Mather et al., 2000].

Microstructural observation during dynamic time-sweep has also been reported for a high molecular weight thermotropic 75%HBA/25%HNA polymer [Romo-Uribe et al. 1997]. This study was performed in a hot-stage and it was observed that during time-sweep experiments, the initial elongated radial structure relaxed to a tight polydomain structure (**Figure 1.8**), which was also accompanied by an increase of complex viscosity.

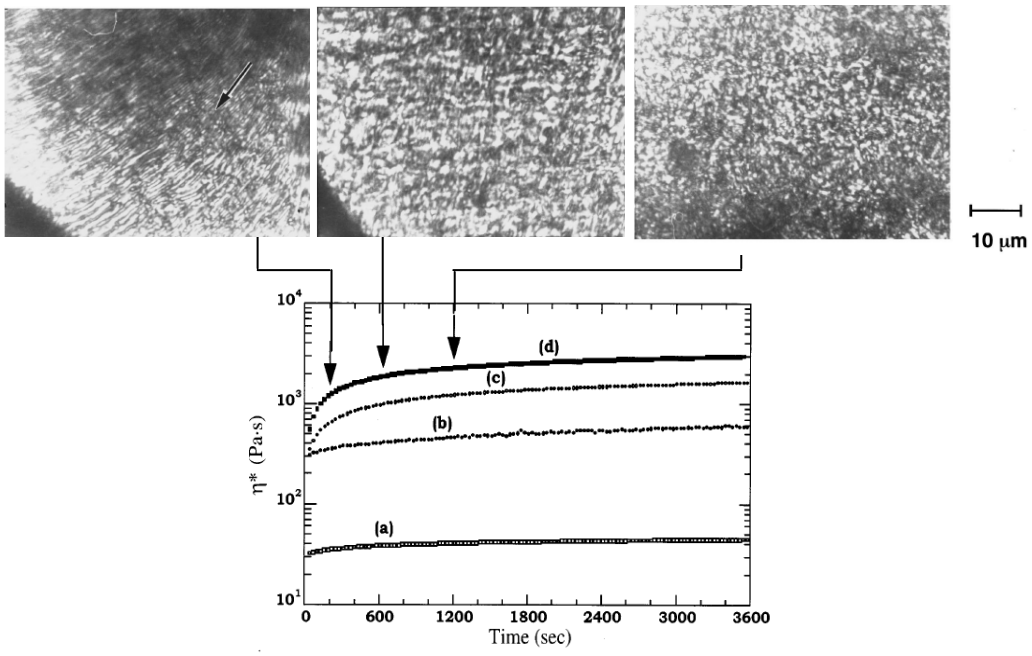

Figure 1.8: Evolution of complex viscosity (η*) with time and the corresponding cross-polarized optical micrographs at different time (shown as arrow) for thermotropic 75%HBA/25%HNA polymer [Romo-Uribe et al., 1997].

X-ray diffraction technique is often used to investigate the change of molecular orientation during shear flow. In a recent study on Vectran V400P, offline WAXD studies elucidated the origin of second maximum in transient shear stress response [Guo et al., 2006]. Burghardt and coworkers used synchrotron X-ray source to capture the microstructural evolution *in situ,* for different thermotropic liquid crystalline polymers [Burghardt et al., 2005]. In another *in situ* X-ray study on Vectra A900, transition in the orientation state has been captured as a function of temperature, shear rates and molecular weights [Romo-Uribe and Windle, 1996].

In contrast to transparent/translucent liquid crystalline polymers, the mesophase pitch is opaque and, therefore, real-time microscopic studies can not be performed. Instead, offline, reflected-mode optical microscopy on solidified pitch samples has been

used. The steady-state microstructure during rheological studies at low shear rates was reported to be flow aligned [Cato and Edie, 2003]. The molecular orientation within the domains changed from primarily edge-on to a mixture of edge-on and face-on when the shear rate exceeded a critical value, which led to a "kink" in the viscosity *vs*. shear rate curve. In another study on naphthalene derived mesophase pitch, it was shown that the domain size decreased with increasing shear rates, and the size approximately followed the Marrucci's polydomain theory for LCPs [Fleurot, 1998; Marrucci, 1984].

1.4.2.2 Microstructural observations during high-shear flows

Microstructure development within a capillary during high-shear flows has been reported in the literature for an alkylybenzene based pitch [Fathollahi and White, 1994] and a naphthalene based pitch [Fleurot, 1998]. It was observed that the microstructure became finer from the center of the capillary/channel to the wall [Fathollahi and White, 1994; Fleurot, 1998]. The structure size was correlated to the shear rates, which changed from zero at the center to the maximum at the wall [Fleurot, 1998]. Fathollahai and White [1994] also showed that introduction of a screen in the flow-path of the mesophase pitch resulted in orthogonal grid-structure in the extruded rod. The relaxation of the grid-structure depended on the viscosity (i.e. the temperature) of the precursor pitch.

1.5 Microstructure of carbon products and the effect of processing conditions

Different microstructures have been observed in mesophase pitch based C-C composites and carbon fibers [Edie, 2003; Fathollahi et al., 2005]. In C-C composites, the mesophase pitch flows through the channels between the fibers (matrix) and it has been reported that the fibers affect the microstructure of mesophase pitch in the vicinity [Fathollahi et al., 2005]. It was also reported in the same study that the microstructure was flow oriented along the local direction of the flow.

Carbon fibers with different transverse microstructure (e.g., radial, onion, etc.) have been reported in the literature [Edie, 2003] and it is shown that different microstructures resulted in different transport and mechanical properties [Bright and Singer, 1979; Rand, 1985; Edie, 2003; Hamada et al., 1987]. The microstructure of carbon fibers depends on the microstructure of as-spun fibers that typically develops during processing. It is also shown that the spinning temperature, and therefore, the viscosity of pitch precursor affect the microstructure of final carbon fibers [Otani and Oya, 1986a & b]. As shown in **Figure 1.9**, radial texture forms at lower temperatures. The radial texture changes to random, or radial texture surrounded by onion skin texture at higher temperature. With further increase of temperature, onion-like texture occurs.

The spinneret geometry was also found to affect the microstructure of carbon fibers [Matsumoto, 1985; Otani and Oya, 1986a]. Matsomoto has shown that increase of capillary length and decrease of capillary diameter resulted in radial microstructure of pitch based carbon fibers. Otani and Oya suggested that change of laminar flow condition

to turbulent flow condition, within the capillary could suppress the radial texture formation of carbon fibers.

Hamada et al. [1987] showed that for a coal-based mesophase pitch, radial texture of carbon fibers could be changed to random or quasi-onion texture by adding a stirrer above the spinning capillary. Also, the carbon fibers spun with stirring were less graphitizable than those spun without stirring. It was shown that the tensile strength of less graphitized fibers (heat treatment temperature 2500°C) was higher than the carbon fibers with a higher degree of graphitization. Higher tensile strength was also observed for carbon fibers with distorted radial texture, which was obtained by adding mesh filter in the spinning nozzle [Matsumoto et al., 1993].

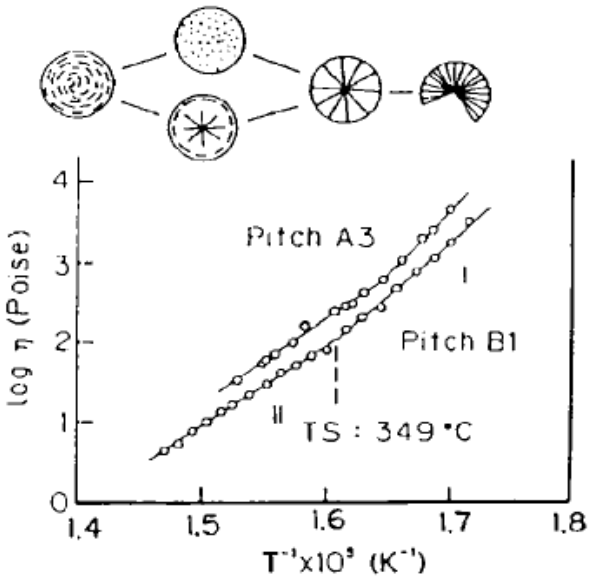

Figure 1.9: Viscosities of mesophase pitches as a function of temperature, and the schematic microstructures of carbon fibers spun at 300 – 400°C [Otani and Oya, 1986b].

1.6 X-ray study on mesophase pitch and carbon fibers

X-ray diffraction technique has been used to characterize the degree of orientation of graphene layer-planes and to determine the crystallite size in carbon fibers [Ruland, 1967; Bright and Singer, 1979; Ogale et al., 2002; Lu et al., 2002]. The theory of X-ray diffraction and how the different layers in carbon fibers lead to diffraction pattern is described in Appendix A. The preferred orientation of aromatic mesogen molecules in mesophase is lower than that observed in graphitized carbon fibers; however, X-ray reflections similar to (002) reflection of graphite crystal are typically observed [Singer, 1978; Ogale et al., 2002]. The degree of preferred orientation of 'as-spun' mesophase fibers, expressed as the full-width at half-maximum (FWHM) of the azimuthal intensity distribution, was measured as 25-30° [Bright and Singer, 1979; Ogale et al., 2002]. The FWHM decreased with an increase in heat treatment temperature, caused by the better alignment of the graphene layers at high temperatures. Also, a slight shift of 2θ peak position was also observed with increasing heat treatment temperature, i.e., with increase of graphitic content. In another study on supercritically extracted mesophase pitch, Barnes et al. [1998] showed that the orientation of as-spun fibers (based on FWHM data) could be used to predict the final fiber properties.

In a recent study, scanning microbeam (diameter ~2μm) X-ray diffraction analysis was used to study the axial and cross-sectional crystallographic texture of mesophase-pitch-based and PAN-based carbon fibers [Paris et al., 2002; Paris et al., 2000]. It was shown that radial-folded cross-sectional texture displayed different response than that was observed for random texture. They also have suggested that radial

texture of carbon fibers can be differentiated from onion texture using this technique. In another study, X-ray goniometry has been used to study the preferred orientation of graphene layer-planes in the transverse texture of carbon/graphite tapes [Lu et al., 2002].

1.7 Flow modeling of carbonaceous mesophase pitch

Several modeling studies have been reported in the literature to describe the flow behavior of nematic liquid crystals, and details are provided in a recent review paper [Rey and Denn, 2002]. Flow of complex nematic liquid crystalline material has been traditionally simulated by solving the dynamics of director (**n**), also known as Leslie-Ericksen model [Larson, 1999]. In another approach, molecular-based modeling [Doi model) provides additional understanding of the underlying physics [Doi and Edwards, 1986; Larson, 1999; Marrucci and Greco, 1993]. In this case, a kinetic equation of the orientation distribution function is solved. While Doi's model can capture the molecular phenomena that affect the macroscopical rheological behavior, the mathematical challenge to use this theory is quite formidable for complex flow geometries.

Another approach to modeling of structured fluid is to solve the dynamics of tensor order parameter Q [Beris and Edwards, 1994; Tsuji and Rey 1997; Rey and Denn 2002]. The tensor order parameter model, developed by Rey and coworkers [Tsuji and Rey, 1997; Grecov and Rey, 2003a & b], was based on the Landau-de Gennes free energy. This model can take into account long-range elasticity, short-range elasticity, and flow-induced effects. For slow flows, the tensor model simplifies to Leslie-Ericksen equation, which can then be solved for different initial twist and tilt angles of the discs

[Grecov and Rey, 2003a]. Simulation results show that the transient response is non-monotonic and largely depends on initial orientation of the discs. Using the same model for different Ericksen numbers (i.e., for different shear rates), a non-Newtonian steady-state rheological behavior was predicted [Grecov and Rey, 2003b]. Depending upon the anchoring of the discs, the viscosity behavior could be shear thinning or shear thickening. Director anchoring along the velocity direction resulted in nonmonotonic first normal stress difference that included a sign change with increasing shear rate. In another study on rod-type liquid crystalline systems [Grecov and Rey, 2004], the Landau-de Gennes tensor order parameter equations were solved to find the effect of textural transformation (defect nucleation and defect coarsening) on the stress growth during shear start-up flow. It was shown that defect nucleation and defect coarsening resulted in change of shear stress during flow.

The complex behavior of nematic liquid crystals in oscillatory shear flow has also been modeled. In a study on nematic liquid crystals, two different slopes of G' with no cross-over frequencies has been predicted [Burghardt, 1991]. In another study on a single-phase nematic mixture, a slope of 2 in the terminal zone followed by a plateau was predicted for G' [Rey, 1996]. Recent modeling studies on discotic mesophases during small-amplitude oscillatory Poseuille flow also display two distinct regions with slopes of 2 and 0.5, respectively, for G' as a function of frequency [de Andrade Lima and Rey, 2004]. Also, in all of these modeling studies, G" was shown to be greater than G', and no cross-over frequency was observed. In these studies, Leslie-Ericksen model was used and no microstructural effect was considered.

Flow modeling of liquid crystalline materials for Poiseuille flow using Leslie-Ericksen model has also been reported in literature [Tseng et al, 1972; de Andrade Lima and Rey, 2003]. In their simulation study, de Andrade Lima and Rey [2003] predicted multiplicity and multistability of Leslie-Ericksen solutions for flow aligning discotic nematic. The concept of solution multiplicity was used to elucidate the texture formation during melt processing of mesophase pitches [de Andrade Lima and Rey, 2003].

Modeling studies also have been extended to simulate the texture development of carbon fibers during melt-processing [McHugh, 1994; Wang and Rey, 1997]. McHugh [1994] used the Leslie-Ericksen theory to predict the development of radial texture of circular carbon fibers during the melt spinning of mesophase pitch. The study was also extended to predict the microstructure development of ribbon-shaped carbon fibers [McHugh, 1994]. Fleurot [1998] and Cato [2002] have used Polyflow®, a finite element based software to capture the flow behavior of mesophase pitch within a spinneret using generalized Newtonian fluid models.

Wang and Rey [1997] predicted the radial microstructure of carbon-fibers at lower processing temperature using the free-energy principle. It was also shown that the structure changed to mixed-type and then to onion-type with an increase of temperature, similar to that observed experimentally [Otani and Oya, 1986a & b]. Wang and Rey [1997] suggested that the changes of microstructure are dependent on the relative magnitude of splay (K_1) and bend (K_3) elastic constants. In a recent study, based on the Landau – deGennes mesoscopic theory, texture formation of carbon fibers has shown to be function of fiber diameter and processing temperature [Yan and Rey, 2002a & b].

1.8 Objectives and outline

Despite several studies, the flow-microstructural behavior of mesophase pitch is not completely understood and therefore, the goal of this study was to investigate flow-microstructural behavior of a recently available, naphthalene-based mesophase pitch (AR-High Performance grade, Mitsubishi Gas Chemical). The softening point of the AR-HP grade of mesophase pitch is 285°C, approximately 10°C lower than that reported for previous grades of mesophase pitches. The lower softening point was likely caused by different molecular constituents as compared to those present in previous grades. Such differences in molecular constituents can result in different flow behavior and processability of the precursor. In fact, AR-HP mesophase exhibited excellent spinnability at processing spinning temperatures that were almost 20°C lower that those used in previous studies [Cho et al., 2003].

Therefore, the primary objectives of this research were to

1. Study the flow behavior of AR mesophase pitch under controlled shear flow conditions, while simultaneously analyzing the microstructural evolution;
2. Extend the flow-microstructural study to processing flow conditions; and
3. Simulate the flow behavior of discotic liquid crystals in simple shear flow to establish a frame work for modeling the flow dynamics of this complex material in different flow situations.

Chapter 2 describes the flow behavior of AR mesophase pitch during low-shear conditions. The rheological experiments were performed both in steady and transient shear flow. For microstructural studies, samples were collected after rheological

experiments from the rheometer using a specially developed protocol. An extensive microstructural analysis was conducted in three orthogonal sections using optical microscopy, and the results are reported in Chapter 3. X-ray diffraction experiments were also performed to investigate the microstructure. Rheological responses were also studied in dynamic flow condition, and the interaction between microstructure and the dynamic properties is discussed in Chapter 4.

The understanding of flow and microstructure that was obtained from controlled-shear experiments was then extended to processing flow conditions. During processing through custom-made dies, mesophase pitch was subjected to various shear rates. The microstructural development within these dies was studied in both longitudinal and lateral sections. The results are reported in Chapter 5.

Chapter 6 reports the results of simulation studies for discotic liquid crystals that were obtained for simple shear flow, corresponding with the experimental studies presented in Chapter 2 and Chapter 3. The simulation study was performed using liquid crystalline constitutive equations developed by Rey and coworkers. The solution scheme of these constitutive equations was implemented by the modeling group of Center for Advance Fibers and Films (CAEFF). Finally, Chapter 7 presents the conclusions drawn from this study, and outlines directions for future work.

CHAPTER 2

RHEOLOGICAL CHRACTERIZATION DURING TRANISENT SHEAR FLOW

The properties of carbon products are a function of the microstructure typically derived from the discotic liquid crystalline pitch precursors [Bright and Singer, 1979; Rand, 1985; Edie 2003; Fathollahi and White, 1994; Fathollahi et al., 2005]. Different microstructures are a consequence of different flow-fields encountered during melt-processing of mesophase pitch. The batch melt-infiltration of pitch into carbon-carbon performs is typically an unsteady-state process [Fathollahi et al., 2005]. At low-medium infiltration pressures, the shear rates would tend to be in the low-medium range (~1-10 s^{-1}).

During fiber spinning, although the overall process is at steady-state (in the Eulerian sense of fixed lab-frame), the flow accelerates in the Lagrangian sense any time there is a change in the cross-sectional area. Thus, the structure evolves to a fully-developed state when the flow converges from pipes and manifolds into spinneret counter-bores and then into capillaries. Within a capillary, the shear rate varies from the maximum value (~1000 s^{-1}) at the capillary wall to zero at the centerline. In pipes and spinneret counter-bores, the maximum wall shear rates tend to be in the low to medium range (of the order of 1-10 s^{-1}). Therefore, rheology and flow characteristics of mesophase pitches have been of interest from experimental [Barr et al., 1976; Collett and Rand, 1978a &1978b; Balduhn and Fitzer, 1980; Nazem 1980 & 1982; Yoon et al., 1994;

Fleurot, 1998; Dumont et al., 2003; Cato et al., 2005] as well as modeling perspectives [Grecov and Rey, 2003 a&b].

In this chapter, which is based on a recent paper [Kundu and Ogale, 2006] the rheological responses are reported in two modes: (i) rate-sweep tests over a range of shear rates, and (ii) transient tests at individual shear rate for a recently available, naphthalene-based mesophase pitch (AR-HP grade, Mitsubishi Gas Chemical). The rheological response is reported from the cone-plate geometry that ensures a uniform shear-rate and shear-stress across the radius of the plate [Larson, 1999]. While a high wall-shear rate (~1000 s^{-1}) cannot be generated in this geometry, it is a valuable technique for measuring flow characteristics at low-medium shear rates (0.1 to 10 s^{-1}) that are encountered during some of the melt-processing steps. Microstructural changes during these rheological tests are reported in Chapter 3. High-shear results are later reported in Chapter 5.

2.1 Experimental

2.1.1 Material

A naphthalene-derived, synthetic mesophase pitch (AR-HP grade, Mitsubishi Gas Chemical Company) was used throughout the study. The pitch was reported by the manufacturer to be a high-performance grade (hence the suffix HP) with a low volatile content and a softening point of 285±5°C [MSDS, CAS No. 25135-16-4, Mitsubishi Gas Chemical Company]. A similar value of softening point was obtained from Metler

Toledo softening point measurement instrument (FP-83). The softening point was lower than 296°C reported for ARA24R (another grade of naphthalene based mesophase pitch) [Cato et al., 2005]. The softening point was also measured from dynamic flow experiments and is reported in Chapter 4. The measured value of softening point from flow experiments was ≈255°C, lower than that measured by FP-83.

To check the thermal stability of this material, thermogravimetric analysis (TGA) was performed. **Figure 2.1a** displays the sample mass loss when the sample was heated from ambient to 900°C at 20°C/min; the major loss took place approximately at 500~550°C, much above the temperature range used during rheological testing (290-305°C). **Figure 2.1b** displays results from an isothermal TGA scan at 300°C lasting about 2 hours, corresponding to the temperature and duration of rheological experiments. The sample loss was found to be less than 0.5 wt%, which suggests that no major degradation should be expected during rheological experiments.

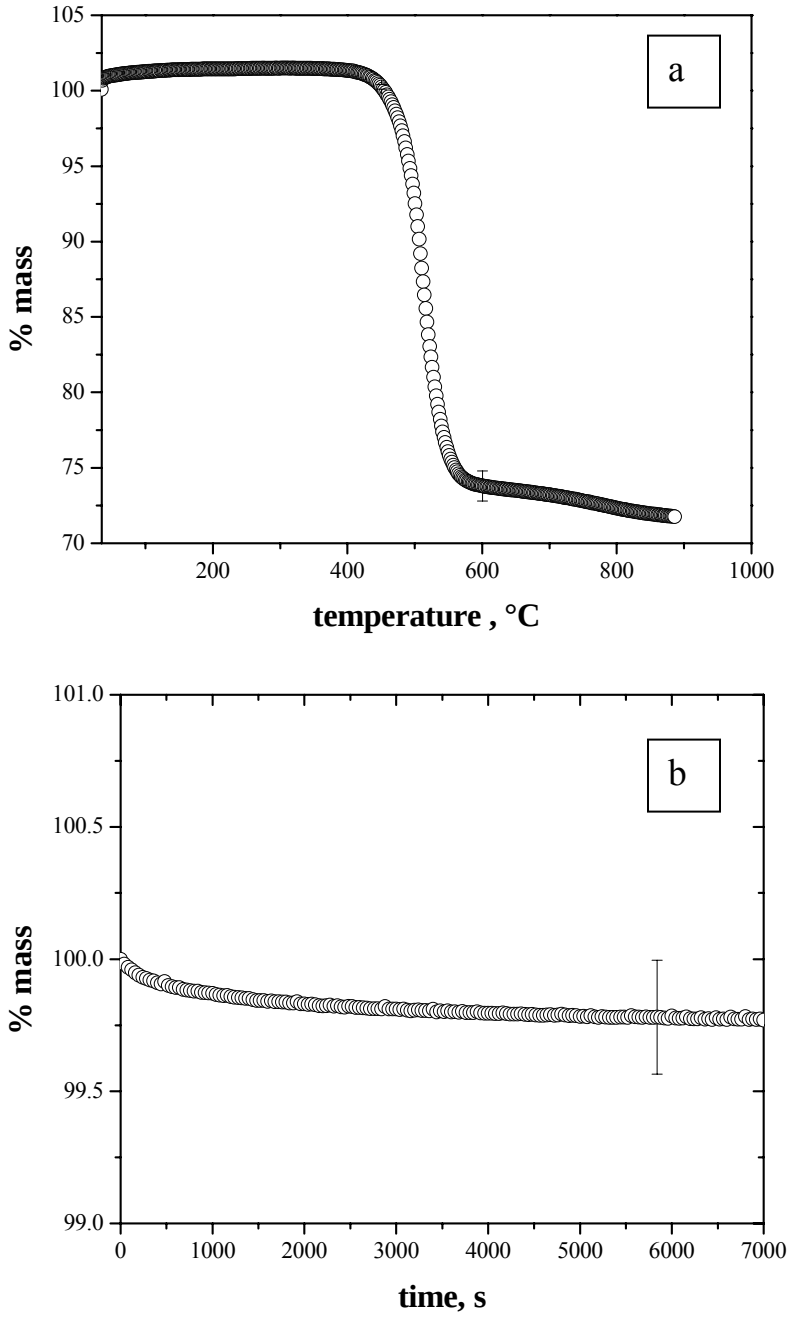

Figure 2.1: Thermo gravimetric analysis (TGA) of mesophase pitch samples: (a) mass loss during a temperature ramp from ambient to 900°C at a heating rate of 20°C/min, and (b) mass loss during an isothermal scan at 300°C.

2.1.2 Experimental set-up

The shear viscosity experiments were conducted on a well-calibrated TA Instruments ARES rheometer using a cone-plate fixture of 25 mm diameter with a cone angle of 0.1 rad. A majority of the tests were conducted at 297°C; limited tests were also performed at 290 and 305°C. These temperatures were selected for rheological experiments due to good melt-processability of AR-HP mesophase in this range [Cho et al., 2003]. All experiments were conducted in an inert nitrogen environment.

For rheological experiments, vacuum-pelletized cylindrical samples of 12.5 mm diameter and of approximately 3 mm height (≈ 0.5g) were loaded on the bottom plate and allowed to equilibrate to the elevated temperature. The melt was allowed to devolatilize for various durations (as discussed below), and the cone was then lowered into the melt. A holding time of 5 minutes was provided for relaxation of normal forces caused due to compression of the sample during the lowering of the cone. The normal force reading dropped to zero within 3 minutes even at the lowest temperature of 290°C. In an attempt to measure the rheological response as a function of changing texture, no preshearing was performed on the samples before the rheological test. All rheological experiments were repeated at least three times for a given condition with fresh samples in the rheometer, and error bars represent 95% confidence interval.

After rheological experiments, the samples were cooled by opening the environmental chamber of the rheometer; the melt reached a solid state in a period of about 30 s. During this cooling step, the "HOLD" button of the TA Orchestrator software was pressed to avoid overloading of the normal force transducer and to maintain

a fixed gap between the cone and plate. Once the sample reached below the softening point, the cone was separated from the plate by a light tap on the bottom plate. (*caution*: excessive force can damage the normal force transducer). Using this special protocol described above, much of the sample could be preserved as a single block, and enabled verification of the sample structure at the conclusion of the rheological experiments.

During initial experiments, the cone was lowered immediately after the melt reached the desired temperature. Shear tests were performed to attain steady state (~30 minutes), and the sample was cooled by separating the cone and plate using the procedure described above. Concentric hollow rings were observed in the sample, as displayed in **Figure 2.2a**. The hollow rings were formed in both sections of the fixture (i.e., upper and lower) in identical locations. Although the standard, vacuum-pelletizing procedure removed much of entrapped air, residual amount still persisted. Also, as measured by TGA thermograms, about 0.5 wt% loss was found in this grade of mesophase at 300°C. Thus, small amounts of volatiles were evolved during the initial melting stage that led to the formation of the rings (from coalescence of the bubbles) during these preliminary rheological tests. Similar rings have also been reported in literature studies for thermotropic LCPs (80% HBA /20% PET copolymer) due to off-gassing of the sample [Kalika et al., 1990].

In an effort to remove these volatiles before the rheological tests were commenced, a conditioning time of 80 minutes in inert nitrogen environment was employed *before* the cone was lowered into the melt. After performing shear tests, the sample was cooled and cone-plate was separated as discussed earlier. A representative photograph is displayed in **Figure 2.2b**. The absence of large, hollow rings after 80

minutes of conditioning suggests that the bubbles were not formed during rheological tests, but that they were primarily generated in the initial melting step. Thus, the 80 min conditioning period helps to romove most of the trapped gases before rheological testing.

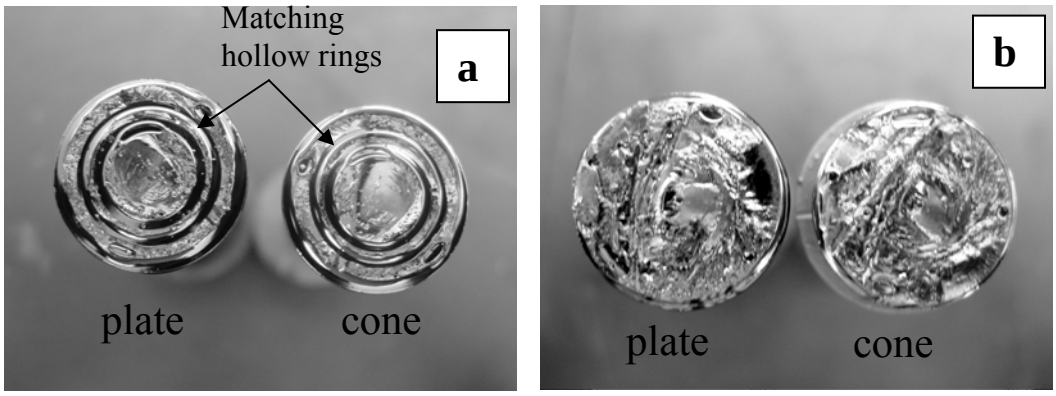

Figure 2.2: Photographs of mesophase pitch samples after they were rapidly cooled from sheared molten state (297°C and 1 s^{-1}) in a cone-plate fixture with: (a) without and (b) with devolatilization prior to shearing.

2.2 Results and Discussion

2.2.1 Rate-Sweep Mode

The steady-shear viscosities of AR-HP mesophase pitch is discussed in this section. Steady shear viscosities, as measured by conventional rate-sweep experiments, are displayed in **Figure 2.3** starting from a low shear rate of $0.1s^{-1}$ and extending to 10 s^{-1}. Shear-thinning (Region I) and Newtonian plateau (Region II) responses were observed for the AR-HP mesophase pitch, which are similar to those reported in prior studies on

other mesophase pitches [Yoon et al., 1994; Fleurot, 1998; Dumont et al., 2003; Cato et al., 2005] and TLCPs [Guo et al., 2005]. However, the plateau viscosity of 15 Pa.s for AR-HP at 305°C was approximately 2-3 times lower than that reported for ARA24R [Cato et al., 2005] and ARA24 [Fleurot, 1998]. Flow-activation energy of 223±6 kJ/mol was calculated for both regions I and II from the steady shear viscosity values. This value is comparable to that obtained for different grades of naphthalene-based pitch [Dumont et al., 2003], but higher than that measured using a high-pressure rheometer [Khandare et al., 2000].

The viscosity in Region I was found to decrease with shear rate, a trend similar to that reported in the literature [Yoon et al., 1994; Fleurot, 1998; Dumont et al., 2003; Cato et al., 2005]. However, the power-law exponent of -0.2 observed for AR-HP grade was found to be smaller in magnitude than -0.5 reported in the literature for ARA24R and ARA24 [Fleurot, 1998; Cato et al., 2005].

The theoretical basis for the -0.5 slope has been provided by the scaling arguments of Marrucci that equate elastic stresses to viscous stresses [Marrucci, 1984; Larson, 1999]. However, for this scaling argument, it was assumed that the number of defects remains unchanged and the domains deform under shear flow without any coalescence or break-up. These simplifying assumptions need not hold in real systems, and as a result the predicted slope need not be exactly -0.5. Literature studies have reported an increase of disclination density with increasing shear rates [Graziano and Mackley, 1984; Larson, 1999].

Further, for naphthalene-derived mesophase pitch, rheological parameters that are quantitatively different have been reported for grades with different softening points

[Yoon et al., 1994]. Since AR-HP possesses a lower softening point relative to the previous AR grades, we believe that its molecular weight/structure is somewhat different, which could lead to a different slope of region I. Although the power-law exponents do not match quantitatively, they are all negative, i.e, shear-thinning. Slopes shallower than -0.5 are not uncommon for liquid crystalline polymers [Walker et al., 1995], with some displaying little initial shear-thinning [Kim et al., 1993] (i.e., a power-law exponent of ≈0).

At the end of the above test cycle, the rate-sweep conditions were reversed, and the shear rate was decreased to 0.1 s^{-1}. As displayed in **Figure 2.4**, with decreasing shear rates, the viscosity values were found to remain fairly unchanged at 290 and 297°C; a small increase of viscosity was observed towards the end of the cycle at 305°C. This is in contrast to the two distinct viscosity regions (shear-thinning and plateau) observed in **Figure 2.3** during increasing shear-rate sweep. The hysteresis loop is generally not observed for liquid crystalline systems. In limited instances, PBLG has shown a hysteresis loop in region I [Larson, 1999]. However, the nature of that loop is opposite to that observed here in that the viscosities were higher for decreasing shear rates.

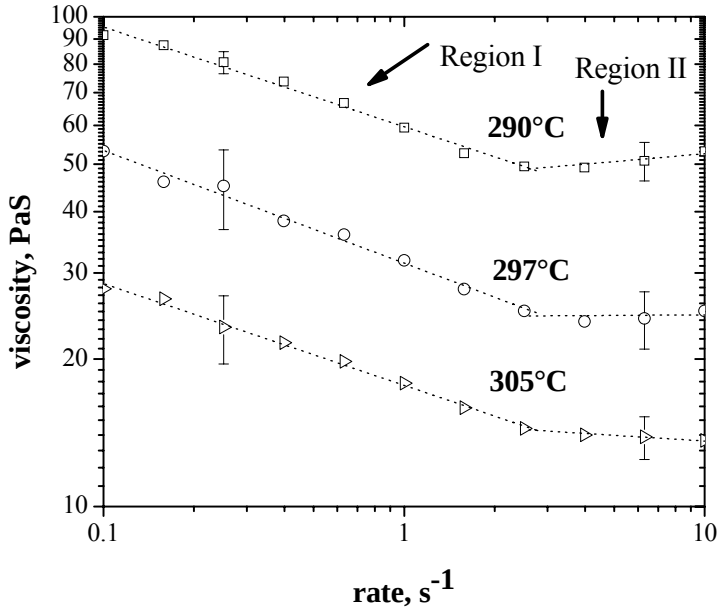

Figure 2.3: Steady shear viscosity of mesophase pitch from rate-sweep experiments for increasing shear rates. Dotted lines represent linear least-squares fit.

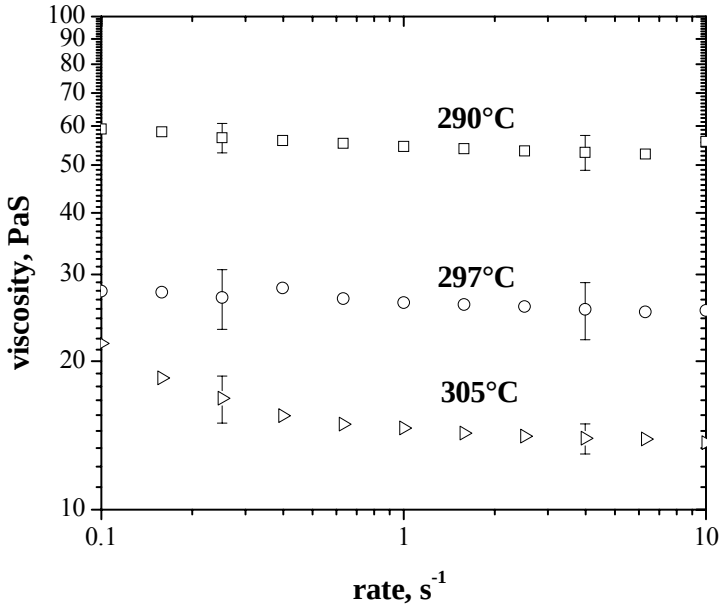

Figure 2.4: Steady shear viscosity of mesophase pitch from rate-sweep experiments for decreasing shear rates.

The primary normal stress difference (N_1) was also measured during the rate-sweep experiments and the results are displayed in **Figure 2.5a**. For all three temperatures (290, 297 and 305°C), the magnitude of N_1 was small. At the higher temperatures, small negative values were observed (~ -40 Pa).

To verify if the negative values were accurate, control experiments were conducted where the rheometer was not loaded with any material. **Figure 2.5b** displays that the normal force reading remained essentially zero for 1 hour at ambient test temperature. When similar control experiments were conducted at 297°C, the N_1 values decreased from slightly positive to about -70 Pa. Thus, such small negative values could be attributed to instrument drift, particularly since these small numbers are within the resolution limit of ±80 Pa for the available hardware. Therefore, within measurement error, N_1 values for AR-HP grade mesophase were not found to be significant, although the viscosity curves displayed non-Newtonian characteristics during increasing rate-sweep. In contrast, for ARA24R grade of mesophase pitch, negative normal stresses have been reported below the shear rate of 10 s^{-1} [Cato et al., 2005].

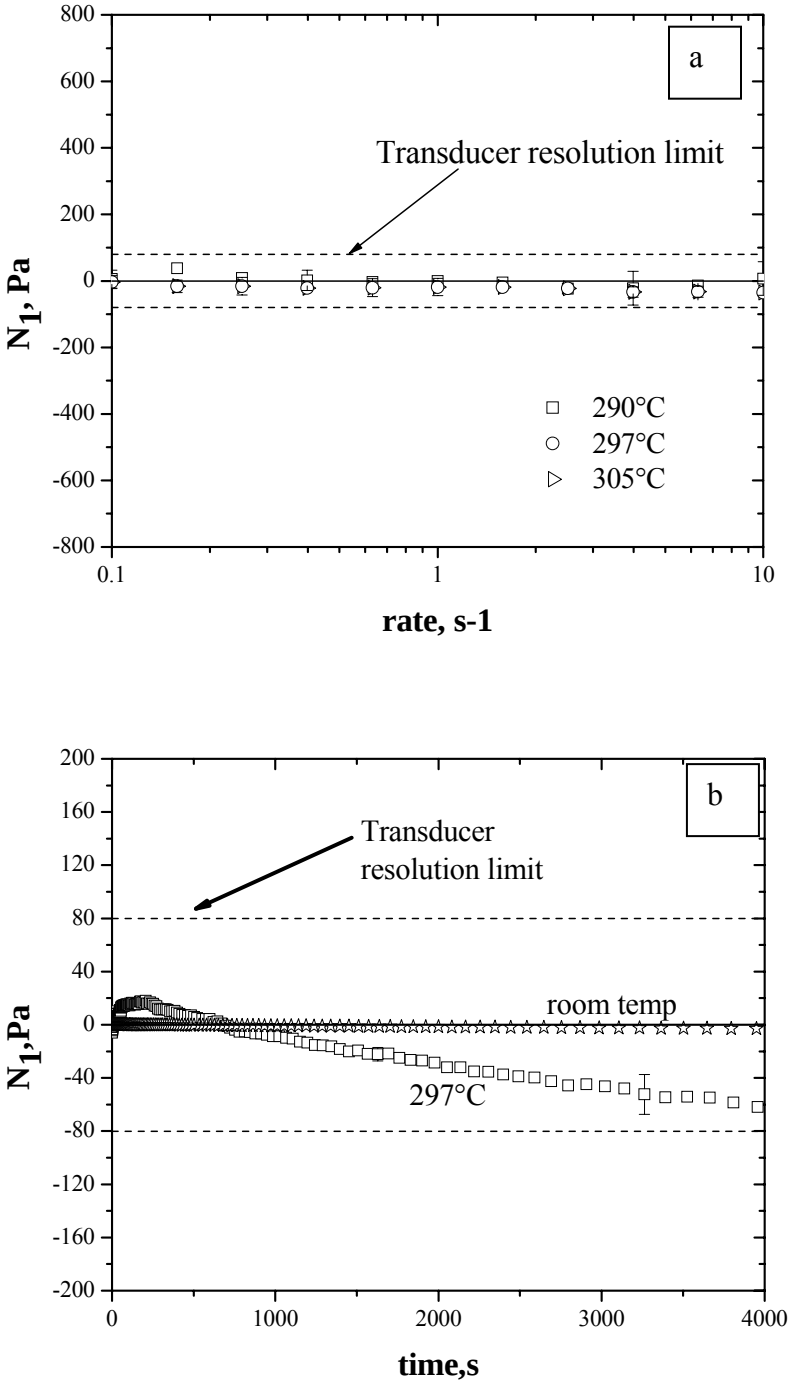

Figure 2.5: Primary normal stress difference (N_1) for: (a) mesophase pitch measured from rate-sweep experiments at different temperatures, and (b) drift of normal force transducer without sample at room temperature and 297°C.

2.2.2 Transient Viscosity Tests

To investigate the different responses observed during increasing *vs* decreasing rate sweep tests, experiments were performed at individual shear rates starting with fresh, unsheared samples. The evolution of the transient shear stress response to a steady state was measured, and is reported as a function of strain (product of shear strain-rate and test time). The viscosity values can be obtained as a ratio of the shear stress divided by the corresponding shear rate. Since time evolution of shear stress depends on the shear rates, to compare the responses for different shear rates, the transient shear stress responses have been plotted as a function of strain. **Figure 2.6** shows the results for a shear rate of 1 s^{-1} at 297°C. After the initial transience, the shear stress approached a steady-state value, and remained fairly constant at 35±2 Pa over 3000 strain units (*su*). This stable response for a period of about 1 hour is consistent with the thermal stability inferred from the 99.5 wt% mass retention observed by TGA tests.

To investigate the transient response that got masked in **Figure 2.6a** due to a compressed strain-scale, the same stress results are plotted up to a strain of 100 units on a logarithmic strain scale (**Figure 2.6b**). A local stress maximum was observed at a strain value ranging from 1.1 to 1.7 *su,* and a local minimum was observed in the range 5-8 *su*; these strain values are approximated as ~1 *su* and ~6 *su*. A small second maximum was observed between 10 and 20 *su*; however, the extent of this maximum was small relative to the first one, and not significantly greater than the experimental error.

To confirm that the nonmonotonic transient responses were not an experimental artifact, the rheological experiments were also performed on a calibration fluid. The shear stress results for calibration fluid, also displayed in **Figure 2.6b,** do not show any maximum or minimum. The steady shear stress and correspondingly the viscosity of 14±1 Pa.s matched within 10% the value of 13 Pa.s reported by the manufacturer.

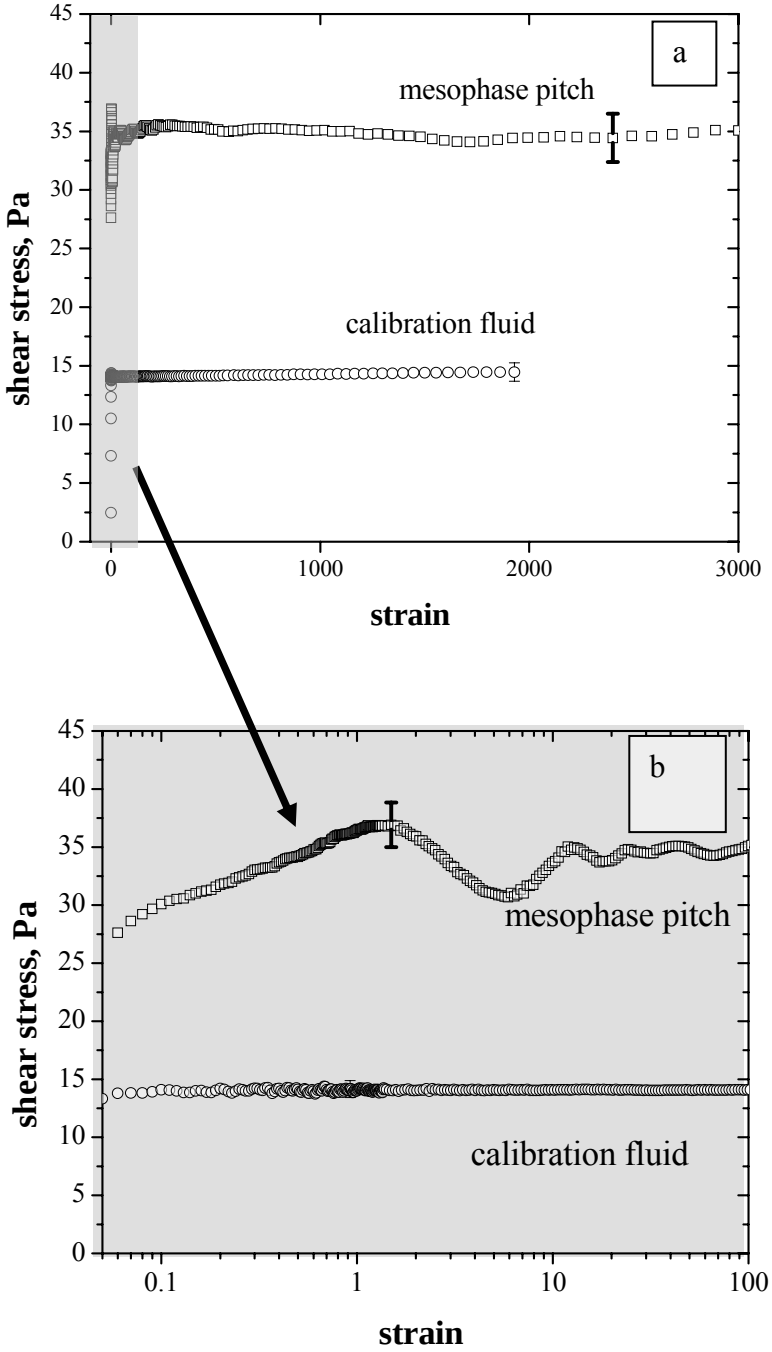

Figure 2.6: Transient response of mesophase pitch at 1 s^{-1} and 297°C: (a) transient shear stress using 25 mm cone-plate in linear strain scale, long term, (b) initial transience, logarithmic strain scale.

The tests on the calibration fluid and mesophase pitch (at 297°C) were also repeated using another cone-plate (ARES) rheometer. Results thus obtained were similar with those reported above. Further, to confirm that the transient rheological responses presented here are independent of fixture geometry, experiments were also performed in two additional fixture geometries, namely, 50 mm cone-plate fixture with a cone angle of 0.04 rad and 25 mm parallel-plate fixture. The normalized shear stress (ratio of transient shear stress and its steady-state value) responses of initial transience are shown in **Figure 2.7**, and the result from 25 mm cone-plate fixture is also plotted. The shear-stress responses for the 25 and 50 mm cone-plate fixture were similar, except a slight shift of maximum was observed for 50 mm fixture. The response obtained from 25 mm parallel-plate fixture was also similar; the numbers were slightly different than that obtained from cone-plate fixture due to varying shear rates within the parallel-plate geometry. In all these cases, local maxima and minima were observed within the same strain range. Therefore, the nonmonotonic transient response observed for AR-HP mesophase pitch appears to be its material property and not an instrumental artifact.

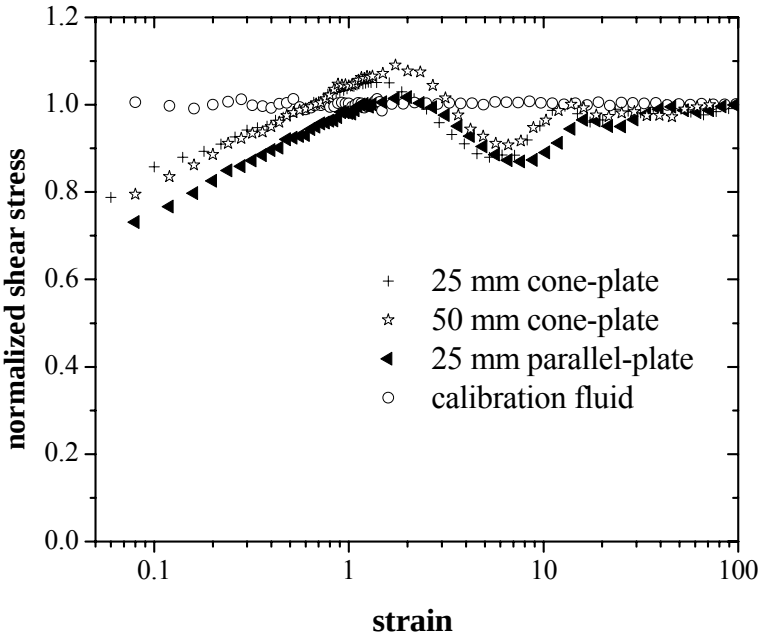

Figure 2.7: Normalized transient shear stress using 25 mm cone-plate fixture (□), 50 mm cone-plate fixture (*), and 25 mm parallel-plate fixture (◀). Also shown is the transient response of a calibration fluid (○).

In some experiments, as shown in **Figure 2.8**, a slight drop of shear stress was observed as the samples approached steady-state (~1000 s). These samples displayed the presence of a few voids or a small ring in the solidified state (inset, **Figure 2.8**) due to the coalescence of small bubbles that remained even after the extensive degassing step. Since the presence of bubbles can affect the transient response, such experiments were excluded from further analysis. It is further noted that the transient response of the early samples that were not devolatilized showed the same trend (i.e., decrease of viscosity). In fact, due to the presence of a significant amount of gas bubbles, the decrease was quite significant as illustrated in **Figure 2.9**. The results for devolatilized samples are also shown for comparison purpose.

For initial samples that were not devolatilized, the progression of bubble coalescence during shearing is illustrated in **Figure 2.10**. With shearing, the dispersed gas bubbles started to coalesce and form hollow rings. The area of these void regions was approximately 10% of total area. Correspondingly, as seen in **Figure 2.9a**, the steady-sheared stress value of such sample was approximately 10% lower than that observed for devolatilized sample.

It is interesting to note that the initial shear-stress values for non-devolatilized samples were higher than that observed for devolatilized samples. This may arise from strong anchoring of disc-like molecules at the bubble surface. Strong anchoring of disc-like molecules at the bubble surface has been reported earlier in the literature [Jian et al., 2003].

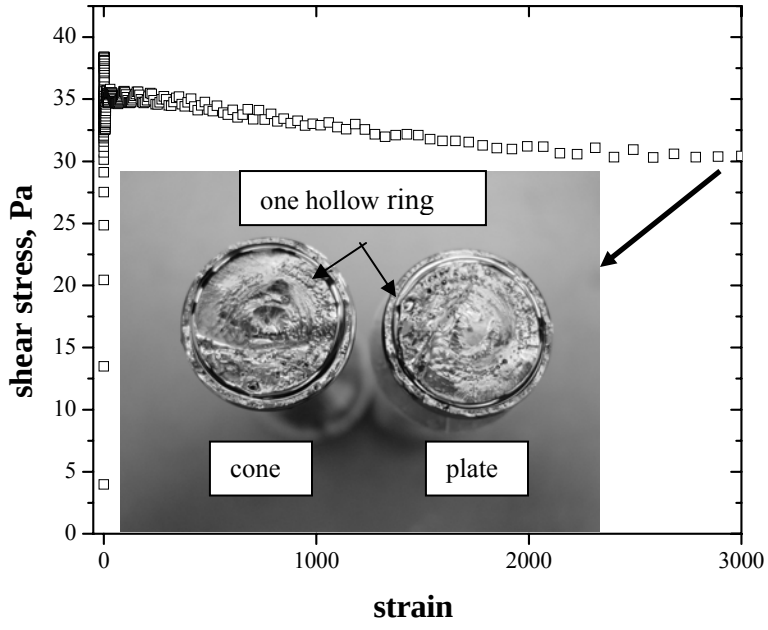

Figure 2.8: Transient shear stress of mesophase pitch at 1 s^{-1} and 297°C for a typical run where slight drop of shear stress was observed. Photograph at inset shows a presence of one hollow-ring at the end of the run.

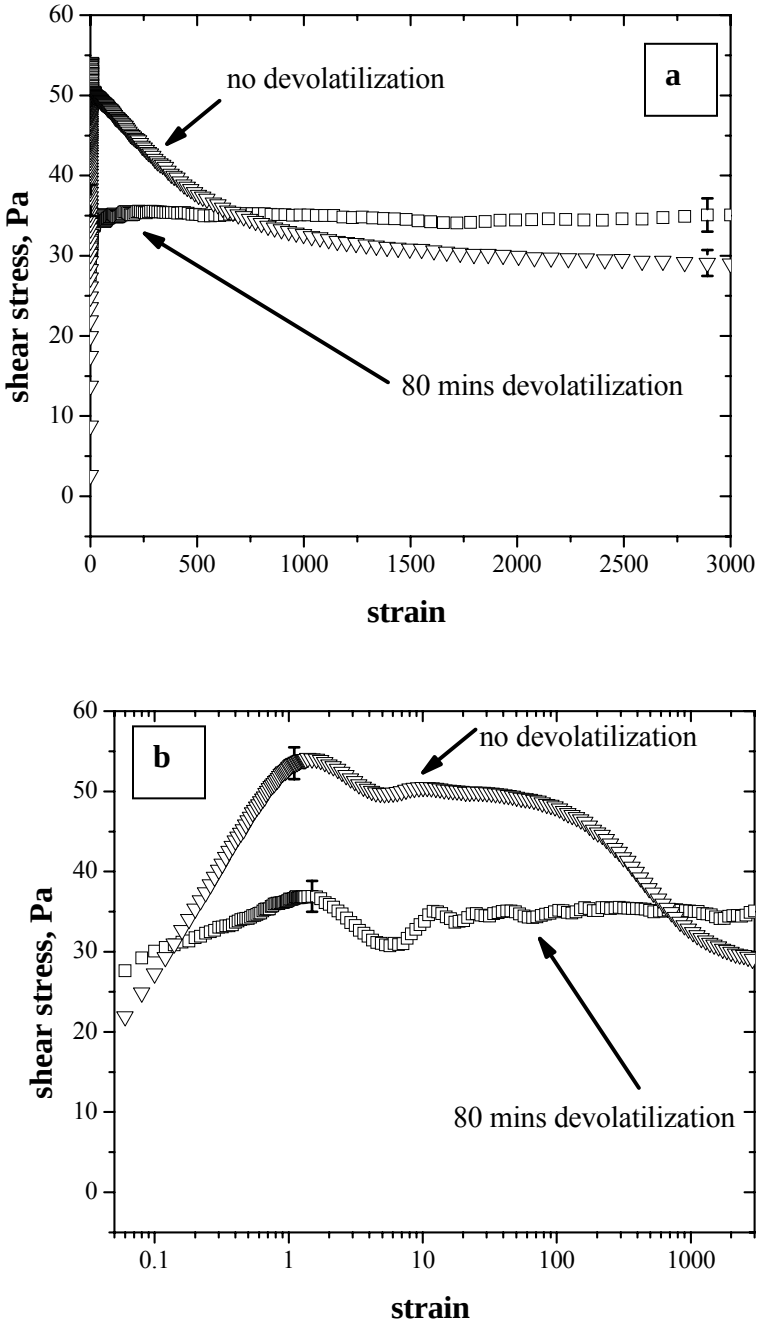

Figure 2.9: Transient response of mesophase pitch at 1 s^{-1} and 297°C for the samples with no devolatilization and 80 mins of devolatilization: (a) transient shear stress using 25 mm cone-plate in linear strain scale, long term, (b) initial transience, logarithmic strain scale.

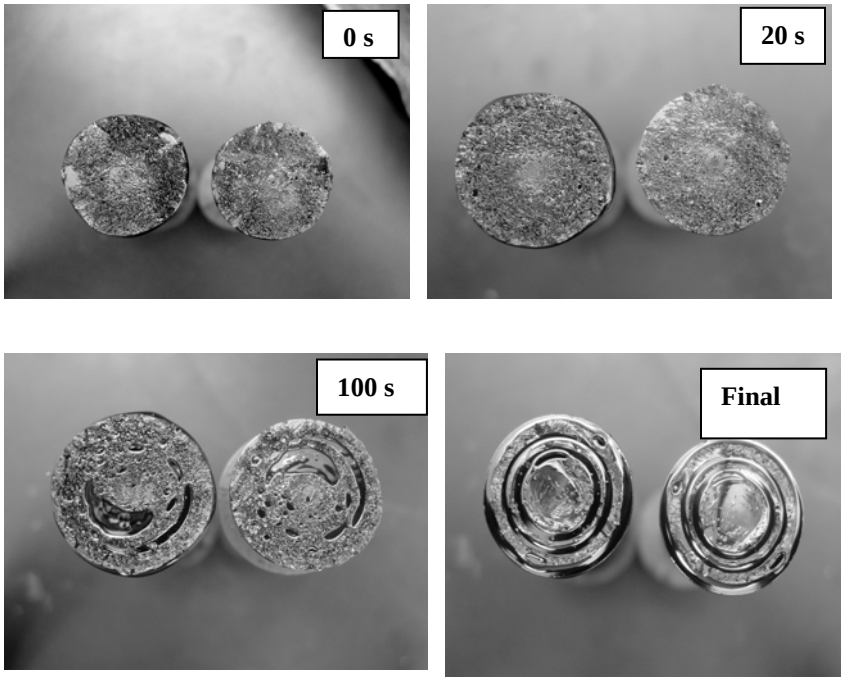

Figure 2.10: Photographs of mesophase pitch samples after they were rapidly cooled from sheared molten state (297°C and 1 s^{-1}) in a cone-plate fixture without devolatilization prior to shearing. The progression of bubble coalescence into hollow rings during shearing is illustrated.

The transient shear stresses of AR-HP at two other temperatures, 290°C and 305°C (with 297°C data provided for reference), at a shear rate of 1 s^{-1} are displayed in **Figures 2.11a** and **b**. At 290°C, a local maximum at ~1 *su* and a minimum at ~6 *su* were observed. The small second maximum was also observed at these temperatures between 10 and 20 *su*. Again, the extent of the maximum was small relative to the first peak and not significant relative to the measurement error. The shear stress values reached a steady state after initial transience. The magnitude of the maxima and minima became less prominent as the temperature increased**.** At 305°C, the maximum and minimum were observed in every experiment, but expectedly the magnitude of the measured stress

had decreased significantly (particularly at the low shear rate of 1 s^{-1}). The decrease of shear stress and the extent of maxima/minima with increasing temperature may be attributed to weaker viscous and elastic forces within the fluid.

The transient experiments at 10 s^{-1} (Region II) were also performed, and are compared with those at 1 s^{-1} in **Figure 2.12.** The normalized shear stress responses (ratio of transient and steady values), plotted as a function of time in **Figure 2.12a**, show that the stress reached a steady-state by ~300 s for both shear rates. However, as shown in **Figure 2.12b,** the maxima/minima did not match on the time scale for the two shear rates. If the stress was plotted as a function of strain (**Figure 2.12c**), the maxima and minima were observed at similar strain locations (~1 and 8 *su*), i.e., the transient responses followed the strain-scaling phenomenon in an approximate sense. Literature studies show that some liquid crystalline polymers follow the strain scaling exactly [Larson, 1999], but some follow it only in an approximate sense [Grizzuti et al., 1990; Han and Kim, 1994].

Although maxima in shear stress have been reported earlier for ARA24/ARA24R pitches [Fleurot, 1998; Cato et al., 2005], minimum in shear stress has not been reported for earlier mesophases. Also, the magnitude of the overshoot was observed to be as high as 5 times the steady state value [Fleurot, 1998; Cato et al., 2005]. We believe that these differences may arise from a lower molecular weight or a different MW distribution of the AR-HP grade, which possesses a lower softening point. Note also that the current grade displayed immeasurably small first normal-stress difference at low-medium shear rates.

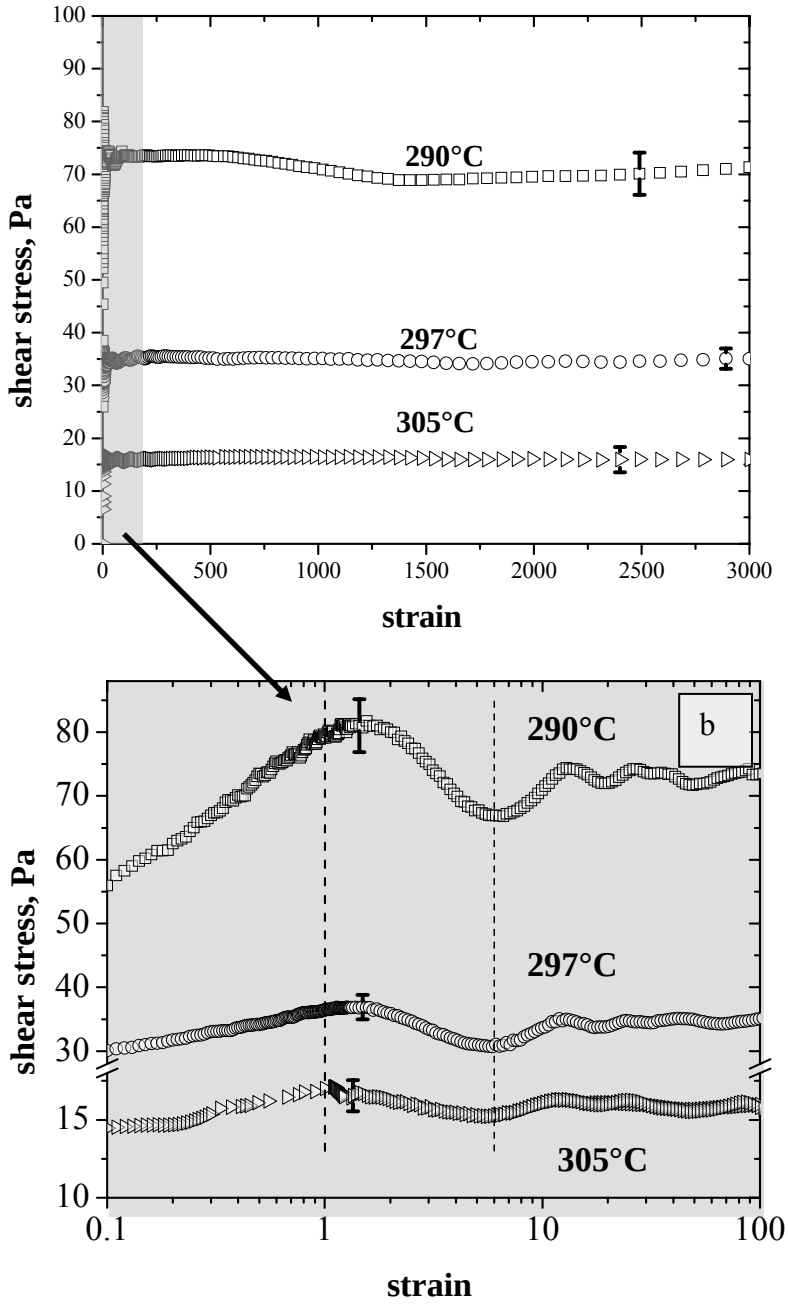

Figure 2.11: Transient shear stress of mesophase pitch at three different temperatures and 1 s^{-1}: (a) linear strain scale, long term, and (b) initial transience for 290, 297, and 305°C, logarithmic strain scale. Response for 305°C is shown on an enlarged scale.

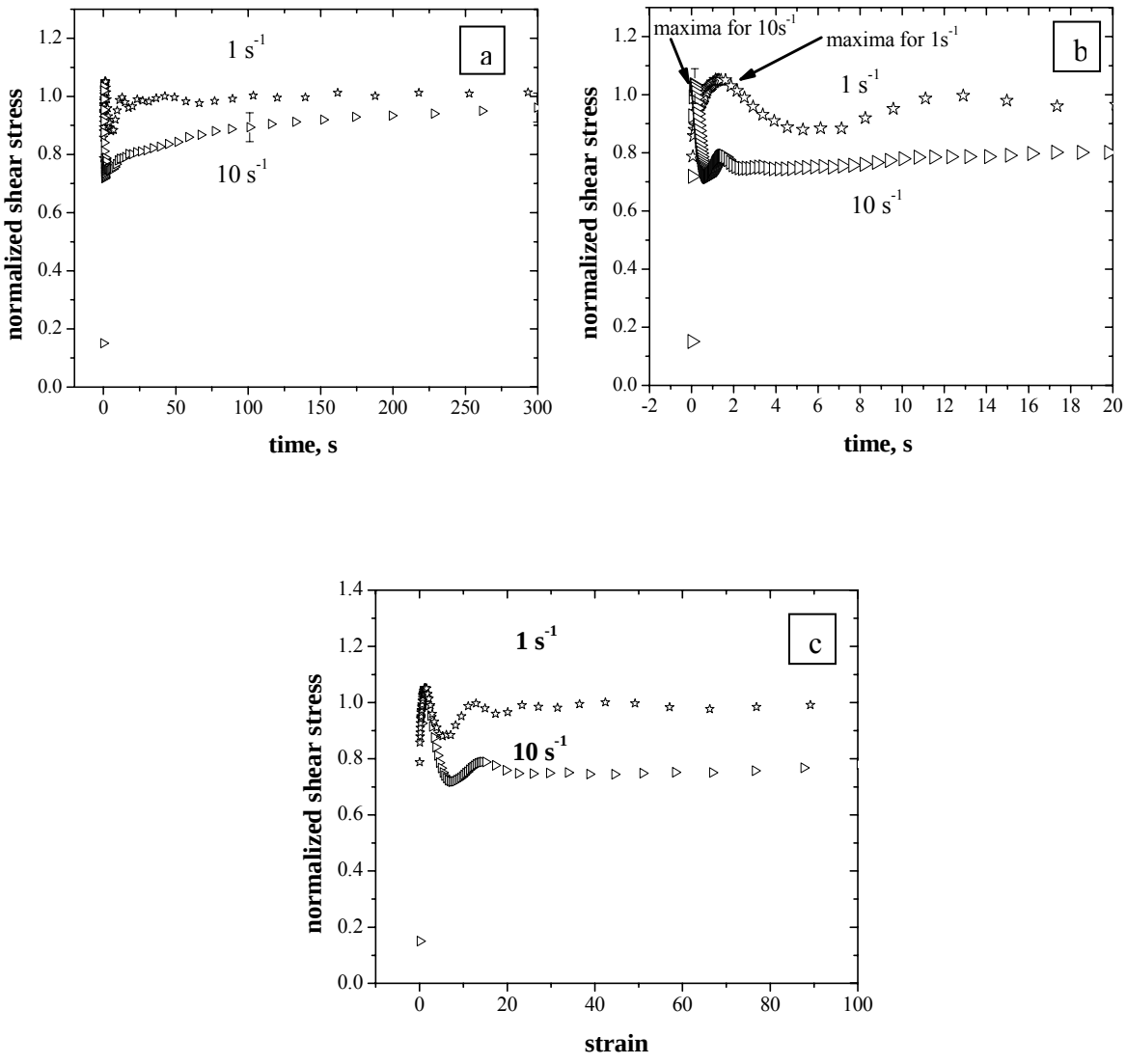

Figure 2.12: Normalized transient shear stress of mesophase pitch at 1 s^{-1} and 10 s^{-1} at 297°C presented on: (a) time scale, 300 s, (b) time scale, 20 s, and (c) strain scale, 100 *su*.

2.2.3 Flow Reversal and Interruption

To further investigate transient effects, flow reversal experiments were performed where the sample was first allowed to reach steady state, and then the flow direction was reversed suddenly. For the experiments conducted at 297°C and 1 s^{-1}, results are displayed in **Figure 2.13**. On a linear strain scale, **Figure 2.13a** shows that after the first steady state was achieved and the flow direction was reversed (at ≈3000 *su*), the stress rapidly approached a similar value as the first one but in the opposite direction. To evaluate the transience associated with flow reversal, these data are plotted in **Figure 2.13b** on a logarithmic strain scale after resetting the time scale for the flow reversal data. It is evident that no maxima or minima were observed during flow reversal. Assuming that the texture had reached a steady state when the viscosity reached its steady state value, flow reversal would not be expected to cause further change in texture, and consequently, no maxima/minima would be expected. These results indicate that the maximum/minimum values during flow startup were directly related to textural changes in the fluid.

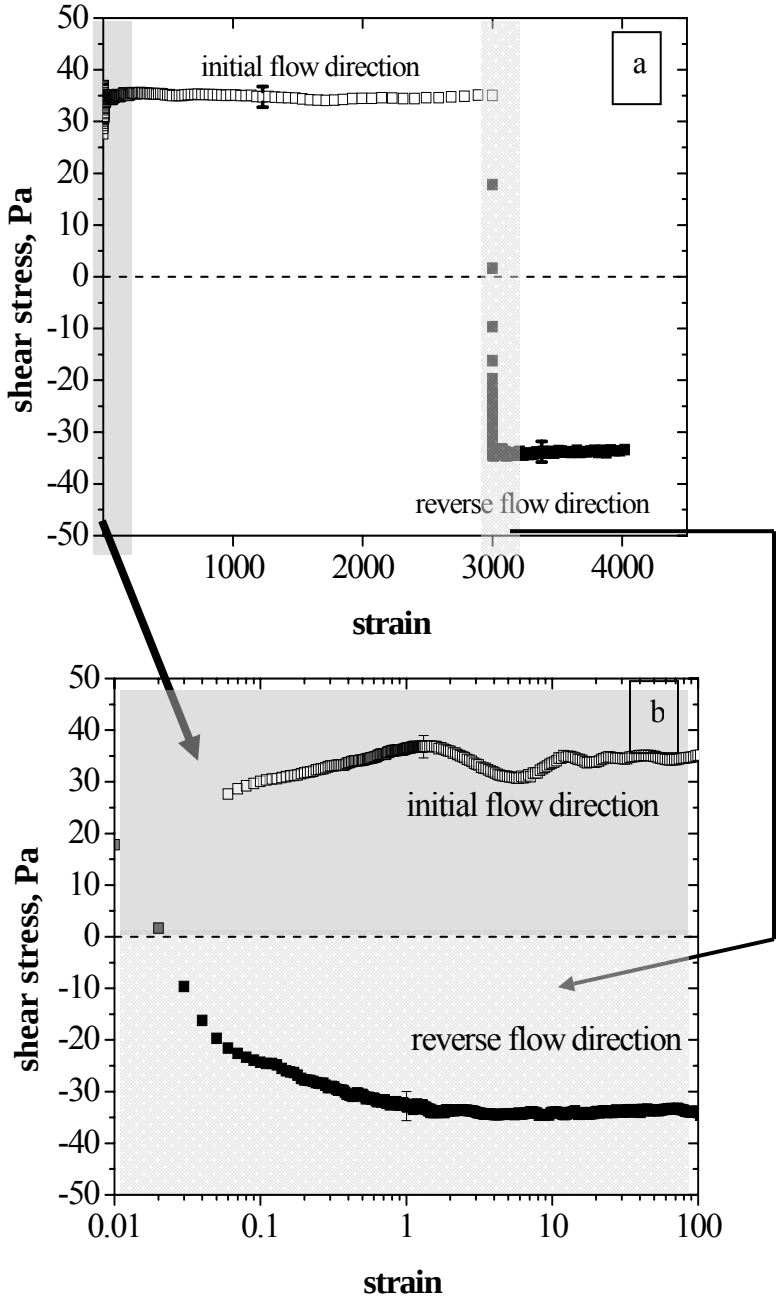

Figure 2.13: Transient shear stress of mesophase pitch before and after flow reversal experiments at 1 s^{-1} and 297°C.

In another set of experiments, multistep shearing with different rest periods between two shearing steps was performed. **Figures 2.14a-d** show the transient responses for a typical run after 1, 10, 100, and 1000 s of rest periods, respectively, at 1 s^{-1} and 297°C; the original transient response is also plotted in each graph for comparison. As observed in **Figure 2.14a**, the shear stress response after 1 s of rest period (following steady-shear) approached steady-state monotonically, which is in contrast to the maximum/minimum behavior observed during initial shearing. After 10 s of rest following steady-shear (**Figure 2.14b**), the transient response remained unchanged, i.e., monotonic approach to steady-state. After 100 s of rest (**Figure 2.14c**), a slight change in response appeared (although not significant). However, after ~1000 s of rest period, the maximum and minimum clearly reappeared in transient shear stress before it approached steady-state. The locations of the maximum/minimum were similar as those observed for the initial response. These results indicate that for a sample originally sheared at 1 s^{-1}, a rest period of ~1000 s leads to significant structural relaxation. No significant increase in the extent of maximum and minimum was noted with an increase of rest time to 3000 s.

Transient stress responses have been studied for flexible-chain polymers as well as liquid crystalline polymers [Ugaz et al., 2001; Han and Kim 1994; Mather et al., 2000; Meissner,1972]. For flexible chain polymers, only an overshoot of shear stress is observed at moderate-high shear rates, and is related to chain/molecular orientation. The situation is more complicated for liquid crystalline systems due to their complex microstructure. In a recent literature study [Grecov and Rey, 2003a], the transient rheology of discotic mesophases subjected to slow shear start-up flows was simulated for

different initial twist and tilt angles of the discs. Simulation results show that the transient response is non-monotonic and depends on orientational changes of the discs. In another simulation study for rod-type liquid crystalline systems [Grecov and Rey, 2004], it was shown that defect nucleation and defect coarsening resulted in change of shear stress during shearing. In real mesophase fluids, orientational change of disc-like layer planes and textural changes can take place, and result in the nonmonotonic rheological responses, such as those observed in this study.

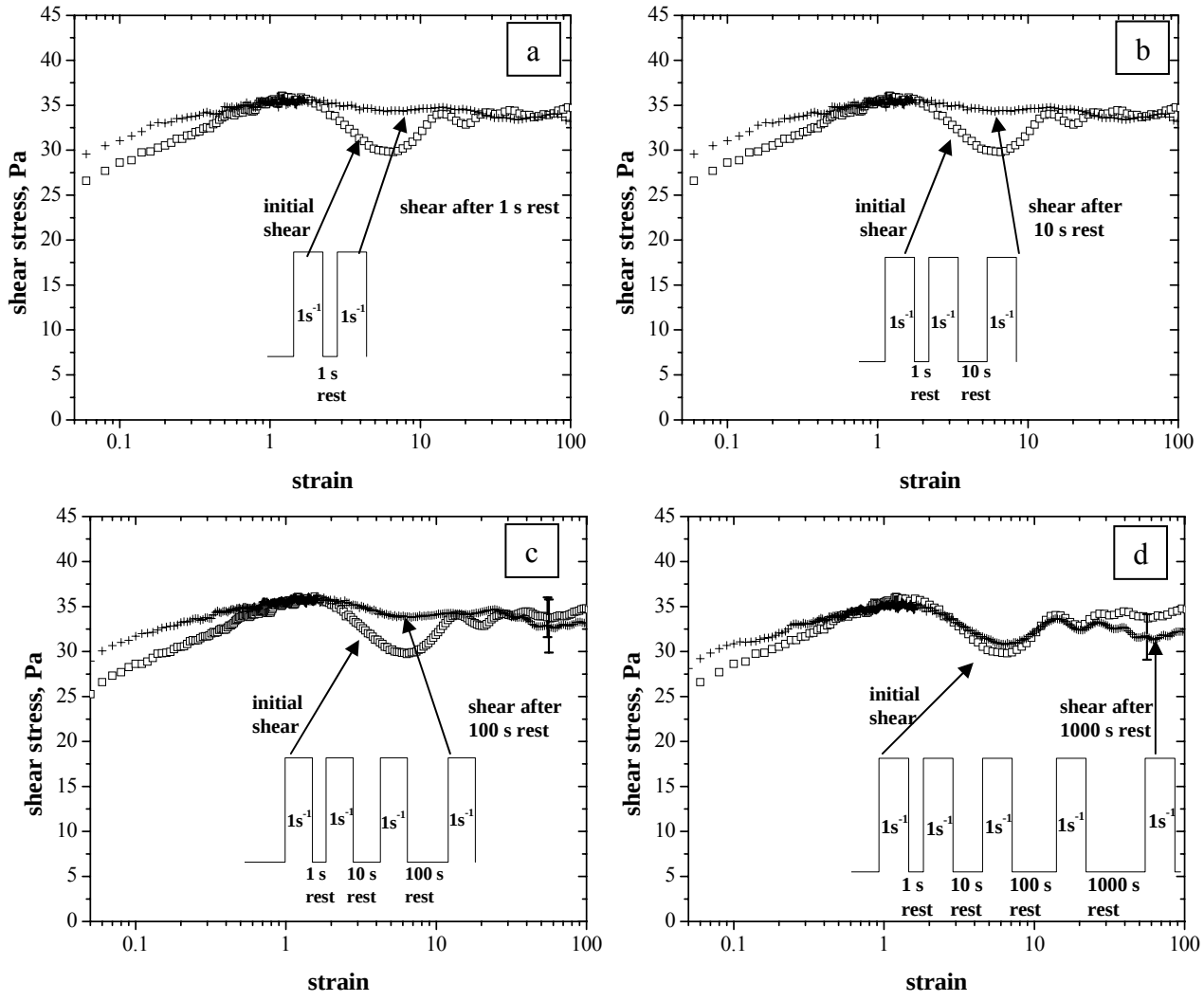

Figure 2.14: Transient shear stresses of mesophase pitch at 1 s^{-1} and 297°C for different rest periods: (a) 1 s, (b) 10 s, (c) 100 s, and (d) 1000 s. Also shown is the initial transient response (□).

2.3 Conclusions

The steady shear viscosities for AR-HP mesophase pitch obtained from increasing rate-sweep experiments exhibited shear-thinning (Region I) and plateau (Region II) responses. But, the primary normal stress difference generated during the viscometric shear flow was found to be small (within instrument resolution). During transient tests, local maxima and minima were observed in transient shear stress for various shear rates and temperatures tested. During flow reversal experiments following steady flow at $1s^{-1}$, where the microstructure was already evolved, absence of maximum/minimum indicates that the nonmonotonic behavior during flow startup was directly related to the initial relaxed state of the discotic AR-HP mesophase pitch. After 1000 s of rest, the maximum/minimum reappeared during shearing, suggesting that such a rest period can lead to significant microstructural relaxation. Thus, transient shear stress/viscosity of discotic mesophase pitch melt was experimentally shown to possess nonmonotonic features that are not observed in flexible-chain polymers, but are generally consistent with those predicted from nematodynamics. The evolution of microstructure during transient experiments is reported next in Chapter 3.

CHAPTER 3

MICROSTRUCTURAL EVOLUTION DURING SHEAR FLOW

Numerous studies, both *in situ* and *ex situ*, have been performed on liquid-crystalline polymers to understand the evolution of microstructure and orientation by optical microscopy [Larson and Mead, 1992; de'Nève et al., 1993; Mather et al., 2000; Guo et al., 2005] and X-ray diffraction [Picken et al., 1990; Romo-Uribe and Windle, 1996; Ugaz et al, 2001]. Unfortunately, due to the opacity of pitch, real-time microscopic studies can not be performed on mesophase pitches; instead, offline and reflected-mode optical microscopy on solidified pitch samples has been used to characterize the microstructure.

In literature studies, the effect of shear flow on the microstructure of mesophase pitch was reported [Fleurot, 1998; Cato and Edie, 2003]. Similar to polymeric systems, diffraction techniques such as X-ray diffraction and electron diffraction technique were used to understand the orientation of the disc-like molecules in as-spun pitch fibers and in mesophase spherules [Brooks and Taylor, 1965; Barnes et al., 1998].

Different microstructures are a consequence of different flow fields encountered during melt-processing of mesophase pitch. It is noted, however, that the flow field in circular tubes and capillaries is not homogeneous in that the shear rates and stresses vary across the capillary cross-section. The high shear rates reported in capillaries during fiber spinning experiments are the values estimated at the capillary wall (~1000 s^{-1}). This high

shear rate (and shear stress) decreases away from the wall and vanishes at the centerline. During other steps of fiber extrusion, such as the flow in pipes, manifolds, and spinneret counter-bores, the shear rates are moderate (of the order of 1-100 s^{-1}). There are also flow situations, such as processing of carbon-carbon composites, that utilize molten mesophase infiltration at low-medium pressures [Fathollahi et al., 2005]. The shear rates in such processes are expected to be in the low-medium range and the flow is transient.

Rheological behavior at low-medium shear rates using the cone-plate geometry was discussed in Chapter 2. Although high shear rates cannot be generated in this geometry, it is a valuable technique for generating homogeneous (constant) shear rate and shear stress within the entire flow geometry. In this chapter the microstructure development during flow startup and transient experiments is reported. A special protocol was developed to preserve the samples with different rheological histories. Microstructural study was primarily performed using optical microscopy. For limited samples, the results were also verified using X-ray diffraction technique. The experimental results presented here led to a systematic understanding of the flow-microstructure relationship, and such understanding has been helpful to interpret the microstructural results that were observed during typical processing flow (presented in Chapter 5). Also, these results helped us to model/simulate the flow behavior of this material in simple-shear flow (presented in Chapter 6).

3.1 Experimental

3.1.1 Sample preparation

Rheology experiments were performed in TA Instruments ARES rheometer (TA Instruments Inc.) primarily using a 25 mm cone-plate fixture. After rheological experiments, the cone and plate were separated using the special protocol described in Chapter 2 (also in Appendix A). Using this protocol, much of the sample was preserved as a single block. The individual, solidified blocks were then embedded in Castolite resin blocks (Leco Corp.) and polished in an automated Buehler ECOMET 2 polisher (320 to 1200 grit papers, Buehler). **Figure 3.1** is a schematic view of the various sections for which the microstructure was studied. The flat surface (r-ϕ or vorticity-flow plane), AA', was easiest to polish, and a series of observations were made on this plane. A select group of samples was also polished in two orthogonal sections, BB' (r-θ or vorticity-gradient plane) and CC' ($\theta-\phi$ or gradient-flow plane). The small thickness of the samples (< 1 mm) in the two orthogonal sections made the polishing and subsequent study of microstructure rather time-consuming and experimentally challenging. At least three replicate samples were prepared for a given condition starting with a fresh sample in the rheometer.

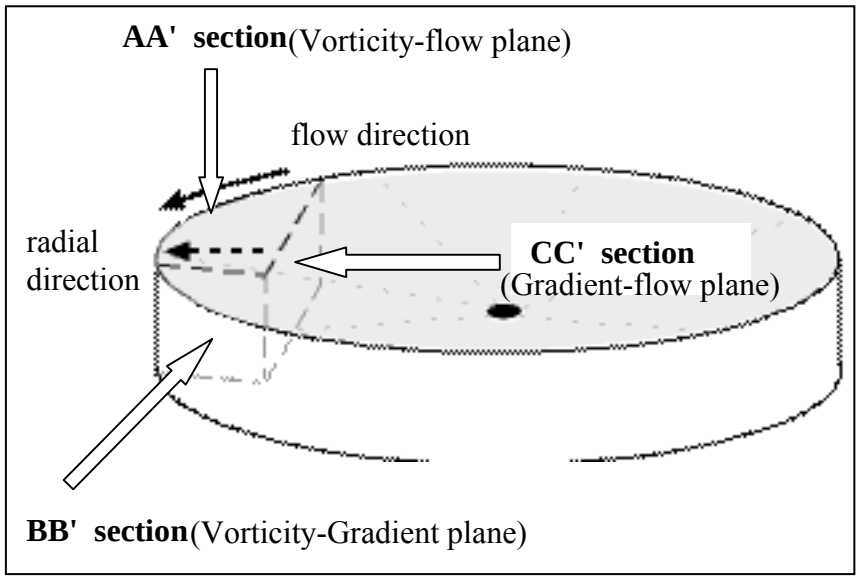

Figure 3.1: Schematic of a typical sample collected for microstructural study with three orthogonal sections identified: AA' section is r-ϕ or vorticity-flow plane, BB' section is r-θ or vorticity-gradient plane, and CC' section is θ–ϕ or gradient-flow plane.

3.1.2 Optical microscopy

The polished samples were examined in two different optical microscopes, Aus Jena Jenapol Interphako and Olympus BX-60 with cross-polarizers and a first-order red plate. During microstructure identification, a pyrolytic graphite sample deposited around a PAN-based carbon fiber was used for calibration purpose, a procedure similar to that reported in the literature [McHugh, 1994]. In this specimen, the graphite layers were aligned parallel to the fibrous core, i.e., tangential. As displayed in **Figure 3.2**, the graphene layers oriented in NE-SW (//) direction appeared blue, those oriented in NW-SE (\\) direction appeared yellow, whereas those in N-S (‖) and E-W (=) orientations appeared magenta, as did the isotropic PAN fiber core at the center. Details of optical

microscopy for various carbon materials is available in the literature [Oberlin et al., 1998].

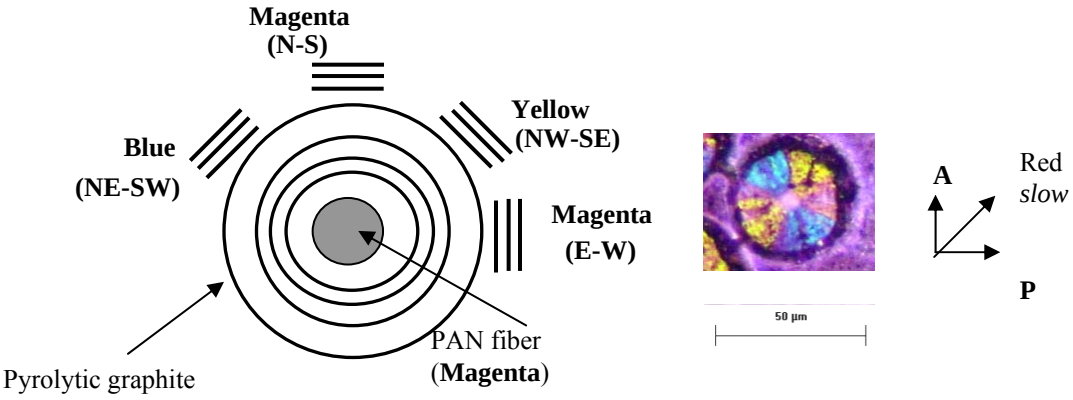

Figure 3.2: Color identification using cross-polarizers and a first-order red plate for pyrolytic graphite deposited around a PAN fiber.

After performing the color calibration, microstructural characterization was performed on the samples collected after rheological experiments. Multiple micrographs were obtained from different sections of a given sample using a Sony digital camera (Cyber-shot DSC-S70). The color contrast was enhanced by using Adobe Photoshop®. Image analysis was performed by using Image-Pro® 4.1 software.

For the micrographs that will be presented in the results section, the radial direction of the cone-plate fixture will be identified by a dashed arrow ( ), whereas the flow direction will be shown by a solid arrow ( ). Most of the micrographs presented here were obtained by placing the samples in such a way that the radial/flow direction was in +45/-45° relative to the polarizer-analyzer. These +45/-45° orientations were chosen (rather than 0/90°) because clear identification of orientation is possible in

terms of blue and yellow colors when the molecular/layer-plane orientation is in +45/-45° directions relative to the polarizers.

3.1.3 X-ray Diffrcation

The microstructure of rheological samples was also investigated using wide-angle X-ray diffraction (WAXD). The Rigaku 2-D diffractometer was equipped with an Osmic Micromax Cu Kα X-ray source and a collimator with a pinhole size of 0.3 mm, and was operated at 45 kV and 67 mA. The distance from the sample to the detector was 114 mm. Diffraction patterns were obtained using image plates, which were scanned in a Fuji BAS 1800 unit. An exposure time of 30 minutes per image was utilized throughout the study, and the diffraction patterns were analyzed using Polar® 2.6.8 software.

As shown in **Figure 3.3a,** for AA′ section (flow-vorticity plane), samples were consistently analyzed at the same location on the rheometer plate (3 o'clock position). For BB′(vorticity-gradient plane) and CC′(gradient-flow plane) sections, position of the samples with respect to the X-ray beam are shown in **Figures 3.3b** and **3.3c,** respectively. All the samples were mounted on transparent Scotch® tape and as indicated in **Figure 3.3**, the X-ray beam was always normal to the plane of interest. After scanning of a sample, the sample was removed from the tape and a scan of the blank tape was performed to obtain background scattering correction.

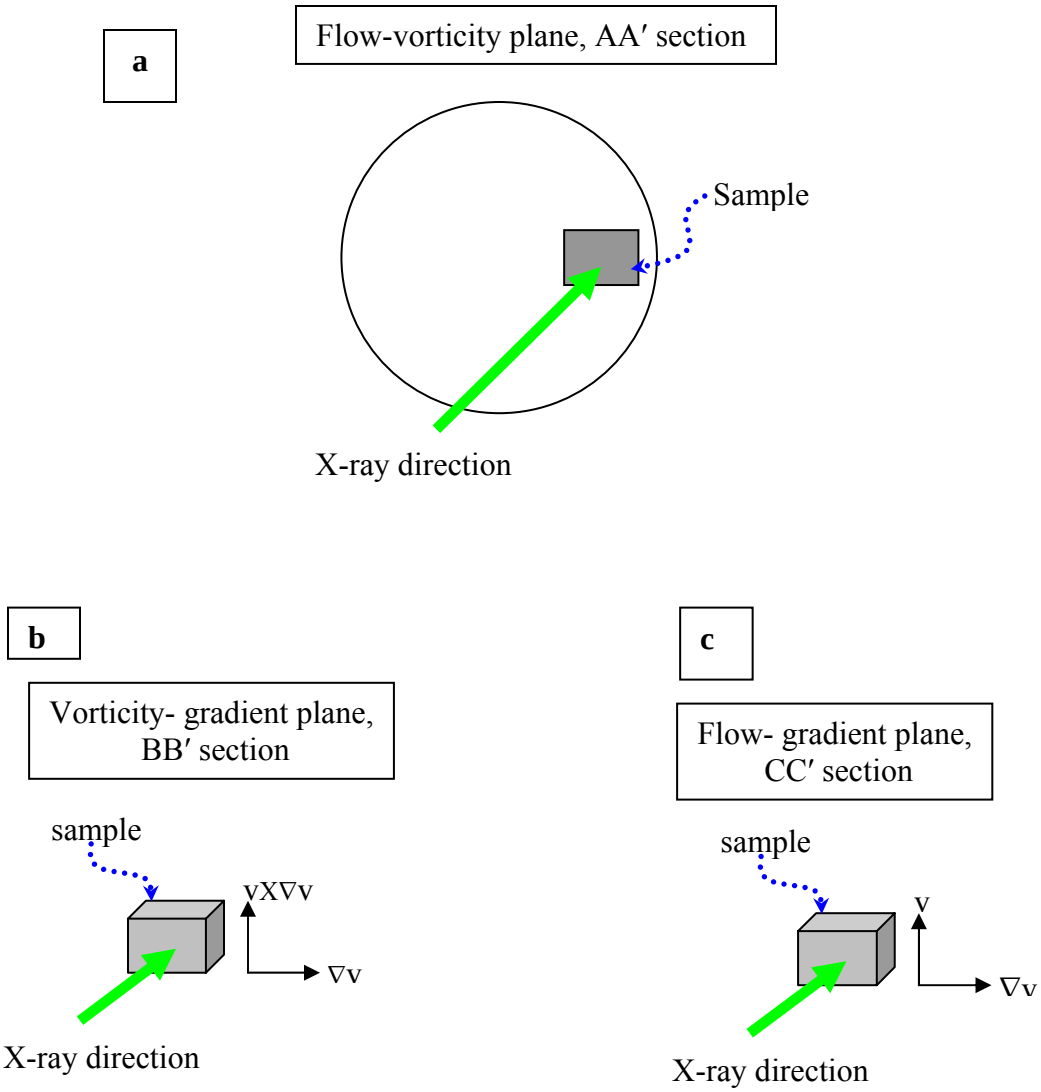

Figure 3.3: Schematic of typical sample location for X-ray experiments: (a) AA′ section, (b) BB′ section, and (c) CC′ section.

The degree of orientation for (002) planes was quantified using an average orientation parameter, which was determined from a second order Legendre polynomial of the orientation distribution. This parameter, *f*, also called Herman's orientation parameter, is given by $f = \frac{1}{2}(3\langle\cos^2\alpha\rangle - 1)$. The azimuthal angle α was measured from

the meridian and is shown in **Figure 3.4**. The limiting value for *f* is -1/2 when the azimuthal intensity is only equatorial (α approaches 90°) and *f* is 1 when the azimuthal intensity is meridianal (α approaches 0°).

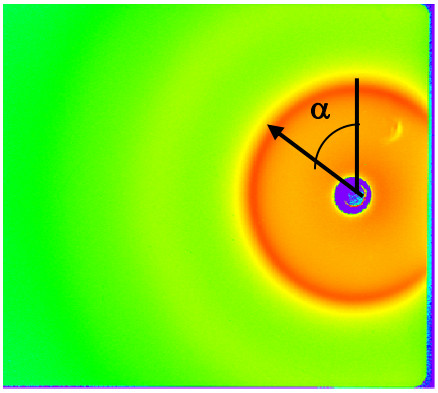

Figure 3.4: Schematic shows the direction of azimuthal angle α, which was used to estimate the Herman's orientation parameter.

3.2 Results and Discussion

3.2.1 Optical microscopy

The microstructure of unsheared and sheared mesophase pitch is discussed in this section, which is based on our recent paper [Kundu and Ogale, 2006]. **Figure 3.5a** displays the microstructure of an unpolished, free surface of a quenched sample that was melted at 297°C and held for 80 minutes on the bottom plate of the rheometer. Similar microstructure was also observed at 290 and 305°C and is displayed in **Figures 3.5b** and **c**. The microstructure was typical of nematic fluids, and similar to that reported in the literature [Jian et al., 2003]. The microstructure of a polished, unsheared sample is

displayed in **Figure 3.5d**. Although less sharper, the microstructure was similar to that observed for free-surfaces.

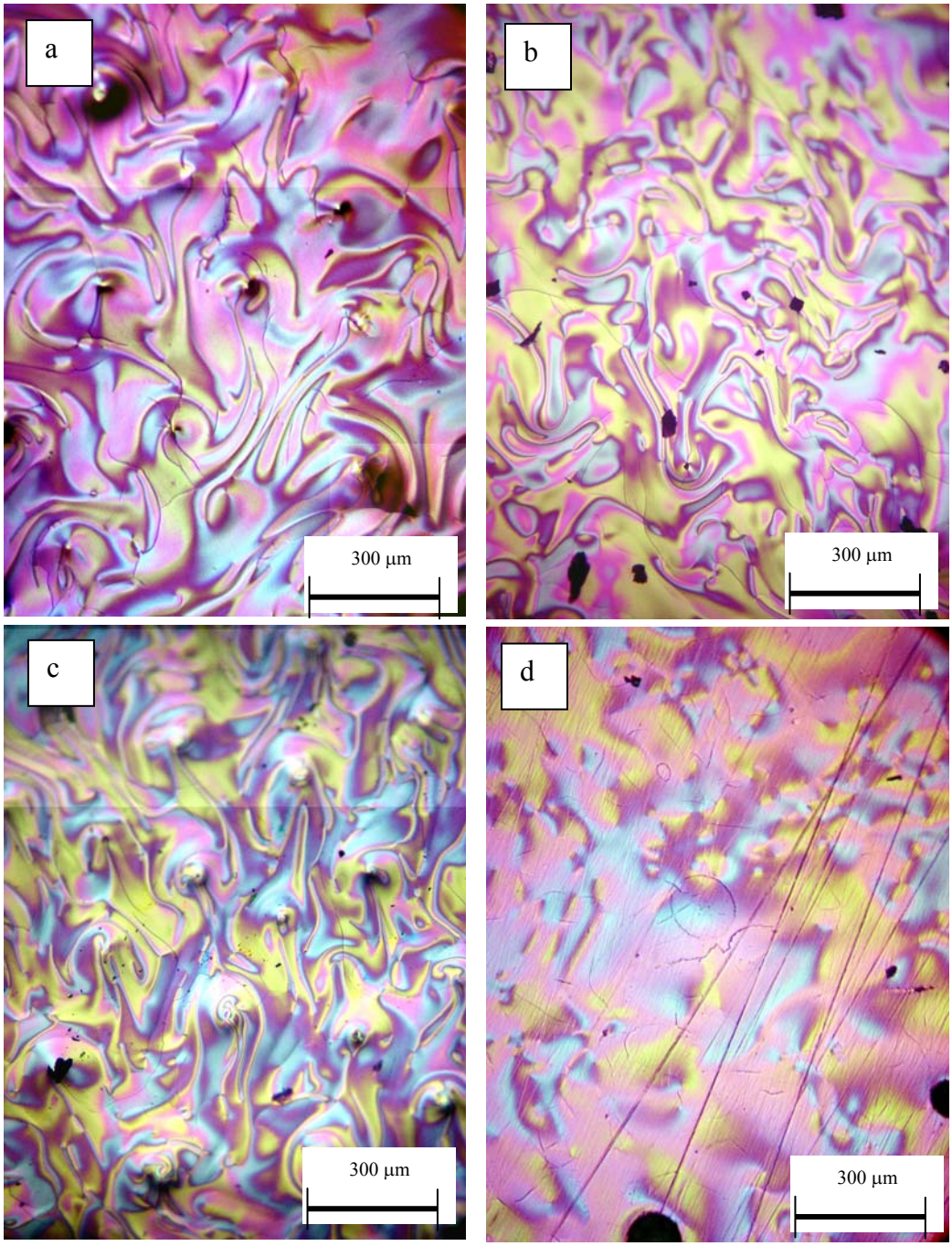

Figure 3.5: Microstructure of solidified, unsheared sample for: (a) free-surface after melting at a temperature of 297°C, (b) free-surface after melting at a temperature of 290°C, (c) free-surface after melting at a temperature of 305°C, (d) polished surface after melting at a temperature of 297°C.

Figure 3.6 displays micrographs of another type of unsheared sample that was obtained from the rheometer after the cone was brought into contact with the melt and the normal stress generated due to squeezing of the sample was allowed to relax, but the shear flow was not started; this condition will be referred to as 0 strain unit (*su*). In AA' section (**Fig 3.6a**), several yellow regions were observed. The director (unit normal to the layer-planes) orientation in these yellow domains was in the flow direction or at some angle relative to the flow direction. The nominal width of these yellow regions was of the order of 70 μm and the area was ≈ 20 % of the total area of the micrograph. A few blue regions (with director orientation along the vorticity direction) were also observed, being approximately 5% of total area of the micrograph; the remaining area was magenta.

Since magenta represents not only face-on layered planes, but also edge-on planes aligned at 0 or 90° with respect to the polarizers, the sample was rotated by 45° and the resulting micrograph is displayed in **Figure 3.6b**. A magenta region, identified as ellipse *A* in **Figure 3.6a**, remained magenta *A′* after rotation of the sample by 45° (**Figure 3.6b**), indicating that layer-planes in region *A* must be face-on i.e, parallel to the image plane, or at shallow angle to the image plane. The director orientation in these magenta regions was along the gradient direction. Another magenta region *B*, on the other hand, became blue *B′* after sample rotation, indicating vertical (90°) layer-plane alignment (in **Figure 3.6a**) within ellipse *B*. In contrast, the yellow region *C* changed to magenta *C′* after sample rotation of 45°, as expected. Image analysis of **Figure 3.6a** showed that the area of yellow, blue, and magenta regions were approximately 10, 5, and 85% of the total area of the micrograph. The ***total*** area of edge-on layer-planes was calculated as the sum of yellow and blue areas from the original and the rotated 45° positions. Thus, the total

edge-on area was approximately 40% (= 20+5+10+5), with the remaining 60% layer-planes being face-on or at a shallow angle to the image plane. Similar values for areas of edge-on and flat layer-planes were obtained from cross-polarized micrographs without the first order-red plate.

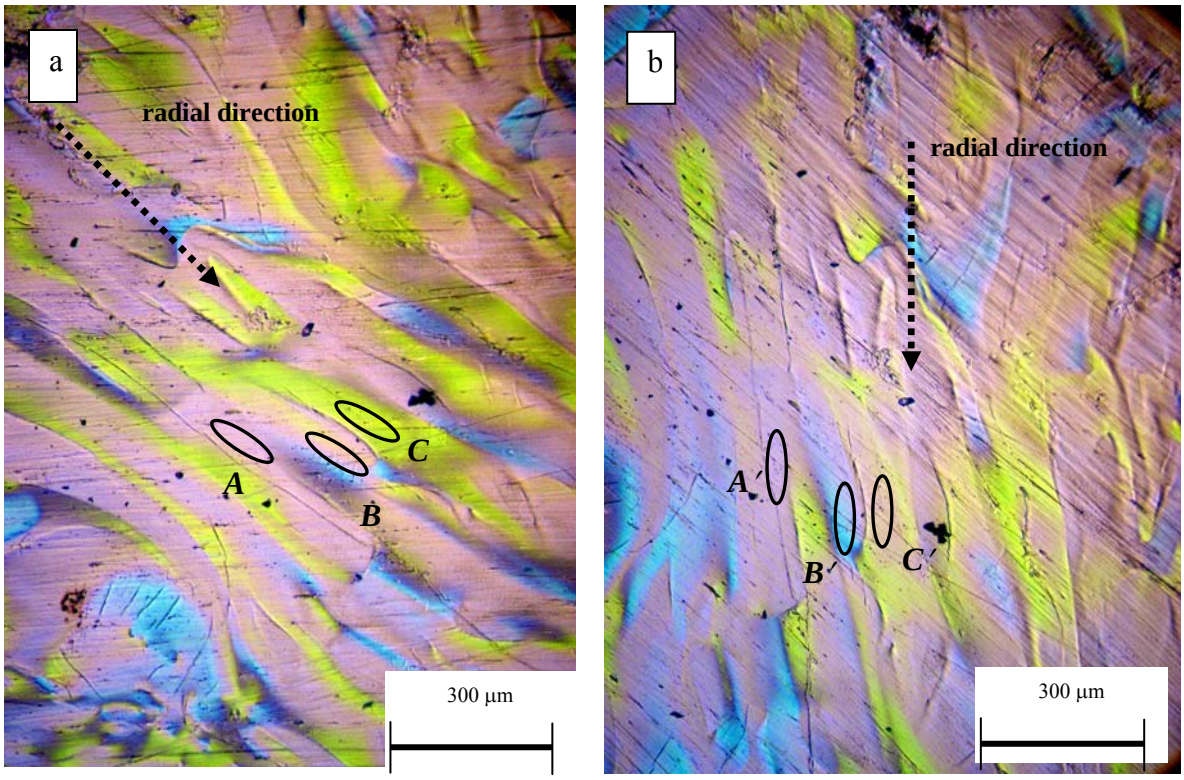

Figure 3.6: Microstructure of a solidified mesophase pitch sample at 0 *su* for: (a) sample placed at 45° relative to polarizer and analyzer, (b) the same sample after rotation of 45°.

Figures 3.7a-c, Figures 3.8 a-d, **Figures 3.9 a-d**, **Figures 3.10 a-c** displays the microstructure of sheared sample at different stages of shearing for three orthogonal sections defined earlier in **Figure 3.1** as AA′(flow-vorticity plane), BB′(vorticity-gradient plane), and CC′(flow-gradient plane). These figures are combined and are displayed in **Figure 3.11** for comparison purpose. The microstructure of 0 *su* sample for two

orthogonal planes (BB′ and CC′) is shown as **Figures 3.7b-c (**also in **Figures 3.11 b-c)**. Similar to section AA′ (**Figure 3.7a**), the predominant color of BB′ section was yellow (≈ 50%, see **Figure 3.7b**), representing significant layer-plane orientation in the radial direction, with director in the gradient direction or at some angle relative to the gradient direction. After rotating the sample by 45°, other edge-on layer-planes were also identified, and the total area of edge-on layer-planes at BB′ section was found to be ≈65%. This is consistent with the ≈60% face-on layers observed in AA' section, which would appear edge-on in BB' section. In contrast, for section CC′ (**Figure 3.7c**), both blue and yellow regions (combined area of ≈ 45%) were observed and the shape of these regions was not as elongated as that observed for sections AA′ and BB′. Total area of edge-on layer-planes for CC′ section was estimated at 90%, the remaining 10% being face-on layer-planes. These face-on layer-planes appear as blue regions in section AA′, and the nominal contents are consistent as measured from the two perpendicular sections.

Micrographs from these three orthogonal sections and the estimated areas of different arrangement of layer-planes suggest a weak, but preferred, orientation of mesophase layers in the radial direction (with director orientation either in the gradient or flow direction or at some angle in between these two directions) of the rheometer cone-plate. The squeezing flow of the sample during lowering of the cone results in a small extensional field in the radial direction of rheometer plate, and causes the mesophase layer-planes to orient in that direction. It is noted that even though the normal stress had relaxed almost completely after a holding time of 5 minutes, the microstructure did not become random and retained the weakly oriented structure.

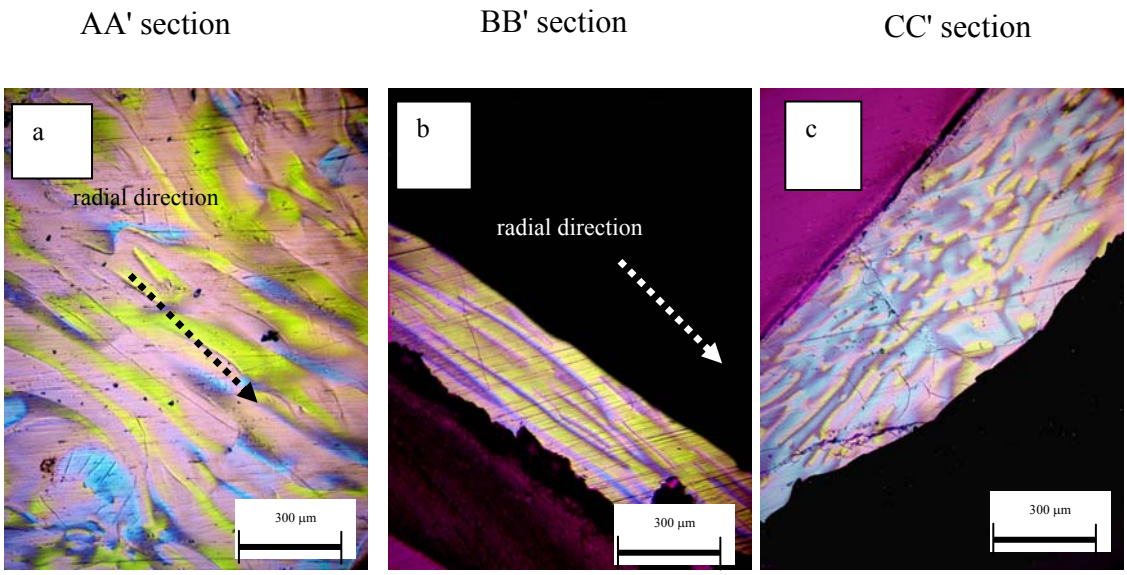

Figure 3.7: Microstructure of solidified mesophase pitch samples at 0 *su* in three orthogonal sections: (a) AA', (b) BB', and (c) CC' (defined in **Figure 3.1**)

The evolution of microstructure during shear flow at a rate of $1s^{-1}$ at 297°C was studied next. **Figures 3.8a-c** (also **Figures 3.11d-f**) display the microstructure of a sample, which was sheared to 1 strain unit. The microstructure of AA′ section, displayed in **Figure 3.8a**, indicates the presence of several yellow regions nominally aligned in the radial direction. The total area of edge-on layer-planes was observed to be ≈ 40% (the remaining 60% magenta), similar to that observed as 0 *su*. However, the width of the yellow regions reduced slightly to a nominal value of 50μm indicating that the microstructure started to deform at 1 *su*.

The deformation was more evident from the micrographs obtained for section BB′ (**Figure 3.8b**) and section CC′ (**Figure 3.8c**). The predominant color of section BB′ was yellow (≈ 50%), representing the layer-plane orientation in the radial direction. The yellow regions remained fairly elongated in the radial direction, but the length of these

regions was smaller when compared to that observed for 0 *su*. After rotating the sample by 45°, other edge-on layer-planes were also identified, and the total area of edge-on layer-planes was found to be ≈80%. This number is higher than that observed initially at 0 *su*, and suggests that fewer flat layer-planes are aligned in the principal orthogonal sections.

For section CC′, significant presence of blue regions (≈50%) were observed and the shape of these regions was somewhat elongated in the flow direction. Few yellow regions were also observed. The sample in **Figure 3.8c** was rotated by 45° and the corresponding micrograph is shown in **Figure 3.8d.** In this micrograph both blue and yellow regions were observed. These edge-on regions and the yellow regions in **Figure 3.8c** will appear edge-on in AA′ section (**Figure 3.8a**). However, as expected, the alignment was higher in CC′ section than that observed in the equivalent section for 0 *su*. These micrographs obtained for three orthogonal sections suggest that the realignment of layer-planes and deformation of microstructure started at 1 *su*.

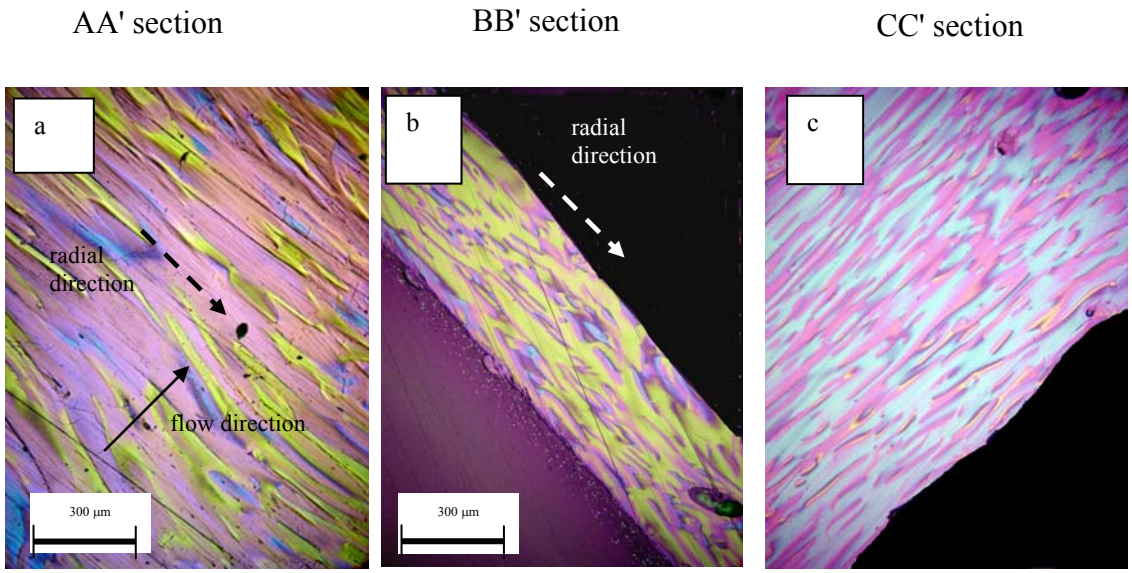

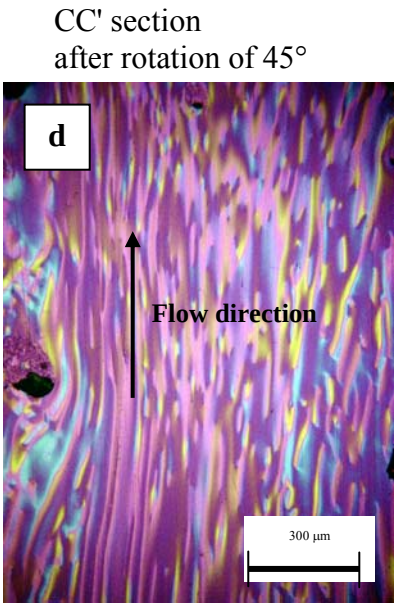

Figure 3.8: Microstructure of solidified mesophase pitch samples at 1 *su* in three orthogonal sections: (a) AA', (b) BB', and (c) CC' (defined in **Figure 3.1**).
(d) Micrograph of same sample as in **Figure 3.8c** but after rotation of 45°.

Figures 3.9a-c (also, Figures 3.11g-i) illustrate the microstructure of samples that were subjected to 6 strain units. A significantly more deformed microstructure was observed in section AA′ (**Figure 3.9a**) with an increase in blue regions to 15% and yellow decreasing to about 5%; the total area of edge-on layers planes was found to be ≈40%. The overall microstructure of BB′ section (**Figure 3.9b**) appeared somewhat elongated but much less than that observed in the equivalent section for 0 *su* and 1 *su*. In **Figure 3.9b**, the percentage area of yellow regions was ≈30% and that of blue was ≈10%. The total area of edge-on layer-planes was found to be ≈70%, also considering the edge-on layer-planes after rotation of the sample by 45°. The presence of blue regions signified that the layer-planes started to align in flow direction because the blue regions in AA′ section will also appear blue in this section. The emergence of flow alignment of layer-planes was more evident for CC′ section (**Figure 3.9c**). The microstructure in CC′ section appears highly elongated in flow direction and significant increase of blue (up to ≈40%) suggests an increase in the layer-plane alignment in flow direction. However, presence of yellow in **Figure 3.9c** and presence of blue and yellow in **Figure 3.9d** (obtained after rotation of same sample of **Figure 3.9d** by 45°) signified the presence of non-aligned layer-planes. Thus, at this stage, the overall microstructure was highly deformed with some layer-plane orientation in the flow direction. It is important to note that for 6 *su* sample the layer-planes were not parallel to the principal orthogonal sections. Therefore, accurate determination of layer-plane orientation was not possible.

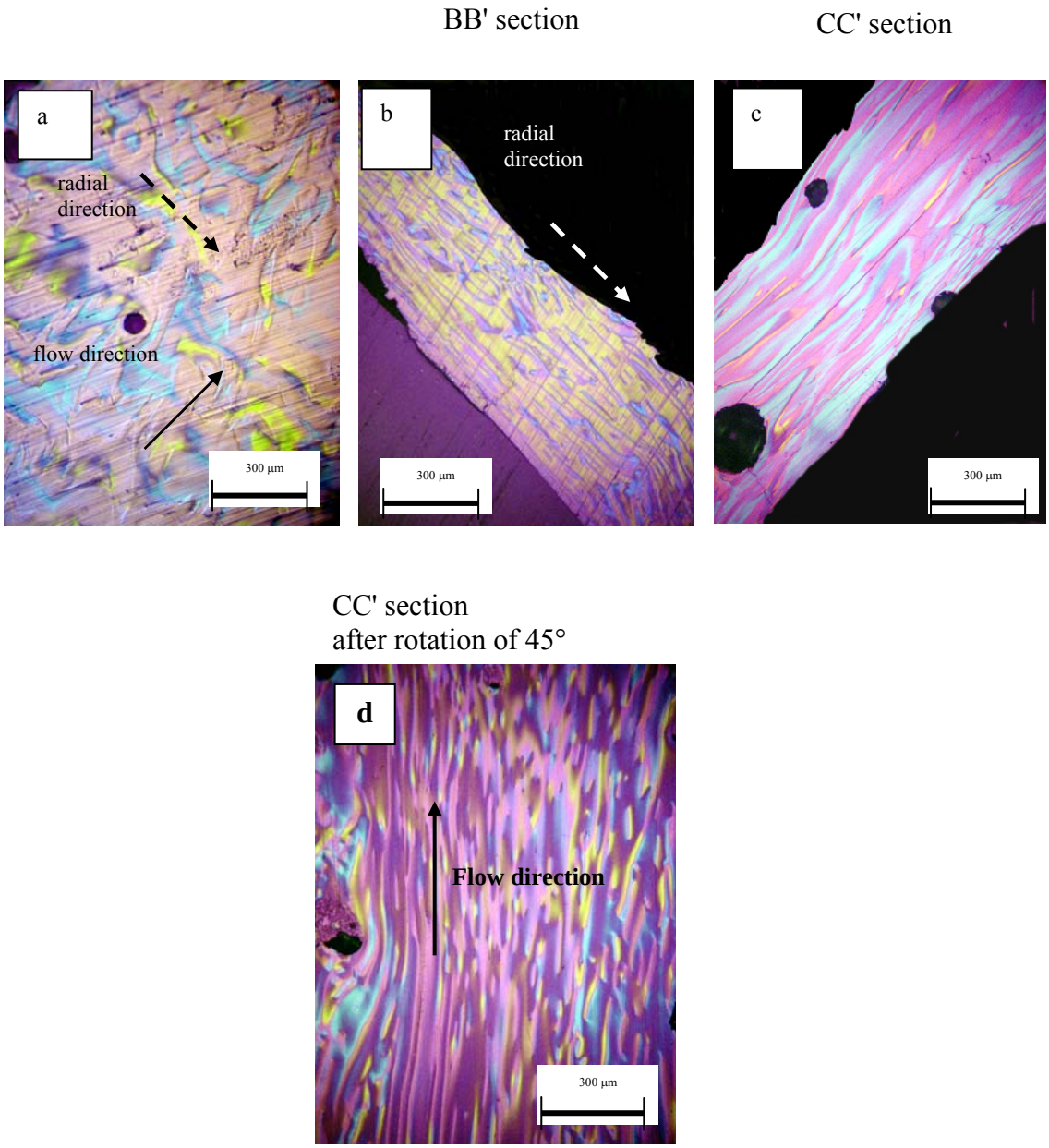

Figure 3.9: Microstructure of solidified mesophase pitch samples at 6 *su* in three orthogonal sections: (a) AA', (b) BB', and (c) CC' (defined in **Figure 3.1**).
(d) Micrograph of same sample as in **Figure 3.9c** but after rotation of 45°.

Finally, the micrographs obtained after 3000 *su*, where the shear stress had attained steady state, are shown in **Figures 3.10 a-c (Figures 3.11j-l)**. In AA′ section, the microstructure appeared highly elongated and aligned in the flow direction (**Figure 3.10a**). Also, significant presence of blue regions (≈30%) indicates layer-plane orientation within these regions to also be in the flow direction, with director of layer-planes oriented in the vorticity direction or at some angle close to the vorticity direction. The total area of edge-on layer-planes was estimated at ≈ 50%. The average width of the blue regions was measured to be nominally 30±10 μm. A significant number of these regions were measured to be about 300 μm long, and some appeared even longer.

The microstructure of CC′ section (**Figure 3.10c**) is similar to that of AA′, i.e., microstructure aligned in the flow direction. Also, significant presence of blue regions (≈40%) indicted layer-plane orientation in the flow direction, with their director oriented in the gradient direction (or in some angle close to the gradient direction). The total area of edge-on layer-planes was found to be ≈55%, slightly higher than that observed in AA′ section. In contrast, no preferred orientation of mesophase layers was observed in BB′ section (**Figure 3.10b**); a mixture of colors (blue, yellow and magenta) was observed. The edge-on orientation of layer-plane in this section was estimated as ≈90% of the total area of micrograph.

The microstructure of AA′ and CC′ sections were similar and resemble the fibrous microstructure reported in literature studies of Zimmer and White [1982]. Also, the microstructure of BB′ section was similar to the cross-sectional view of fibrous microstructure [Zimmer and White, 1982]. Significant presence of blue color in AA′ and CC′ sections represents preferred orientation of mesophase layers in the flow direction

with the director orientation in the vorticity or gradient direction, or at some angle in between. In a simulation study for discotic nematics [Rey, 2006], it was shown that steady shearing led to dual-mode orientation of the discs. It was found that significant director orientation was in the gradient direction, but in a few cases director orientation was also in the vorticity direction. Present microstructural evidence appears to be consistent with those findings. It is also noted that, with shearing, the initial weakly oriented structure transformed to a finer, flow aligned one.

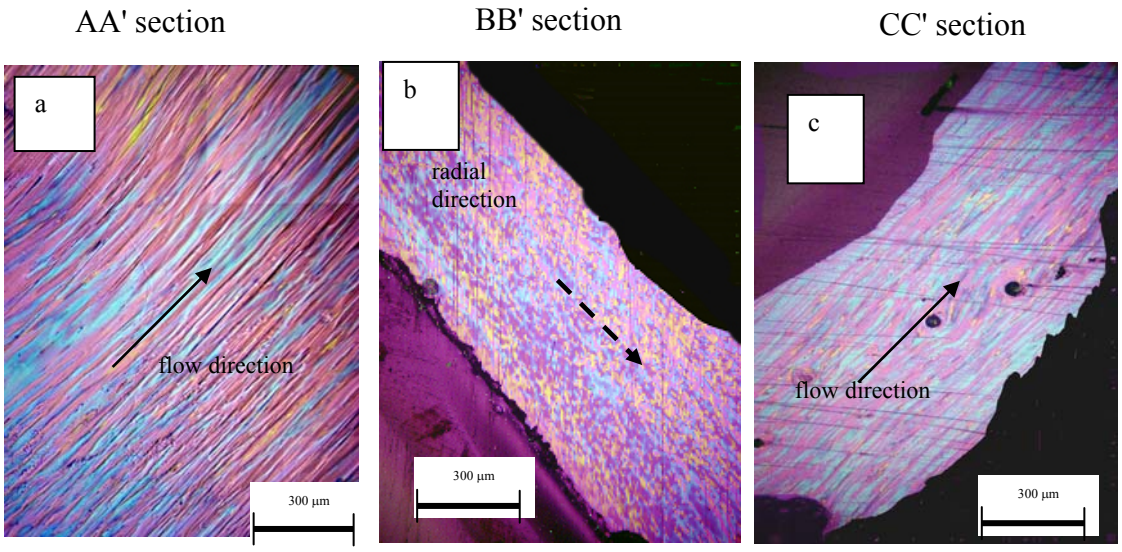

Figure 3.10: Microstructure of solidified mesophase pitch samples at steady state (≈3000 *su*) in three orthogonal sections: (a) AA', (b) BB', and (c) CC' (defined in Figure 3.1).

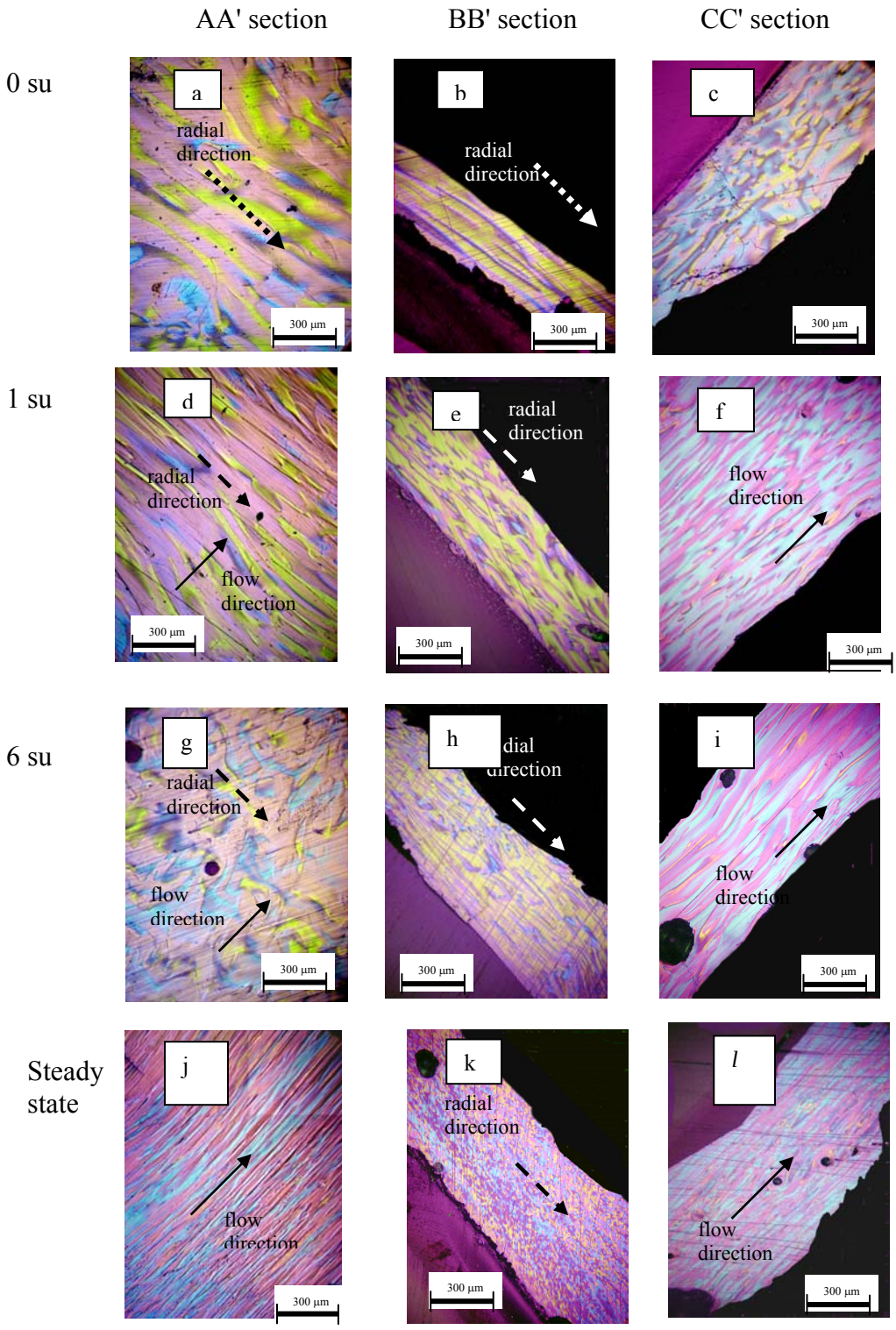

Figure 3.11: Microstructure of solidified mesophase pitch samples after different stages of shearing at $1s^{-1}$ and 297°C as measured in three orthogonal sections: AA', BB', and CC' (defined in Figure 3.1)

Based on the microstructural evidence, a possible three-dimensional schematic for the steady-sheared mesophase sample is constructed and is shown in **Figure 3.12**. The projected microstructure for three orthogonal sections is also shown. The flow direction is identified in the schematic and the rectangular boxes representing the isochromatic regions observed in the optical micrographs. These boxes indicate the average orientation of collection of molecules in a particular direction. The average director orientation is along the normal to the largest rectangular face. For the typical configuration of polarizer -analyzer and first order red plate that was used in this study, sections of the ioschoromatic regions where the layer-plane orientation was edge-on in AA′ (vorticity-flow plane) and CC′ (gradient-flow plane) sections will appear blue. As indicated earlier, the director orientation of steady-sheared sample was in the vorticity or gradient direction or at some angle in between. Therefore, similar microstructure was observed in AA′ and CC′ sections. The cross-sectional view of these structures, as viewed in BB′ section, would be rounded, finer, and oriented in all directions, leading to blue, yellow, and magenta colors (note the polarizer-analyzer direction for CC′ section).

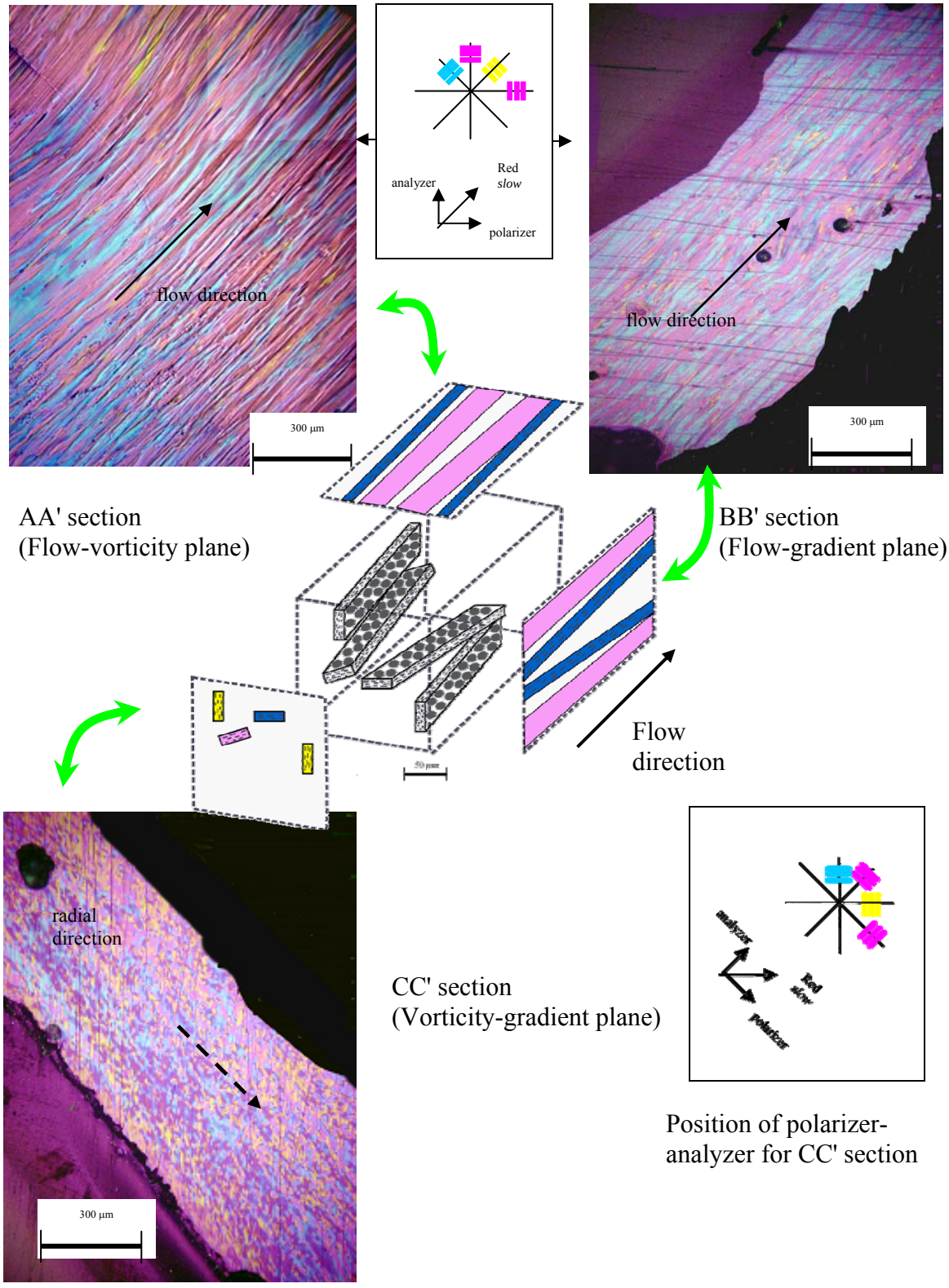

Figure 3.12: Microstructure for three orthogonal sections for a steady-sheared sample at $1s^{-1}$ together with possible schematic of 3-d structures is shown. A few isochromatic regions are shown schematically. Position of polarizer-analyzer is also shown.

The steady-state microstructures were characterized for other test temperatures and shear rates. For test temperatures of 290 and 305°C, there was weak preferred initial orientation along the radial direction of the plate caused by the squeezing flow generated while lowering of the cone into the melt. Shearing of the melts at these temperatures also caused a flow-aligned structure, and no significant detectable difference in microstructure was observed relative to that at 297°C.

For a higher shear rate of 10 s^{-1}, **Figure 3.13** displays microstructure of AA′ sections at two intermediate states (≈10 *su and 100 su*) and at steady state (≈ 3000 s^{-1}). The microstructures of other two orthogonal sections (BB′ and CC′) for steady-sheared sample are displayed in **Figure 3.14**. The initial microstructure, which is independent of shear rate, was similar to that displayed in **Figure 3.7a**. The rheometer could not be stopped at 0.6 s, corresponding to 6 *su* for a shear rate of 10 s^{-1} to collect sample; it could be stopped at 1 s corresponding to 10 *su*.

While the evolution of initial microstructure as a function of shearing time was different for this case (versus that at 1 s^{-1} because of the significantly different shear rates), it was similar when observed as a function of applied strain. The initial radial structure transformed to a deformed structured at 10 *su*. At 100 *su*, the microstructure became finer and layer-plane orientation along the flow direction increased. With further shearing, the microstructure of AA′ section continued to become finer. When the shear stress reached steady state, the width of the flow aligned regions (blue) in many cases was less than 10 μm, and could not be measured accurately. Micrograph of this sample at a higher magnification is also presented as an inset. The color of this steady-sheared sample was predominately blue (≈60%) and total area of edge-on oriented planes was

approximately 70%. As seen in **Figure 3.14b**, the microstructure for the CC' section was similar to that observed for AA' section, with significant presence of blue regions. In the BB' section (**Figure 3.14a)**, all e three colors (blue, yellow and magenta) were observed, which is more evident from the higher magnification micrograph (presented as inset). In this section, microstructure was fine and random, with presence of all three colors (blue, yellow and magenta).

The microstructure for steady-sheared sample at 10 s^{-1} was similar to that observed for $1s^{-1}$. The microstructure was fibrous [Zimmer and White, 1982] in nature, although much finer in size. The flow aligned microstructure obtained here in a *rheometric* flow at low-medium shear rates was qualitatively similar to that observed at fairly high wall-shear rates encountered in a capillary rheometer and in a spinneret during mesophase pitch fiber spinning [Fathollahi and White, 1994; McHugh and Edie, 1996].

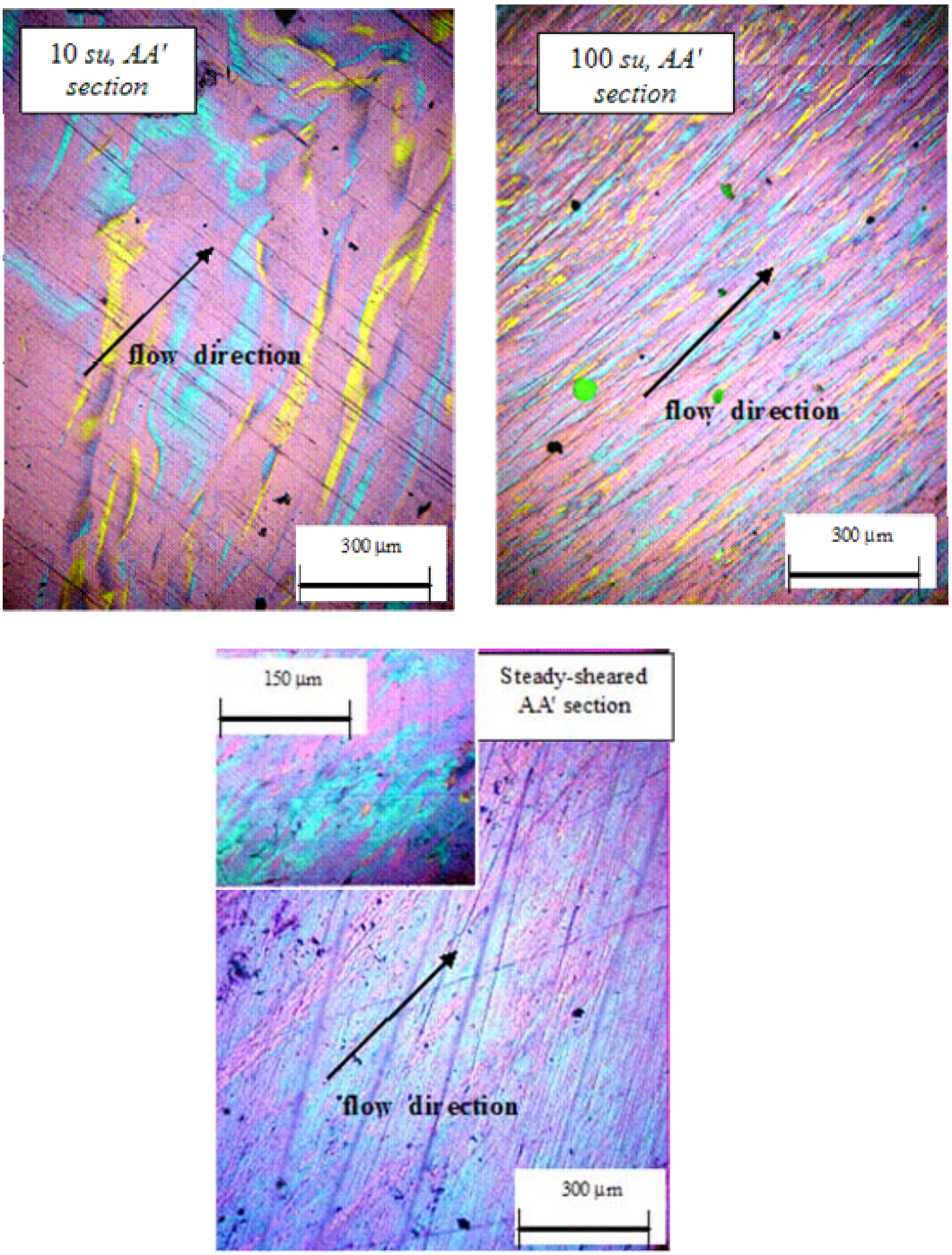

Figure 3.13: Evolution of microstructure of mesophase pitch at 297°C at10 s^{-1}

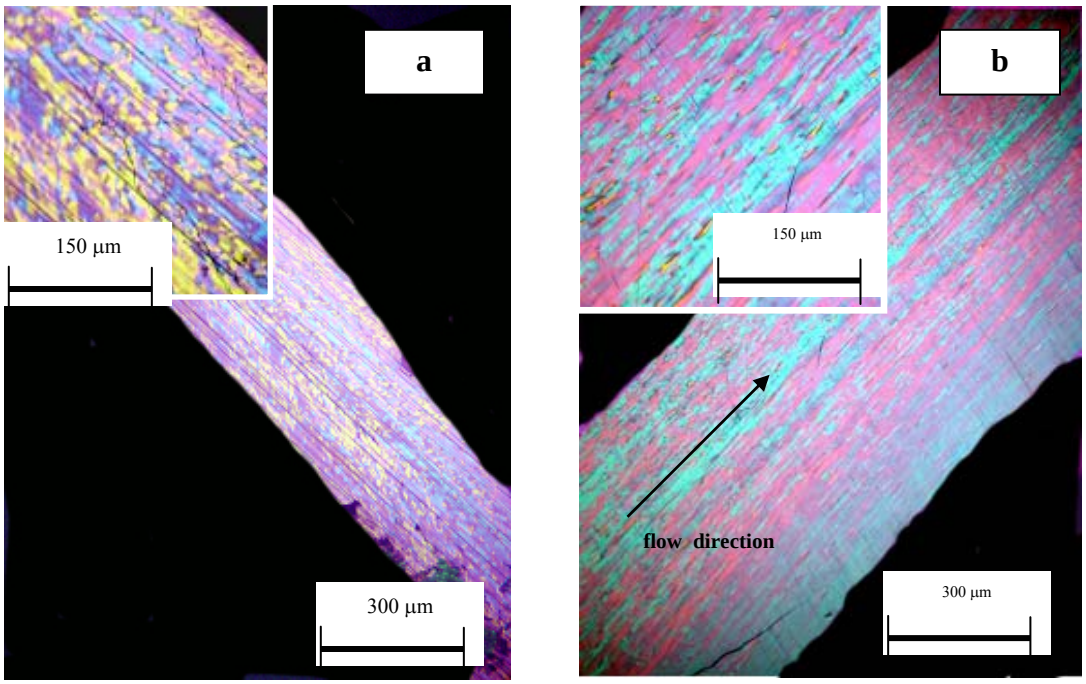

Figure 3.14: Steady-sheared microstructure of mesophase pitch at 297°C and10 s^{-1}: (a) BB′ section, and (b) CC′ section.

3.2.1 X-ray measurements

The wide-angle X-ray diffraction results obtained on the solidified sheared samples are presented in this section. For different sections, the positions of the samples with respect to the X-ray beam are shown in **Figure 3.3.** The 2θ scan of AA' section for a steady-sheared sample at $1s^{-1}$ are displayed in **Figure 3.15**. A peak was observed at the 2θ value of ≈25°, which corresponds to 0.355 nm Braggs spacing of (002) reflections. This is consistent with the values reported earlier for other grades of mesophase pitches [Lu et al., 2002; Barnes et al., 1998].

Other than (002) peak, another peak was observed at 2θ value of ≈7°, corresponding to a nominal Braggs spacing of 1.25 nm. Such a peak has not been reported in the literature for mesophase pitch. However, a peak at 2θ ≈9° was reported in literature for partially pyrolyzed PCTDA (3,4,9,10-perylenetetracarboxylic dianhydride) sample, and this peak was related to the arrangement of pyrolyzed PCCTDA molecules in a discotic phases [Murthy et al., 2001]. To check if the low-angle peak observed for AR-HP mesophase pitch is reproducible, additional experiments were performed at the Air Fore Research Labs, in which the sample-to-detector distance was varied. The 2θ–plots obtained by Dr. David Anderson are displayed in **Figure 3.16**. It is noted that the peak at 2θ ≈7° appeared for all sample-to-detector distances and, therefore, the peak has been determined to be real. It is hypothesized that the peak may arise from ordering formed in the layer-planes with an average periodicity of ~1.25 nm.

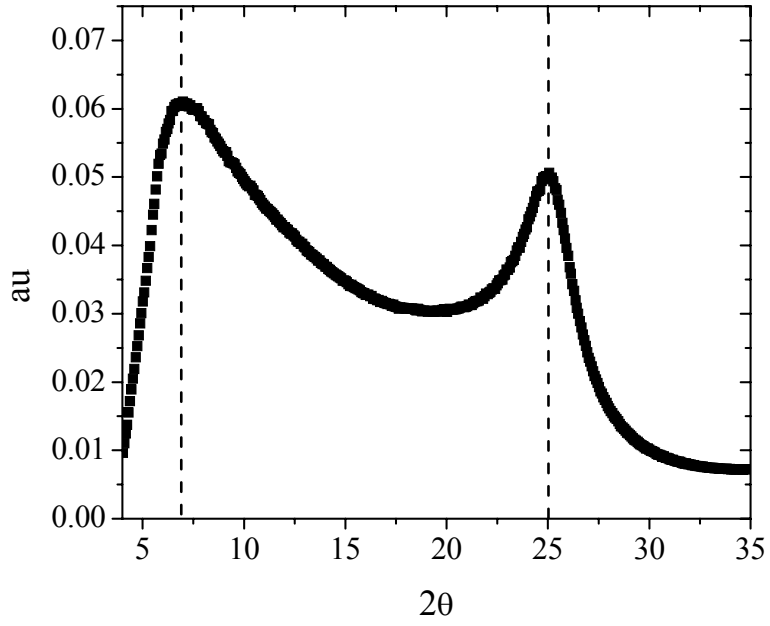

Figure 3.15: A representative 2θ scan of the XRD profile of AA' section for a steady-sheared sample at $1s^{-1}$.

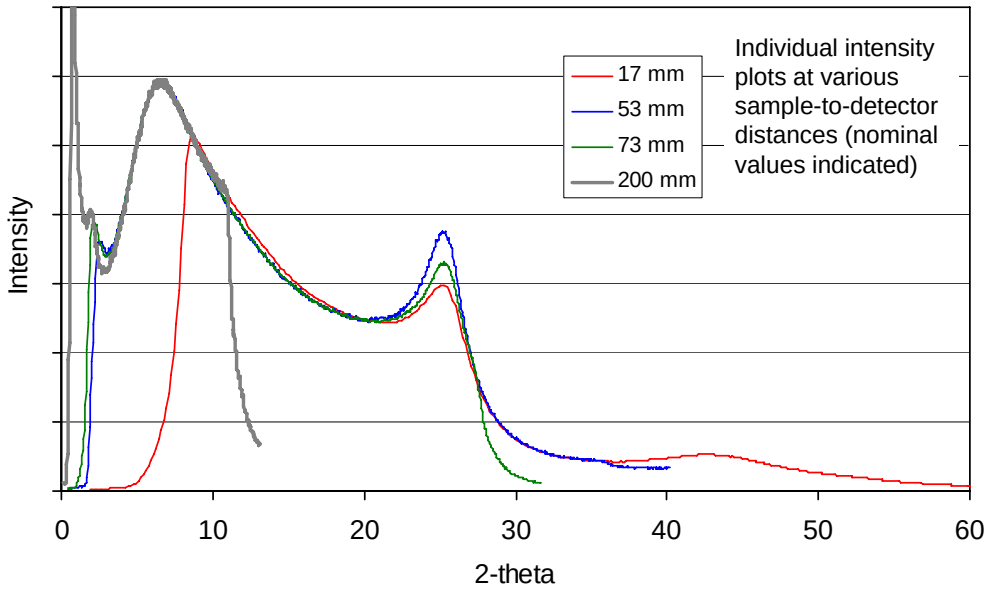

Figure 3.16: 2θ scan of the XRD profile of AA' section for a steady-sheared sample at $1s^{-1}$ for different detector distance from the sample [courtesy of Dr. David Anderson].

The X-ray diffractograms for samples with different shear histories are shown in **Figure 3.17a-k**. For (002) peak, the azimuthal distributions for these samples are displayed in **Figures 3.18a-c** as a function of azimuthal angle, α. As seen in **Figure 3.17a,** the free-surface displayed a diffuse-ring diffraction pattern. The absence of any intense arc translates to a relatively flat azimuthal distribution, presented in **Figure 3.18a**. The lack of significant layer-plane orientation in this sample is consistent with a similar observation made from optical microscopy. At 0 *su*, peak intensity was observed at the meridional location (**Figure 3.17b**) and correspondingly a broad meridional peak was observed in azimuthal distribution, centered around $\alpha = 0°$ (**Figure 3.18a**).

After shearing for 1s at $1s^{-1}$, the peak position remained in the meridional region (**Figure 3.17c**) but became slightly broader. For 0 *su* and 1 *su* cases, peaks at the meridional position were observed because of layer-plane orientation in the radial direction that was seen by optical microscopy (**Figures 3.11a-f**).

At 6 *su,* no single representative diffractogram was obtained. Different diffraction patterns, such as shown in **Figure 3.17d-f,** were obtained at different locations of the same sample. In these three diffractograms, the peak position changed with location. This behavior was consistent with the deformed microstructure seen in **Figure 3.11 g-I,** where no preferred layer-plane orientation was observed.

For steady-sheared samples, as seen in **Figure 3.17g**, the peak shifted to the equatorial location (90°) and the azimuthal distribution became sharper (**Figure 3.18a**). The equatorial peak indicates that the orientation of layer-planes was in the flow direction with director orientation either in the vorticity or gradient direction (or at some position in between), such that it satisfies the Braggs's condition.

The X-ray diffractograms were also obtained for the orthogonal sections, BB′ and CC′, and are displayed in **Figures 3.17h** and **3.17i**, respectively. The azimuthal distribution for these three orthogonal sections is shown in **Figure 3.18b**. The diffraction pattern of the CC′ section was similar to that obtained for AA′ section; however, the diffraction pattern was quite diffuse for BB′ section. These results indicate that for steady-sheared sample, the layer-plane orientation was in the flow-direction with director orientation either in the vorticity or gradient direction (or at some angle in between), as observed in optical microscopy.

The diffraction patterns for steady-sheared samples at $10s^{-1}$ are displayed in **Figures 3.17 j-k**. The diffractogram obtained for AA′ and CC′ sections in this case were similar to those obtained for the equivalent sections at the shear rate of $1s^{-1}$. The azimuthal profiles of steady-sheared samples (≈3000 *su*) at 1 and $10s^{-1}$ are compared in **Figure 3.18c**. As expected, the peak became sharper at the higher shear rate, but remained centered at 90°.

Calculated values of the orientation parameter, *f*, are summarized in **Table 1**. It is noted that the magnitude of *f* changed with change of layer-plane orientation. As expected, with increasing shear rates, the value of *f* increased to about -0.3. It is noted that for a perfect equatorial alignment of layer-planes, the limiting value of *f* is -0.5.

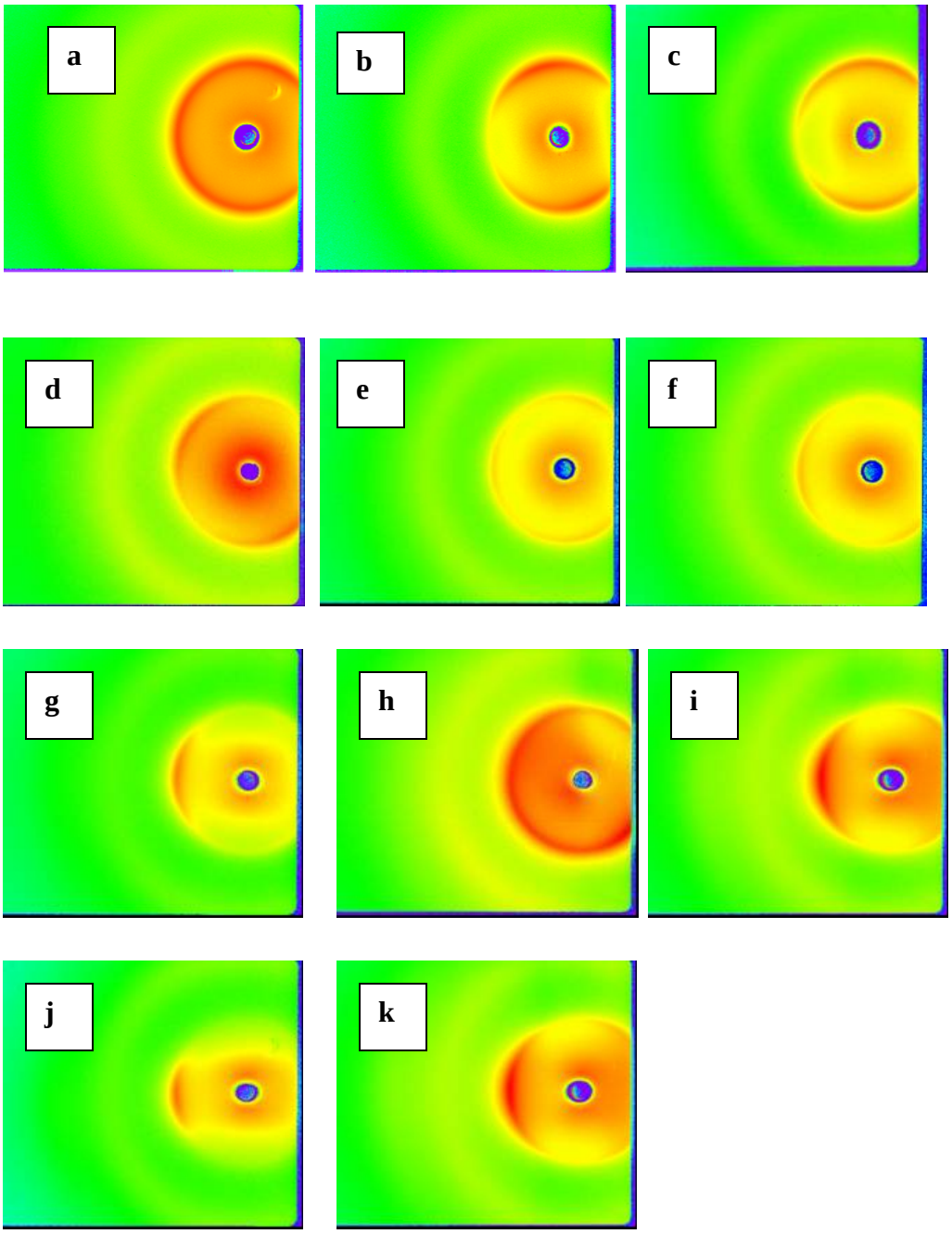

Figure 3.17: X-ray diffractograms for the samples with different flow histories: (a) free-surface, (b) after bringing cone-plate together (0 *su*), (c) after shearing for 1s at $1s^{-1}$(1 *su*), (d, e, f) sample after shearing for 6s at $1s^{-1}$(6 *su*), (g) AA′ section of steady-sheared (≈3000 su) at $1s^{-1}$, (h) BB′ section of steady-sheared (≈3000 su) at $1s^{-1}$, (i) CC′ section of steady-sheared (≈3000 su) at $1s^{-1}$, (j) AA′ section of steady-sheared (≈3000 su) at 10 s^{-1}, and (k) CC′ section of steady-sheared (≈3000 su) at 10 s^{-1}.

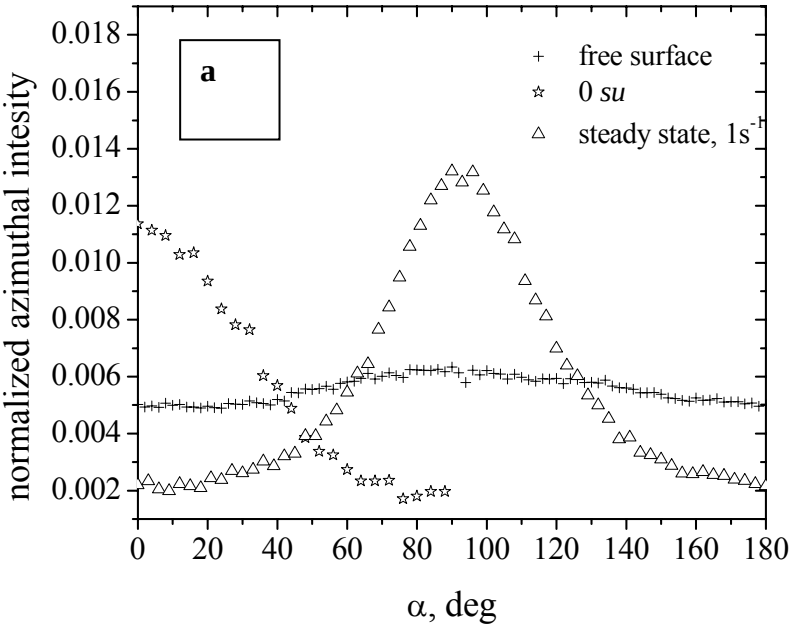
a
free surface
0 su
steady state, 1s-1
normalized azimuthal intesity
α, deg
0.002
0.004
0.006
0.008
0.010
0.012
0.014
0.016
0.018
0
20
40
60
80
100
120
140
160
180

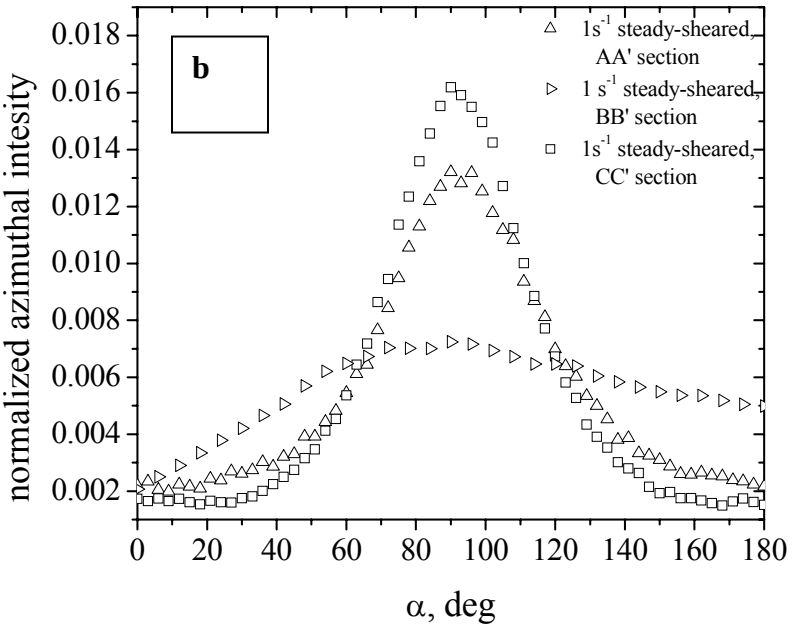
b
1s-1 steady-sheared, AA' section
1 s-1 steady-sheared, BB' section
1s-1 steady-sheared, CC' section
normalized azimuthal intesity
α, deg
0.002
0.004
0.006
0.008
0.010
0.012
0.014
0.016
0.018
0
20
40
60
80
100
120
140
160
180

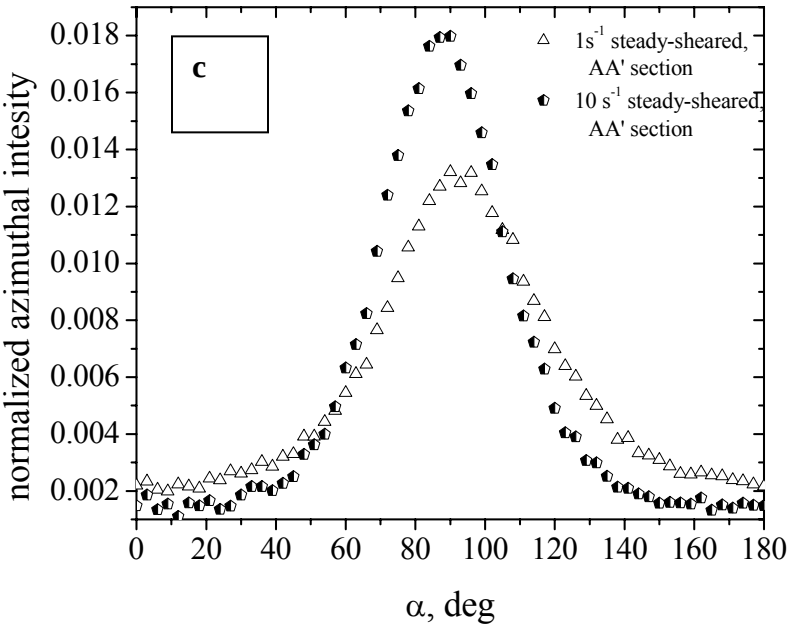

Figure 3.18: The normalized azimuthal distribution plots of the samples with different shear histories plotted against angle, α. (a) Normalized azimuthal distribution of free surface, 0 su sample, steady-sheared sample state at $1s^{-1}$; (b) Normalized azimuthal distribution of three different sections (AA', BB', and CC') for a steady-sheared sample at $1s^{-1}$; (c) Normalized azimuthal distribution of AA' section at two different shear rates, $1s^{-1}$ and $10s^{-1}$

Table-1: The calculated orientation parameter for the samples with different shear histories.

sample condition	**Orientation Parameter, *f***
free surface	-0.04
0 su	0.19
$1s^{-1}$, 1 su	0.12
$1s^{-1}$, 6 su	*
$1s^{-1}$, steady AA' section	-0.21
$1s^{-1}$, steady, BB' section	-0.1
$1s^{-1}$, steady, CC' section	-0.26
10 s^{-1}, steady, AA' section	-0.26
10 s^{-1}, steady, CC' section	-0.29

* The peak location was not fixed for 6 *su* sample and therefore, the orientation parameter could not be calculated unambiguously.

3.2.3 Relation between stress evolution and microstructure

Finally, the interrelationship between the evolving microstructure and the shear stress response (reported in Chapter 2) was explored. While rheological models attempt to utilize these factors quantitatively to predict flow properties, this study attempts to identify the relationship between rheology and the microstructure experimentally.

In **Figure 3.19**, the evolution of microstructure (AA′ section) is mapped on to the evolution of transient shear stress for a shear rate of $1s^{-1}$ at 297°C. The shear stress increased with applied shear strain till 1-2 *su*, where the preferred orientation of the layer-planes was in the radial direction; however, size of the microstructure decreased slightly. Subsequently, a breakdown and deformation of initial microstructure was observed, which is evident from the diffuse and distorted boundaries of yellow regions at 3 *su*. This change of the initial microstructure results in a reduction of the stress that the material can sustain. Therefore, a peak is observed at 1-2 *su*. The maximum in shear stress response has also been observed for liquid crystalline polymers in the literature, and has been explained as likely resulting from the yielding of initial microstructure [Mather et al., 2000; Han and Kim, 1994].

Over the next several strain units (~10 *su*), the microstructure continues to *yield* in terms of size and orientation, and is accompanied by a decrease in shear stress. At 6 *su,* the deformation of initial microstructure appears to be accomplished. Subsequently, the shear stress starts to increase with increasing strain, and this upturn corresponds to a local minimum in the stress (and transient viscosity). Further shearing leads to some

refinement of microstructure (shape and size) along with molecular layer-planes orientation in the flow direction.

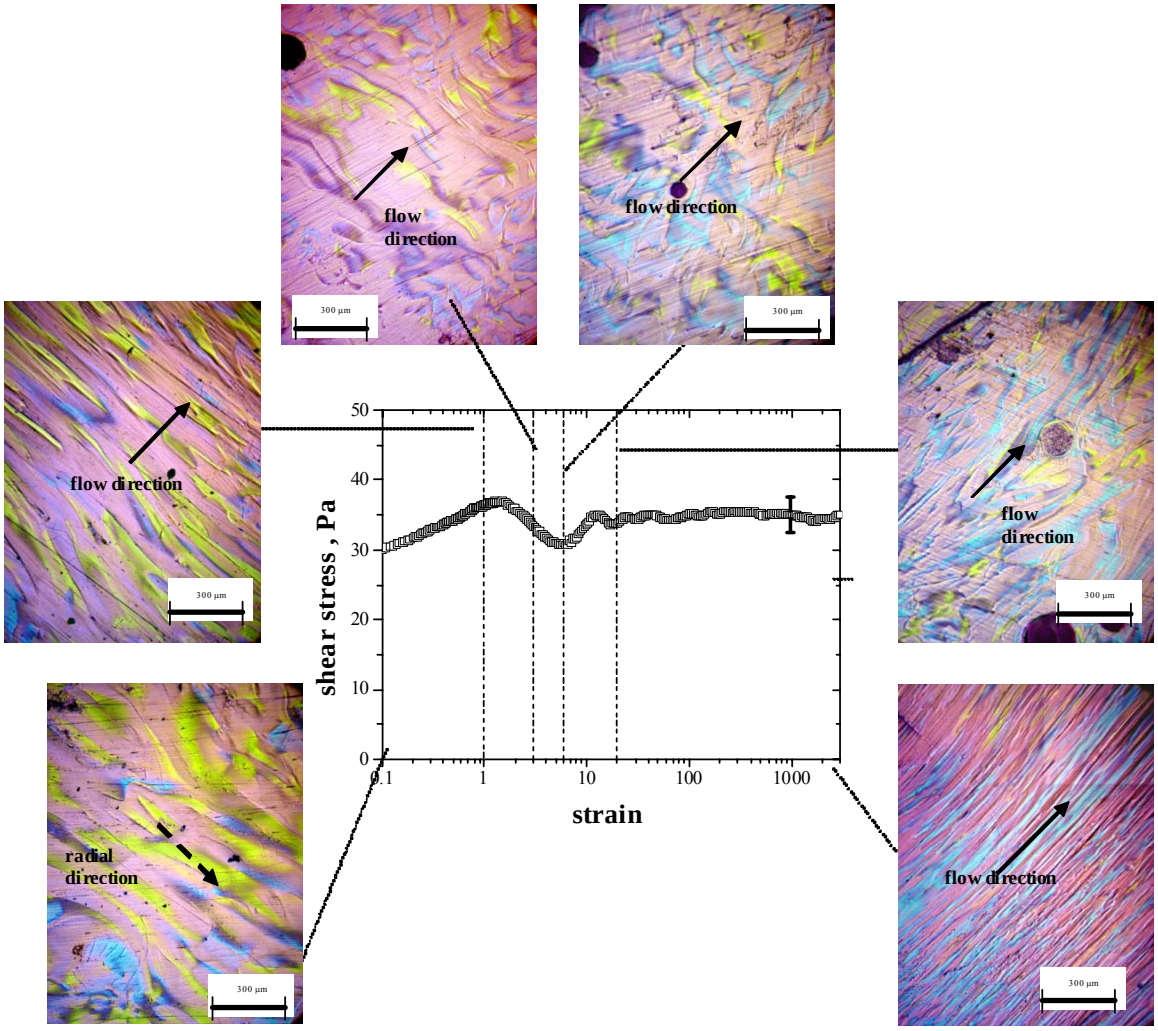

Figure 3.19: Rheo-structural evolution of mesophase pitch at 297°C and a shear rate of $1s^{-1}$.

It was shown in Chapter 2 that, following steady flow, a reversal of flow direction or a very short interruption in flow did not lead to a maximum or minimum in the transient shear stress, but the maxima and the minima reappeared in the transient stress

after sufficient rest time (~15 mins). The microstructure of a sample that was subjected to steady shearing (for 3000 *su*) at 1 s^{-1} and then allowed a rest period of over 15 mins is compared in **Figure 3.20** with the steady-sheared microstructure **(**same as **Figure 3.11j**). Clearly, the microstructure became relaxed after ~1000 s of rest. A few blue regions with a nominal width of 70 μm were observed, but they appear relaxed and less stretched as compared with steady-sheared samples. The relative area of edge-on layer orientation reduced from 50% for steady-sheared sample to 40% for the relaxed sample (the remaining 60% being face-on). The total area of these edge-on layer-planes was similar to that observed for 0 *su* sample. Also, an overall decrease of layer-plane orientation in the flow direction was observed due to the relaxation process. The relaxation of layer-plane orientation was more evident from X-ray azimuthal distribution plot of this sample. As seen in **Figure 3.21**, the azimuthal distribution has a peak at $\alpha = 90°$ but the peak was broader than that observed in prior steady-sheared sample. The magnitude of orientation parameter, *f*, was -0.14 compared to -0.21 observed for steady-sheared sample. Therefore, the sample relaxes after ~15 mins of holding time, and this relaxed microstructure influences the transient stress (and viscosity) response.

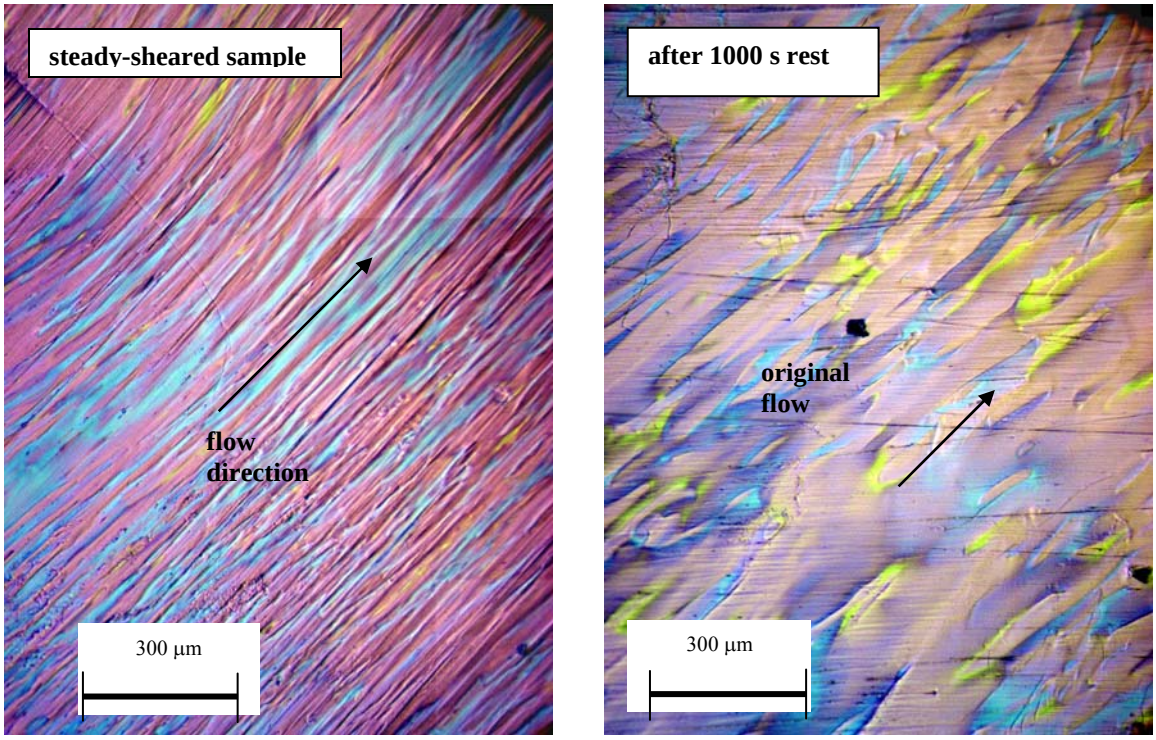

Figure 3.20: Microstructure of solidified pitch sample after 1000 s of rest following steady-shearing (~3000 su) at $1s^{-1}$ and 297°C

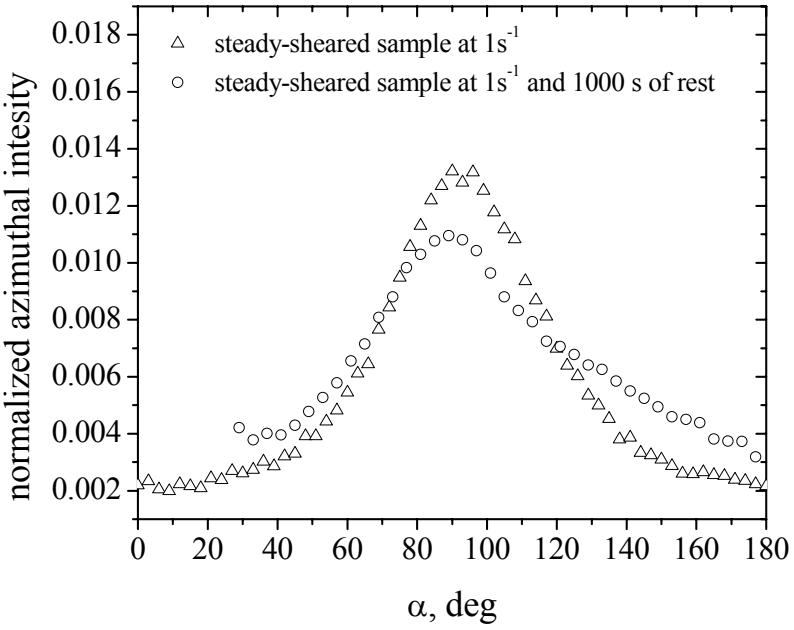

Figure 3.21: The normalized azimuthal distribution plots for steady-sheared sample at $1s^{-1}$ and for a sample with 1000 s of rest followed by steady-shearing at $1s^{-1}$.

In the TLCP literature, the experimentally observed shear stress maximum has been attributed to yielding of initial microstructure with its location depending on the type of polymer and its molecular weight [Kim and Han, 1993; Mather et al., 2000]. For PSHQ10 TLCP, the shear maximum occurred at ~4 *su* [Mather et al., 2000], whereas that for PHB/PET was observed at a strain of less than 1 *su* [Viola and Baird, 1986]. In modeling studies of discotic mesophases, simulation results qualitatively capture the non-monotonic response of transient shear-stress for a uniform 2-dimensional structure with a uniaxial initial orientation of mesophase molecules (i.e., no microstructural variation) [Grecov and Rey, 2003a & 2005]. This response was shown to result from a change of molecular orientation of discs. In another simulation study for rodlike liquid crystalline systems [Grecov and Rey, 2004], it was shown that defect nucleation and defect coarsening resulted in change of shear stress during shearing. For the present experimental results, the initial microstructure of the sample was three-dimensional. Therefore, orientational changes of disc-like layer-planes *and* long-range microstructural changes can take place during flow, and such experimental results can help in the validation of advanced constitutive models.

3.3 Conclusions

By developing an experimental protocol to preserve the rheological samples, microstructural results were obtained from the same mesophase pitch specimens as those used for rheological testing. The microstructure was examined in three orthogonal sections for samples sheared to various stages: 0 *su*, 1 *su*, 6 *su*, and steady-sheared. The

initial texture was found to be coarse and with weak, but preferred, orientation of layer-planes in the radial direction of the cone-plate due to the initial squeezing flow. Microscopic observations confirm that the local maximum in the shear stress was likely caused by the yielding of the initial microstructure. With further shearing, the microstructure became flow-aligned, and the microstructure became finer as the shear rate increased from 1 s^{-1} to $10s^{-1}$. The optical microscopy results were also supported by the azimuthal X-ray diffraction analysis, which confirms that the initial orientation was centered along the radial direction ($\alpha \rightarrow 0°$), but then changed to one that was centered in the flow direction ($\alpha \rightarrow 90°$). The steady-sheared flow-aligned structure was similar to the *fibrous* structure reported in literature and the directors of the layer-planes were oriented in the vorticity or gradient directions (or at some intermediate angle). Based on the microstructural evidences, a possible 3D schematic of overall microstructure was presented.

CHAPTER 4

MICROSTRUCTURAL EFFECTS ON THE DYNAMIC RHEOLOGY

The rheology and microstructure of mesophase pitch in steady-shear conditions was discussed in Chapter 2 and 3. To complement such high-strain steady-shear experiments, dynamic experiments were performed in the linear viscoelastic region where no significant deformation of fluid takes place. Such dynamic experiments can be used to investigate the structure of complex fluids [Romo-Uribe et al., 1997; Burghardt, 1998]. In contrast to liquid crystalline polymers, the dynamic rheology of mesophase pitch has been reported only in the limited literature studies [Cato, 2002, Cheung et al., 1996]. Since the rheological response depends upon the constitution of a fluid (grade of pitch, initial state of specimen, etc.), the objective of this study was to probe the effect of microstructure on the dynamic response for AR-HP mesophase pitch. The relaxation behavior was investigated on different presheared samples using dynamic time-sweep experiments and cross-polarized optical microscopy to further elucidate the flow-microstructure interrelationship.

4.1 Experimental

Similar to steady-shear experiments (Chapter 2), the dynamic rheological experiments were also conducted in a TA Instruments ARES rheometer (TA Instruments Inc.). The softening point of AR-HP mesophase pitch was measured by dynamic

temperature-sweep experiments. The experiments were performed in a 25 mm parallel-plate fixture, starting with a high temperature of 290°C, and the temperature reduced at a rate of 5°C/min. During this cooling step, the sample was subjected to a frequency of 5 rad/s. The storage modulus (G') and tanδ, as a function of temperature, are displayed in **Figures 4.1a** and **b.** A steep increase of G' was observed at ≈255°C and at the same temperature a peak of tanδ was observed. Therefore, the softening point of this material, as measured from rheological experiments, was ≈255°C. The softening point was also measured for ARA24R grade of mesophase pitch (used in a previous study) and results are shown in **Figures 4.1 a** and **b**. The softening point for ARA24R pitch was estimated as ≈272°C, higher than that obtained for AR-HP pitch. The measured values of softening points from this technique were lower than that measured from Metler-Toledo softening point measurement instrument (FP-83). These results signify that the material has some processability even below the softening point measured using Metler-Toledo FP-83 temperature.

Next, experiments were performed at four different temperatures (280, 290, 297, and 305°C) in an inert N_2 environment. For frequency-sweep experiments, the lower limit of the frequencies was limited by torque resolution limit. Most of the experiments were performed using a cone-plate fixture of 25 mm diameter with a cone angle of 0.1 rad. The geometric independence of all the results was confirmed with the use of a parallel-plate fixture. Samples with different rheological histories were collected after the experiments, and the microstructural studies were performed using the procedure discussed earlier in Chapter 3.

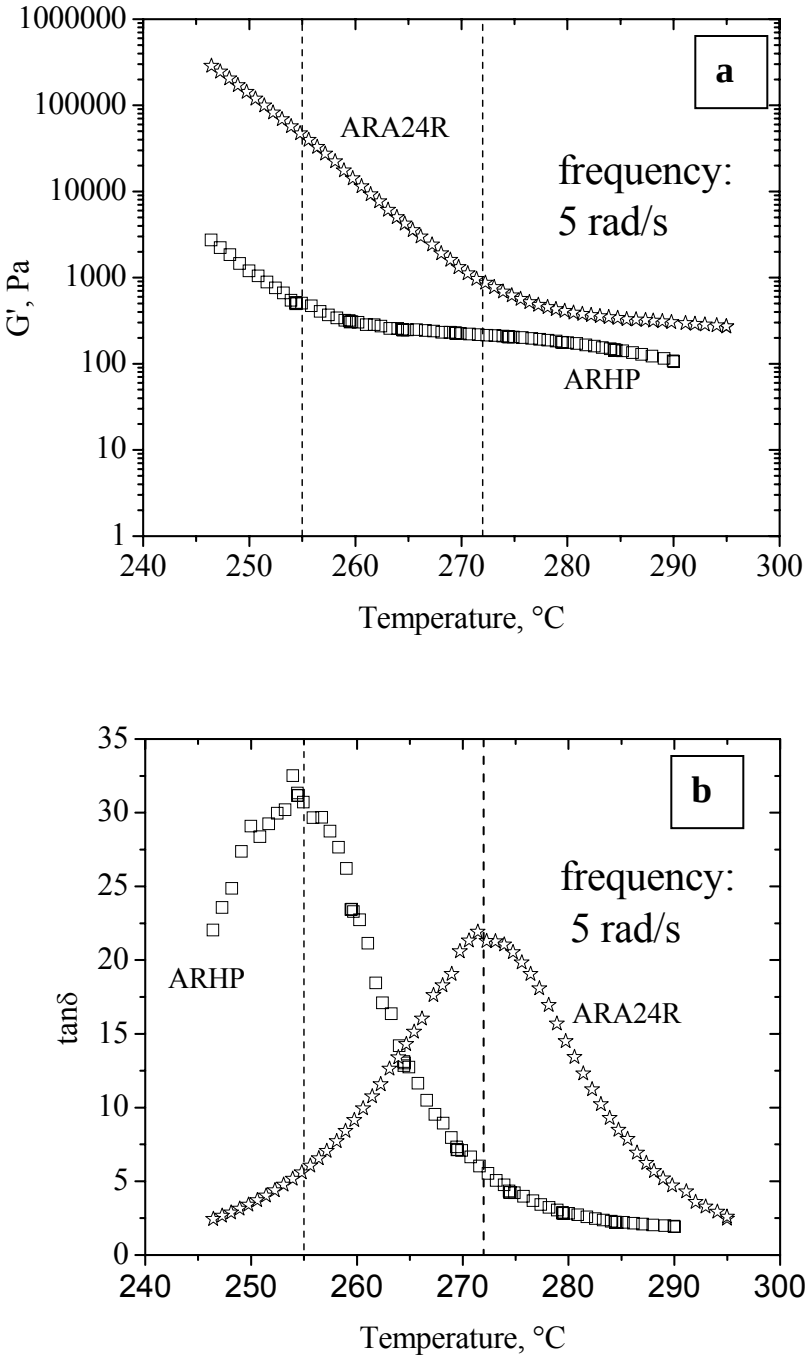

Figure 4.1: Temperature-sweep experiments on mesophase pitch samples at a frequency of 5 rad/s: (a) storage modulus (G'), and (b) tanδ. The dotted lines indicate the softening points for two grades of pitch.

4.2 Results and Discussion

4.2.1 Frequency-sweep experiments on fresh samples

For the present study, the frequency-sweep experiments were performed in the linear viscoelastic region (LVER) to probe the microstructure without perturbing it during measurement. To determine the linear region, the loss (G") and storage (G') moduli were measured as a function of strain for three different frequencies and temperatures. As seen in **Figures 4.2a** and **b**, for G", no significant variation from LVER was observed at strain values upto 100%, but G' started to decrease at a strain of ≈25% for a frequency of 100 rad/s.

Figure 4.2c displays moduli obtained at a frequency of 100 rad/s (the highest frequency in this study) at 280°C and 305°C. The non-linear behavior was observed for G' starting at ≈25% strain for these extreme temperatures too. At lower frequencies (1 and 10 rad/s), the LVER extended to higher strains (≈40%). For all subsequent experiments, a maximum strain of 10% was used. For conventional flexible-chain polymers, the onset of non-linearity typically does not depend on the applied frequency. However, dependence of LVER on frequency has been reported in the literature for some liquid crystalline polymers [Guskey and Winter, 1991; Somma and Nobile, 2004], but not others [Romo-Uribe et al., 1997].

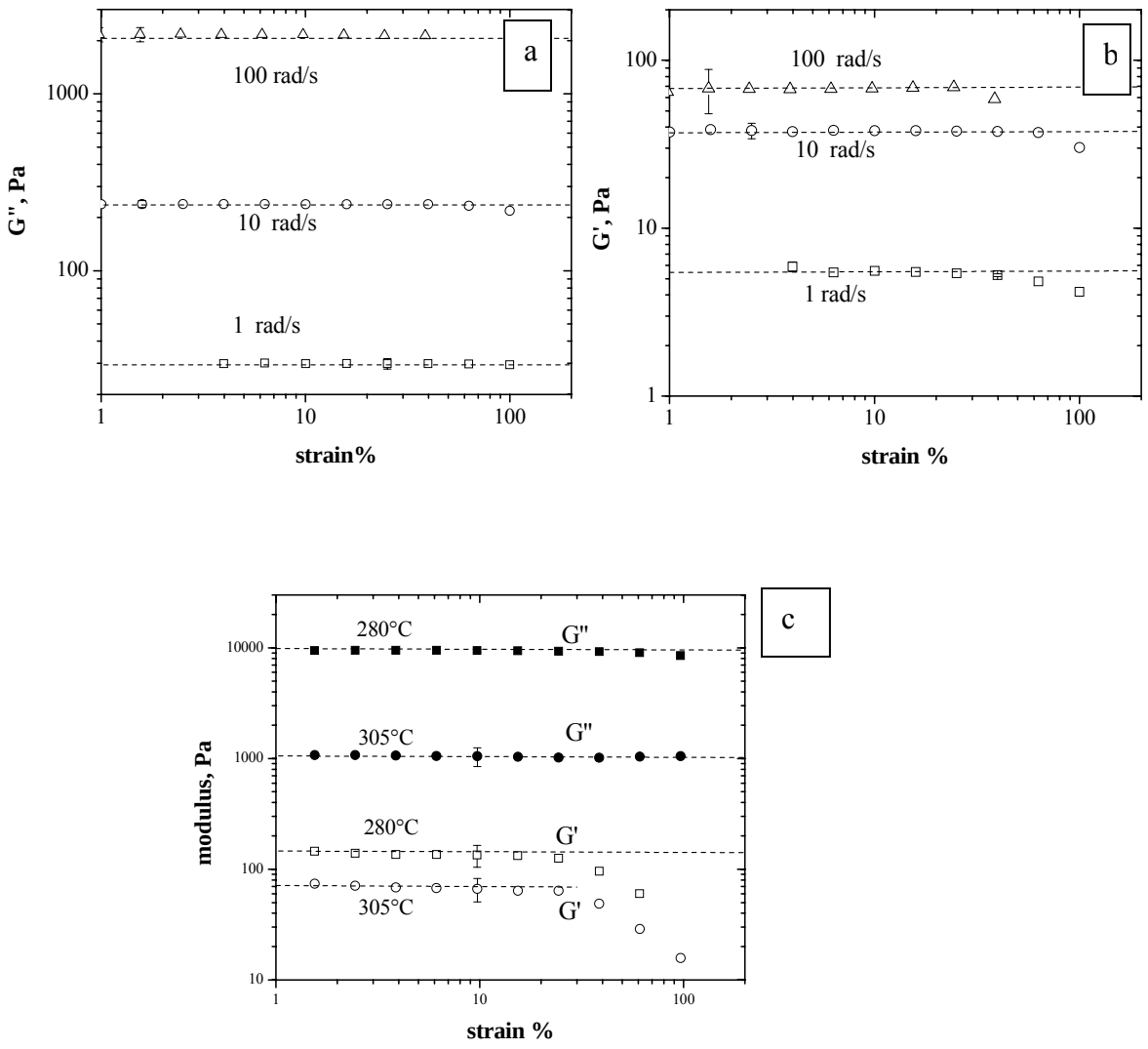

Figure 4.2: **(**a) Loss modulus (G") as a function of strain at 297°C for three different frequencies.
(b) Storage modulus (G') as a function of strain at 297°C for three different frequencies.
(c) loss (G") and storage moduli (G') as a function of strain at 100 rad/s for 280°C and 305°C. (Dotted horizontal lines are trend, no model fit)

Figures 4.3a-b display G' and G" as a function of frequency at four different temperatures: 280, 290, 297, and 305°C. **Figure 4.4** displays loss angle (δ) as a function of frequency. At a given frequency, as expected, the values of G' and G" decreased with increasing temperature. For a given temperature, an increase of G" was observed with increasing frequency. The estimated slope of ~0.9 (close to a value of 1) was similar to that reported for other grades of mesophase pitch [Cato, 2002], TLCPs [Kim and Han, 1993], and also for flexible chain polymers [Larson, 1999]. In few instances, slopes lower than 1 have been reported for some TLCPs [Driscoll and Masuda, 1991; Guskey and Winter, 1991; Somma and Nobile, 2004].

Figures 4.3a-b also indicates that the storage modulus displayed two different slopes: the low-frequency terminal zone had a slope of ~0.8, whereas the higher frequency response was almost a rubber-like plateau. Also, the onset of rubber-like plateau was temperature dependent and occurred at lower frequencies for lower temperatures. These frequency-sweep results also show that the loss modulus values were higher than the storage modulus over the entire frequency range, i.e., no cross-over frequency was observed. As displayed in **Figure 4.4,** values of the loss angle approaches 90° (π/2), signifying the higher magnitude of the loss modulus compared to that of the storage modulus. This behavior is consistent with that reported in prior studies on other types of synthetic mesophase pitches [Cato, 2002], but different from that observed for heat-soaked mesophase pitches prepared from isotropic Ashland A240 [Cheung et al., 1996].

At higher frequencies, a viscoelastic material behaves like a solid (elastic) due to insufficient molecular relaxation, and displays a G' plateau. At lower frequencies,

however, sufficient molecular relaxation takes place and a decrease of G' is observed with decreasing frequency. The storage modulus could not be measured at low frequencies due to the limitation of the torque transducer. At low frequencies, the slope of G' is ~2 for flexible chain polymers, whereas smaller slopes have typically been observed for other types of synthetic mesophase pitches [Cato, 2002] and liquid crystalline polymers [Guskey and Winter, 1991; Somma and Nobile, 2004; Driscoll and Masuda, 1991]. However, in some instances a value of ~2 has been reported for TLCPs [Kim and Han, 1993], and the plateauing of G' has also been observed at very low frequencies [Guskey and Winter, 1991; Somma and Nobile, 2004]. The plateauing of the storage modulus is generally associated with an ordered microstructure, which gives the material the enhanced (extra) elasticity. Yielding of such ordered microstructure of mesophase pitch also resulted in stress maximum during high-strain transient experiments (Chapter 3).

Modeling studies on nematic liquid crystals predict two different slopes of G' for two different frequency regime [Burghardt, 1991; De Andrade Lima and Rey, 2004]. A slope of 1 was predicted for G" and the magnitude of loss modulus was found to be higher than that observed for storage modulus [De Andrade Lima and Rey, 2004]. However, the intricate texture of real fluids cannot be fully considered in the modeling studies. Therefore, some quantitative differences may be observed between the modeling and experimental studies for the slope of the terminal zone of G'.

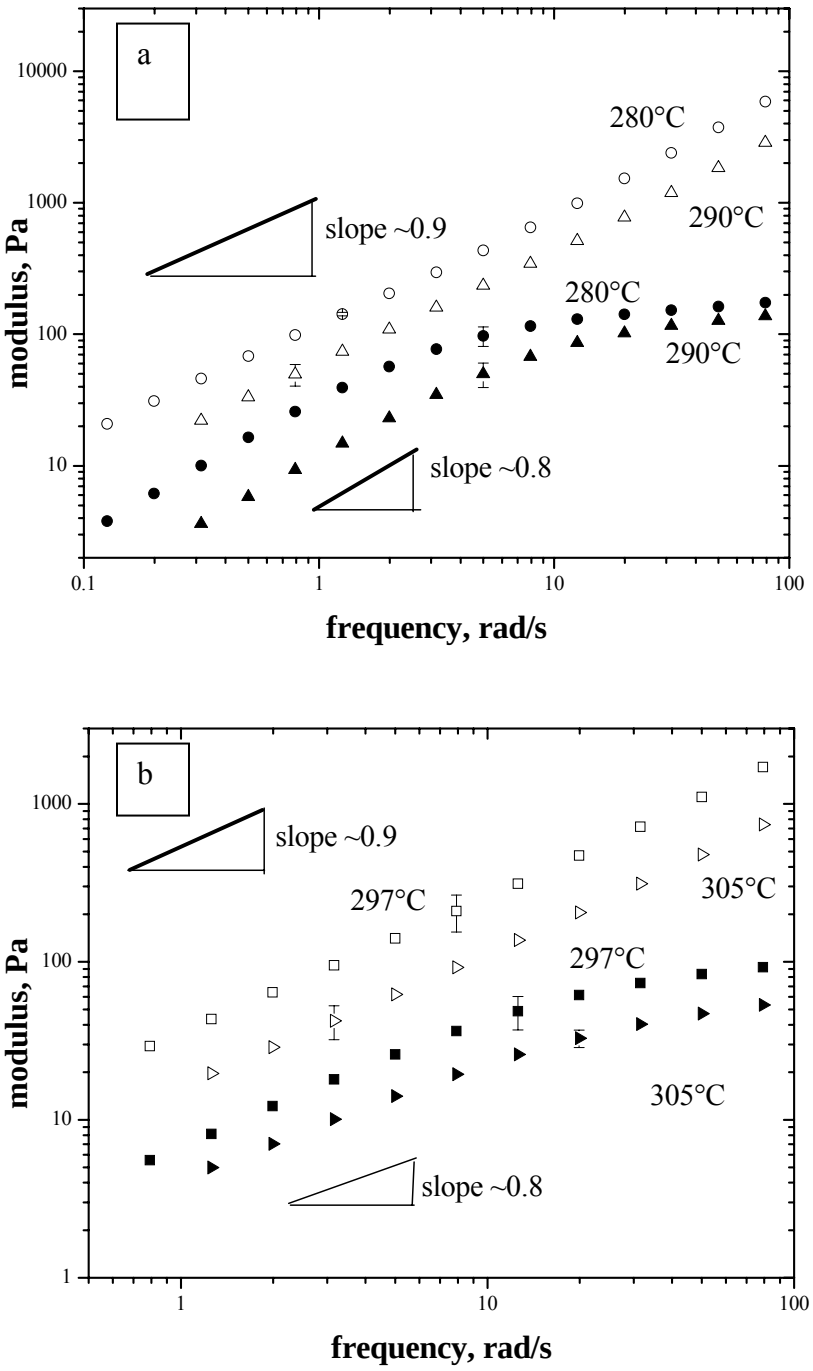

Figure 4.3: Storage moduli (solid symbols) and loss moduli (open symbols) as a function of frequency at (a) 280°C (○,●), 290°C (∆,▲); and (b) 297°C(□,■), 305°C(▷, ▶).

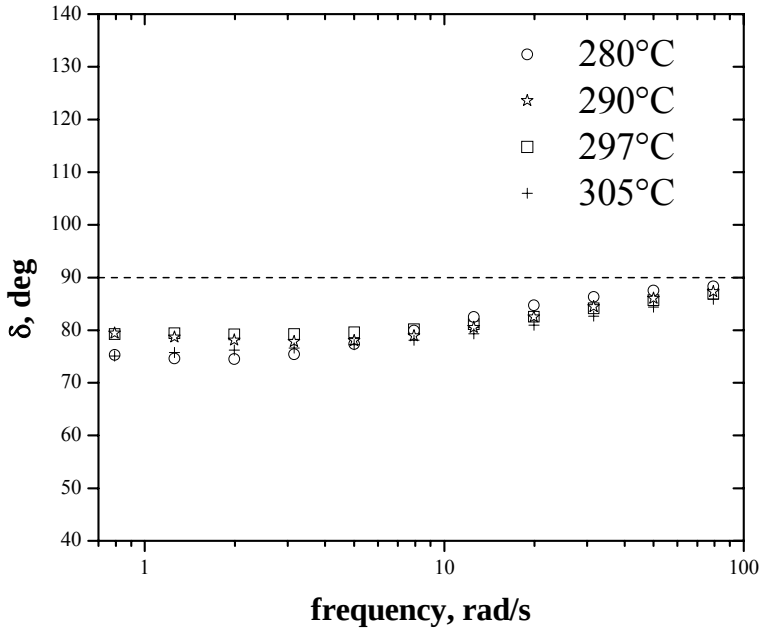

Figure 4.4: Loss angle (δ) of mesophase pitch as a function of frequency.

Figure 4.5 displays the complex viscosities and shear viscosities plotted against frequencies and shear rates, respectively, for a temperature of 297°C. The trend of shear and complex viscosities was similar. At lower shear rates or frequencies, the viscosities decreased with increase of frequencies or shear rates, and then reached a plateau. However, these two curves are not superimposable, i.e., this material did not follow the Cox-Merz rule. Deviations from Cox-Merz rule have been reported in literature for other mesophase pitches [Cato, 2002] and liquid crystalline polymers [Driscoll and Masuda, 1991], likely caused by the textured nature of these materials.

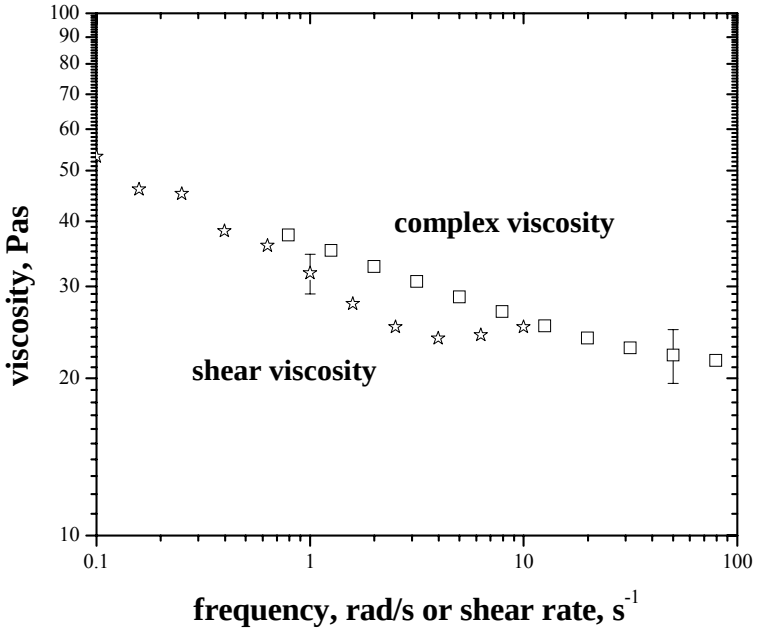

Figure 4.5: Shear and complex viscosities of mesophase pitch at 297°C as functions of shear rate (s^{-1}) and frequency (rad/s).

4.2.2 Effect of microstructure on dynamic response

To investigate the role of different textures on the dynamic response, samples were preconditioned by either preshearing or pre-oscillating (at large strain) before dynamic experiments. The preshearing was performed at two different shear rates, 1 and 10 s^{-1}, to steady state. In Chapter 2, it was noted that the shear stress and microstructure attained a steady state at ≈ 3000 strain unit. The dynamic moduli measured for these samples are displayed in **Figures 4.6a** and **b**, together with results presented earlier for unpresheared sample (for comparison purpose). It is evident from **Figure 4.6a,** that the different preconditioning steps had little effect on the loss modulus. In contrast, as seen in **Figure 4.6b**, the G' values were significantly affected by preconditioning. G' values were highest for the unpresheared sample and decreased with preshearing. The extent of decrease depended on the preshearing rate in that an order of magnitude decrease in the plateau value was observed for a preshearing of 10 s^{-1} as compared with that for unpresheared sample.

Samples were also preconditioned by applying large oscillatory strain of 60% (in nonlinear region) at a high frequency of 300 rad/s, in an attempt to disrupt the initial microstructure, but to not orient it. The G' response, also displayed in **Figure 4.6b,** was significantly different than that observed for unprehearsed sample. G' increased with frequency and then plateaued, resembling a solid-like behavior. The plateau values were similar to those obtained after a preshearing at 10 s^{-1}. It is evident from above results that preshearing has a significant effect on the elastic response of mesophase pitch. For a thermotropic polyester similar drop of G' was reported for presheared samples [Wissbrun

and Griffin, 1982]. A drop of complex viscosity (η*) was also observed for PSHQ10 samples after preshearing [Kim and Han, 1994].

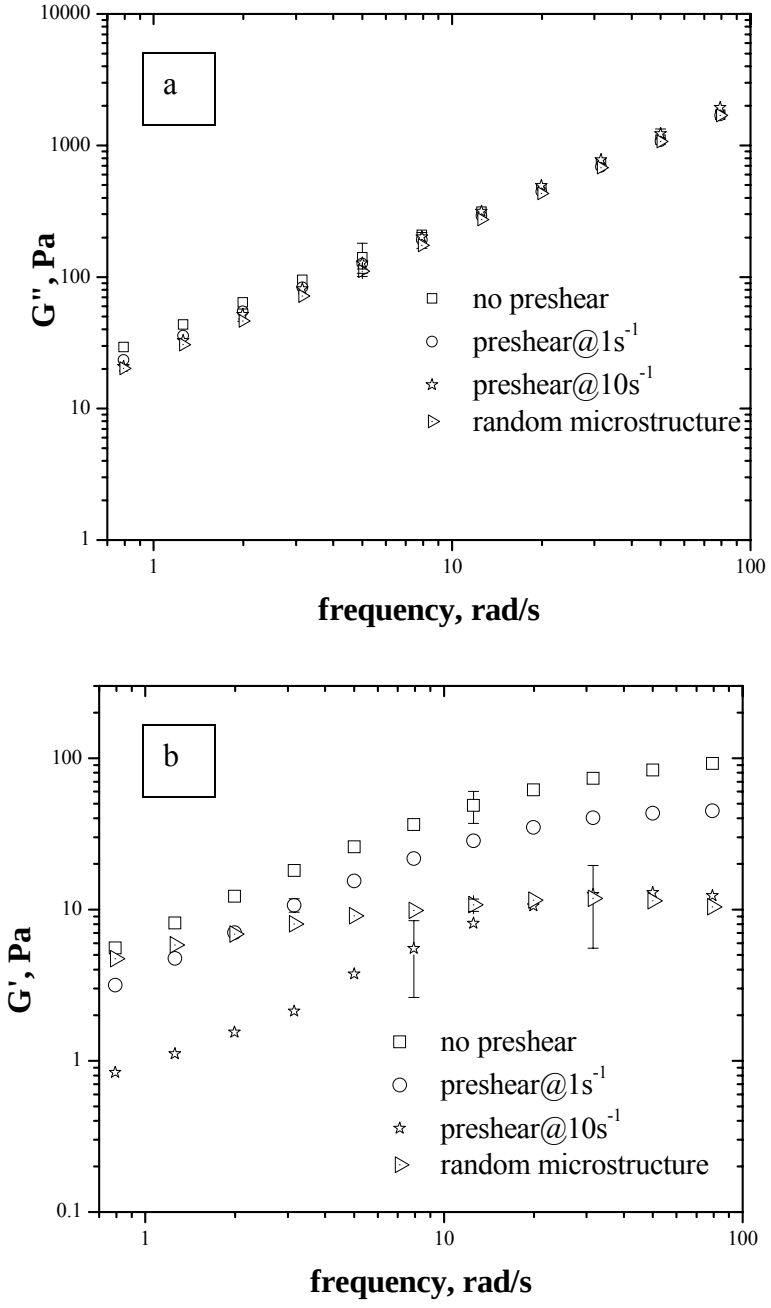

Figure 4.6: Effect of preconditioning on dynamic moduli at 297°C: (a) loss modulus, G" and (b) storage modulus G'.

The microstructure of these samples is presented next in **Figures 4.7a-c** and **Figures 4.8a-l**. The orientation of the discotic layer-planes was determined using the first order red plate. For a specified sample position (relative to the polarizer-analyzer), edge-on layer-planes in the shear-flow direction appear blue, whereas those in the radial direction of the rheometer cone-plate appear yellow (see Chapter 3).

Figure 4.7a displays the resulting microstructure of AA' section for oscillatory preconditioned sample. In contrast to the elongated radial texture that was observed after squeezing the sample in the cone-plate fixture (**Figure 4.8a),** the texture was rounded and finer, with the size estimated at ~20 μm. The relative area of blue and yellow regions was approximately equal, indicating that there was no preferred orientation of layer-planes. Similar fine and random microstructure was observed for other orthogonal sections, BB' and CC' (**Figsures 4.7b, c**). Thus, the initial radial texture due to lowering of the cone was broken or disrupted into smaller random structure as a consequence of the oscillatory preconditioning.

Unlike other cases, the size of the microstructure can be obtained fairly unambiguously for the oscillatory preconditioning and the value can be used to determine the average elastic constant, *K*. It has been reported in the literature that G' scales as K/a^2, where *a* is the domain/structure size [Larson, 1999]. Therefore, $K \sim G' a^2$. The measured value of G' was ~10 Pa and for a structure size (*a*) of 20 μm, the estimated value of *K* is $4*10^{-9}$ N. The estimated value of average elastic constant was similar to that reported in literature for other grades of mesophase pitch [Cato et al., 2005].

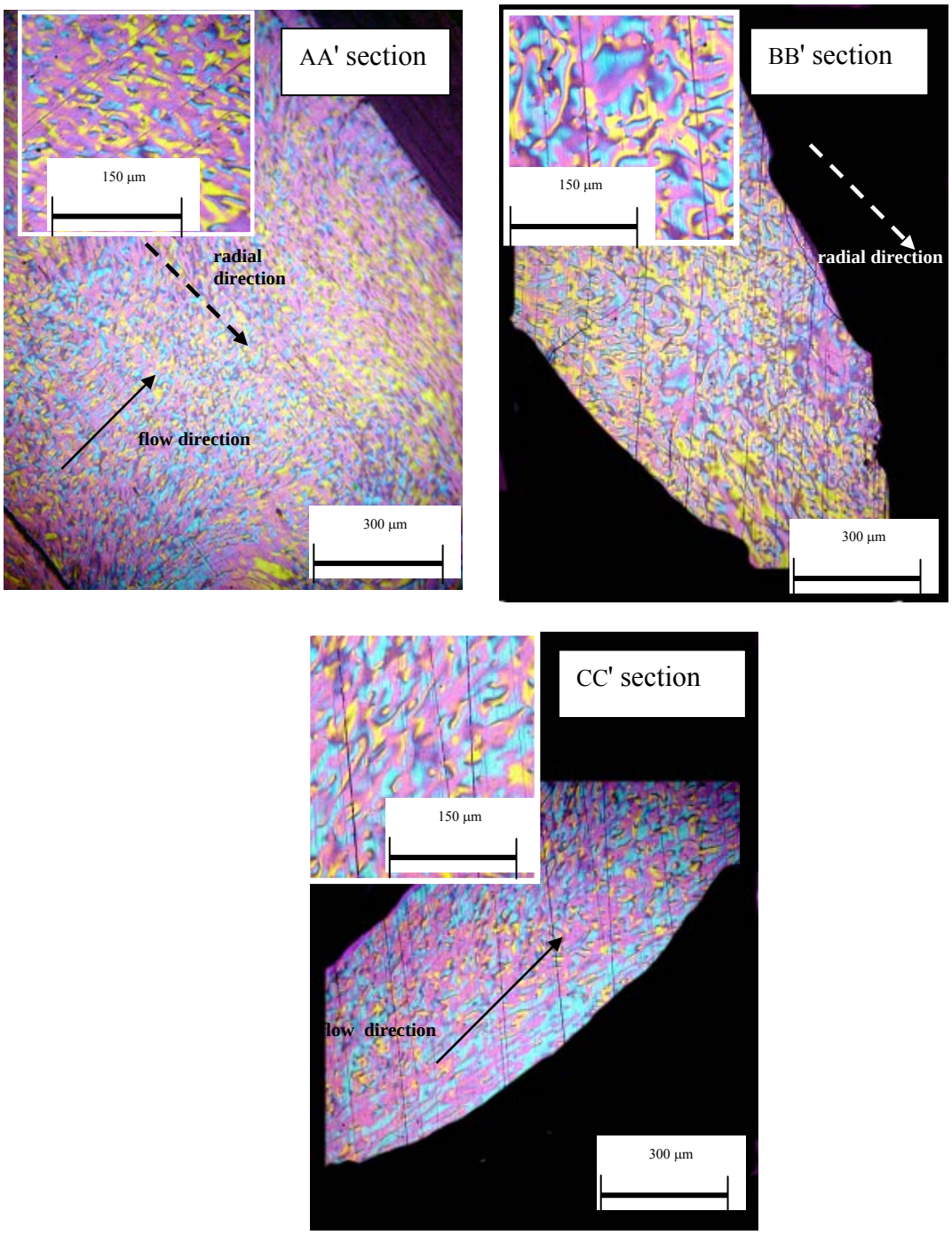

Figure 4.7: Microstructure of solidified pitch samples after preoscillating at 300 rad/s and ≈60% strain in three orthogonal sections: AA', BB', and CC' (defined in Chapter 3).

Figures 4.8a-c display the microstructure for an unpresheared sample in three orthogonal sections (AA', BB' and CC'). **Figures 4.8d-f** and **Figures 4.8g-i** display the micrographs in three orthogonal sections obtained after steady shearing (≈3000 su) at 1 s^{-1} and 10 s^{-1}, respectively. It is noted that **Figures 4.8a-i** were studied in detail in Chapter 3. For unpresheared sample (**Figures 4.8a-c**), due to the small extensional flow encountered during sample loading, a weak but preferred orientation was observed in the radial direction of the rheometer plate. After shearing for ≈3000 *su* at 1 s^{-1}, the microstructure became flow oriented (**Figsures 4.8d-f**). For a steady-sheared sample at $1s^{-1}$, the nominal width (minor axis) of the edge-on flow-aligned regions (blue) was measured to be ~30 μm. A significant number of these regions were measured to be about 300 μm long, and some appeared even longer because the boundary of such regions in the longitudinal direction (major axis) was not clear.

Figures 4.8g-i display the microstructure of the three orthogonal sections for a steady-sheared sample at $10s^{-1}$. As displayed in **Figure 4.8g**, the flow-oriented microstructure became finer as the shear rate increased to 10 s^{-1}. The width of the edge-on flow-aligned regions (blue regions) in many cases was found to be less than 10 μm, and could not be measured accurately due to the resolution limitation of optical microscopy. Significant presence of edge-on flow-aligned layer-planes (blue) was also observed in CC' section, whereas in BB' section the microstructure was fine and random, with presence of all three colors (blue, yellow and magenta). Similar to steady-sheared sample at 1 s^{-1}, it can be inferred that layer-planes became flow oriented after steady shearing at $10s^{-1}$; however, the microstructure became much finer. Micrographs obtained

for oscillatory preconditioned samples are also shown (**Figure 4.8 j-l**), for comparison purpose only.

From the above results, it is evident that the different elastic responses observed earlier are related to different textures found in AR-HP mesophase pitch. Coarsest structures possessed the highest G', whereas finer and oriented structures that emerged from preshearing led to lower G' values. Also, finer but random microstructure (pre-oscillated sample) resulted in a more solid-like behavior that manifested in a broader G' plateau.

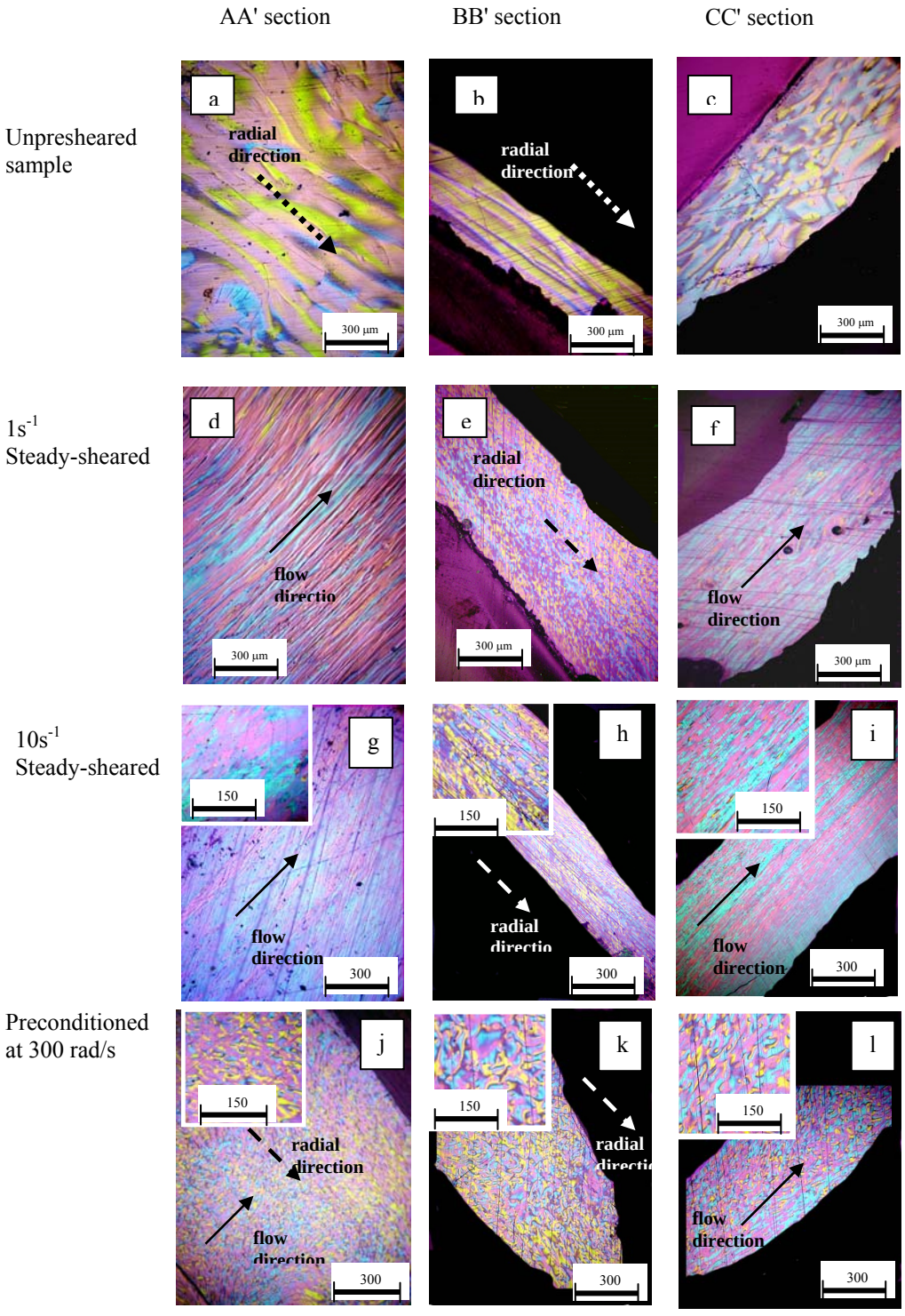

Figure 4.8: Microstructure of solidified pitch samples in three orthogonal sections: AA', BB', and CC' (defined in Chapter 3).
(a-c) initial microstructure after bringing the cone and plate fixture together,
(d-f) after steady-shearing (≈3000 *su*) at $1s^{-1}$,
(g-i) after steady-shearing (≈3000 *su*) at $10s^{-1}$,
(j-l) after preoscillating at 300 rad/s and ≈60% strain.

4.2.3 Relaxation behavior after flow cessation

To probe the microstructural changes that occur after cessation of steady shear flow, dynamic time-sweep experiments were performed at a constant frequency of 5 rad/s but over an extended duration. The G" responses are displayed in **Figure 4.9a**. Similar to the response observed in earlier experiments on presheared samples, the loss modulus remained essentially unchanged within experimental error during textural relaxation after shear-flow cessation.

Figure 4.9b displays the evolution of G' at a frequency of 5 rad/s and strain of 10% in continuous (solid lines) and intermittent testing modes (□). The consistency of results from continuous and intermittent experiments indicates that the material response was not significantly affected by the extended small-strain oscillation itself and, therefore, the relaxation of the texture can be studied using the small-strain dynamic test. Henceforth, these experiments will be referred as *relaxation* experiments.

It is evident from **Figure 4.9b** that the storage moduli initially increased with time and almost plateaued after 4500 s of relaxation. The magnitude of storage modulus was not similar for samples with different flow histories. The relative increase of G' was highest (≈400%) for the sample presheared at 10 s^{-1}.

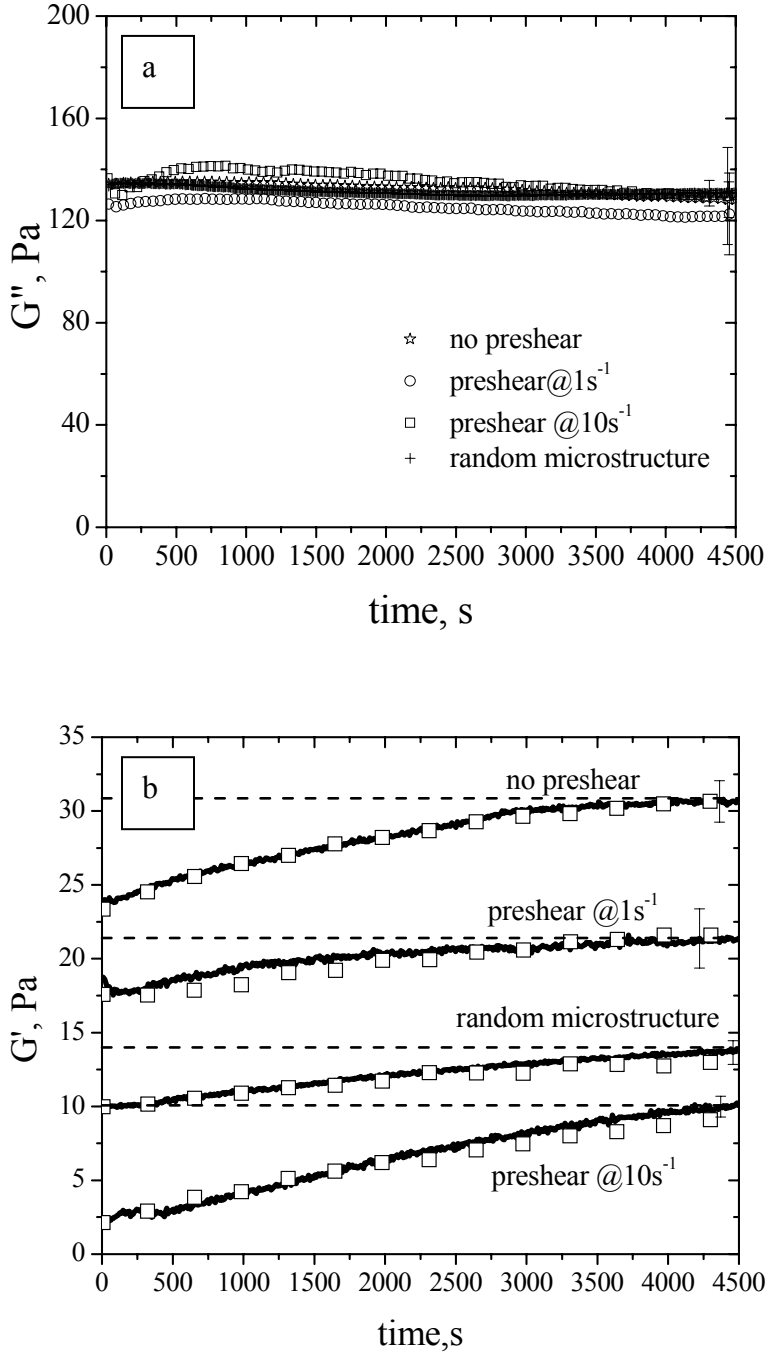

Figure 4.9: Evolution of G" and G' with relaxation at 297°C and 5 rad/s for samples with different initial conditions.

The relaxation behavior of AR-HP mesophase pitch after cessation of shear flow has some similarities with other thermotropic liquid crystalline polymers [Han and Kim, 1994; Lee and Han, 2003] and lyotropic solution of HPC [Grizzuti et al., 1993; Burghardt, 1998]. During dynamic time-sweep experiments, an increase of G' and G" was observed for the presheared samples of PI-nCN, a side chain liquid crystalline polymeric system, and the extent of increase was a function of the molecular weight of the polymer [Lee and Han, 2003]. However, for PSHQ10, only an increase of G" was observed [Han and Kim, 1994].

For HPC, both G' and G" (also complex modulus, G*) were found to increase with time [Grizzuti et al. 1993; Burghardt, 1998]. But the molecular orientation, as estimated from birefringence, decreased with increasing test time [Burghardt, 1998]. Increasing preshearing rates resulted in higher modulus values [Burghardt, 1998; Grizzuti et al., 1993]. Experiments over prolonged duration showed that the modulus plateaued for any given shear rate. Since literature studies on liquid crystalline polymer suggest that the change of dynamic moduli is caused by microstructural changes that occur during relaxation process [Grizzuti, et al. 1993; Han and Kim, 1994; Burghardt, 1998; Lee and Han, 2003], the microstructural observations for mesophase pitch during relaxation after cessation of shear flow are presented next.

Figures 4.10a-f, Figures 4.11a-f, and **Figures 4.12a-c** display the detailed microstructure of samples after they were subjected to relaxation for various durations starting with different initial textures. These figures are combined and are displayed in **Figure 4.13** for comparison purpose. Optical micrographs from cross-polarized and first order red plate are shown for the three orthogonal sections: AA', BB', and CC' (defined

earlier). **Figures 4.10a-c** and **Figures 4.10d-f,** respectively, show the different microstructure resulting from structure evolution after 1000 s and 4500 s of relaxation; the initial microstructure (i.e., at 0 s) was displayed in **Figures 4.8a-c**. As observed from AA' section, after 4500s of relaxation **(Figure 4.10d)**, the relative area of radially aligned, edge-on regions (yellow) regions was estimated at ≈20%, similar to that observed at 0 s. The relative area of edge-on regions parallel to the periphery of the rheometer plate (blue regions) increased from an initial value of ≈5% to ≈10%. The total relative area of edge-on layer-planes was found to increase from an initial value of ≈50% to ≈65% after 4500 s of relaxation. Although, the relative area of edge-on radial regions (yellow regions) after relaxation was similar to that observed initially, the increased area of edge-on regions parallel to the periphery of the rheometer plate (blue regions) and subsequent increase of the edge-on layer-planes at $AA^{'}$ section suggests that radial orientation of layer-planes decreased during relaxation.

This is confirmed by studying the microstructural evolution of other two orthogonal sections: $BB^{'}$ and $CC^{'}$. The initial elongated structure of $BB^{'}$ section changed to somewhat random and coarser structure during the relaxation process (**Figures 4.8b, 4.10b, 4.10e**). Similarly, the initial random microstructure of $CC^{'}$ section became coarser (**Figures 4.8c, 4.10c, 4.10f**). Therefore during relaxation, it can be inferred that the three dimensional microstructure became coarser, and the initial orientation of the layer-planes along the radial direction decreased. This relaxation of microstructure is accompanied by an increase of G' that was observed in **Figure 4.9b.**

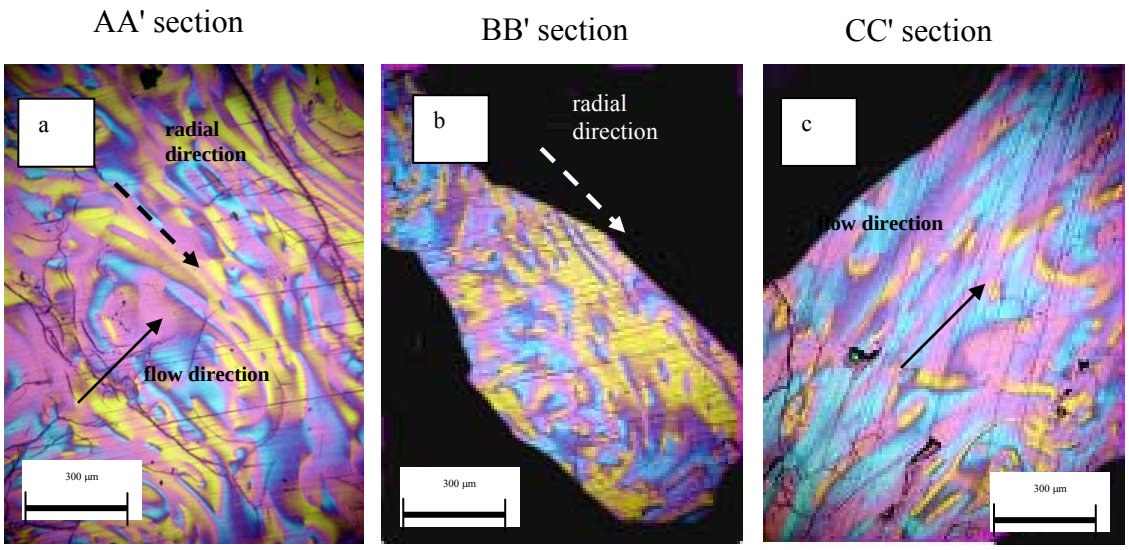

Unpresheared sample→ 1000 s of oscillation

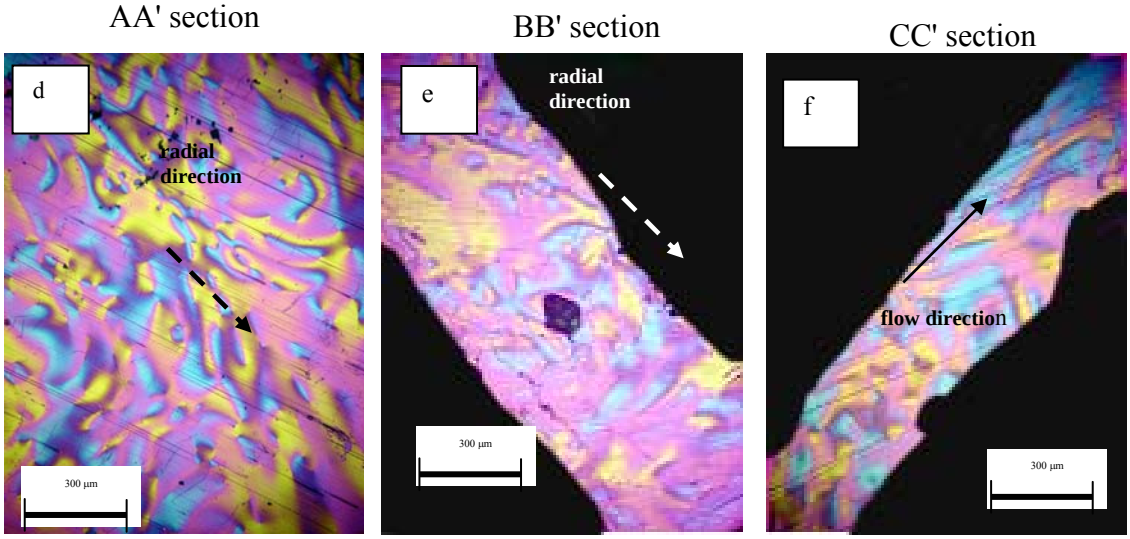

Unpresheared sample→ 4500 s of oscillation

Figure 4.10: Microstructure of solidified mesophase pitch in three orthogonal sections, AA', BB', and CC' (defined in Chapter 3), collected after relaxation experiments at 5 rad/s and 297°C on the unpresheared samples: (*a-c*) after 1000 s of relaxation, *(d-f)* after 4500 s of relaxation.

Figures 4.11a-c illustrate the micrographs obtained in three orthogonal sections after 4500 s of relaxation on the samples presheared at 1 s^{-1}. As seen from AA' section, the initial flow-oriented microstructure after steady-shearing (**Figure 4.8d)** changed to a random one (**Figure 4.11a**). The relative area of edge-on flow-aligned regions (blue regions) reduced to ≈20% from an initial value of ≈30% (**Figure 4.8d**). In contrast to flow-aligned micrograph (**Figure 4.8d**), which was almost free of radially aligned edge-on regions (yellow regions), a 10% area of the micrograph was found to be yellow. Also, the total area of edge-on layers increased from ≈50% to 65%. Coarsening of microstructure was observed, and the length and width of some blue/yellow regions was found to be as large as ~300 and ~100 μm, respectively.

As seen in **Figure 4.11c,** for CC' section, the relative area of edge-on flow-aligned regions (blue regions) was ≈20%, less than ≈35% observed initially (**Figure 4.8f**) and significant coarsening of microstructure took place during 4500 s of relaxation. Similar to CC' section, a significant coarsening of initial fine structure was observed for BB' section (**Figure 4.11b**). Presence of edge-on, flow-aligned regions (blue regions) in AA' and CC' sections suggest that during relaxation the initial orientation of layer-planes along the flow direction was not totally lost; however, the microstructure coarsened significantly.

Change of microstructure for the sample presheared at 10 s^{-1} (**Figures 4.11d-f)** was similar to that for samples presheared at $1s^{-1}$ in terms of orientation effects. However, the changes in textural size were significantly different. The initial fine microstructure became significantly coarser and the length and width of some blue/yellow regions were

found to be as large as ~500 μm and ~100 μm, respectively, i.e., approaching the thickness of the flow-geometry.

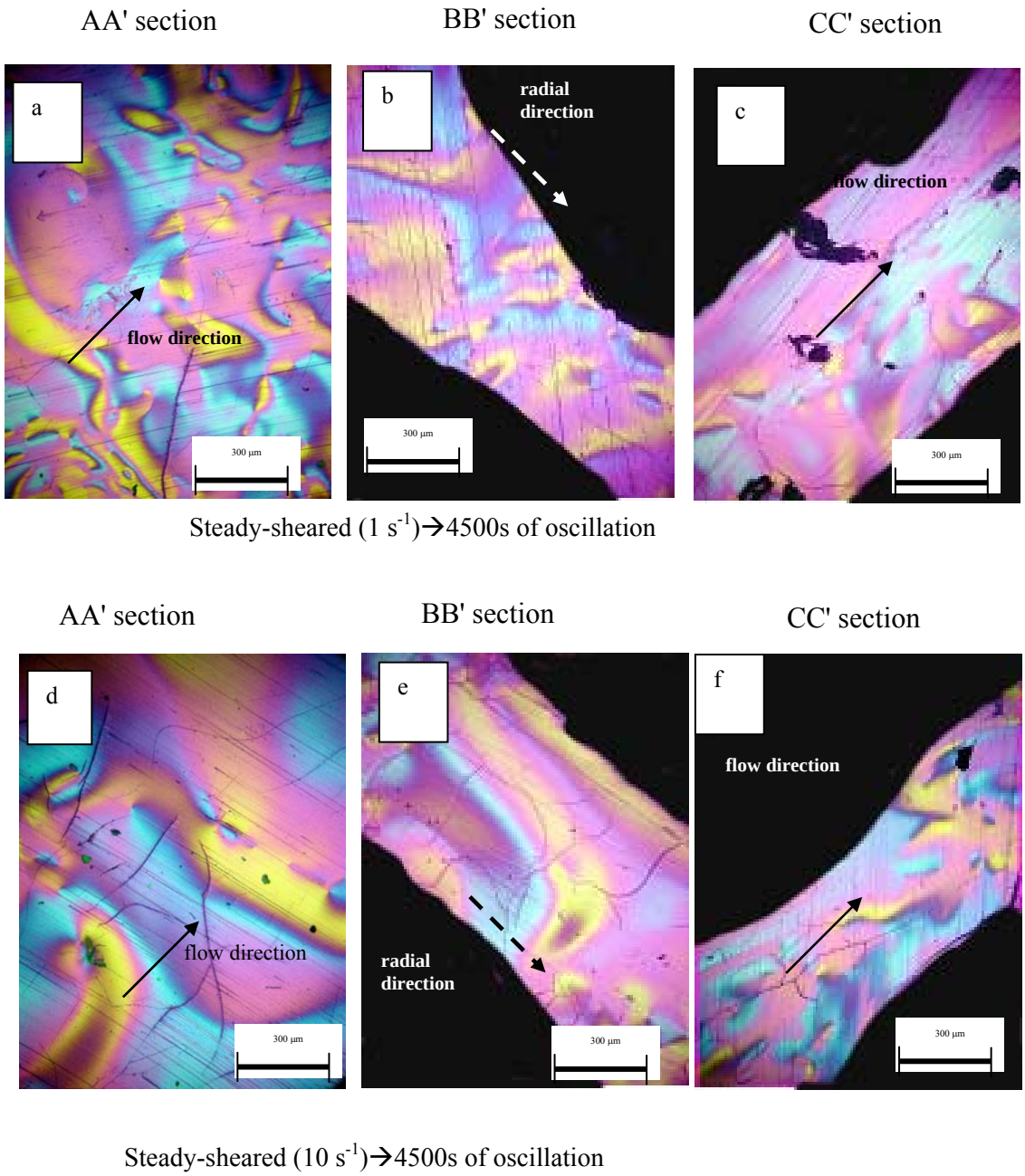

Figure 4.11: Microstructure of solidified mesophase pitch in three orthogonal sections: AA', BB', and CC' (defined in Chapter 3), collected after relaxation experiments at 5 rad/s and 297°C. *(a-c)* after 4500 s of relaxation on the samples presheared at $1s^{-1}$, *(d-f)* after 4500 s of relaxation on the samples presheared at $10s^{-1}$,

Starting with a fine, random texture obtained after large-strain pre-oscillatory deformation at 300 rad/s (**Figures 4.7a-c**), the microstructure obtained after 4500 s of relaxation is displayed in **Figures 4.12a-c.** The microstructure remained random (**Figures 4.12a-c**), as inferred from the similar areas of blue and yellow regions in all three orthogonal sections. However, significant coarsening of microstructure was observed. The length and width of the blue/yellow regions were found to be ~200 μm and ~100 μm, respectively. Thus, the increase of elastic modulus observed in **Figure 4.9b** was primarily due to the coarsening of microstructure.

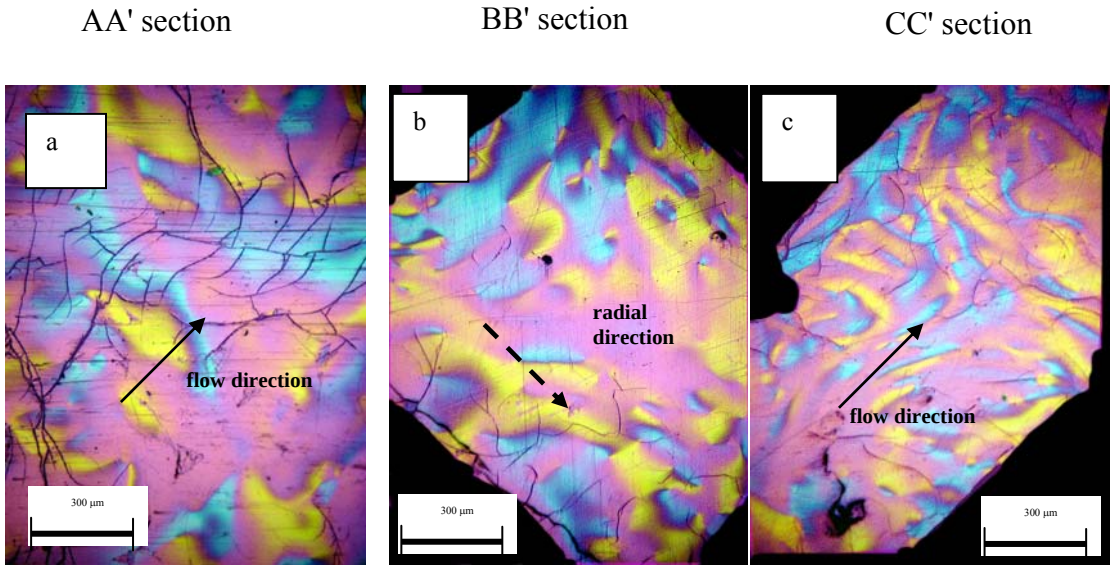

Figure 4.12: Microstructure of solidified mesophase pitch in three orthogonal sections: AA', BB', and CC' (defined in Chapter 3), collected after relaxation experiments at 5 rad/s and 297°C after 4500 s of relaxation on the samples with random microstructure.

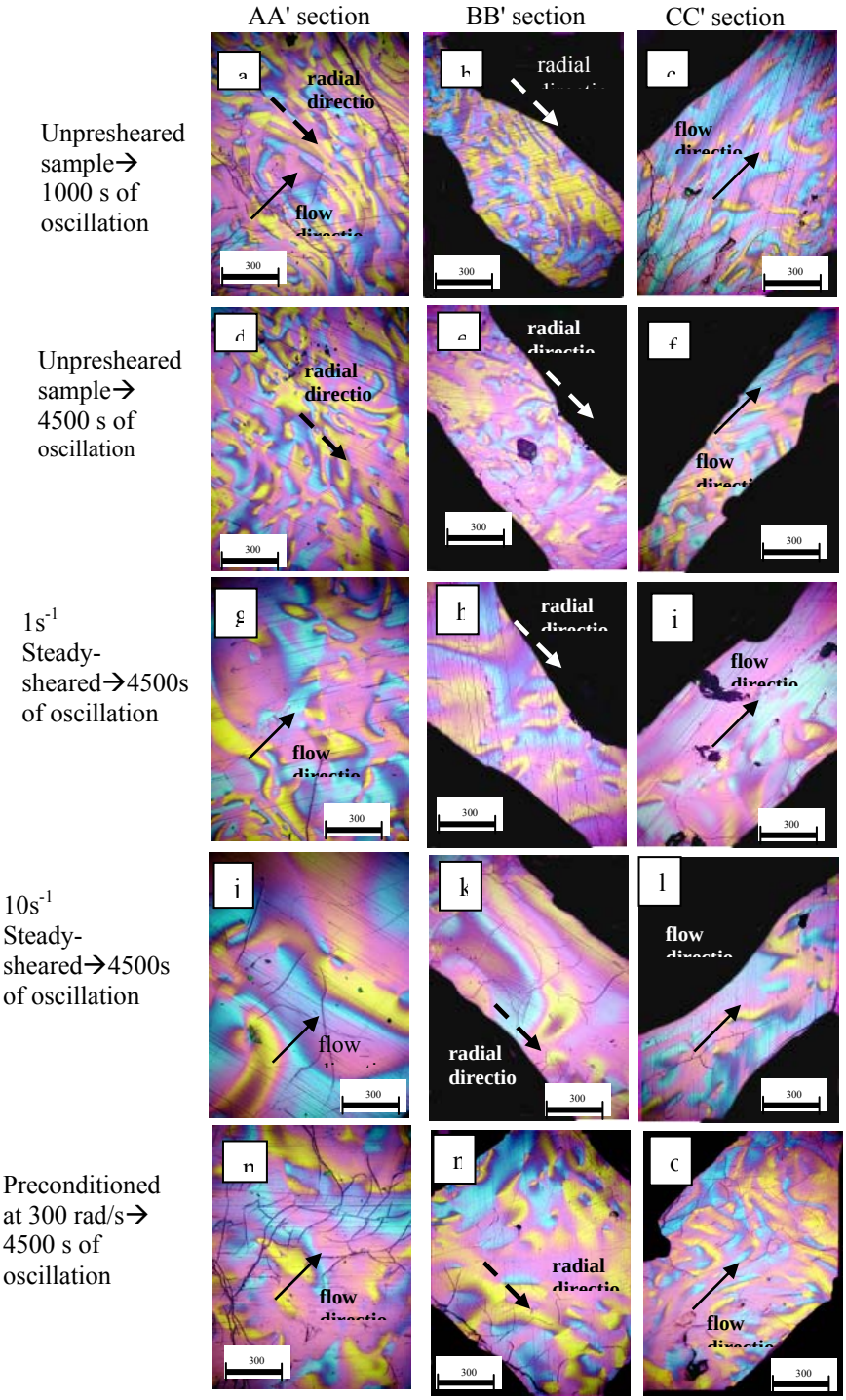

Figure 4.13: Microstructure of solidified mesophase pitch in three orthogonal sections: AA', BB', and CC' (defined in Chapter 3), collected after relaxation experiments at 5 rad/s and 297°C.
(*a-c*) after 1000 s of relaxation on the unpresheared samples,
(d-f) after 4500 s of relaxation on the unpresheared samples,
(g-i) after 4500 s of relaxation on the samples presheared at $1s^{-1}$,
(j-l) after 4500 s of relaxation on the samples presheared at $10s^{-1}$,
(*m-o*) after 4500 s of relaxation on the samples with random microstructure.

The textural relaxation time (τ) can be approximated from scaling arguments as $\tau \sim \eta a^2/K$, where a is the structure size, η is the characteristic viscosity, and K is an average elastic constant [Burghardt, 1998; Larson, 1999]. If K and η are assumed constant, then $\tau \sim a^2$, i.e., relaxation time is a strong function of textural size and should decrease siginificantly with decreasing textural size. For the present case, the relaxation dynamics were not significantly different for different textural sizes. However, it is noted that the relative increase of G' depended on the microstructure and was highest for the sample presheared at 10 s^{-1}, which was also the most oriented texture. Therefore, along with the textural size, layer-plane orientation influences the relaxation process possibly by affecting K and η. Also, it is reported in Chapter 2 that the slope of the region 1 was only ~-0.2 (i.e., different than -0.5), signifying that the relationship $\tau \sim \eta a^2/K$ does not hold exactly for this material.

Microstructural observations during relaxation experiments have been reported in limited literature studies [Romo-Uribe et al., 1997]. During oscillatory shearing of rod-like HBA/HNA polymers, initial elongated structure relaxed to a "tight" structure, and was accompanied by an increase of moduli, similar to that observed in the present study for a disk-like system. Also, the decrease of layer-plane orientation observed in the present results for AR-HP mesophase pitch appears to be consistent with the loss of orientation measured by *in situ* X-ray measurements for HBA/HNA polymers [Romo-Uribe et al., 1997].

4.3 Conclusions

The textured nature of AR-HP mesophase pitch contributed to a lower slope of ~0.8 for the elastic modulus in the low-frequency terminal region as compared to ~2 observed for flexible chain polymers. Different preshearing conditions led to different initial textures. While the loss modulus (viscous component) remained largely unaffected by the texture, the elastic response of AR-HP mesophase pitch was found to be strongly dependent on the texture. Coarsest textures led to the highest elastic modulus, whereas finer and oriented structure that emerged from preshearing led to lower G' values. Also, finer but random microstructure resulted in more solid-like behavior that manifested in a broader G' plateau. Relaxation of microstructure resulted in an increase of storage moduli, and it is postulated that the relaxation process is influenced not only by the textural size, but also by layer-plane orientation.

CHAPTER 5

MICROSTRUCTURE DEVELOPMENT DURING PROCESSING FLOW

Mesophase pitch can experience a wide range of flow conditions during processing. During manufacturing of mesophase pitch-based C-C composites, pitch flows through a porous medium of continuously changing cross-sectional area during infiltration through the matrix. The literature studies show that the fibers affect the microstructure of the infiltrated pitch in the matrix [Fathollahai et al., 2005]. Also, during carbon-fiber spinning, the mesophase pitch experiences various flow conditions as it passes through the extruder, the counterbore, and the spinneret. In the spinneret, the mesophase pitch is subjected to high wall shear rates (~1000 s^{-1}), which in turn affect the final texture of mesophase pitch. Literature studies suggest that the texture of carbon fibers is strongly influenced by the processing conditions and the spinneret geometries [Matsumoto, 1985; Otani and Oya, 1986a & b; Hamada et al., 1987].

Microstructure development within a capillary has been reported in the literature for different grades of mesophase pitches [Fathollahai and White, 1994; Fleurot, 1998]. It was noted that the size of microstructure decreased with increasing shear rates. In another study, the microstructural aspect of as-spun fibers was studied, and effort was made to correlate with the texture of carbonized fibers [White et al., 2003]. Despite several studies, the microstructural development of mesophase pitch during various processing conditions is not fully understood.

This chapter first reports the flow behavior of AR-HP mesophase pitch at high shear rates as characterized using capillary rheometer (ACER). Such high wall shear rates are generally observed during fiber-spinning or during high-pressure infiltration step. To investigate the microstructure during processing flow, custom-made dies were used and mesophase pitch was processed through these dies using a single-screw extruder. At steady state, the dies were quenched and the solidified pitch material within was studied in various orthogonal sections. In these dies, the wall-shear rate was low (~$10s^{-1}$) in the counterbore, but quite high (~1000 s^{-1}) in the capillary. Such varying flow situations are observed in different stages of processing of carbonaceous precursors.

5.1 Experimental

5.1.1 High shear rate experiments

The high shear rate (300-10,000 s^{-1}) viscosity was measured using a TA Instruments Advanced Capillary Extrusion Rheometer (ACER). The diameter of the barrel was 20 mm, whereas diameter of the capillary was 1 mm. Capillaries with three different aspect ratios (L/D ~5, 20, and 30) were used. The pressure drop across the capillary was measured using well calibrated pressure transducers (maximum ΔP ~ 20 MPa and 70 MPa). The lowest shear rate that could be measured at a particular temperature was determined by the lower limit of pressure transducer (10% of maximum limit). Also, at lower shear rates, the variation of measured viscosity values was likely

caused by presence of bubble in the melt. The sample loading technique and details of the capillary rheometer are described in Appendix A.

5.1.2 Processing flow experiments

To study the microstructural development within the capillaries, dies with different dimensions were machined by the Machining and Technical Services from 28 mm pieces of threaded brass rod (1/2″– 20 threaded rod). As shown in **Figure 5.1**, there were three regions in any given die: counterbore with a diameter of 4 mm, a contraction region, and a capillary with a diameter of 1 mm. A standard drill head was used to machine these dies, and the entry angle for the capillaries was about 120°. Capillaries with two different lengths, 3 and 20 mm were used; however, the total length of the dies remained constant at 28 mm. As shown in **Figure 5.2**, a small blind hole was drilled in the die wall, near the exit of the die, to insert an external thermocouple.

A die with desired dimension (L/D) was attached to a single screw extruder with a screw diameter of ¾″ (**Figure 5.2)**. During experiments, temperature of the external thermocouple was maintained to a desired value by changing the temperature settings of the four temperature controllers connected to the extruder. The free extrudate that came out of the die was collected and was weighed to measure the flow rate (density ≈1230 kg/m^3). The desired flow rate was maintained by changing the speed of the screw. For a desired flow rate, once the pressure reached a steady state, the motor was turned off and the die was quenched immediately by submerging the tip of the die into a bowl

containing ice-water. The die was then unscrewed from the extruder. The details of experimental procedure are described in Appendix A.

The quenched dies containing solidified pitch were then prepared for microstructural studies. As shown in **Figure 5.3**, the microstructure was studied longitudinally and at different cross-sectional planes. For microstructural study in the longitudinal mid-plane, the dies were embedded in epoxy and then ground to the vicinity of the mid-plane using Buehler Automet polisher/grinder. The exposed section was then polished using polishing-papers with increasing level of fineness. The final polishing was performed using 1 μm diamond suspension followed by 0.05 μm alumina suspension on polishing cloths. For microstructural studies of cross-sectional planes, dies were cut at the desired sections using a hand-saw and then embedded in epoxy. These epoxy-embedded samples were polished using the same procedure as described above (details provided in Appendix A).

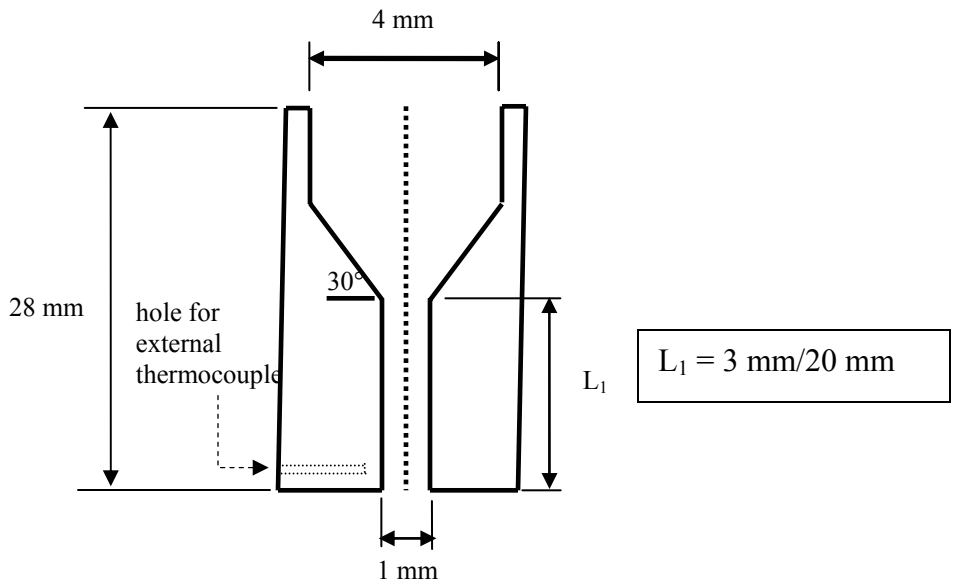

Figure 5.1: Schematic of the custom made dies for two different lengths (L_1), 3 and 20 mm.

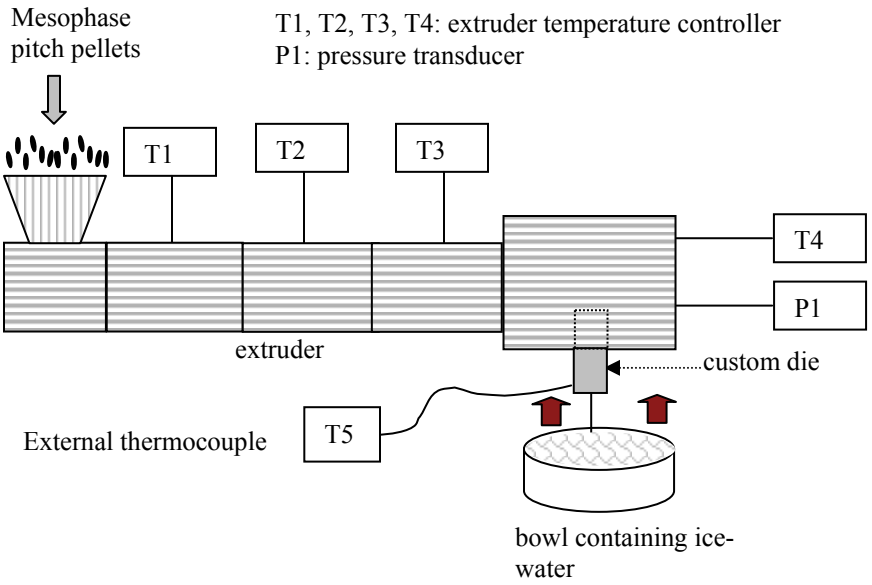

Figure 5.2: Schematic of a single-screw extruder with die and external thermocouple.

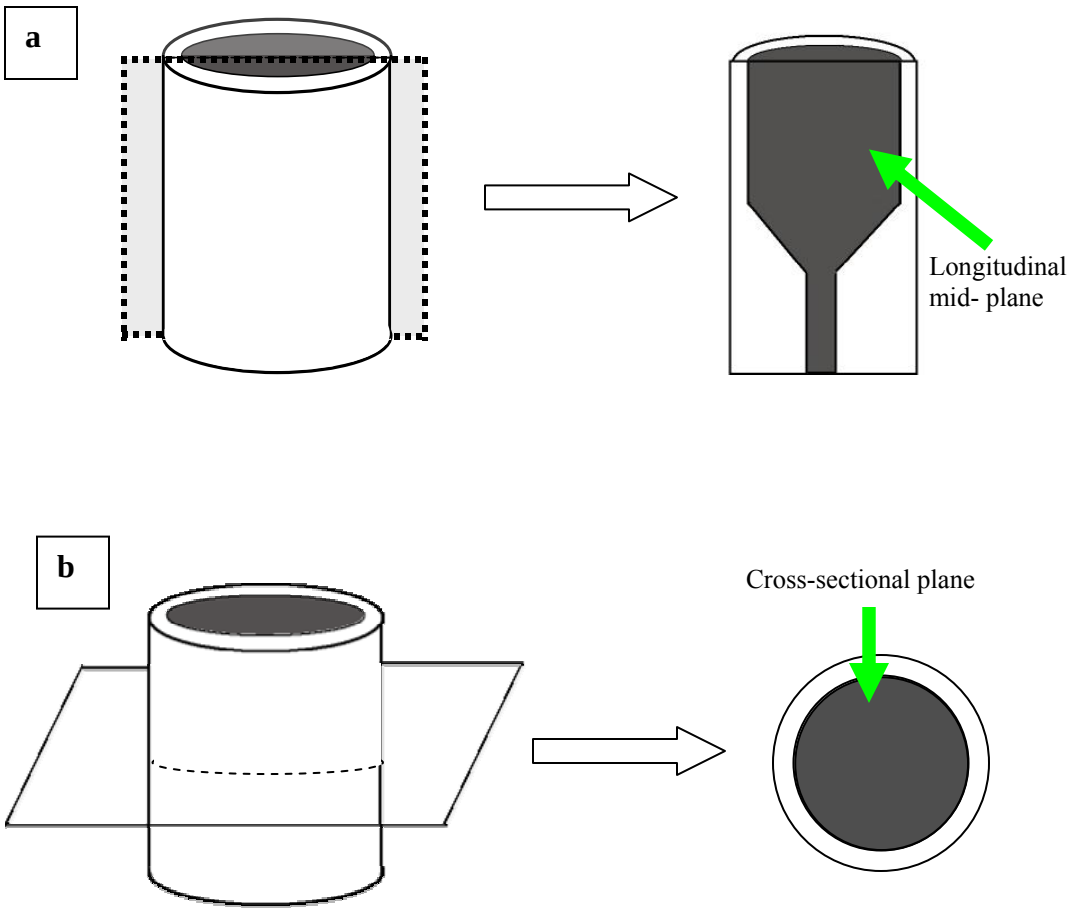

Figure 5.3: Schematic of a typical die and the locations where it was cut to obtain different sections for microstructural studies.

5.2 Results and Discussion

5.2.1 Flow behavior at high shear rates

Figure 5.4 displays the apparent viscosity of mesophase pitch at high shear rates as measured by the capillary rheometer (ACER). Results are shown for three different temperatures: 280, 290 and 297°C. As indicated in the experimental section, capillaries with three different L/D ratios were used. It is noted that at lower shear rates, the

measured viscosities were not significantly different for capillaries with different lengths. Similar behavior was observed in an earlier study for another grade of mesophase pitch [Cato, 2002]. It is shown in Chapter 2 that this material is not strongly viscoelastic and as a result entry and exit effects were not significant; therefore, measured viscosity values were not significantly different for different capillary lengths.

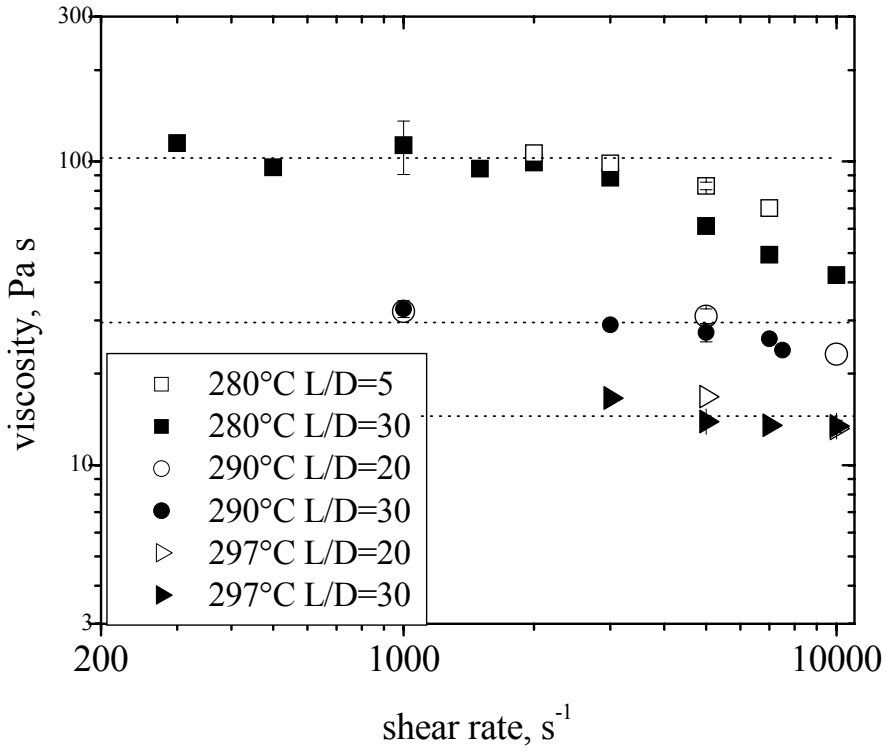

Figure 5.4: Apparent viscosity of mesophase pitch as a function of shear rates. Dotted lines represent the trend.

The viscosities were also found to be constant, i.e., independent of shear rate at lower shear rates. However, a drop of viscosity was observed at higher shear rates. Such a drop of viscosity could be a consequence of shear-thinning behavior or caused by viscous heating, which increases the fluid temperature and reduces the viscosity. To estimate the

extent of viscous heating, a commercial fluid dynamics software, Polyflow® was used following a protocol used earlier by Cato [2002]. As shown in Appendix B, the simulation was performed on a Newtonian fluid with viscosity of 100 Pa.s. The inlet fluid temperature and the wall temperature were maintained at 280°C. For a capillary with L/D ratio of 20 and at a shear rate of 7000 s^{-1}, maximum temperature rise was estimated to be approximately 12°C. The increase of temperature resulted in decrease of pressure drop. Correspondingly, the estimated viscosity decreased by 50 Pa.s, somewhat similar to that observed experimentally. As seen in **Figure 5.4**, the drop of viscosity was lower for a capillary with shorter length (L/D = 5 at 280°C). Expectedly, the viscous heating was lower for a shorter capillary and as a result the drop of measured viscosity was also lower.

From the above explanation it can be surmised that viscosity does not display a true shear-thinning behavior, and the drop of viscosity was caused by viscous heating. However, it is noted that in real fluids, change of temperature can also affect the orientation parameter because of a change of magnitude of the nematic potential, which in turn can affect the viscosity values. Newtonian behavior at high shear rates has been reported in the literature for other grades of mesophase pitch [Fathollahi and White, 1994; Cato et al., 2005]. For a particular temperature, the viscosity at high shear rates was likely the continuation of Region-II observed in low-shear experiments. However, the plateau viscosities values measured from capillary rheometer were slightly lower than that measured from cone-plate rheometer. These small differences can result from minor variation of instrumental calibration.

For the processing-flow experiments using a single-screw extruder, the temperature of the external thermocouple was maintained at 297±1°C by changing the set points of four temperature controllers connected to the extruder. A portion of the die (~ 7mm) protruded out of the extruder and the simulation study suggested that there was no significant variation of temperature across the capillary length [Appendix C].

Due to the typical flow characteristic of an extruder, the mesophase pitch experiences a positive pressure gradient in the metering zone, which facilitates to purge most of the volatiles out of the melt towards the throat of the extruder. As a result, stable pressure readings could be obtained for flow inside the capillary. For different screw speeds, the pressure drop across the capillaries was recorded and the apparent viscosity was estimated using Poiseuille equation.

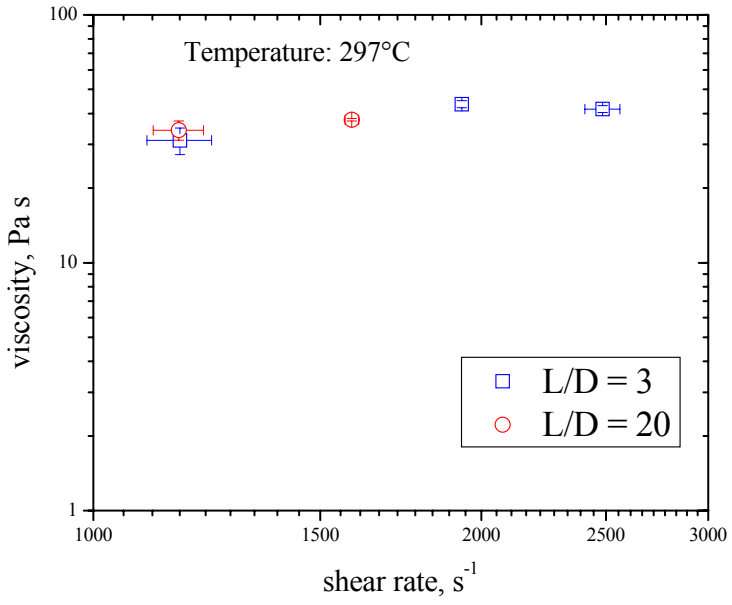

Figure 5.5: Viscosities as a function of shear rates measured from single-screw extruder. The measurement was performed for capillaries with two different L/D ratios.

Figure 5.5 shows the apparent viscosities as a function of shear rates for two different dies with L/D ratios of 3 and 20. The apparent viscosities were found to be independent of capillary length, similar to that observed in ACER rheometer. Also, the viscosities remained almost constant with increasing shear rates. The measured viscosities were slightly higher than that measured from ACER, likely due to slight variation of temperatures between different instruments.

5.2.1 Microstructure

For microstructural study, the shear rate at the capillary wall was maintained at ≈1100 s^{-1}, which was of the same order of magnitude as that nominally observed in the fiber-spinning process. Typical of Poiseuille flow, the shear rate changes from maximum at the wall to zero at centerline. For the present flow geometry, the wall shear rate at the counterbore wall was ≈ 20 s^{-1}.

Figure 5.6 shows the micrograph of the counterbore cross-section for a die with L/D = 3, and the axial location was approximately 15 mm from the inlet. The micrographs presented in this chapter were constructed by carefully combining multiple pictures (as many as 20) captured at the different locations of a given sample.

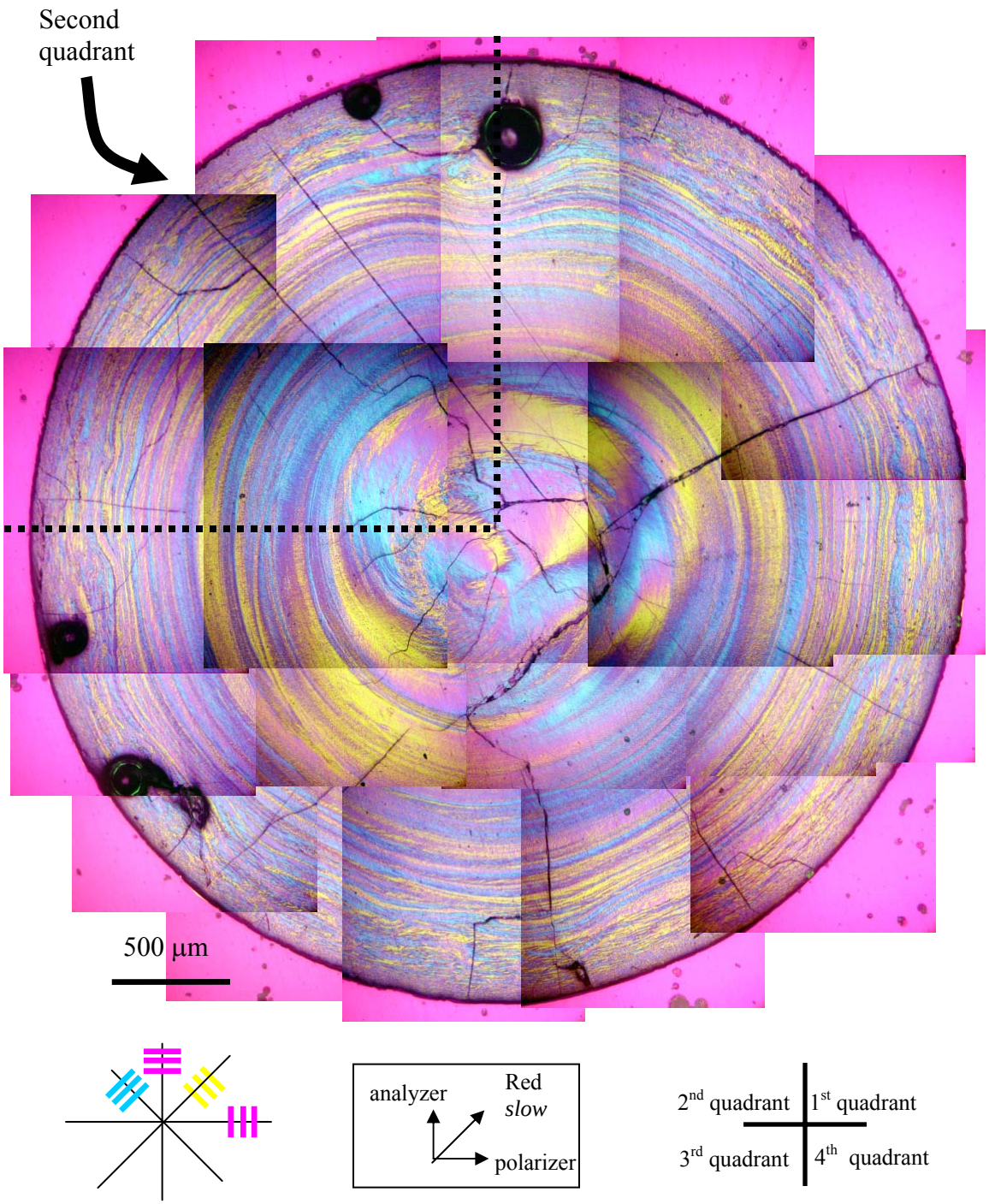

Figure 5.6: Micrograph of the cross-section of counterbore for a die with L/D =3 and the location of the sample was approximately 15 mm from the inlet. Position of polarizer-analyzer is also shown.

To examine the microstructure in detail, the magnified view of second quadrant of **Figure 5.6** is shown in **Figure 5.7a** (quadrants are identified in the **Figure 5.6**). It is evident from these micrographs that the microstructure was quite coarse at the center and then became finer near the wall. In the second quadrant, as observed in **Figure 5.7a**, the microstructure was very fine near the wall, i.e., within a region of about ~50 μm from the periphery. The color of the majority of the edge-on layer-planes was blue (~65% of total colored regions). This signifies that orientation of layer-planes in those regions was approximately tangential with their directors oriented along the radial direction of the counterbore.

Inside this 50 μm rim, another region could be identified that extended about 700 μm. In this region, approximately 60% of the edge-on regions were yellow, i.e., the layer-plane orientation was along the radial direction of the counterbore (directors were tangential). Patches of blue regions were also observed. The edge-on layer-planes constituted about 30% of the total area. In this region extending ~700 μm from the wall, the width of the microstructure was approximately 10 μm, i.e., coarser than that observed in the region close to the die-wall.

Figure 5.7b displays the same sample as **Figure 5.7a** but rotated by 45°. During sample rotation, the position of the polarizer-analyzer and that of the first order red plate was not changed. After rotation of the sample, some of the magenta regions changed to yellow and blue (each ~15 % of the total area). The yellow and blue regions in this micrograph were the layer-planes that were imperfectly oriented along the radial direction. The total relative area of edge-on layer-planes in the second quadrant and in the ~700 μm region from the wall was ~70%, estimated from **Figure 5.7a** and **Figure 5.7b**.

As seen in **Figures 5.6** and 5.**7**, the microstructure, both in terms of size and layer-plane orientation, was significantly different in the center region that extended another 500 μm. For instance, in the second quadrant of **Figure 5.6** (i.e., **Figure 5.7a**), the predominant color was blue, with the other color being magenta. It is also noted that a significant portion of magenta regions in **Figure 5.7a** changed to yellow after rotation of the sample by 45° (**Figure 5.7b**); one of such regions is shown as an ellipse in **Figures 5.7a** and **b**. Therefore, the orientation of the layer-planes deviated significantly from the radial orientation. In the core region of a pipe flow, the shear rate is very low and approaches zero at the centerline. The microstructure became less defined and a mixture of color was observed.

For the cross-section, a circular symmetry of microstructure was observed and the microstructural features in the first and third quadrants were similar to that observed in second and fourth quadrants, i.e., the microstructure was very fine near the wall and became coarser towards the center. Also, the overall orientation of the layer-planes in all of these quadrants was similar.

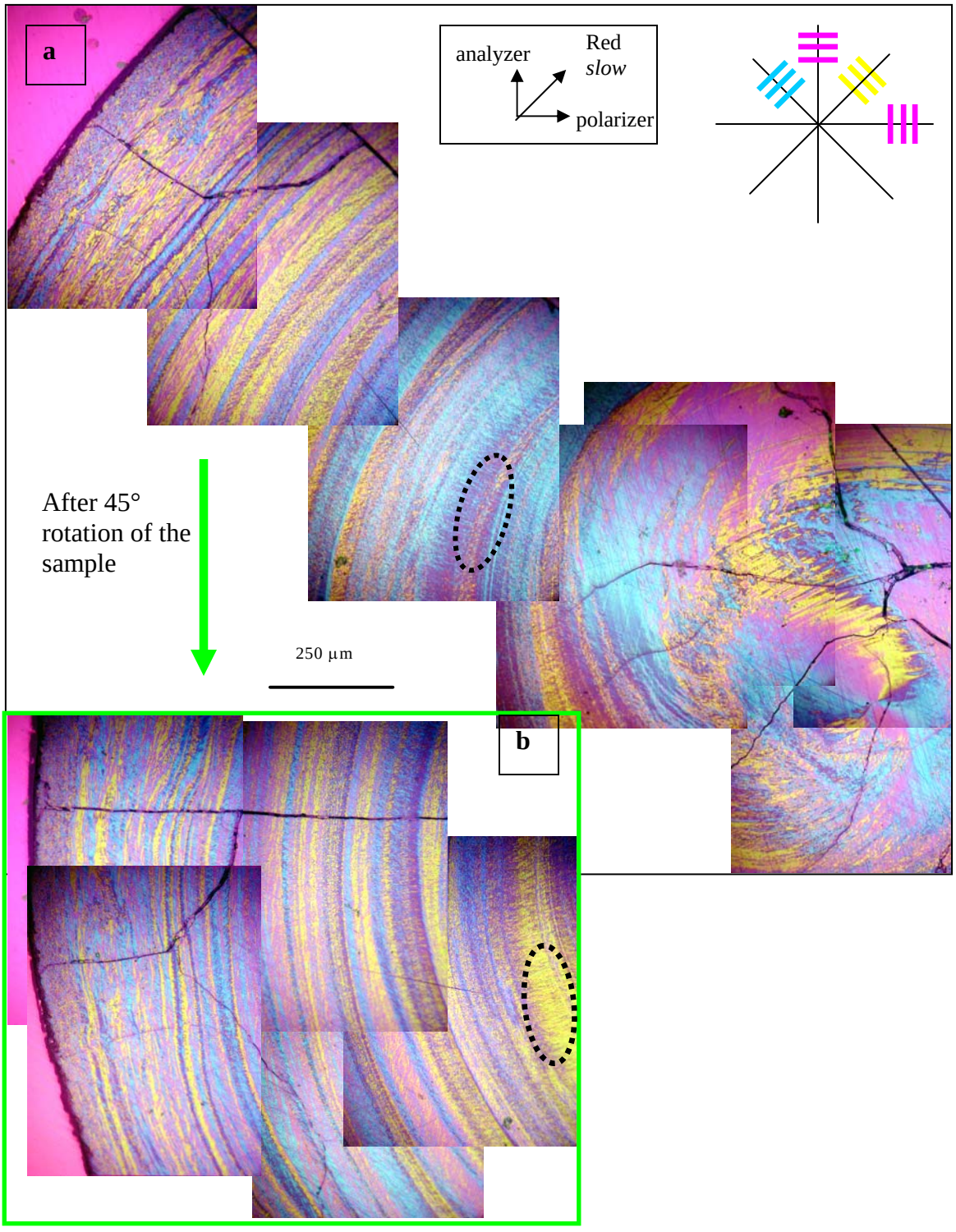

Figure 5.7: (a) Enlarged micrograph of second quadrant of Figure 5.6; (b) micrograph of same sample in *a*, but rotated by 45°. Position of polarizer-analyzer is also shown.

For detailed understanding of the microstructure, samples were also studied in longitudinal mid-plane. **Figure 5.8** shows such a micrograph for a die with a capillary of L/D = 3. The micrographs were obtained for the counterbore region at an axial distance of 15 mm from the inlet. **Figure 5.8a** shows the micrograph of the sample positioned 45° with respect to the polarizer-analyzer. After the initial transience, the flow appears to reach a fully developed state. **Figure 5.8a** displays several yellow regions, where the layer-planes were parallel to the flow direction. In this micrograph, since significant magenta color was observed, the sample was rotated by 45° (i.e., parallel to the polarizer) and the corresponding micrograph is shown in **Figure 5.8b**. After the rotation, the yellow regions of **Figure 5.8a** became magenta and some magenta regions of **Figure 5.8a** changed to yellow and blue.

It is interesting to note that there is little presence of blue regions in **Figure 5.8a**. The blue color represents a layer-plane orientation normal to the flow direction with the director oriented along the flow direction. Therefore, the layers-planes nominally remained in the flow plane and the magenta regions in **Figure 5.7**, which remained unchanged with rotation, were layer-planes that were aligned parallel (or at a shallow angle) with respect to the image-plane.

The micrographs from two orthogonal planes indicate that the microstructure was very fine near the wall, with weak orientation of layer-planes along the tangential (or hoop) direction of the counterbore. In the next region, extending about ~700 μm, there was a weak orientation of layer-planes along the radial direction of the counterbore. Beyond 750 μm, the orientation of the layer-planes in the counterbore cross-section was

not clearly defined and it deviated significantly from the radial orientation. However, the layer-planes remained in the flow plane when viewed longitudinally.

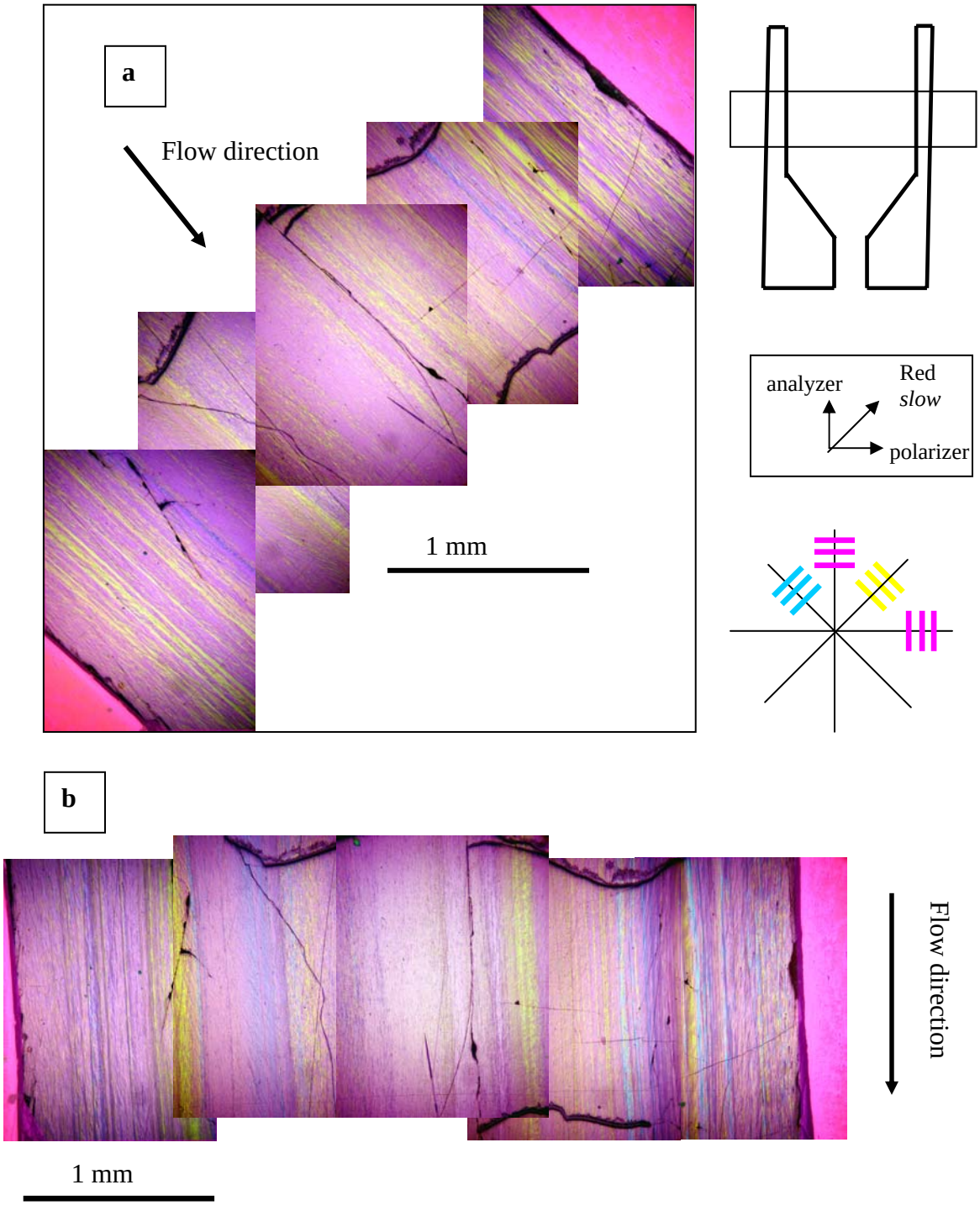

Figure 5.8: Micrograph of a portion of the counterbore (approximately 15 mm from inlet) of a die with L/D = 3: (a) sample at an angle 45° to the polarizer-analyzer; (b) sample parallel to the polarizer. The position of the micrograph with respect to the die is shown (rectangular box). Also shown are the flow direction and the position of polarizer-analyzer

Next, the microstructure of mesophase pitch within a capillary of L/D =20 is presented at a wall shear rate ~1100 s^{-1}, is presented. A typical micrograph of a cross-section is shown in **Figure 5.9a**, whereas the magnified view of the second quadrant is shown in **Figure 5.9b**. As observed in **Figure 5.9b,** within a distance of ~200 μm from the wall, a majority of the edge-on layer-planes were oriented radially, as identified by yellow regions. The relative area of these yellow regions is approximately 35% of the total area. The microstructure was similar to that observed during fully developed flow in the counterbore (**Figure 5.8**). However, the tangential orientation of the layer-planes near the wall, observed in the counterbore, was not present in the capillary cross-section. Also, fewer blue regions were observed in the capillary as compared to those observed in the counterbore.

Figure 5.9c displays the cross-section of the same sample (**Figure 5.9b)**, but rotated by 45°. After the rotation, some of the magenta layers changed to yellow and blue, signifying the imperfect orientation of the layer-planes along the radial direction of the capillary. The relative area of the edge-on layer-planes in the cross-section was estimated as ~70%. The microstructure was very small near the wall and could not be measured accurately. However, away from the wall and within the ~200 μm band, the width of the blue and yellow regions was found to be less than 5μm. Therefore, it may be inferred that the microstructure within the capillary was much smaller than that observed in counterbore. It was shown in Chapter 3 that microstructural size decreases with increasing shear rates. Therefore, the smaller size of microstructure in the capillary is clearly a consequence of the higher shear rates experienced in the capillary.

As observed in **Figure 5.9a,** in a region extending another ~100 μm towards the center, the microstructure was coarser. In the second quadrant (and also in the fourth quadrant), the microstructure became less defined in the core and a mixture of color (blue, yellow, and magenta) was observed. The change of microstructure within the capillary was similar to that observed during fully developed flow in the counterbore, but the size was much smaller in the capillary.

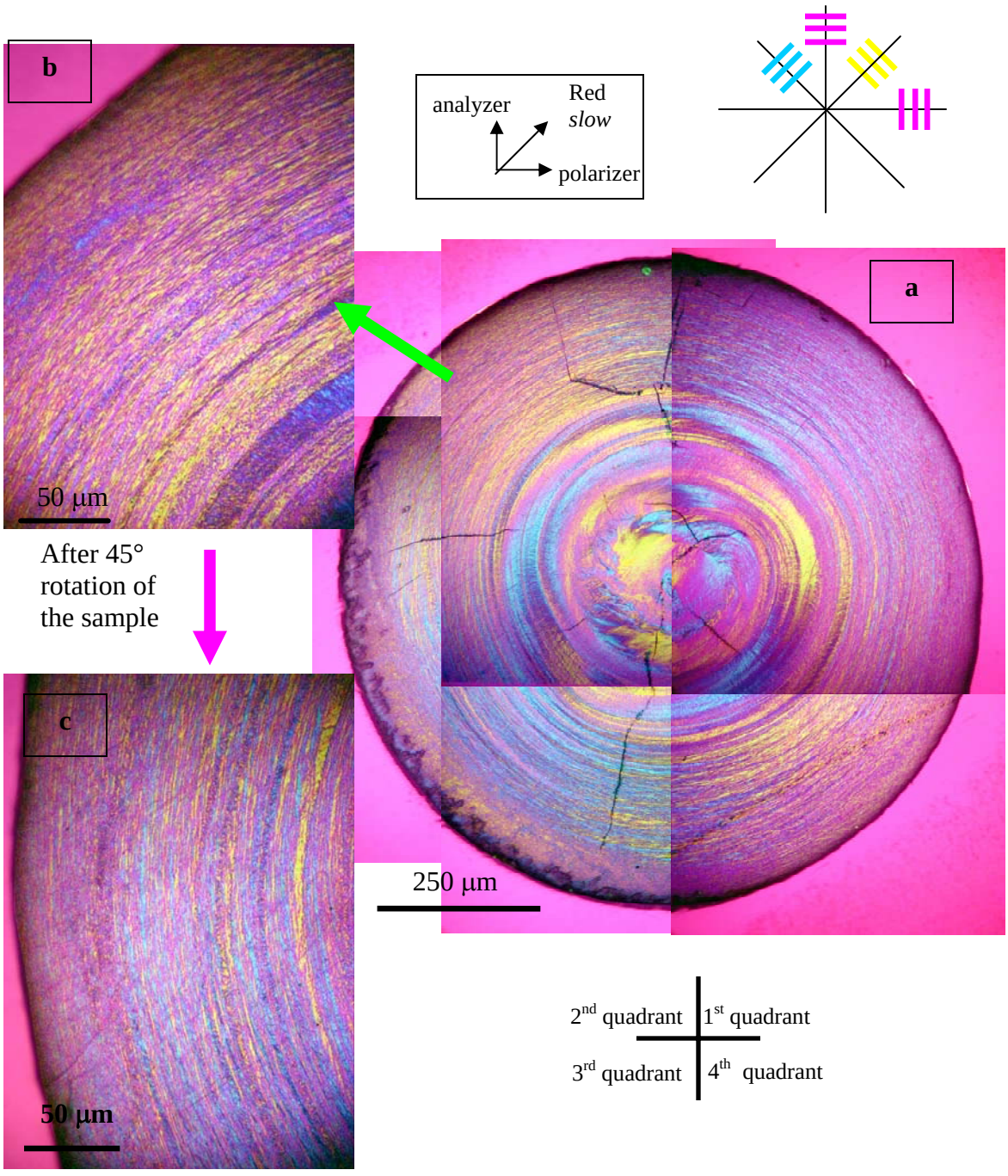

Figure 5.9: (a) Micrograph of the cross-section of capillary for a die with L/D =3; (b) magnified view of the 2nd quadrant; (c) micrograph of the same sample presented in (b) but rotated by 45°. The location of the sample was approximately 15 mm from the capillary inlet. Position of polarizer-analyzer is also shown.

Figure 5.10 is a micrograph of the same sample as shown in **Figure 5.9**, but rotated by 45°. In the second quadrant, near the wall (~200 μm band), the predominant color was yellow and was similar to that observed in **Figure 5.9**. Therefore, a circular symmetry was present in the sample. Also, beyond the ~200 μm band blue, yellow and magenta regions were observed. The magenta regions observed in **Figure 5.9** changed to yellow after rotation of the sample by 45°. This signifies that the orientation of the layer-planes deviated significantly from the radial orientation.

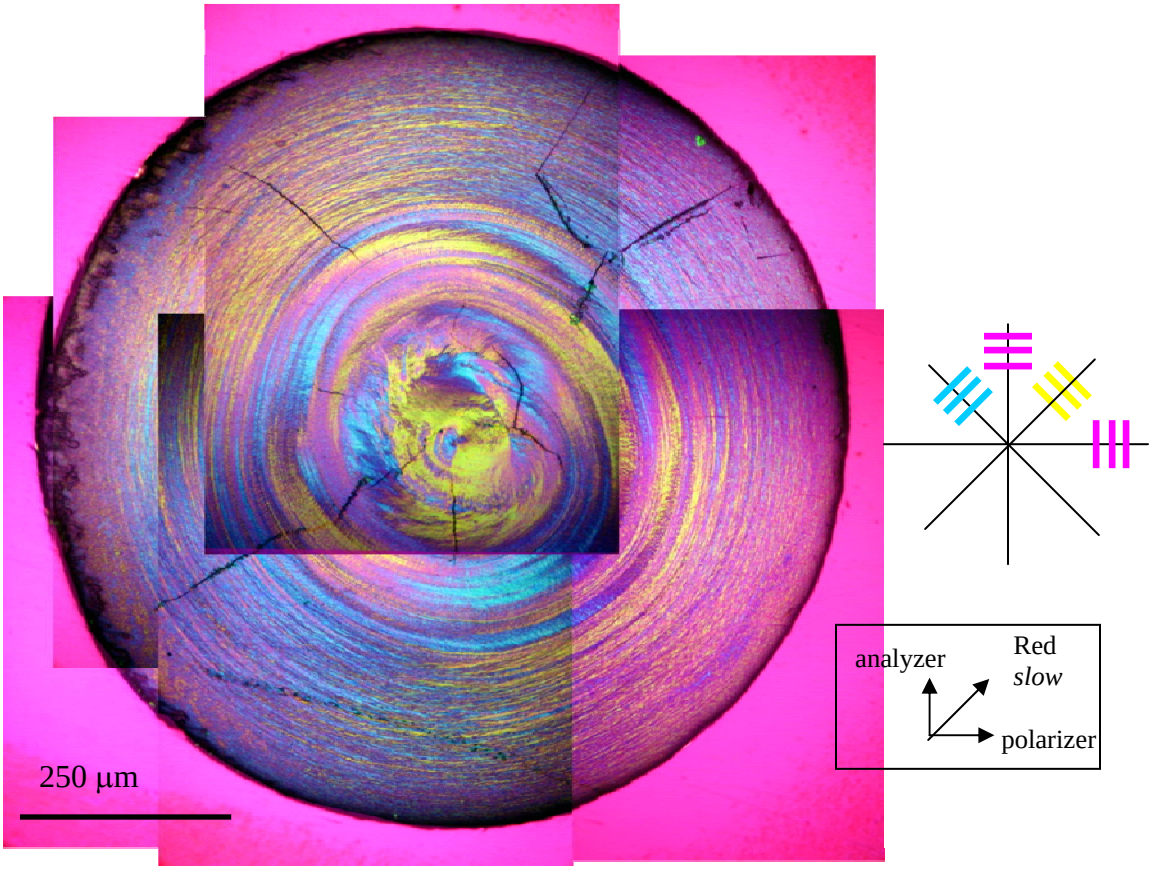

Figure 5.10: Micrograph of the same sample in Figure 5.9 but rotated by 45°. Position of polarizer-analyzer is also shown.

Figure 5.11 displays the cross-sectional view of a capillary with a shorter L/D of 3. The location of the sample was near the exit of the capillary. Few voids were observed away from the center. Similar to that observed earlier for L/D=20, the microstructure was coarse near the center and became finer towards the wall. Away from the center region, the predominant color in the second and fourth quadrant was yellow (blue in first and third quadrant). Therefore, the orientation of the layers-planes was approximately radial. These observations were similar to that observed for L/D=20.

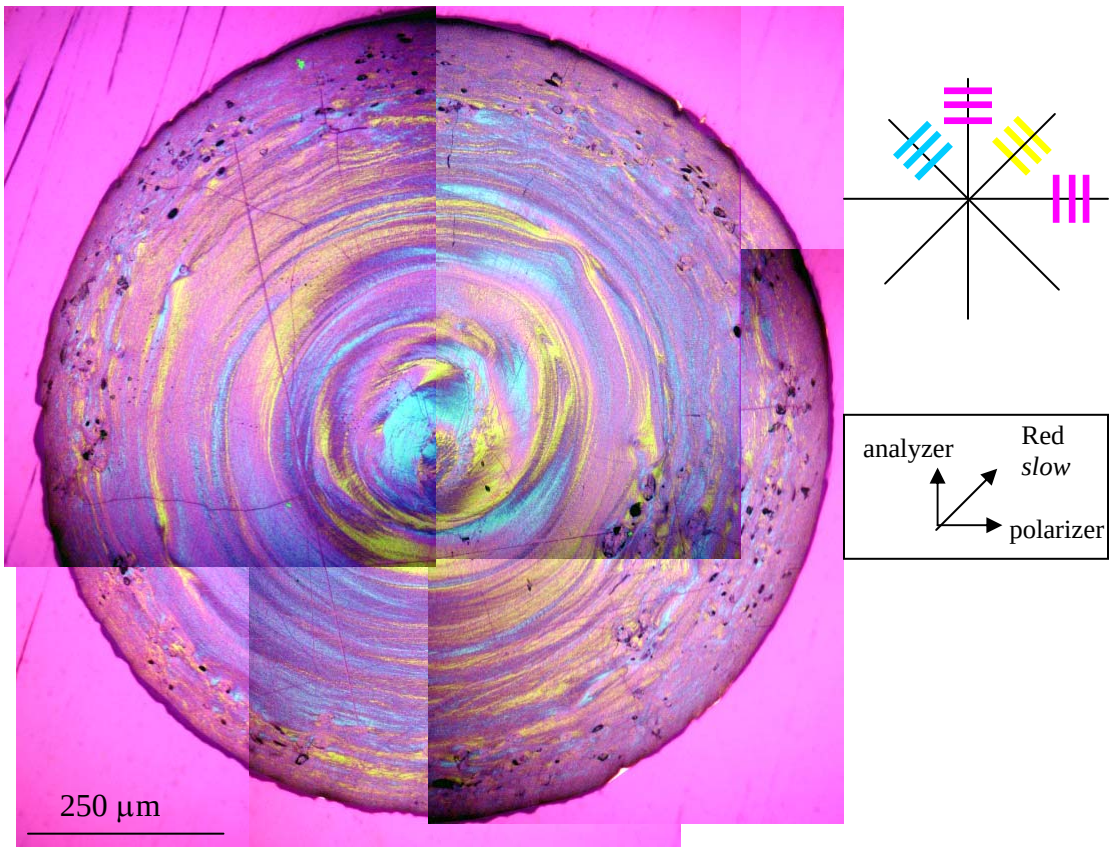

Figure 5.11: Micrograph of the cross-section of a capillary for a die with L/D =20. The location of the sample was near the exit of the capillary. Position of polarizer-analyzer is also shown.

The microstructure was also studied in the longitudinal mid-plane and **Figure 5.12** displays the micrograph of such a plane for a die with L/D = 20. **Figure 5.12a** displays the micrograph, in which the sample was placed at an angle 45° to the polarizer-analyzer, whereas, **Figure 5.12b** displays the micrograph of same sample but rotated by 45°, i.e., the sample was positioned parallel to the analyzer. As seen in these figures, the microstructure became finer towards the wall, similar to that observed in the counterbore (**Figure 5.8**). As observed in **Figures 5.12a** and **b**, the region within a distance of ~200 μm from the wall, the percentage area of the edge-on layer-planes was ~ 40% and most of them appeared yellow in **Figure 5.12a**. Microstructure was not very well defined away from the wall and as seen in **Figure 5.12a**, streaks of yellow regions were observed. In some instances, as displayed in **Figure 5.13**, cup-like microstructure was observed near the center of the capillary.

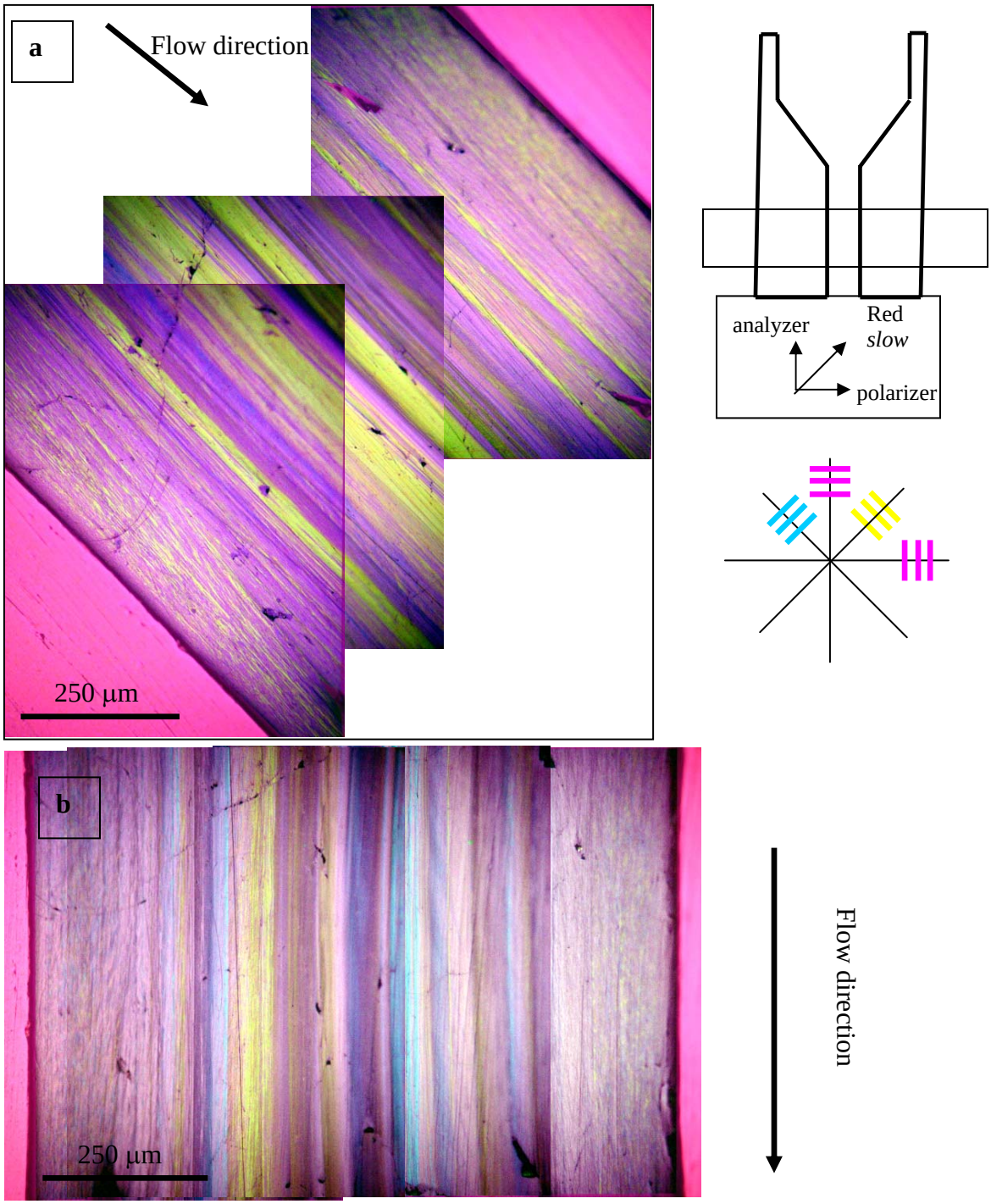

Figure 5.12: Micrograph of a portion of the capillary of the die with L/D = 20: (a) sample at an angle 45° to the polarizer-analyzer; (b) sample parallel to the polarizer. Position of the sample with respect to the die is shown (rectangular box). Also shown are the flow direction and the position of polarizer-analyzer

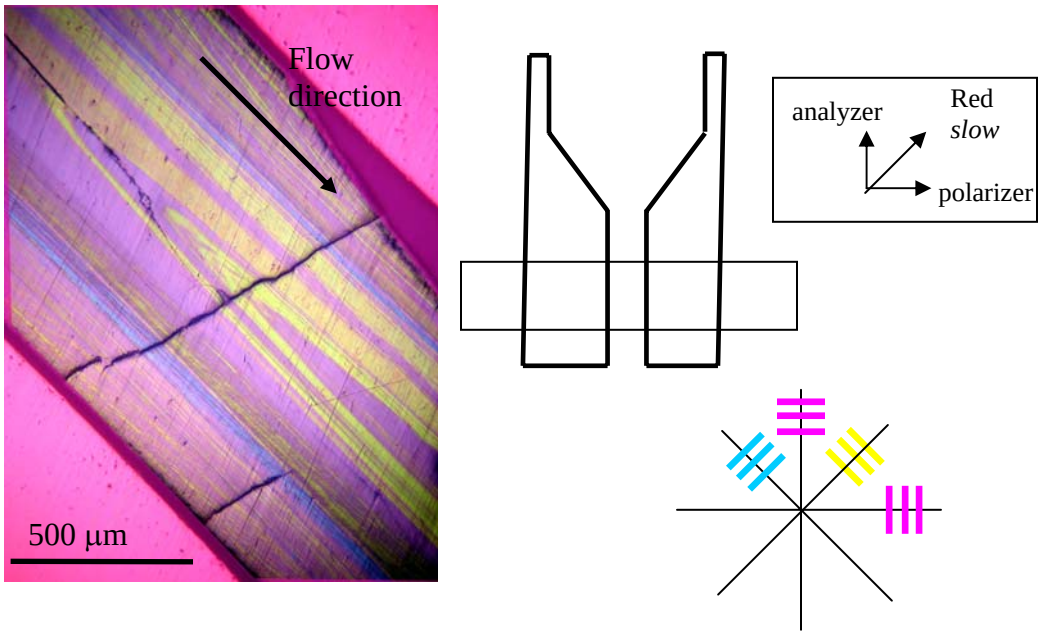

Figure 5.13: Micrograph of a portion of the capillary of the die with L/D = 20. Similar to **Figure 5.12**, the sample was at an angle 45° to the polarizer-analyzer. The position of the micrograph with respect to the die is shown (rectangular box). Also shown are the flow direction and the position of polarizer-analyzer

From the above micrographs, a schematic showing the layer-plane orientation for a typical cross-section is displayed in **Figure 5.14** for the microstructure shown in the second quadrant. The lines in this schematic represent the edge-on layer-planes. It was inferred from the micrographs that within the capillary the layer-plane orientation was approximately radial near the wall (shown in Figure 5.14). However, the radial orientation was not perfect and the imperfection of the orientation from the radial direction resulted in blue and yellow colors in the micrographs of the cross-sectional planes after rotation of the sample by 45°. Away from the wall, the deviation of orientation of the layer-planes from the radial direction was significant and some layer-planes were oriented tangentially. In the core, the microstructure was coarse and no preferred orientation of mesophase layer-planes was observed. Radial orientation of

layer-planes was reported in literature for as-spun fibers [White et al., 2003]. They have also reported zig-zag or corrugated orientation of layer-planes in the as-spun fibers (from TEM studies) and in the carbonized fibers (from SEM studies). In their study, the microstructure was more radial towards the center. In contrast, in this study the radial orientation was more imperfect towards the center. It is noted that a different grade of mesophase pitch was used in the present studies and the fiber diameter was much smaller (~10 μm) than the capillary diameter studied here.

In this study, it is also noted that the degree of orientation increased within the capillary as compared to that observed in the counterbore. As a result, the microstructure was more radial in the capillary. The increase of orientation was likely caused by the high shear rates (shear stresses) experienced in the capillary and also an effect of extensional flow field that the material was subjected to during the flow through the contraction.

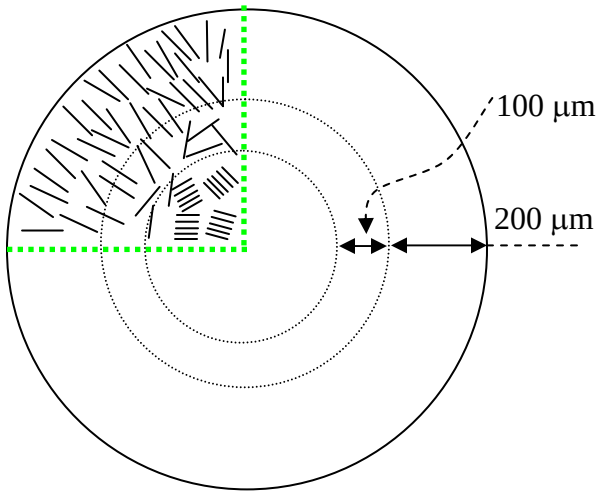

Figure 5.14: Schematic showing the layer-plane orientation in the second quadrant for a typical capillary cross-section.

The effect of contraction was also studied in detail **Figure 5.15** shows the micrograph in the longitudinal mid-plane of the counterbore for a die with capillary of L/D = 20. Similar to **Figure 5.8,** the yellow regions represent the layer-planes that are oriented in the flow direction. Before the contraction, regions (~2 mm) with blue color were observed near the wall. The blue color occurred due to change of orientation of layer-planes at those regions and likely caused by the vortex formation.

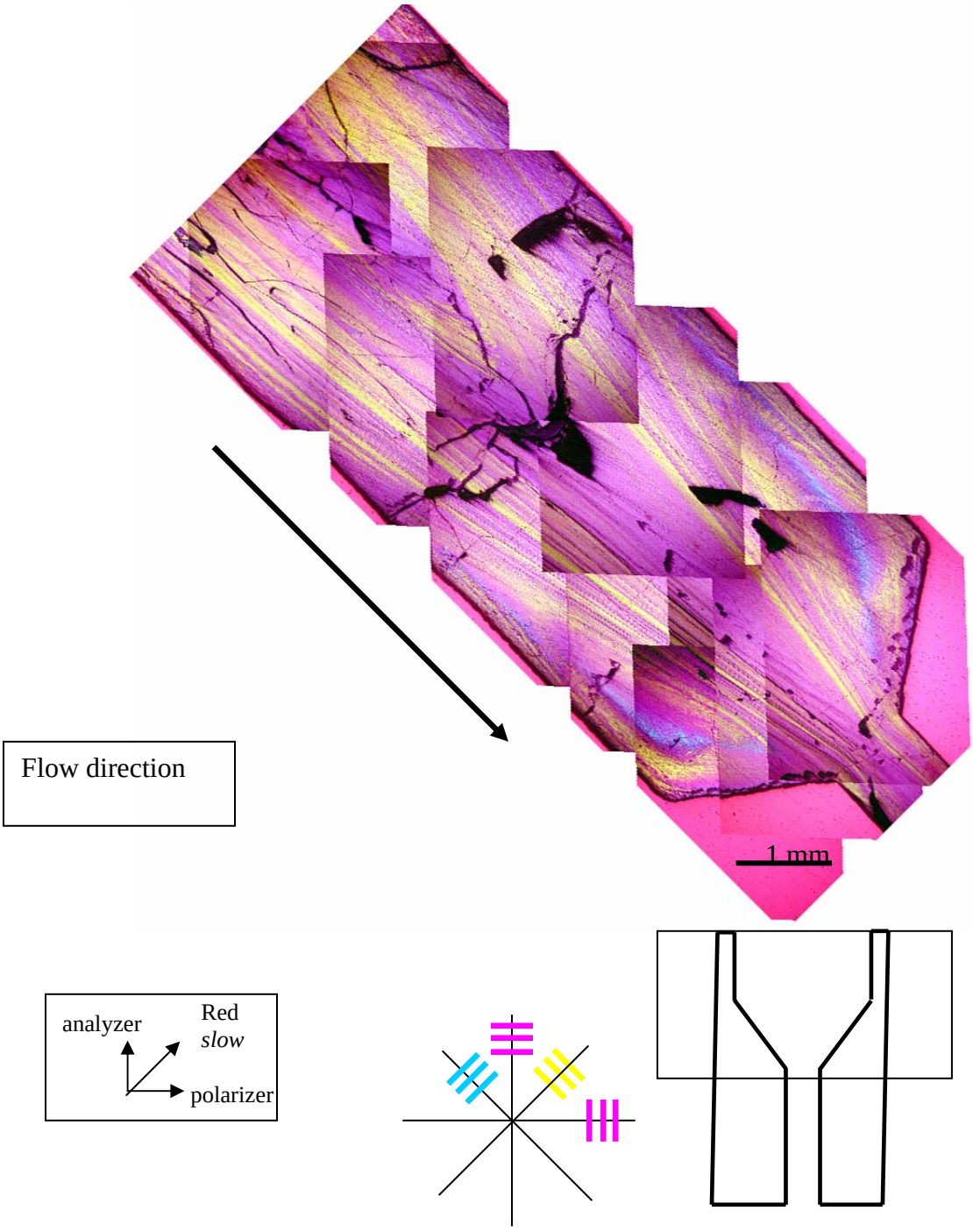

Figure 5.15: Evolution of the microstructure within the counterbore of a die with L/D of 20. The position of the sample with respect to the die is shown (rectangular box). Also shown are the flow direction and the position of polarizer-analyzer.

To study the sample in further detail, it was rotated by 45° (now the sample is parallel to the analyzer) and the corresponding micrograph is shown as **Figure 5.16**. The vortex formation is evident in this micrograph. Just before contraction and near the wall, regions with yellow and blue color were observed. The mixture of color was due to the vortex formation caused by the recirculation flow. Similar vortex formation was reported in literature for a different grade of mesophase pitch [Fleurot, 1998]. Vortex formation was likely caused by the viscoelastic nature of mesophase pitch.

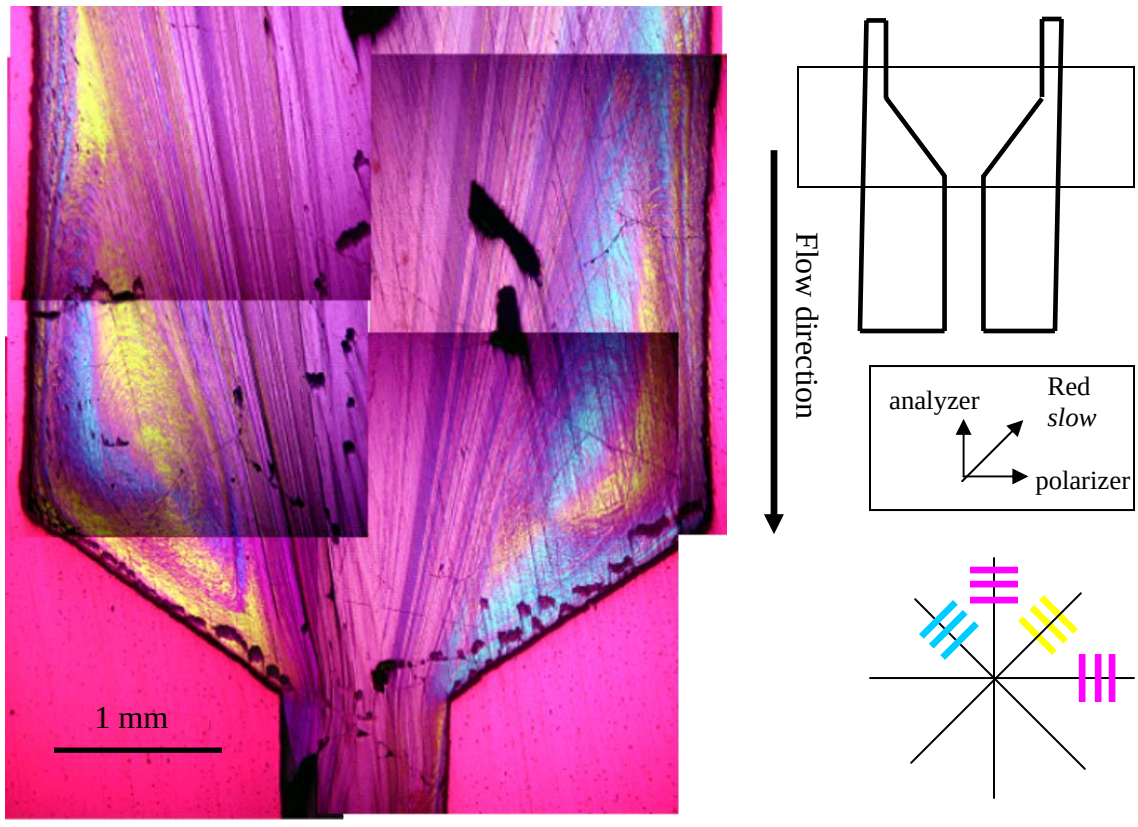

Figure 5.16: Micrograph shows the vortex formation within the counterbore before the contraction for a die with L/D of 20. The position of the sample with respect to the die is shown (rectangular box). Also shown are the flow direction and the position of polarizer-analyzer.

The approximate radial microstructure observed in this study is somewhat similar to the radial texture of the carbon fibers obtained from this grade of mesophase [Cho et al., 2003]. However, in carbon fibers, the orientation of graphite layer-planes was more severe, likely caused by drawdown of the extruded fibers. Also, the graphitization process increases the orientation of the graphene layer-planes.

In a recent simulation study for discotic liquid crystals in Poiseuille flow, it was shown that the flow-alignment angle of the discs depends on the anchoring angle at the boundary surface [de Andrade Lima and Rey, 2003]. In another study, by applying a strong anchoring condition of the discs at the capillary wall, radial orientation of the discs was predicted [McHugh, 1994]. Other than shear-rates, the extensional flow also can contribute to the refinement of orientation of the layer-planes [Singh, 2000]. It is suggested in the literature that during extensional flow, the disc-like molecules align with their largest dimension parallel to the extension [Singh, 2000]. In present case, the mesophase pitch was subjected to extensional flow when it entered the counterbore and also in the contraction zone before entering the capillary. The extensional flow could also contribute to form approximate radial orientation of layer-planes in the capillary and in the counterbore.

5.3 Conclusions

By developing an experimental protocol, the microstructure within the custom-made dies was studied for varying shear rates such as typically observed during processing flows. In these dies, the wall-shear rate was low (~$10s^{-1}$) in the counterbore, but quite high (~1000 s^{-1}) in the capillary. The viscosity at high shear rates was also

measured during these processing flow and also using a capillary rheometer (ACER). The viscosity did not change significantly with shear rates, except at very high shear rates, likely an artifact of viscous heating. For a particular temperature, the viscosity at high shear rates was likely the continuation of Region-II observed in low-shear experiments (reported in Chapter 2).

Microstructure study of cross-sections of the counterbore and the capillary clearly shows that size of microstructure decreased towards the wall, where shear rate was highest. Such a change of microstructure with the shear rate was also reported in Chapter 3. Along with the microstructural size, variation of the orientation of the layer-planes was also observed in a given cross-section. In the counterbore, the orientation of the layer-plane was approximately tangential near the wall (~50 μm), which then changed to approximate radial one away from the wall (till ~750 μm). Further away from the wall, where the shear rate was very low, the orientation deviated significantly from the radial one. In the capillary, the radial orientation near the wall (~200 μm) deviated significantly away from the wall (beyond 200 μm) and some layer-planes were oriented tangentially. In the core of the capillary, the microstructure was coarse and no preferred orientation of mesophase layer-planes was observed. It is noted that the degree of orientation (more radial near the wall) increased within the capillary as compared to that observed in the counterbore. The increase of orientation was likely caused by the high shear rates and stresses experienced in the capillary and also an effect of extensional flow field that the material was subjected to during the flow through the contraction. As observed from the microstructure in the longitudinal mid-plane, both in the counterbore and in the capillary, the layer-planes nominally remained in the flow plane.

CHAPTER 6

FLOW SIMULATION OF DISCOTIC LIQUID CRYSTALS IN SIMPLE SHEAR FLOW

Finally, this chapter reports on simulation studies that were performed using constitutive equations for discotic liquid-crystalline materials developed by Rey and coworkers [Tsuji and Rey, 1997; Singh, 2000; Grecov and Rey, 2003a & b]. The simulation results were obtained for simple shear flow, corresponding with the flow geometry investigated in details for the experimental studies reported in Chapters 2 and 3. This study was performed in collaboration with various CAEFF researchers including Dr. Oehsen, Mr. Duffy, and Prof. Cox (Clemson University), and Prof. Rey and coworkers (McGill University).

The objective of this simulation study was to establish a frame work, using CAEFF computational facility and expertise, for modeling the flow dynamics of this complex material in different flow situations. It is anticipated that after further development this approach will help CAEFF researchers to design carbon-based materials in a more efficient manner.

6.1 Literature Review

Several modeling studies have been reported in the literature describing the flow behavior of nematic liquid crystals, and details are provided in recent reviews [Rey and

Denn, 2002; Rey and Tsuji, 1998]. For liquid crystalline materials, stress is a function not only of strain rate, but also the average local orientation of the constituent molecules. For polydomain samples, the texture size plays an important role on the stress response.

6.1.1 Leslie-Ericksen theory

Different theories have evolved over last few decades to consider the effect of change of local average orientation of liquid-crystalline molecules during flow. Of those theories Leslie-Ericksen theory is most widely reported in the literature [Rey and Denn, 2002]. In this theory, Ericksen theory of viscous stress was combined with Frank theory for elastic stress. Here, the viscous stress tensor τ_v is

$$\boldsymbol{\tau}_v = \alpha_1 \mathbf{nnnn} : \mathbf{A} + \alpha_2 \mathbf{nN} + \alpha_3 \mathbf{Nn} + \alpha_4 \mathbf{nn} \cdot \mathbf{A} + \alpha_5 \mathbf{nn} \cdot \mathbf{A} + \alpha_6 \mathbf{A} \cdot \mathbf{N} \quad (1)$$

Here, **A** is the rate of strain tensor

$$A = \tfrac{1}{2}(\nabla \mathbf{v} + \nabla \mathbf{v}^T) \quad (2)$$

n is the unit vector, called director (**n.n** = 1), which describes the local average of the molecular orientation. The six parameters α_i (i = 1 to 6), are the Leslie coefficients or viscosities, and the physical significance of the Leslie coefficients for discotic liquid crystals is described by McHugh [1994]. Only five of these coefficients are independent, and the Parodi's relationship relates one of the coefficients in terms of the others [Larson, 1999].

$$\alpha_6 = \alpha_2 + \alpha_3 + \alpha_5 \quad (3)$$

N in (1) is defined as

$$\mathbf{N} \equiv \dot{\mathbf{n}} - \mathbf{n}.\mathbf{W} \quad (4)$$

N is the rate of rotation of the director **n**, relative to the background fluid. Here, **W** is the vorticity tensor.

$$\mathbf{W} = \tfrac{1}{2}(\nabla\mathbf{v} - \nabla\mathbf{v}^{T}) \quad (5)$$

Flow field has a direct effect on the director and can be accounted using angular momentum balance, which gives

$$\mathbf{h} - \mathbf{nn} \,.\, \mathbf{h} - \gamma_2 (\mathbf{n} \,.\, \mathbf{A} - \mathbf{nnn} : \mathbf{A}) - \gamma_1 \mathbf{N} = 0 \quad (6)$$

The vector **h** is called the *molecular field*, and represents the contribution of free energy of distortional elasticity, E_d. The molecular field can be expressed as

$$\mathbf{h} = \nabla . \frac{\partial F_d}{\partial \nabla \mathbf{n}} - \frac{\partial F_d}{\partial \mathbf{n}} \quad (7)$$

In equation (6), the coefficients γ_1 and γ_2 are represented in terms of Leslie coefficients as

$$\gamma_1 = \alpha_3 - \alpha_2, \qquad \gamma_2 = \alpha_6 - \alpha_5 \quad (8)$$

The distortional elastic free energy (excess free energy density), F_d, associated with distortions in the director field can be expressed as quadratic in the director field gradient, provided the change of director orientation is small over the length of a molecule [Larson, 1999; Ugaz, 1999]. Then

$$F_d = \tfrac{1}{2} K_{11} (\nabla \,.\, \mathbf{n})^2 + \tfrac{1}{2} K_{22} (\mathbf{n} \,.\, \nabla \times \mathbf{n})^2 + \tfrac{1}{2} K_{33} (\mathbf{n} \times \nabla \times \mathbf{n})^2 \quad (9)$$

where the coefficients K_{11}, K_{22}, and K_{33} are elastic constants associated with splay, twist, and bend deformation, respectively (**Figure 6.1**).

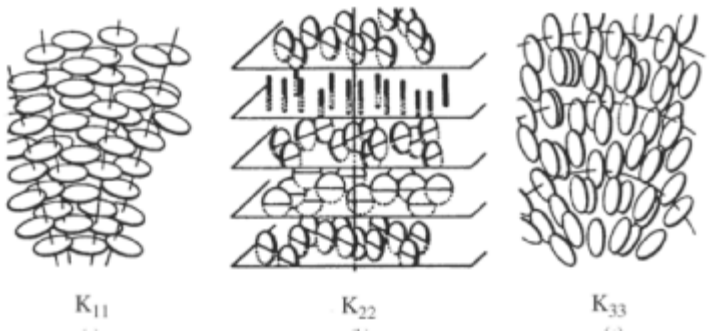

Figure 6.1: Schematic representation of splay (K_{11}), twist (K_{22}), and bend (K_{33}) deformation in discotic nematic liquid crystals [Sokalski and Ruijgrok, 1982].

The splay, twist, and bend contributions of the molecular field, **h** has been discussed in the literature [Larson, 1999]. If all the elastic constants are assumed equal (K $\equiv K_{11} = K_{22} = K_{33}$), **h** is given by [Larson, 1999]

$$\mathbf{h} = K\nabla^2 \mathbf{n} \tag{10}$$

The extra stress tensor is the sum of the viscous stress (1) and the Frank distortional stress, which is given by [Larson, 1999]

$$\boldsymbol{\tau}_{\mathbf{d-e}} = \frac{\partial F_d}{\partial \nabla \mathbf{n}} \cdot (\nabla \mathbf{n})^T \tag{11}$$

and $\boldsymbol{\tau}_{d\text{-}e} = -K \nabla n \,.\, (\nabla n)^T$ (if $K \equiv K_{11} = K_{22} = K_{33}$) (12)

The viscous and distortional stresses are then substituted in momentum balance equation and can be solved for a flow system. For simplification, the distortional elastic effect may be neglected and the simplified system is known as transversely isotropic fluid [Ugaz, 1999]. The limitation of Leslie-Ericksen model is that it cannot be applied for large distortion of director field. Therefore, this model is unsuitable for describing behavior of disclinations filled polydomain texture typically observed in real liquid crystalline polymers.

6.1.2 Doi theory

The flow behavior of liquid crystalline materials has also been described by molecular-based models, which provide more fundamental understanding of the underlying physics. Doi used probability density function of molecular orientation, $\Psi(\mathbf{u})$, which describes the probability of finding a molecule oriented parallel to a unit vector **u** [Doi and Edwards,1986; Larson 1999; Marruci and Greco, 1993]. A kinetic equation (Smoluchowski equation) was derived for $\Psi(\mathbf{u})$ to capture the motion of the molecules for a given flow field [Doi and Edwards, 1986; Larson 1999]. While Doi theory can capture the molecular phenomenon that affect the macroscopical rheological behavior, the mathematical challenge involved in using this theory for complex flow geometry is quite formidable [Rey and Tsuji, 1998; Ugaz, 1999]. Also, the Doi theory can only consider the short-range elasticity but the not the long-range elasticity (distortional elasticity) [Rey and Tsuji, 1998; Ugaz, 1999].

6.1.3 Tensor order parameter based theory

A generalized approach that has been described in the literature is to solve the dynamics of tensor order parameter *Q* (Beris and Edwards, 1994; Tsuji and Rey 1997; Rey and Denn 2002). Based on the Landau-de Gennes theory of liquid crystals, Rey and coworkers have simulated the rheological behavior of discotic liquid crystals using the second moment of orientation distribution function, known as tensor order parameter Q

[Tsuji and Rey, 1997; Grecov and Rey, 2003a & b]. The tensor order parameter Q can be expressed by [Yan and Rey, 2002b; Grecov, 2006]

$$\mathbf{Q} = \int_{Z^2} \left(\mathbf{uu} - \frac{\mathbf{I}}{3} \right) f(\mathbf{u})\, dA \tag{13}$$

where, **u** is a unit vector normal to the disc like molecules, f (**u**) is the orientation distribution function, **I** is the identity tensor, Z^2 denotes the unit sphere and dA the differential area in spherical coordinates .

Q can also be represented in diagonalized form as [Grecov and Rey, 2003 b]

$$\mathbf{Q} = S\,(\mathbf{nn} - 1/3\mathbf{I}) + P/3\,(\mathbf{mm} - \mathbf{ll}) \tag{14}$$

which is equivalent to

$$\mathbf{Q} = \begin{bmatrix} -\frac{1}{3}(\mathrm{S}-\mathrm{P}) & 0 & 0 \\ 0 & \frac{1}{3}(\mathrm{S}+\mathrm{P}) & 0 \\ 0 & 0 & \frac{2}{3}\mathrm{S} \end{bmatrix} \tag{15}$$

(**m**, **l**, **n**) are the eigen vectors and are orthogonal to each other. The three eigen values are λ_m = -1/3 (S –P), λ_l = 1/3 (S +P), and λ_n = 2/3 S.

Here $\mathbf{n}.\mathbf{n} = \mathbf{m}.\mathbf{m} = \mathbf{l}.\mathbf{l} = 1$; $\quad \mathbf{nn} + \mathbf{mm} + \mathbf{ll} = \mathbf{I} = \begin{bmatrix} \mathbf{1} & \mathbf{0} & \mathbf{0} \\ \mathbf{0} & \mathbf{1} & \mathbf{0} \\ \mathbf{0} & \mathbf{0} & \mathbf{1} \end{bmatrix}$

Q is symmetric (i.e., $\mathbf{Q} = \mathbf{Q}^T$) and traceless (i.e., tr(**Q**) = 0).

S is the uniaxial scalar order parameter and measures the average molecular orientaion along the uniaxial director **n**. S can be expressed as 3/2 (**n**.**Q**.**n**). Similarly P is the biaxial scalar order parameter and measures the molecular orientation in a plane

perpendicular to the direction of **n**. Thus, P can be expressed as 3/2 (**m**.**Q**.**m - l**.**Q**.**l)**. The following restrictions are applicable on S and P [Grecov and Rey, 2003 b],

$- 1/2 \leq S \leq 1$ and $-3/2 \leq P \leq 3/2$.

In Landau-de Gennes model, the tensor order parameter is used to describe the nematic ordering for different states: biaxial ($S \neq 0, P \neq 0$), uniaxial ($S \neq 0, P = 0$), and isotropic ($S = 0, P = 0$). Details of tensor order parameter (**Q**), order parameters (S and P), and the interrelationship of the two order parameters are described in the literature [Singh and Rey, 1995; Mottram and Newton, 2004].

The free energy density, **F,** is a quadratic function of gradients of **Q,** i.e., **∇Q** and is also a function **Q** itself [deGennes, 1993]. For small distortion and applying Lagrange condition [deGennes, 1993; Mottram and Newton, 2004; Grecov and Rey, 2003 b], the following relation is obtained

$$\mathrm{ckTH} = \left[\nabla . \frac{\partial F}{\partial \nabla Q} - \frac{\partial F}{\partial Q} \right]^{s} \tag{16}$$

Here, k is the Boltzman constant, c is concentration of molecules per unit volume, T is sample temperature in absolute unit and **H** is the molecular field.

According to Landau-deGennes model, in absence of external fields, the bulk free energy density can be written as [Yan and Rey, 2002a]

$$F = F_0 + F_s + F_l \tag{17}$$

where F_0 is the free-energy density of the isotropic state, and is related to the temperature and pressure of the system, but independent to **Q**. F_s is the short-range energy density, which dictates the state of liquid crystal, i.e., isotropic, uniaxial or biaxial. Using one

parameter Doi's model, F_s can be expressed as [Doi and Edwards, 1986; Yan and Rey, 2002a]

$$F_s = ckT \left[\tfrac{1}{2}(1-1/3U)\, \mathbf{Q}:\mathbf{Q} - 1/3\, U\, \mathbf{Q}:(\mathbf{Q}.\mathbf{Q}) + \tfrac{1}{4}\, U\, (\mathbf{Q}:\mathbf{Q})^2 \right] \quad (18)$$

where U is the nematic potential and can be given as [Grecov and Rey, 2003 b]

$$U = 3\, T^*/T \quad (19)$$

Here, T is the sample temperature and T* is the nematic-isotropic transition temperature, both in absolute temperature units.

F_l in Eqn. 17 is the long-range energy density. Only the second-order contribution of long-range energy density is considered here, and, for uniaxial case, this results in the two elastic constants K_{11} and K_{33} being equal. To remove this restriction, the third-order term of long-range energy density needs to be considered [Yan and Rey, 2002a]. The long-range contribution depends on the gradient, $\nabla\mathbf{Q}$. Also, translational and rotational motion should not change the distortional energy and such restrictions reduce the total number of allowable $\mathbf{Q}$ derivatives. For the present case, considering only the second order terms, F_l can be written as [Tsuji and Rey, 1997]

$$F_l = ckT \left[(L_1/2ckT)\, \{\nabla\mathbf{Q} \vdots (\nabla\mathbf{Q})^T\} + (L_2/2ckT)\, \{(\nabla . \mathbf{Q}).(\nabla . \mathbf{Q})\} \right] \quad (20a)$$

$$= \left[(L_1/2)\, \{\nabla\mathbf{Q} \vdots (\nabla\mathbf{Q})^T\} + (L_2/2)\, \{(\nabla . \mathbf{Q}).(\nabla . \mathbf{Q})\} \right] \quad (20b)$$

L_1 and L_2 are the Landau coefficients and are related to macroscopic Frank's elastic constants. Due to second order approximation, $K_{11} = K_{33} = K$. For uniaxial orientation, it can be shown that [Grecov and Rey, 2003 b]

$$L_1 = K_{22}/2S^2 \text{ and } L_2 = (K - K_{22})/S^2 \quad (21)$$

Thermodynamic constraints relate L_1 and L_2, and it has been shown that $L_2 < 0$ for disc type liquid crystals [Yan and Rey, 2002a]. This happens because twist elastic constant is highest for the discotic nematics. Then, by combining Eqn. 18 and Eqn. 20, the following relation was obtained

$$F = ckT \left[\tfrac{1}{2}(1-1/3U)\, \mathbf{Q} : \mathbf{Q} - 1/3\, U\, \mathbf{Q} : (\mathbf{Q}.\mathbf{Q}) + \tfrac{1}{4}\, U\, (\mathbf{Q}:\mathbf{Q})^2 \right] + \left[(L_1/2)\, \{\nabla \mathbf{Q} \vdots (\nabla \mathbf{Q})^T\} + (L_2/2)\, \{(\nabla . \mathbf{Q}).(\nabla . \mathbf{Q})\} \right] \quad (21)$$

From Eqn. 21, RHS of Eqn. 16 can be obtained,

$$ckT\mathbf{H} = - ckT \left[(1-1/3U)\mathbf{Q} - U\mathbf{Q}.\mathbf{Q} + U\{(\mathbf{Q}:\mathbf{Q})\mathbf{Q} + 1/3(\mathbf{Q}:\mathbf{Q})\mathbf{I}\} \right] + \left[L_1\nabla^2\mathbf{Q} + (L_2/2)\, [\nabla(\nabla.\mathbf{Q}) + \{\nabla(\nabla.\mathbf{Q})\}^T - 2/3\, \mathrm{tr}\{\nabla(\nabla.\mathbf{Q})\}\mathbf{I}] \right] \quad (22a)$$

Dividing both side by ckT*

$$\mathbf{H} = - \left[(1-1/3U)\mathbf{Q} - U\mathbf{Q}.\mathbf{Q} + U\{(\mathbf{Q}:\mathbf{Q})\mathbf{Q} + 1/3(\mathbf{Q}:\mathbf{Q})\mathbf{I}\} \right] + (U/3) \left[(L_1/ckT^*)\nabla^2\mathbf{Q} + (L_2/2ckT^*)\, [\nabla(\nabla.\mathbf{Q}) + \{\nabla(\nabla.\mathbf{Q})\}^T - 2/3\, \mathrm{tr}\{\nabla(\nabla.\mathbf{Q})\}\mathbf{I}] \right] \quad (22b)$$

The dynamics of tensor order parameter is the sum of the flow contribution (**F**), long-range ($\mathbf{H}^{lr}$) and short-range contribution ($\mathbf{H}^{sr}$) of the molecular field. Therefore,

$$\hat{\mathrm{Q}} = \mathrm{F}(\mathrm{Q}, \nabla v) + \mathbf{H}^{sr}\left(\mathbf{Q}, \overline{\mathrm{D}}_r(\mathbf{Q})\right) + \mathrm{H}^{lr}(\nabla Q) \quad (23)$$

where, $\hat{\boldsymbol{Q}}$ is the corotational time derivative (Jaumann derivative) of **Q**.

$$\hat{\mathbf{Q}} = \frac{\partial \mathbf{Q}}{\partial \mathrm{t}} + (\mathbf{v} \cdot \nabla)\mathbf{Q} - \mathbf{W} \cdot \mathbf{Q} + \mathbf{Q} \cdot \mathbf{W} \quad (24)$$

The flow contribution **F** can be shown as [Tsuji and Rey, 1997]

$$\mathbf{F}(\mathbf{Q}, \nabla \mathbf{v}) = \tfrac{2}{3}\boldsymbol{\beta}\mathbf{A} + \boldsymbol{\beta}\left[\mathbf{A} \cdot \mathbf{Q} + \mathbf{Q} \cdot \mathbf{A} - \tfrac{2}{3}(\mathbf{A} : \mathbf{Q})\mathbf{I}\right] - \tfrac{1}{2}\boldsymbol{\beta}\left[(\mathbf{A} : \mathbf{Q})\mathbf{Q} + \mathbf{A} \cdot \mathbf{Q} \cdot \mathbf{Q} + \mathbf{Q} \cdot \mathbf{A} \cdot \mathbf{Q} + \mathbf{Q} \cdot \mathbf{Q} \cdot \mathbf{A} - \{(\mathbf{Q} \cdot \mathbf{Q}) : \mathbf{A}\}\mathbf{I}\right] \quad (25)$$

$\overline{D}_r$ is the microstructure dependent rotational diffusivity. D_r, which is considered constant here, is the rotational diffusivity for a disc in an isotropic solution of similar discs [Larson, 1999].

$$\overline{D}_r = D_r \left[1 - \tfrac{3}{2} (\mathbf{Q} : \mathbf{Q}) \right]^{-2} \tag{26}$$

The concept of rotational diffusivity was introduced by Doi and Edwards [1986]. It is surmised that motion of each molecule is confined in a tube-like region because of the constraints created by neighboring molecules. Due to limited flexibility of the liquid-crystalline molecules, the orientation of the entire molecule must be changed in order for molecules to escape the tube, which is accomplished by the small random change of orientation. This mechanism is defined as rotational diffusivity [Ugaz, 1999] and corresponding time scale is related to rotational diffusion constant. β is a thermodynamic parameter which decides the flow alignment of the molecules and as indicated by Grecov and Rey [2003a], β is not determined by molecular shape.

The short range elastic contribution can be derived as [Grecov and Rey, 2003b]

$$\mathbf{H}^{sr}\left(\mathbf{Q}, \overline{D}_r(\mathbf{Q})\right) = -6\overline{D}_r \frac{3}{U}\left[\left(1 - \tfrac{1}{3}U\right)\mathbf{Q} - U\mathbf{Q}\cdot\mathbf{Q} + U\left\{(\mathbf{Q}:\mathbf{Q})\mathbf{Q} + \tfrac{1}{3}(\mathbf{Q}:\mathbf{Q})\mathbf{I}\right\}\right] \tag{27}$$

The long range elastic contribution can be derived as [Grecov and Rey, 2003b]

$$\mathbf{H}^{lr}(\mathbf{Q}) = 6D_r \left[(L_1/ckT^*)\nabla^2\mathbf{Q} + (L_2/2ckT^*)[\nabla(\nabla.\mathbf{Q}) + \{\nabla(\nabla.\mathbf{Q})\}^T - 2/3\ \mathrm{tr}\{\nabla(\nabla.\mathbf{Q})\}\mathbf{I}]\right] \tag{28}$$

From (25), (26), (27), and (28) the governing equation for the tensor order parameter **Q** can be written as

$$\hat{Q} = \tfrac{2}{3}\beta\mathbf{A} + \beta\left[\mathbf{A}\cdot\mathbf{Q} + \mathbf{Q}\cdot\mathbf{A} - \tfrac{2}{3}(\mathbf{A}:\mathbf{Q})\mathbf{I}\right] -$$
$$\tfrac{1}{2}\beta\left[(\mathbf{A}:\mathbf{Q})\mathbf{Q} + \mathbf{A}\cdot\mathbf{Q}\cdot\mathbf{Q} + \mathbf{Q}\cdot\mathbf{A}\cdot\mathbf{Q} + \mathbf{Q}\cdot\mathbf{Q}\cdot\mathbf{A} - \{(\mathbf{Q}\cdot\mathbf{Q}):\mathbf{A}\}\mathbf{I}\right]$$
$$-6\bar{D}_r\frac{3}{U}\left[\left(1-\tfrac{1}{3}U\right)\mathbf{Q} - U\mathbf{Q}\cdot\mathbf{Q} + U\left\{(\mathbf{Q}:\mathbf{Q})\mathbf{Q} + \tfrac{1}{3}(\mathbf{Q}:\mathbf{Q})\mathbf{I}\right\}\right]$$
$$+ 6D_r\left[(L_1/ckT^*)\nabla^2\mathbf{Q} + (L_2/2ckT^*)[\nabla(\nabla.\mathbf{Q}) + \{\nabla(\nabla.\mathbf{Q})\}^T - 2/3\right.$$
$$\left.\mathrm{tr}\{\nabla(\nabla.\mathbf{Q})\}\mathbf{I}\right] \qquad (29)$$

$$\mathrm{Er}\,\hat{\mathbf{Q}}^* = \mathrm{Er}\left[\frac{2}{3}\beta\mathbf{A}^* + \beta\left[\mathbf{A}^*\cdot\mathbf{Q} + \mathbf{Q}\cdot\mathbf{A}^* - \frac{2}{3}(\mathbf{A}^*:\mathbf{Q})\mathbf{I}\right]\right.$$
$$\left. -\frac{1}{2}\beta\left[(\mathbf{A}^*:\mathbf{Q})\mathbf{Q} + \mathbf{A}^*\cdot\mathbf{Q}\cdot\mathbf{Q} + \mathbf{Q}\cdot\mathbf{A}^*\cdot\mathbf{Q} + \mathbf{Q}\cdot\mathbf{Q}\cdot\mathbf{A}^* - \{(\mathbf{Q}\cdot\mathbf{Q}):\mathbf{A}^*\}\mathbf{I}\right]\right]$$
$$-\frac{3}{\mathrm{U}}\cdot\frac{\mathrm{R}}{\left(1-\frac{3}{2}\mathbf{Q}:\mathbf{Q}\right)^2}\left[\left(1-\frac{1}{3}\mathrm{U}\right)\mathbf{Q} - \mathrm{U}\mathbf{Q}\cdot\mathbf{Q} + \mathrm{U}\left\{(\mathbf{Q}:\mathbf{Q})\mathbf{Q} + \frac{1}{3}(\mathbf{Q}:\mathbf{Q})\mathbf{I}\right\}\right]$$
$$+\frac{3}{\left(1-\frac{3}{2}\mathbf{Q}:\mathbf{Q}\right)^2}\left[\nabla^{*2}\mathbf{Q} + \frac{1}{2}L^*{}_2\left[\nabla^*(\nabla^*\cdot\mathbf{Q}) + \{\nabla^*(\nabla^*\cdot\mathbf{Q})\}^T - \frac{2}{3}\mathbf{tr}\{\nabla^*(\nabla^*\cdot\mathbf{Q})\}\mathbf{I}\right]\right]$$

Here, $t^* = \dot{\gamma}t$, $\nabla^* = H\nabla$, $A^* = \dfrac{A}{\dot{\gamma}}$, $\mathrm{L}^*{}_2 = \mathrm{L}_2/\mathrm{L}_1$ (30)

The dimensionless parameters are denoted by superscript *. $\dot{\gamma}$ is the characteristic shear rate. Er (Ericksen number) and R (energy ratio) are two dimensionless numbers that are given by

$$\mathrm{Er} = \frac{\dot{\gamma}\mathrm{H}^2\mathrm{ckT}^*}{2\mathrm{L}_1\mathrm{D}_r},\ \mathrm{R} = \frac{3\mathrm{H}^2\mathrm{ckT}^*}{\mathrm{L}_1} \qquad (31)$$

Ericksen number (Er) represents the ratio of viscous flow effect to long-range order elasticity; whereas, energy ratio (R) represents the ratio of short-range order elasticity to long-range order elasticity. For this case Deborah number (De) is defined as

$$\mathrm{De} = \mathrm{Er}/\mathrm{R} \qquad (32)$$

As discussed in the literature [Grecov and Rey, 2003a], the total extra stress tensor, $\boldsymbol{\tau}$, is given by the sum of symmetric viscoelastic stress tensor $\boldsymbol{\tau}^s$, anti-symmetric stress tensor $\boldsymbol{\tau}^a$, and Ericksen stress tensor $\boldsymbol{\tau}^{Er}$

$$\boldsymbol{\tau} = \boldsymbol{\tau}^s + \boldsymbol{\tau}^a + \boldsymbol{\tau}^{Er} \tag{33}$$

Further, $\boldsymbol{\tau}^s$ is summation of a symmetric viscous stress contribution $\boldsymbol{\tau}^v$ and an elastic stress contribution $\boldsymbol{\tau}^e$ [Grecov and Rey, 2003a]

$$\boldsymbol{\tau}^s = \boldsymbol{\tau}^v + \boldsymbol{\tau}^e \tag{34}$$

The antisymmetric contribution $\boldsymbol{\tau}^s$ appears when **H.Q** is not symmetric and is given by [Grecov and Rey, 2003a]

$$\boldsymbol{\tau}^a = ckT\,(\mathbf{H.Q-Q.H}) \tag{35}$$

The Ericksen stress contribution caused by long range elasticity $\boldsymbol{\tau}^{Er}$ and can be given by [Grecov and Rey, 2003a]

$$\boldsymbol{\tau}^{Er} = -\frac{\partial f}{\partial \nabla \mathbf{Q}} : (\nabla \mathbf{Q})^T = \left[-L_1 \nabla \mathbf{Q} : (\nabla \mathbf{Q})^T - L_2\,(\nabla . \mathbf{Q}).(\nabla \mathbf{Q})^T\right] \tag{36}$$

Combining all these terms the extra stress tensor can be written as

$$\begin{aligned}\boldsymbol{\tau} = {} & \nu_1\,\mathbf{A} + \nu_2\,\{\mathbf{Q}.\,\mathbf{A} + \mathbf{A}.\mathbf{Q} - 2/3\,(\mathbf{Q}:\mathbf{A})\mathbf{I}\} + \nu_4[(\mathbf{A}:\mathbf{Q})\mathbf{Q} + \mathbf{A.Q.Q} + \mathbf{Q.A.Q} + \mathbf{Q.Q.A} - \\ & \{(\mathbf{Q.Q}):\mathbf{A}\}\mathbf{I}]) + (ckT)\,[-2/3\beta\mathbf{H} - \beta\,\{\mathbf{H.Q} + \mathbf{Q.H} - 2/3\,(\mathbf{H}:\mathbf{Q})\,\mathbf{I}\}] + 1/2\,\beta\,[(\mathbf{H}:\mathbf{Q})\,\mathbf{Q} + \mathbf{H.Q.Q} + \mathbf{Q.H.Q} + \mathbf{Q.Q.H} - \{(\mathbf{Q.Q}):\mathbf{H}\}\mathbf{I}] + ckT\,(\mathbf{H.Q-Q.H}) + [-L_1 \nabla \mathbf{Q} : (\nabla \mathbf{Q})^T - \\ & L_2\,(\nabla . \mathbf{Q}).(\nabla \mathbf{Q})^T]\end{aligned} \tag{37}$$

where, ν_1, ν_2, and ν_4 are viscosity coefficients. Relations between these viscosity coefficients and Leslie coefficients are available in literature [Grecov and Rey, 2003b]. Nondimensionalization of (37) gives

$$\boldsymbol{\tau}^* = \mathrm{Er}/\mathrm{R}\left(\nu^*_1\,\mathbf{A}^* + \nu^*_2\left\{\mathbf{Q}.\,\mathbf{A}^* + \mathbf{A}^*.\mathbf{Q} - 2/3\,(\mathbf{Q}:\mathbf{A}^*)\mathbf{I}\right\} + \nu^*_4\left[\left(\mathbf{A}^*:\mathbf{Q}\right)\mathbf{Q} + \mathbf{A}^*.\mathbf{Q}.\mathbf{Q} + \mathbf{Q}.\mathbf{A}^*.\mathbf{Q} + \mathbf{Q}.\mathbf{Q}.\mathbf{A}^* - \left\{\left(\mathbf{Q}.\mathbf{Q}\right):\mathbf{A}^*\right\}\mathbf{I}\right]\right) + 3/\mathrm{U}\left[-2/3\beta\mathbf{H} - \beta\left\{\mathbf{H}.\mathbf{Q} + \mathbf{Q}.\mathbf{H} - 2/3\,(\mathbf{H}:\mathbf{Q})\,\mathbf{I}\right\}\right] + (3/2\mathrm{U})\,\beta\left[\left(\mathbf{H}:\mathbf{Q}\right)\mathbf{Q} + \mathbf{H}.\mathbf{Q}.\mathbf{Q} + \mathbf{Q}.\mathbf{H}.\mathbf{Q} + \mathbf{Q}.\mathbf{Q}.\mathbf{H} - \left\{\left(\mathbf{Q}.\mathbf{Q}\right):\mathbf{H}\right\}\mathbf{I}\right] + 3/\mathrm{U}\,(\mathbf{H}.\mathbf{Q} - \mathbf{Q}.\mathbf{H}) + 3/\mathrm{R}\left[-\nabla^*\mathbf{Q}:(\nabla^*\mathbf{Q})^{\mathrm{T}} - \mathrm{L}_2/\mathrm{L}_1\,(\nabla^*.\mathbf{Q}).(\nabla^*\mathbf{Q})^{\mathrm{T}}\right] \tag{38}$$

H in nondimensionalization form is

$$\mathbf{H} = -\left[(1-1/3\mathrm{U})\mathbf{Q} - \mathrm{U}\mathbf{Q}.\mathbf{Q} + \mathrm{U}\{(\mathbf{Q}:\mathbf{Q})\mathbf{Q} + 1/3(\mathbf{Q}:\mathbf{Q})\mathbf{I}\}\right] + \mathrm{U}/\mathrm{R}\left[\nabla^{*2}\mathbf{Q} + (\mathrm{L}^*_2/2)\left[\nabla^*(\nabla^*.\mathbf{Q}) + \{\nabla^*(\nabla^*.\mathbf{Q})\}^{\mathrm{T}} - 2/3\ \mathrm{tr}\{\nabla^*(\nabla^*.\mathbf{Q})\}\mathbf{I}\right]\right] \tag{39}$$

where , $\boldsymbol{\tau}^* = \boldsymbol{\tau}/\mathrm{ckT}^*$, $\nu^*_1 = \nu_1 6\mathrm{D_r}/\mathrm{ckT}^*$, $\nu^*_2 = \nu_1 6\mathrm{D_r}/\mathrm{ckT}^*$, $\nu^*_4 = \nu_1 6\mathrm{D_r}/\mathrm{ckT}^*$ (40)

It is noted that the total dimensionless extra stress tensor is neither symmetric nor traceless.

According to Doi model of short-range energy, the temperature dependence of S at equilibrium is

$$\mathrm{S_{eq}} = ¼ + ¾\left(1 - \frac{8}{3U}\right)^{½} \tag{41}$$

where, U is the nematic potential and defined earlier.

It has been shown by Doi and Edwards [1986] that for U≤8/3 the stable phase is isotropic, for 8/3 ≤ U ≤ 3 there is biphasic equilibrium, and for U ≥3 the phase is unixaial nematics.

At the bounding surface, the discotics are uniaxial (P = 0), and S = $\mathrm{S_{eq}}$. The magnitude of U can be calculated from (41) for a value of $\mathrm{S_{eq}}$. Therefore, the tensor order parameter at bounding surface can be calculated as

$$\mathbf{Q}_s = S_{eq}(\mathbf{n}_s\mathbf{n}_s - \mathbf{I}/3) \quad (42)$$

6.2 Flow geometry and solution scheme

6.2.1 Simple shear flow

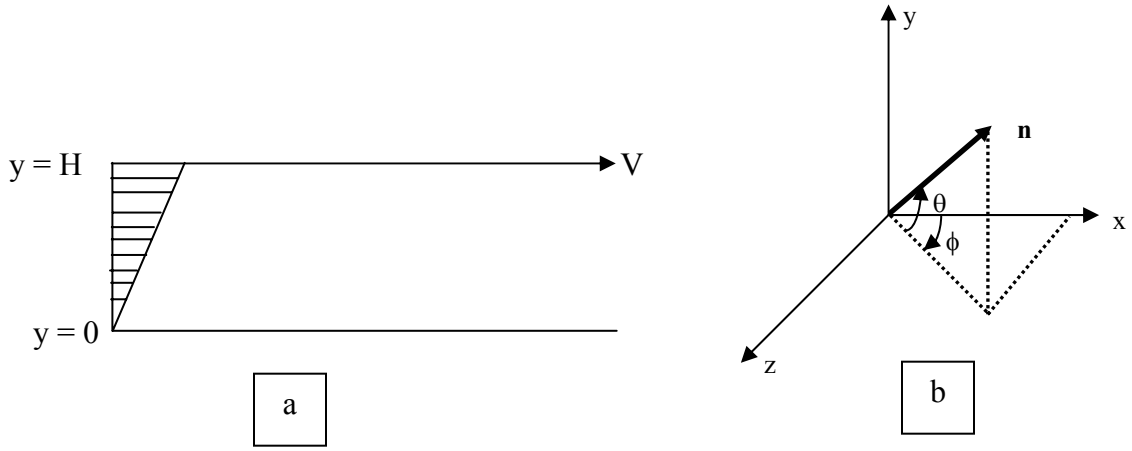

Figure 6.2: (a) Simple shear flow between two parallel plates separated by a gap, H. (b) Cartesian coordinate system used in this study, where x is the flow direction, y is the velocity-gradient direction, and z is the vorticity direction. **n** represents the director orientation. θ and ϕ are the tilt and twist angles, respectively.

The simulations were performed for a simple-shear flow defined in **Figure 6.2a**. The flow situation is similar to that observed in rheometric flow, reported in Chapters 2 and 3. In this case the bottom plate is stationary, the upper plate moves at a velocity V, and the gap between the parallel plates is H. The shear rate, $\dot{\gamma}$, is uniform across the gap. For the coordinate system shown in **Figure 6.2b**, x-direction represents the velocity direction, y-direction represents the gradient direction, and z-direction represents the vorticity direction. The tilt and twist angles are denoted by θ and ϕ.

For simple shear flow $V = V_x = \dot{\gamma} y$. The velocity vector can be written as

$$\mathbf{V} = (\dot{\gamma} y, 0, 0) \tag{43}$$

and velocity gradient is $\nabla \mathbf{v} = \begin{pmatrix} 0 & 0 & 0 \\ \dot{\gamma} y & 0 & 0 \\ 0 & 0 & 0 \end{pmatrix}$ (44)

No change of velocity in z direction was considered. Therefore,

$$\nabla = \mathbf{i} \frac{\partial}{\partial x} + \mathbf{j} \frac{\partial}{\partial y} \tag{45}$$

The problem is solved in a dimensionless form, i.e., from y *= 0 to y* = 1.

$$\text{So, } V_x^* = \frac{V_x}{\dot{\gamma} H} = \frac{\dot{\gamma} y}{\dot{\gamma} H} = \frac{y}{H} = y^* \tag{46}$$

Therefore, the dimensionless component of x-velocity (V_x^*) is equal to the dimensionless gap y*.

The simulation studies were performed in the following computational domain depicted in **Figure 6.3**. The dimensionless length of the computational domain was 5, whereas the dimensionless width was 1. A very fine meshing was used near upper and lower boundaries, i.e., y* = 0, and y* = 1. As mentioned above, at the bottom boundary (y* = 0), all the velocity components were zero and at the upper boundary (y* =1), velocity is only in the x-direction, i.e, $v_x^* = V_x^*$, $v_y^* = 0$, $v_z^* = 0$. For the present simulation studies, the dimensionless velocity of the top boundary was set to 1.

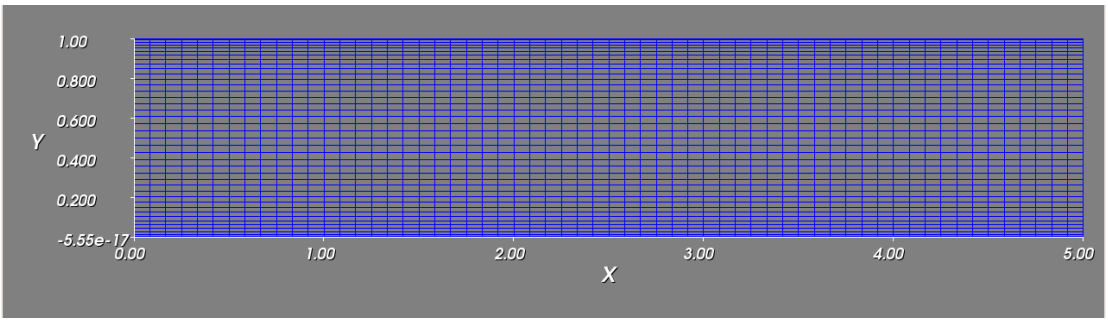

Figure 6.3: Computational domain with dimensionless length of 5 and dimensionless width of 1.

In this chapter, results are presented for decoupled situations. For the decoupled cases, only the microstructure evolution equation (30) was solved. Here, the flow field was assumed unchanged during the microstructure evolution. Thus, for a given flow field

$$\frac{\partial Q^*}{\partial t^*} = f(Q, v) \tag{47}$$

A modified Runga-Kutta technique was used to solve Eq.47. The solution scheme is shown bellow [von Oehsen et al., 2006]

$$k_1 = f\left(Q_n^*\right) \tag{48}$$

$$k_2 = f\left(\frac{1}{4}\Delta t^* k_1 + Q_n^*\right) \tag{49}$$

$$k_3 = f\left(\frac{3}{32}\Delta t^* k_1 + \frac{9}{32}\Delta t\, k_2 + Q_n^*\right) \tag{50}$$

$$k_4 = f\left(\frac{1932}{2197}\Delta t^* k_1 - \frac{7200}{2197}\Delta t^* k_2 + \frac{7296}{2197}\Delta t^* k_3 + Q_n^*\right) \tag{59}$$

$$k_5 = f\left(\frac{439}{216}\Delta t^* k_1 - 8\Delta\Delta k_2 + \frac{3680}{513}\Delta t^* k_3 - \frac{845}{4104}\Delta t^* k_4 + Q_n^*\right) \tag{51}$$

$$k_6 = f\left(\frac{-8}{27}\Delta t^* k_1 + 2\Delta\Delta k_2 - \frac{3544}{2566}\Delta t^* k_3 + \frac{1859}{4104}\Delta t^* k_4 - \frac{11}{40}\Delta t^* k_5 + Q_n^*\right) \tag{52}$$

$$Q_{n+1} = Q_n + \frac{25}{216}\Delta t^* k_1 + \frac{1408}{2565}\Delta t^* k_3 + \frac{2197}{4104}\Delta t^* k_4 - \frac{1}{5}\Delta t^* k_5 \quad (53)$$

$$z = Q_n + \frac{16}{135}\Delta t^* k_1 + \frac{6656}{2565}\Delta t^* k_3 + \frac{28561}{56430}\Delta t^* k_4 - \frac{9}{50}\Delta t^* k_5 + \frac{2}{55}\Delta t^* k_6 \quad (54)$$

$$\mu = \max\left|(Q_{n+1})_i - z_i\right| \quad (55)$$

$$\Delta t_{n+1} = \Delta t\left(\frac{\varepsilon \Delta t}{2\mu}\right)^{\frac{1}{4}} \qquad \varepsilon \approx 10^{-8} \quad (56)$$

It is noted that Q^* is symmetric and traceless; therefore, only five components of the Q^* tensor were solved.

A few simulations were also performed using backward Euler technique and this technique is generally used for stiff problems. In this technique the following solution scheme was used [von Oehsen et al., 2006]

$$\frac{\partial Q^*}{\partial t} = f\left(Q^*\right) \quad (57)$$

$$Q^*_{n+1} = Q^*_n + \Delta t\, f\left(Q^*_n\right) \quad (58)$$

For coupled cases, other than microstructural equation (30), the flow equations also need to be solved.

For a flow system the continuity equation is

$$(\nabla . \mathbf{v}) = 0 \quad (59)$$

and the momentum balance equation is

$$\rho \frac{D\mathbf{v}}{Dt} = -\nabla P - \nabla . \boldsymbol{\tau} \quad (60)$$

where, $\mathbf{v}$ is the velocity vector, $\boldsymbol{\tau}$ is the extra stress tensor, P is pressure, ρ is density.

After non-dimensionalization

$$\frac{\rho H^2\dot{\gamma}^2}{ckT^*}\frac{D\mathbf{v}^*}{Dt^*} = -\nabla^* P^* - \nabla^*.\boldsymbol{\tau} \tag{61}$$

Where $\frac{\rho H^2\dot{\gamma}^2}{ckT^*}$ is a dimensionless number, and $\mathbf{v}^* = \frac{\mathbf{v}}{H\dot{\gamma}}$, $\nabla^* = H\nabla$, $A^* = \frac{A}{\dot{\gamma}}$, $W^* = \frac{W}{\dot{\gamma}}$,

$$t^* = \dot{\gamma}t \tag{62}$$

Further, it can be shown that, for slow flow such as encountered during simple shear flow the dimensionless term $\frac{\rho H^2\dot{\gamma}}{ckT^*}$ is small. Therefore, the term on the left hand side of the Eqn. 61 can be ignored. Then, momentum balance equation in dimensionless form is,

$$\nabla^* P^* + \nabla^*.\boldsymbol{\tau}^* = 0 \tag{63}$$

Also, the continuity equation in dimensionless form is

$$\nabla^*.\mathbf{v}^* = 0 \tag{64}$$

To solve the flow problems, an auxiliary variable, G*, is introduced signifying

$$\mathbf{G}^* = \nabla^*\mathbf{v} \tag{65}$$

Also, a stability term was incorporated in the momentum balance equation (63). Then the momentum balance equation can be written as [von Oehsen et al., 2006]

$$\nabla.\left(\nabla\mathbf{v}^* + \nabla\mathbf{v}^{*T}\right) - (1-\alpha)\nabla.\left(\nabla\mathbf{G}^* + \nabla\mathbf{G}^{*T}\right) + \nabla P^* + \nabla.\boldsymbol{\tau}'^* = 0 \tag{66}$$

where α is the stability factor such that $0 < \alpha < 1$

and $\boldsymbol{\tau}'^* = \boldsymbol{\tau}^* - \alpha\left(\mathbf{G}^* + \mathbf{G}^{*T}\right)$ (67)

For a given flow condition, the microstructural evolution equation and the momentum balance equation are solved initially for an applied velocity field. For the next time step, the calculated Q^*_{n+1} is used in the stress equation. The momentum balance

equation was then solved using the estimated stress values. This process was performed until a steady state was reached.

6.2.2 Initial Conditions

It was shown in Chapter 3 that mesophase pitch displays a complex microstructure. However, simulation studies for such complex microstructure are still unachievable. Therefore, the present studies were performed for simpler initial conditions. In this study, two different initial conditions were considered. In one of such conditions, the initial director orientation was in the flow direction (x direction), i.e., $\mathbf{n_s} = (1, 0, 0)$. At the top and the bottom boundaries the tensor order parameter, **Q** was defined as

$$\mathbf{Q}(y=0) = \mathbf{Q}(y=1) = S_{eq}\left(\mathbf{n_s n_s} - \frac{\mathbf{I}}{3}\right) \tag{68}$$

where, S_{eq} is defined in (41).

As shown in Chapter 3, for a shear rate of 10 s^{-1} and in the flow-gradient plane, the orientation parameter calculated from X-ray diffraction (002) peak was about -0.3. The (002) diffraction peak was observed at the meridional position. The parameter was normalized by dividing it with -0.5. The estimated value of S was 0.6, i.e., S= Seq = 0.6. This S_{eq} value was used in (41) to obtain an estimated value of 3.4 for the nematic potential, U.

Other than the director orientation in the flow direction, another case was considered where the initial director orientation was in the vorticity direction (z), i.e, $\mathbf{n_s} = (0, 0, 1)$. In both of these cases, except at the top and the bottom boundaries, over the entire computation domain, **Q** was initialized in the following way [von Oehsen et al., 2006]

$$\mathbf{Q}_0 = \varepsilon_1 S_{eq}\left(\mathbf{n}_0^2 - \frac{\mathbf{I}}{3}\right) \tag{69}$$

$\mathbf{n}_0$ can be defined in following way [von Oehsen et al., 2006]

$$n_0 = \begin{bmatrix} \cos(\varepsilon_2\pi)\cos(\varepsilon_3\pi) \\ \sin(\varepsilon_2\pi) \\ \cos(\varepsilon_2\pi)\sin(\varepsilon_3\pi) \end{bmatrix} \tag{70}$$

Here, $0<\varepsilon_1<a_1$, $-a_2/2<\varepsilon_2<a_2/2$, $0<\varepsilon_3<2a_3$

ε_1, ε_2, and ε_3 are the random numbers and the maximum limits of these numbers depend on the magnitude of a_1, a_2 and a_3. Those numbers can be defined in such a way that the director orientation over the entire computation domain was same as that of the boundaries. In selected cases, a small random fluctuation was applied over the computation domain except at the boundaries.

It is noted that two of such director orientations presented here are observed during experimental studies. As shown in **Figure 3.6** of Chapter 3, after squeezing the sample between the cone and the plate, the layer-planes were in the radial direction with significant director orientation in the radial direction. For the sample that was steady-sheared and then allowed to relax for ~1000 s (**Figure 3.20**), some layer-planes were found to be oriented in the flow direction. The director orientation of these planes was in the vorticity direction.

In this study, the microstructural equation was solved in dimensionless form and the magnitude of the elastic constants was not needed. Instead, it was assumed that $L_2^* = \frac{L_2}{L_1} = -0.5$. This signifies that $K_{22} = 4/3K$, i.e, the twist elastic constant is 4/3 times of the blend and the splay elastic constants ($K=K_{11}=K_{33}$).

Experimentally, the bend/splay and twist elastic constants could not be measured individually, however the average elastic constant of this material was estimated in the range of $1*10^{-9}$ to $1*10^{-10}$ N (Chapter 4). For discotic materials, twist elastic constant is higher than the bend/splay constant, and K_{22} = 4/3 K is a reasonable assumption. It is noted that for rodlike liquid crystals, twist elastic constant (K_{22}) is smaller than the bend/splay constant (K) and it is indicated in literature that the blend/splay constant (K) may be as high as$10K_{22}$ [Larson, 1999].

The viscosity coefficients cannot be measured experimentally. Instead, the values of the dimensionless viscosity coefficients used in this study were similar to that used by Grecov and Rey [2003b] and the values were $\nu_1^* = 1, \nu_2^* = 1, \nu_4^* = 6$. It was shown by Grecov and Rey (2003b) that the discotic molecules will be flow aligned for $\beta \leq -1.2$. This value of β was considered because the experimental results suggest that mesophase pitch is flow-aligned in nature. The flow-alignment angle can be given by [Grecov and Rey, 2003b]

$$\cos(2\theta_{al}) = \frac{6S}{\beta\left(4 + 2S - S^2\right)} \tag{71}$$

where, θ_{al} is the alignment angle.

Using S = 0.6 and β = -1.2, the alignment angle is estimated as 115.9° or -64.1°. It was shown that the alignment is stable when the director is in the second or in the fourth quadrant (de Andrade Lima and Rey, 2003b). For the simulation studies presented here Ericksen number (Er) was set to 10^7 and the energy ratio (R) was 10^{10}.

6.2.2 Visualization

Parallelopipeds (eigen-boxes) were used to represent the orientation of the discs [von Oehsen et al., 2006]. As shown in **Figure 6.4**, the sides of the parallelopiped are related to the eigenvalues of the tensor order parameter, Q. The eigenvectors are represented by director triads (m, l, n). Blue, green, and red colors represent the faces of the parallelopiped. For uniaxial orientation, blue and green faces are equivalent.

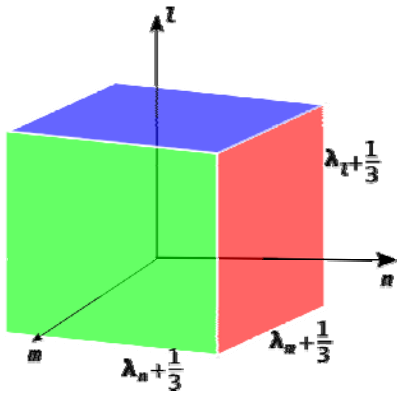

Figure 6.4: Representation of eigenvalues and eigenvectors.

6.3 Results and discussion

6.3.1 Director in the flow direction

In this case the directors were oriented in the flow direction initially. **Figure 6.5** shows the eigen-boxes after 5 iterations. These boxes were elongated in the x-direction signifying that the director orientation was in the flow direction. **Figures 6.6a and b** represent the contour plot of tilt angle (θ) and twist angle (ϕ) over the entire computation domain after 5 iterations. It is noted that the magnitude of tilt and twist angle were mostly zero, i.e., directors were oriented in the flow direction. The orientation of the discs across the width was obtained and **Figure 6.7** shows the change of tilt angle across the width at $x^* = 2.5$. **Figure 6.8** represents the histograms of the distribution of tilt angle for all nodes after 5 iterations. It is noted that the tilt angle at most of the nodes was $\approx 0°$.

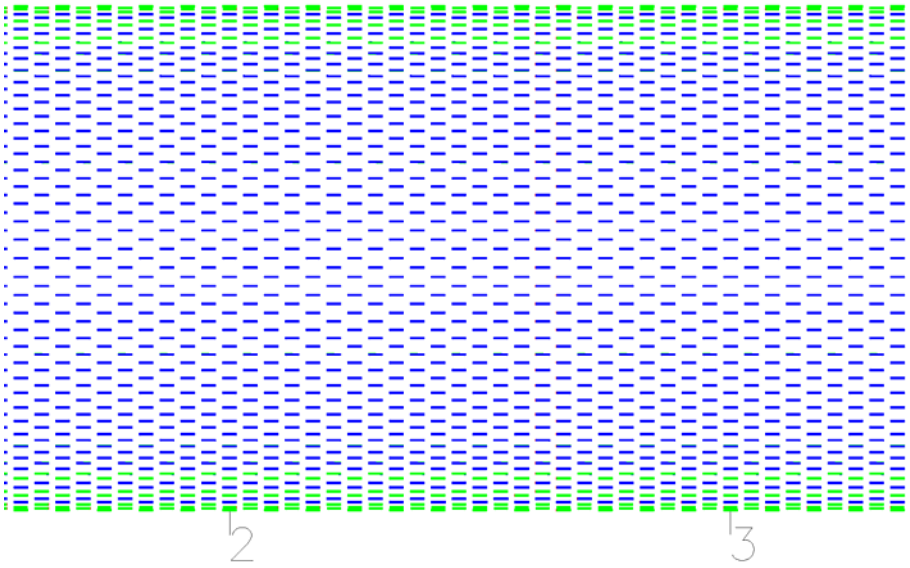

Figure 6.5: Parallelopipeds represent the orientation of the discs after 5 iterations. The size and orientation of the parallelopipeds are related to eigenvalues and eigenvetors of tensor order parameter, Q.

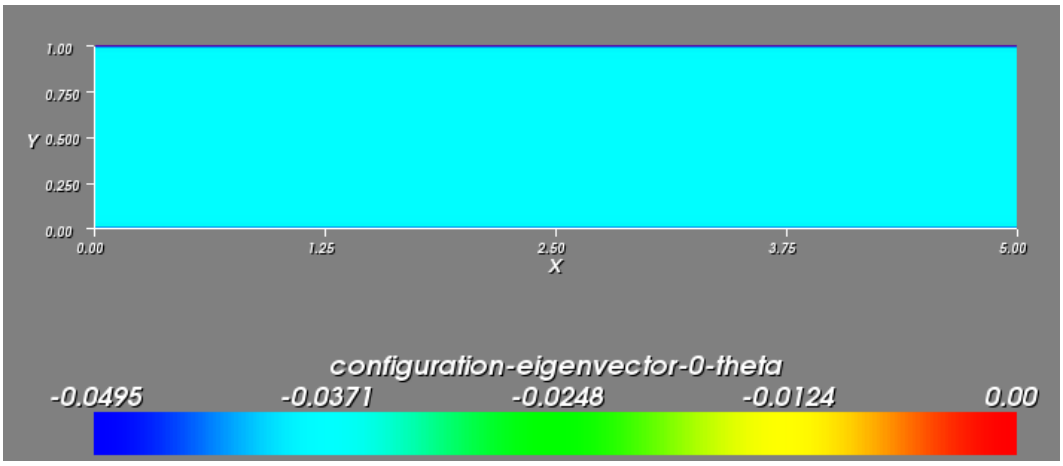

Figure 6.6a: Contour plot of tilt angle, θ, over the entire computational domain after 5 iterations

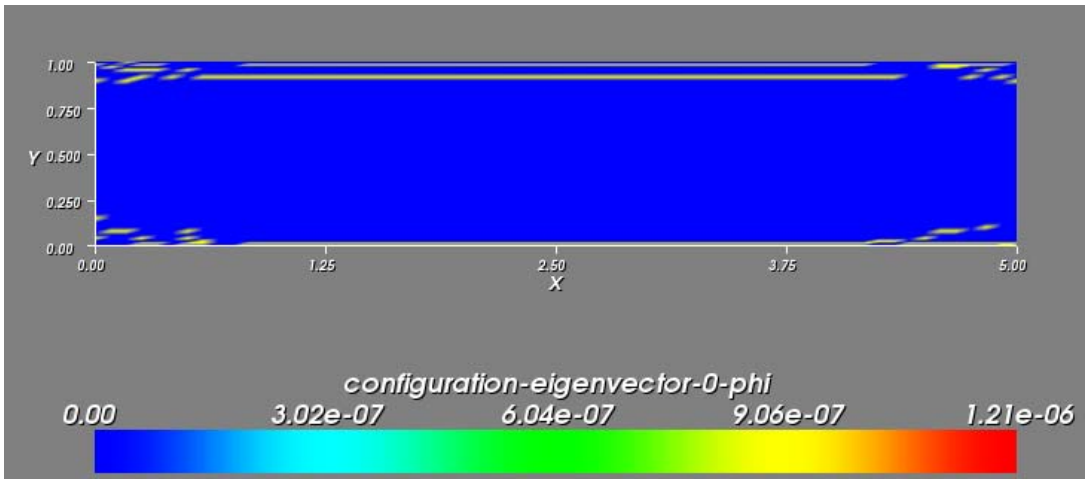

Figure 6.6b: Contour plot of twist angle, ϕ, over the entire computational domain after 5 iterations.

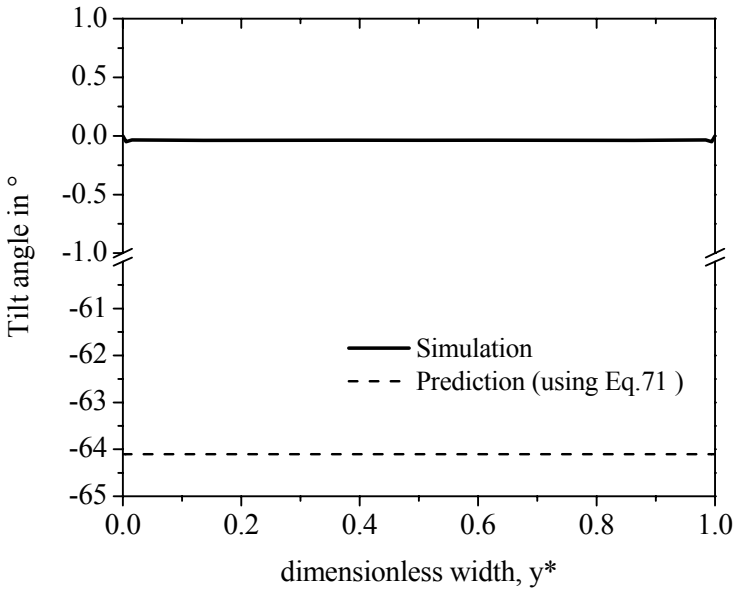

Figure 6.7: Change of tilt angle across the width at x* = 2.5 after 5 iterations. Also shown the prediction obtained using Eqn. 71.

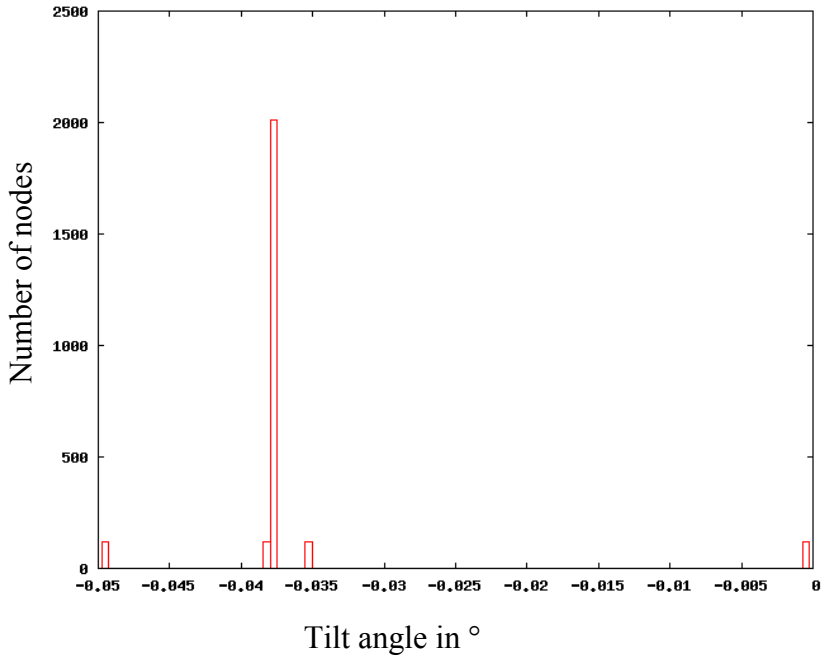

Figure 6.8: Histogram shows the distribution of tilt angle for all nodes after 5 iterations.

The iterations were continued until the error reached $\approx 10^{-8}$ and the results of the final iteration was considered as steady state. The results obtained for such steady-state situations are presented. After 52550 iterations ($t^* \approx 11$), **Figure 6.9** displays the eigen-boxes. It is noted that the orientation and the size of these parallelopipeds differ significantly from **Figure 6.5**. At the top and the bottom boundaries, the parallelopipeds were oriented in the flow direction, whereas away from the boundaries these parallelopipeds were oriented at some angle (flow-alignment angle). The tilt angle across the width of the geometry was measured at $x^* = 2.5$ and is shown in **Figure 6.10**. It is noted that at $y^* = 0$ and $y^* = 1$ the magnitude of the tilt angle was still zero due to strong anchoring at the boundaries (Dirichlet boundary condition). However, away from the boundaries, the tilt angle changed gradually. The flow-alignment angle was found to be -64.1°, which matches with the analytical solution obtained using Eqn.71.

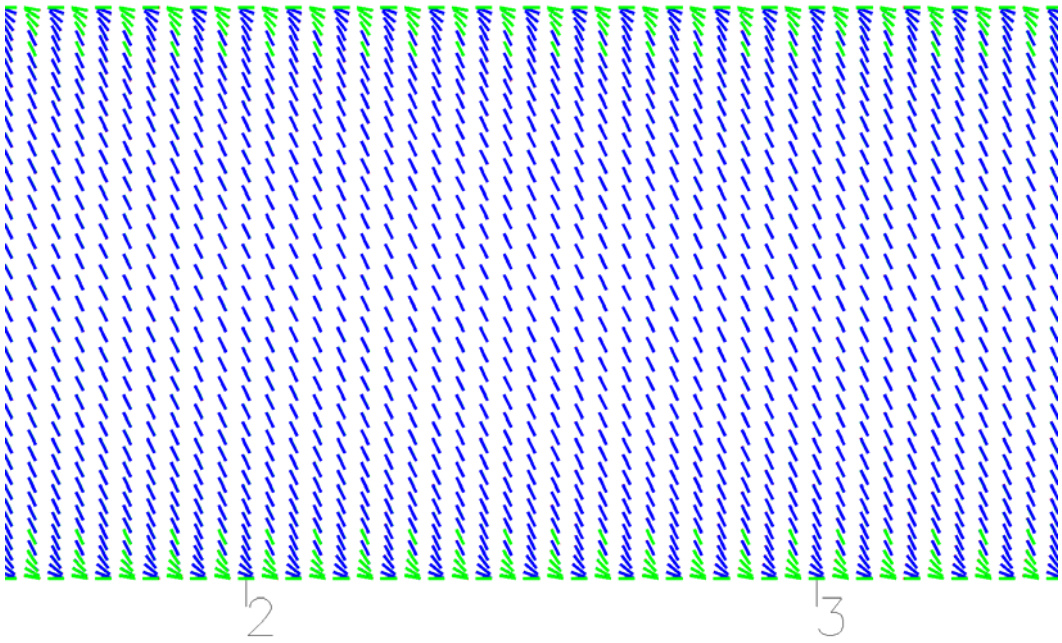

Figure 6.9: Parallelopipeds represent the orientation of the discs after 52550 iterations. The size and orientation of the parallelopipeds are related to eigenvalues and eigenvetors of tensor order parameter, Q.

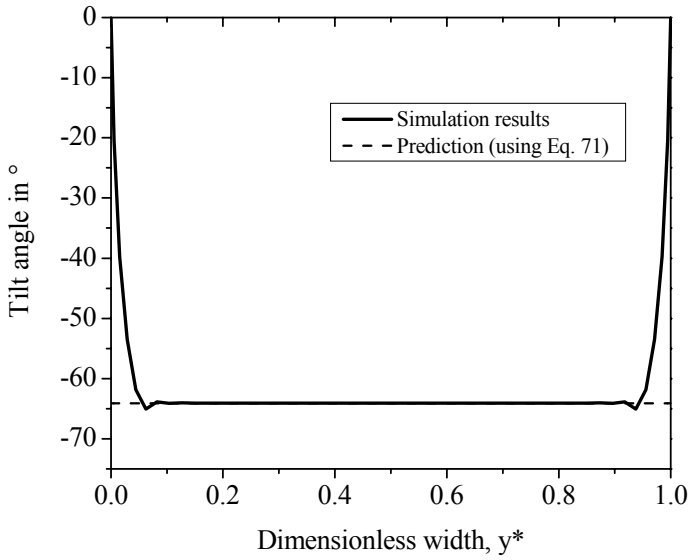

Figure 6.10: Change of tilt angle across the width at x* = 2.5 after 52550 iterations. Also shown the prediction obtained using Eqn. 71.

Figures 6.11a and **b** display the contour plot of tilt (θ) and twist angle (ϕ) over the entire computation domain after 52550 iterations. It is noted that, except near the boundaries, the tilt angle possesses a single value over the entire computation domain. Also, the values of twist angle were zero everywhere. Histograms of tilt angle at all the nodes were obtained (**Figure 6.12**) and it was observed that tilt angle at most of the nodes was -64.1°. This signifies that, except near the boundaries, the directors were oriented at an angle -64.1°. These results are similar to that presented by Grecov and Rey [2003b].

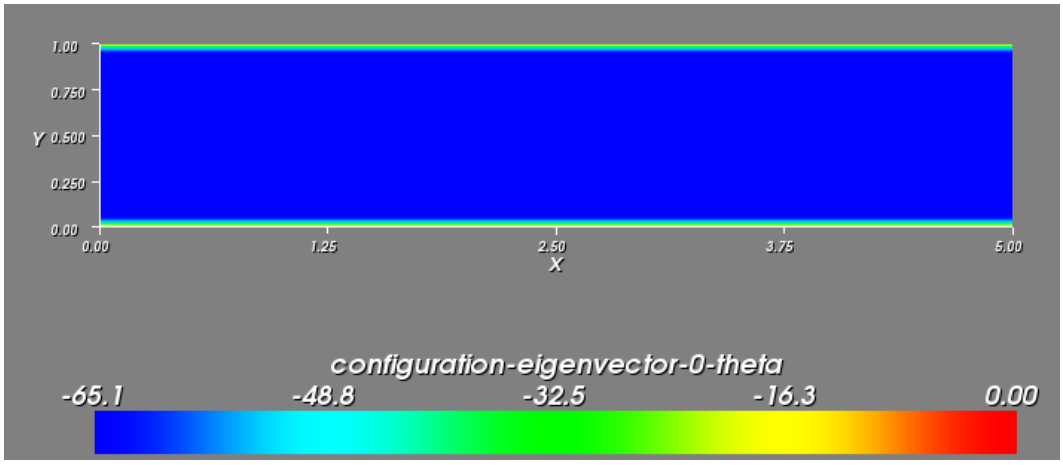

Figure 6.11a: Contour plot of tilt angle, θ, over the entire computational domain after 52550 iterations.

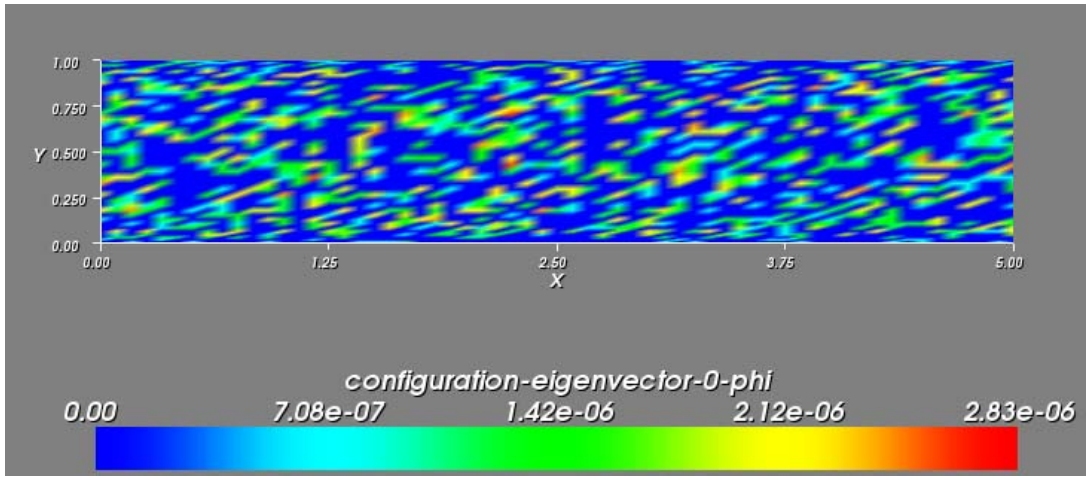

Figure 6.11b: Contour plot of twist angle, ϕ, over the entire computational domain after 52550 iterations.

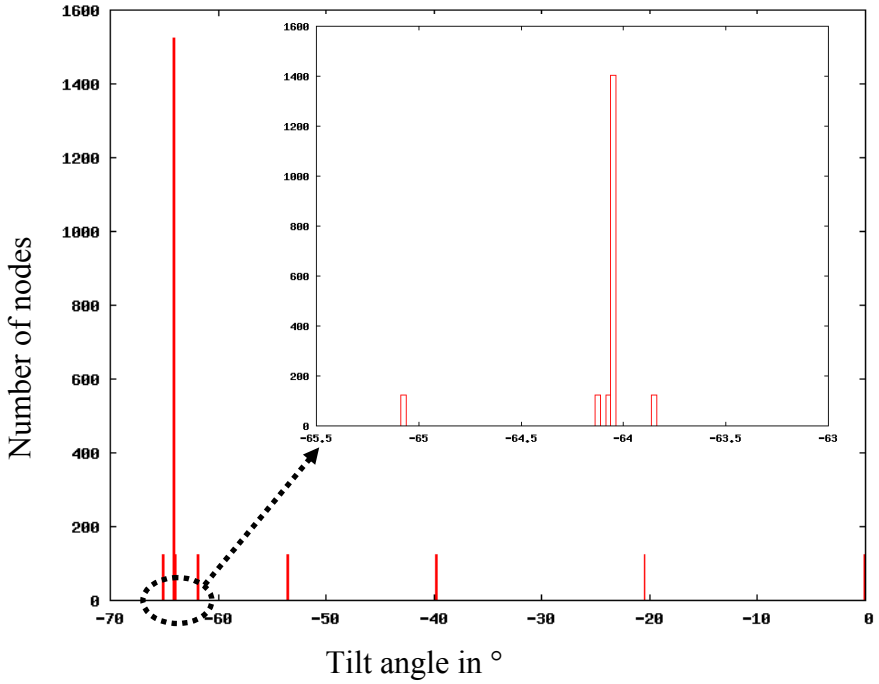

Figure 6.12: Histogram shows the distribution of tilt angle for all nodes after 52550 iterations. The inset shows the magnified view for the tilt angle -63° to -65.5°.

6.3.2 Director in the vorticity direction

In this case the directors were oriented in the vorticity direction initially. **Figure 6.13** shows the eigen-boxes after 5 iterations. These boxes were elongated in the z-direction signifying that the director orientation was in the vorticity direction. **Figures 6.14a and b** represent the contour plot of tilt angle (θ) and twist angle (ϕ) over the entire computation domain after 5 iterations. It is noted that the magnitude of tilt was mostly zero, whereas the magnitude of twist angle was mostly 90°, i.e., directors were oriented in the vorticity direction. The orientation of the discs across the width was obtained and **Figure 6.15** shows the change of tilt angle across the width at x* = 2.5. **Figures 6.16 a** and **b** represent the histograms of the distribution of tilt and twist angle for all nodes after 5

iterations. It is noted that the tilt angle (**Figure 6.16a**) at most of the nodes was ≈0°, whereas twist angle (**Figure 6.16b**) was ≈90°.

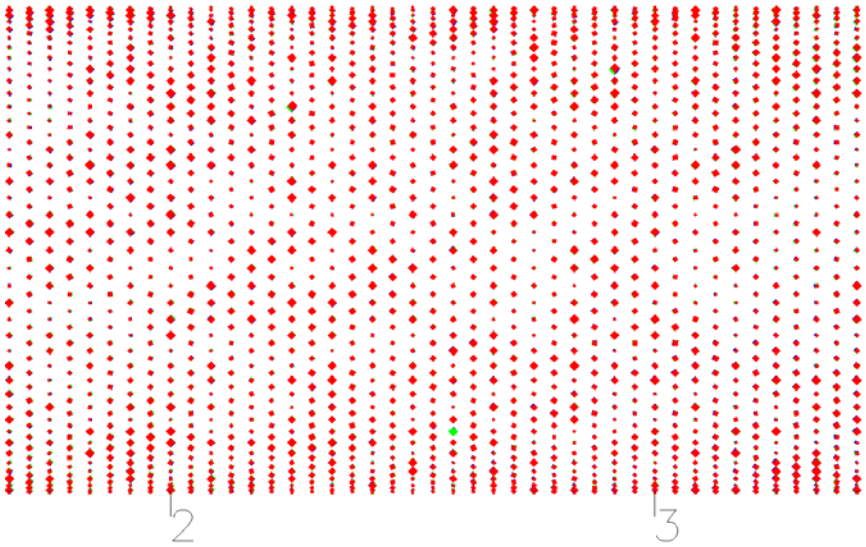

Figure 6.13: Parallelopipeds represent the orientation of the discs after 5 iterations. The size and orientation of the parallelopipeds are related to eigenvalues and eigenvetors of tensor order parameter, Q.

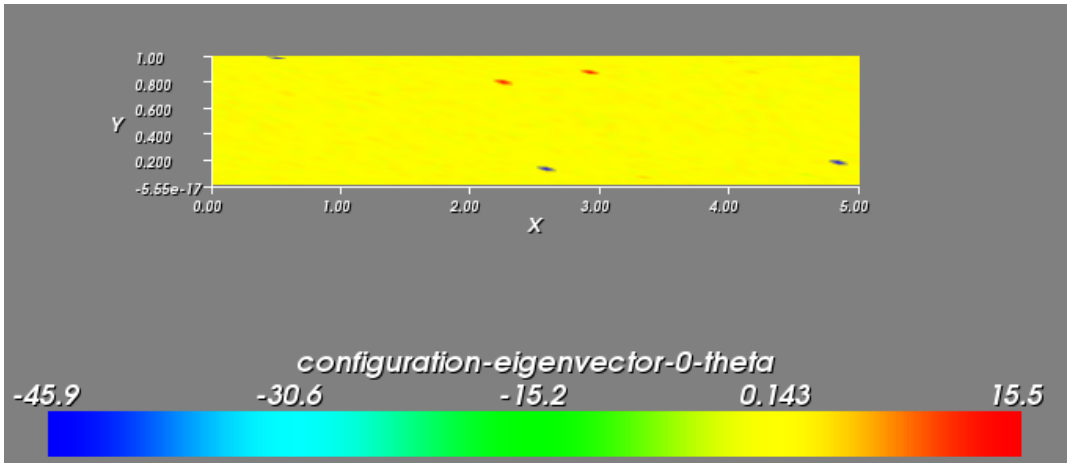

Figure 6.14a: Contour plot of tilt angle, θ, over the entire computational domain after 52550 iterations.

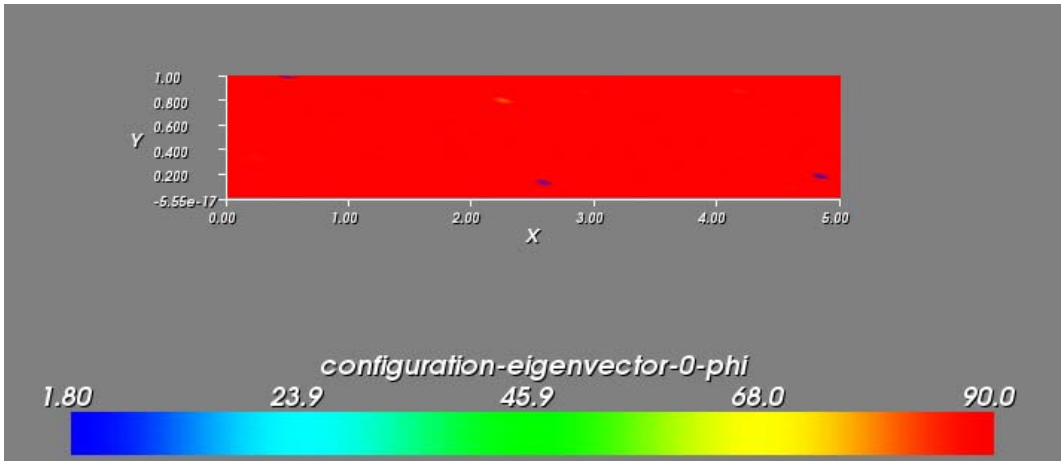

Figure 6.14b: Contour plot of twist angle, ϕ, over the entire computational domain after 5 iterations.

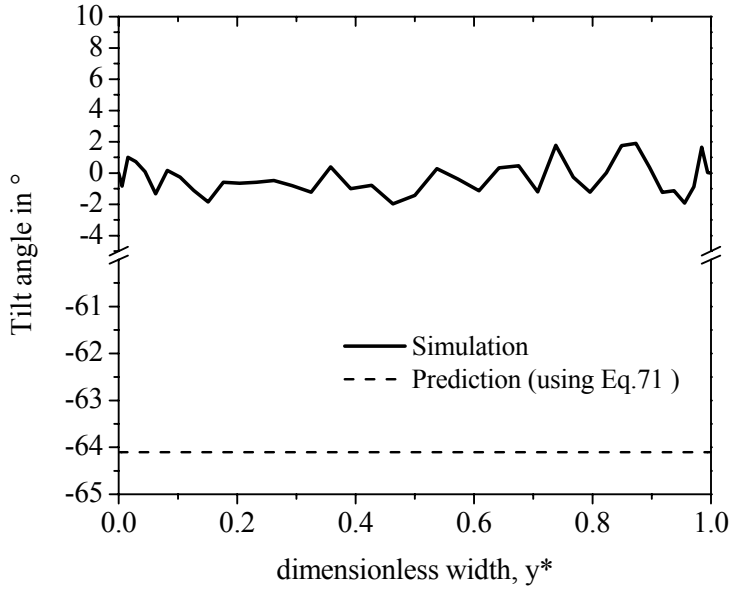

Figure 6.15: Change of tilt angle across the width at x* = 2.5 after 5 iterations. Also shown the prediction obtained using Eqn. 71.

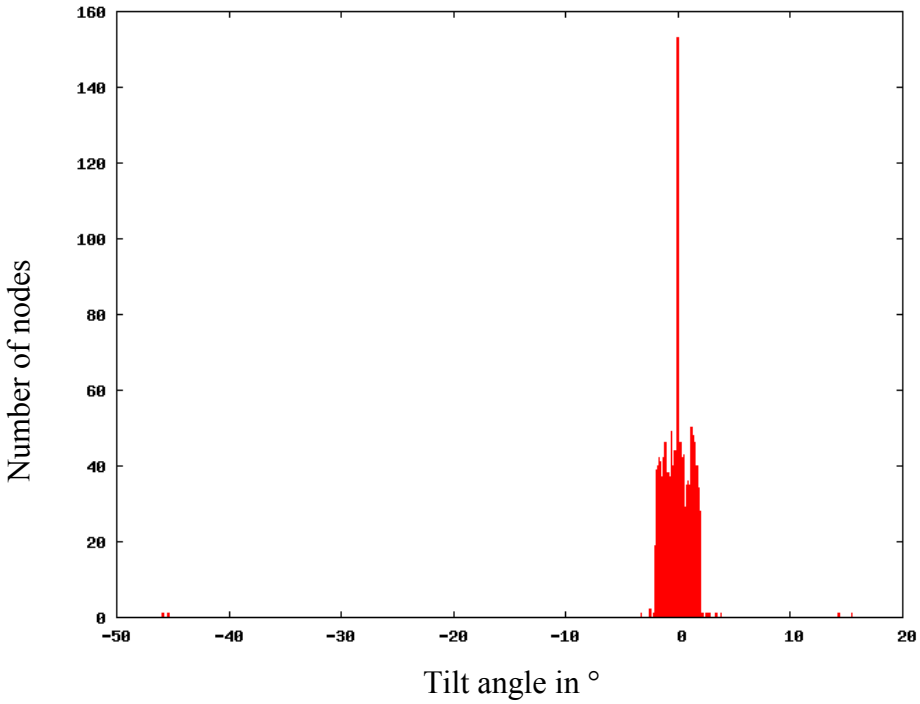

Figure 6.16a: Histogram shows the distribution of tilt angle for all nodes after 5 iterations.

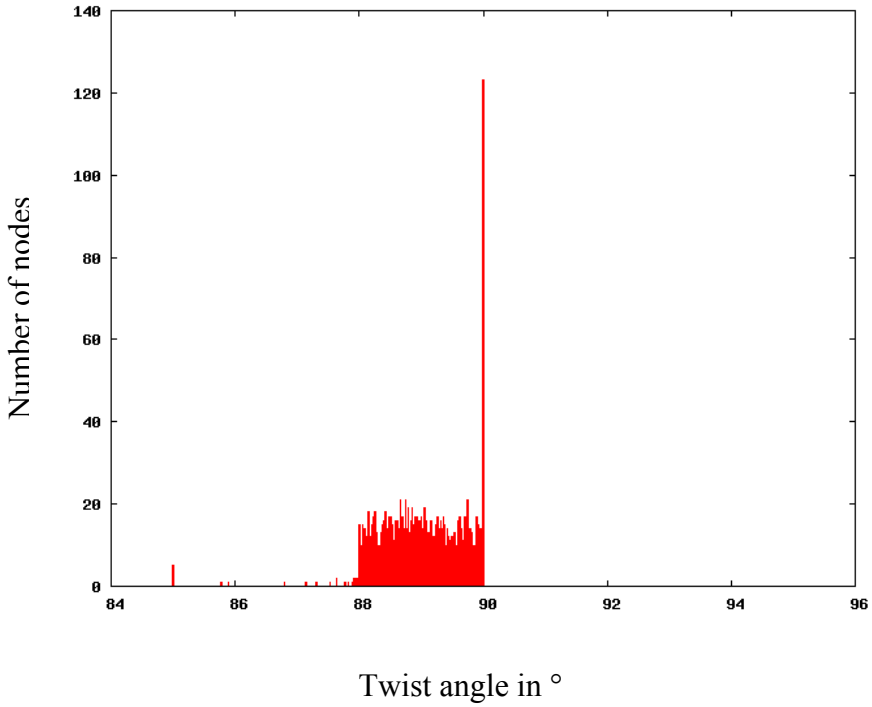

Figure 6.16b: Histogram shows the distribution of twist angle for all nodes after 5 iterations.

The iterations were continued until the error reached $\approx 10^{-8}$ and the results of the final iteration was considered as steady state. The results obtained for such steady-state situations are presented. After 261052 iterations ($t^* \approx 50$), **Figure 6.17** displays the eigen-boxes. It is noted that the orientation and the size of these parallelopipeds differ significantly from **Figure 6.13**. At the top and the bottom boundaries, the parallelopipeds were oriented in the vorticity direction, whereas away from the boundaries these parallelopipeds were oriented at flow-alignment angle. After 261052 iterations ($t^* \approx 50$), the tilt angle across the width of the geometry was measured at $x^* = 2.5$ and is shown in **Figure 6.18**. It is noted that at $y^* = 0$ and $y^* = 1$ the magnitude of the tilt angle was still zero due to strong anchoring at the boundaries (Dirichlet boundary condition). However, away from the boundaries, the tilt angle changed gradually to flow-alignment angle. The flow-alignment angle was found to be -64.1°, which matches with the analytical solution obtained using Eqn.71.

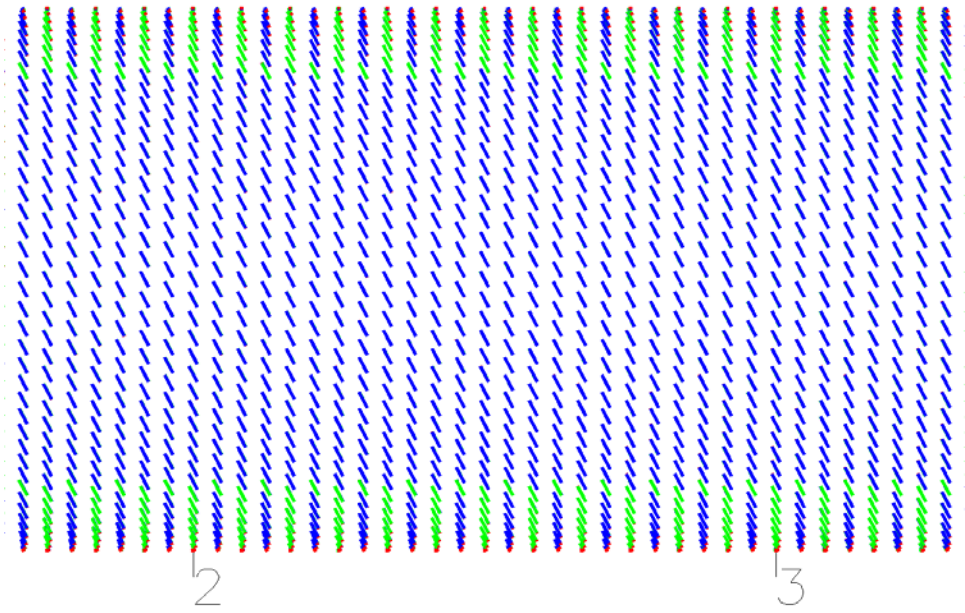

Figure 6.17: Parallelopipeds represent the orientation of the discs after 261052 iterations. The size and orientation of the parallelopipeds are related to eigenvalues and eigenvetors of tensor order parameter, Q.

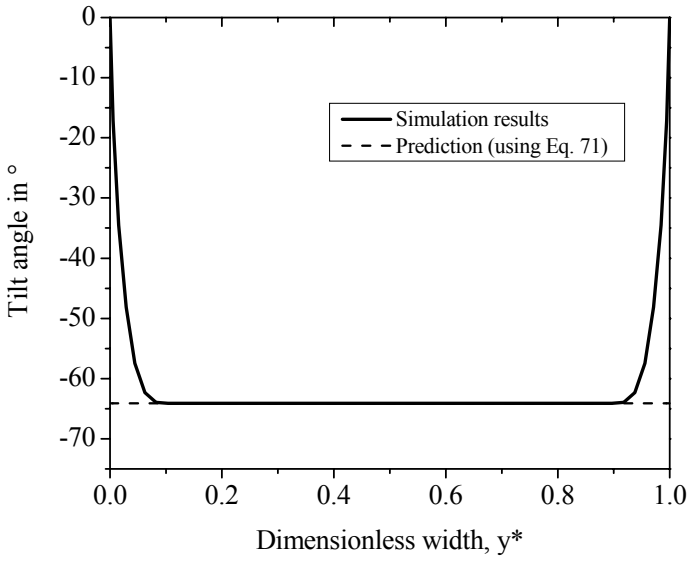

Figure 6.18: Change of tilt angle across the width at x* = 2.5 after 261052 iterations. Also shown the prediction obtained using Eqn. 71.

Figures 6.19a and **b** display the contour plot of tilt (θ) and twist angle (ϕ) over the entire computational domain after 261052 iterations. It is noted that, except near the boundaries, the tilt angle possesses a single value over the entire computation domain. Also, the values of twist angle changed to zero away from the boundaries. Histograms of tilt angle at all the nodes were obtained (**Figure 6.20**) and it was observed that tilt angle at most of the nodes was -64.1°. This signifies that, except near the boundaries, the directors were oriented at an angle -64.1°.

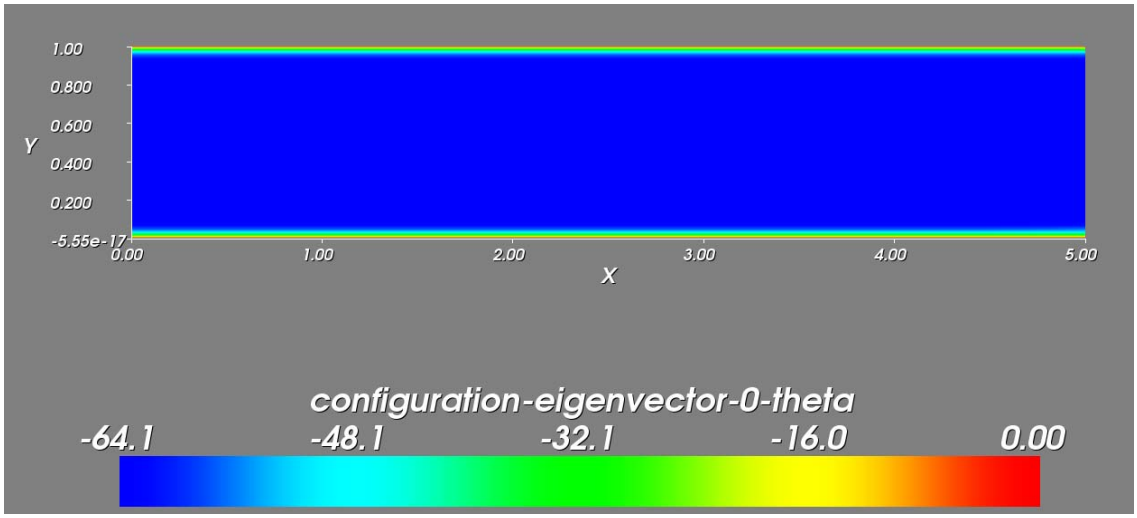

Figure 6.19a: Contour plot of tilt angle, θ, over the entire computational domain after 244973 iterations.

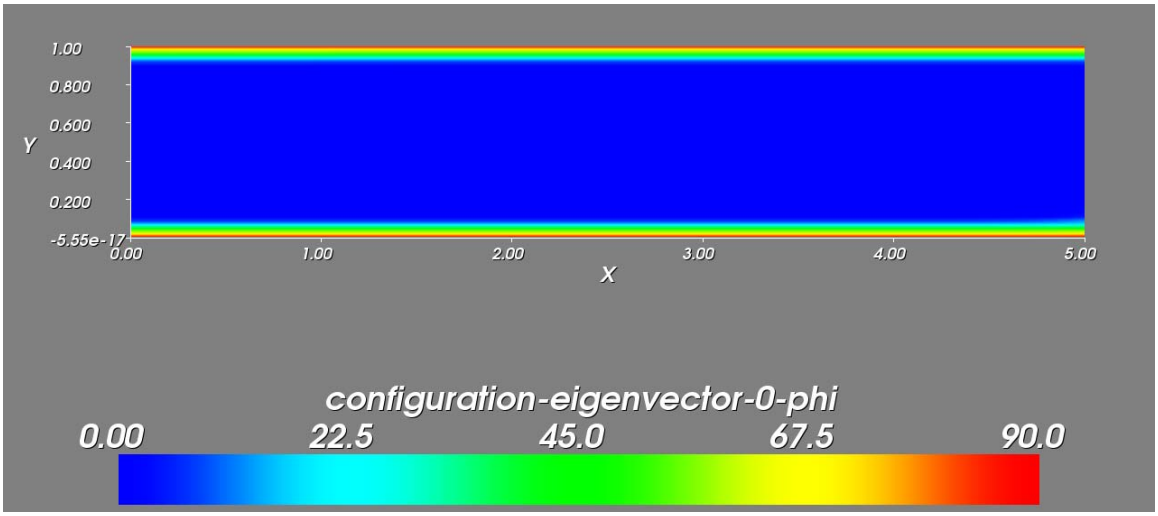

Figure 6.19b: Contour plot of twist angle, ϕ, over the entire computational domain after 244973 iterations.

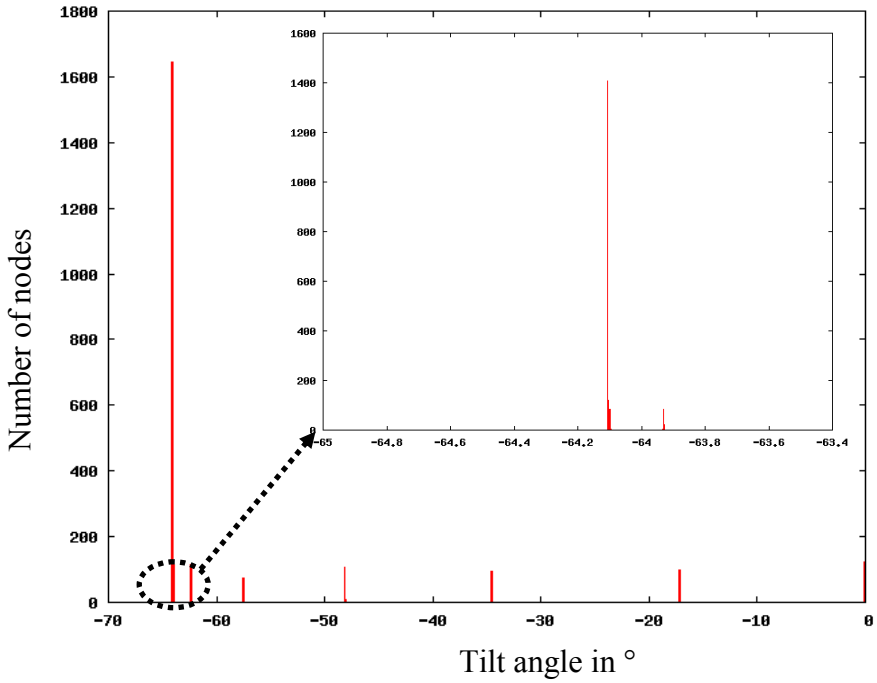

Figure 6.20: Histogram shows the distribution of tilt angle for all nodes after 261052 iterations. The inset shows the magnified view for the tilt angle -63° to -65.5°.

For both of the initial conditions, i.e., director along the flow direction and vorticity direction, at steady state, the orientation of discs was similar, i,e., the values of tilt angle at most of the nodes were -64.1°. During experimental studies too, different initial conditions led to similar flow-aligned structures. However, the experimentally observed flow-aligned structure was more complex that that observed here. Also, in these simulations the effect of microstructure on the flow was not considered (coupled situation), which will be reported in future studies [von Oehsen et al., 2006].

6.4 Conclusions

In this chapter simulation results were presented for simple-shear flow and decoupled conditions. The studies were performed for two different initial conditions that were also observed experimentally. At steady state, simulation results indicate that the bulk of the discs were found to be oriented at a flow-alignment angle. At the boundaries, the orientation was pre-determined by the strong anchoring, but the orientation gradually changed to a flow-aligned state. Although the simulation studies could not capture the complex flow-aligned structure observed experimentally, similarities in results were observed. This study establishes a frame work for future simulation of the flow dynamics of complex mesophase pitch system in multiscale-mulidimensional problems.

CHAPTER 7

CONCLUSIONS AND RECOMMENDATIONS

The primary goal of this research was to investigate the flow and microstructural behavior of a synthetic mesophase pitch (AR-HP) in rheometric and processing flow conditions. Simulations studies were also performed to establish a frame-work for modeling the flow-behavior of this complex material for different flow-situations. This chapter summarizes the findings of this study, and directions for future work are included.

7.1 Conclusions

- The steady shear viscosities obtained from a cone-plate rheometer during increasing rate-sweep experiments exhibited shear-thinning and plateau responses. At higher shear rates, as measured from capillary rheometers, the viscosity values remained almost constant. At very high shear rates, a small drop of viscosity was observed, likely caused by viscous heating. The two-region viscosity behavior observed here was similar to that reported in earlier studies for other grades of mesophase pitches. However, the slope of the shear-thinning region was calculated as -0.2, lower than -0.5 typically observed in liquid-crystalline polymers, likely caused by the different molecular constituents of AR-HP mesophase pitch. Also, the primary normal stress difference generated during rate-sweep experiments in cone-plate rheometer was found to be small (within instrument resolution), although the material exhibited non-Newtonian characteristics during increasing rate-sweep.
- During transient tests, local maxima and minima were observed in transient shear stress for various shear rates and temperatures tested. During flow reversal

experiments following steady flow at $1s^{-1}$, where the microstructure was already evolved, absence of maximum/minimum indicates that the nonmonotonic behavior during flow startup was directly related to the initial relaxed state of the discotic AR-HP mesophase pitch. After 1000 s of rest, the maximum/minimum reappeared during shearing, suggesting that such a rest period can lead to significant microstructural relaxation. The minimum in shear stress was not observed for previous grades of mesophase pitches. Also, the extent of local maximum was found to be lower than that reported in the previous studies.

- By developing an experimental protocol to preserve the rheological samples, microstructural features were obtained from the same mesophase pitch specimens as those used for rheological testing. The initial microstructure, examined in three orthogonal sections, was found to have a weak, but preferred, orientation of mesophase layers in the radial direction of the rheometer plate (due to initial squeezing flow). Microscopic observations indicate that the local maximum in the shear stress was likely caused by the yielding of the initial microstructure. With further shearing, the microstructure became flow-aligned and the microstructure became finer as the shear rate increased from 1 s^{-1} to 10 s^{-1}. The optical microscopy observations were also supported by the X-ray diffraction results. The steady-sheared flow-aligned structure was similar to the *fibrous* structure reported in literature, with the director of the layer-planes oriented in vorticity or ̲gradient̲ direction (or at an intermediate angle). Based on the microstructural evidence, a possible 3D schematic of overall microstructure was generated.
- Dynamic testing was performed under different preshearing/preoscillating conditions, which led to different initial textures. While the loss modulus (viscous component) remained largely unaffected by the texture, the elastic response of AR-HP mesophase pitch was found to be strongly dependent on the texture. Coarsest textures led to the highest elastic modulus, whereas finer and oriented structure that emerged from preshearing led to lower G' values. Also, finer but random microstructure resulted in more solid-like behavior that manifested in a broader G' plateau. The textured nature of AR-HP mesophase pitch contributed to

a lower slope of ~0.8 for the elastic modulus in the low-frequency terminal region as compared to ~2 observed for flexible chain polymers. Yielding of such textured structure resulted in maximum of shear stress during high-strain transient experiments. Relaxation of microstructure resulted in an increase of storage moduli. However, the relaxation time did not follow the scaling argument, $\tau \sim \eta a^2/K$. It is postulated that the relaxation process is influenced not only by the textural size, but also by layer-plane orientation.

- The flow-microstructural study was extended to processing flows that are typically observed in various stages of product development. In these tests, pitch was extruded through custom-made dies using a single-screw extruder. In the counterbore of these dies, pitch was subjected to wall shear rate of ~10 s^{-1}, and after the contraction flow, the wall shear rate increased to ~1000 s^{-1}. Microstructure of cross-sections of the counterbore and the capillary suggest that the size of microstructure/domains decreased towards the wall, where shear rate was highest. This observation is similar to that observed during controlled-shear experiments. Along with the microstructural size, variation of the orientation of the layer-planes was also observed in a given cross-section. In the counterbore, the orientation of the layer-plane was approximately tangential near the wall (~50 μm), which then changed to approximate radial away from the wall (until ~750 μm). Further away, where the shear-rate was very low, the orientation deviated significantly from radial. In the capillary, the radial orientation near the wall (~200 μm) deviated significantly away from the wall (beyond 200 μm). It is noted that the degree of orientation (more radial near the wall) increased within the capillary as compared to that observed in the counterbore. The increase of orientation was likely caused by the high shear rates and stresses experienced in the capillary and also an effect of extensional flow field that the material was subjected to during the flow through the contraction. As observed from the microstructure in the longitudinal mid-plane, both in the counterbore and in the capillary, the layer-planes nominally remained oriented in the flow-plane.
- Simulation studies were performed using constitutive equations developed by Rey and coworkers for discotic liquid-crystalline materials. The results were obtained

for simple shear-flow, corresponding with the experimental studies. The simulation studies were performed for two different initial conditions that somewhat resemble the experimental results. At steady-state, i.e., after the error reached a desired low level, the bulk of the discs were found to be oriented at a flow-aligned angle. At the boundaries, the orientation was predetermined by the strong-anchoring, but the orientation gradually changed to a flow-aligned one in the bulk. Although, the simulation studies could not capture the complex flow-aligned structure observed experimentally, similarities in results were observed. This study establishes a frame-work to simulate the flow-dynamics of complex mesophase pitch in multiscale-mulidimensional problems, using CAEFF computational facility and expertise.

7.2 Recommendations

The following are the proposed recommendations for future research based on the current study:

- Initial microstructure different than that studied in this study should be considered for transient shear experiments. Two different initial conditions may be considered:
  a) Random and very coarse microstructure that was obtained after 4500 s of relaxation of a pre-sheared sample at $10s^{-1}$ (Chapter 4),
  b) Random and very small microstructure that was obtained after oscillatory precondition, performed at very high frequency (300 rad/s) and high strain (≈60%).

  The shear-stress evolution as a function of initial microstructure will provide a better understanding of nonmonotonic transient shear stress behavior.
- In Chapter 3, the microstructural development during shearing was studied from offline X-ray measurement. This study may be extended, in collaboration with

Argonne National Laboratory, for online X-ray measurements such as those performed for some TLCPs. The online measurements along with the optical microscopy observation will provide a more fundamental understanding of the microstructural change during flow.

- A more sensitive normal force transducer without instrumental drift may be used to capture the primary normal stress difference at different shear-rates. In the recently available rheometers (Anton-Parr Physica series, Rheologica Nova) it is claimed that the much smaller normal force (lower limit ~0.1 gm_f) can be measured at higher temperature without drift.
- During certain steps of processing, pitch is subjected to extensional flow situations. However, the flow and microstructural characteristic of mesophase pitch in extensional flow-field is not widely studied in literature and may be studied in a future work. A Rheometrics extensional rheometer (RME) or an Extensional viscosity fixture (EVF) connected to ARES can be used to measure the extensional viscosities.
- In an ongoing effort, the simulation study in simple-shear flow conditions can be extended to the coupled-situation where the flow is affected by the microstructure. The study may also be extended to more complicated flow-geometries that are typically observed during various stages of processing.

APPENDICES

Appendix A

Experimental Methods

A1. Preparation of Pitch Pellets for Rheological Experiments

The low-shear and dynamic rheological experiments were performed on pelletized cylindrical pitch samples. The diameter and height of these vacuum-pelletized cylindrical samples were approximately 12.5 mm and 3 mm, respectively. The following procedure was used to make all pitch pellets. Please refer to **Figure A.1** when following this procedure.

1. Take a thoroughly cleaned mortar and place 5-10 grams of pitch sample into it (if the mortar is dirty, perform step #13 before continuing this procedure).
2. Use a clean pestle to grind the pitch into fine powder.
3. Place the clean pellet mold on its base. Place approximately 0.5 gm of ground pitch in the pellet mold (between the lower and upper metal discs).
4. Put the piston above the upper metal disc.
5. Connect the pellet mold to a vacuum pump.
6. Place the pellet mold with the base in a Carver™ press.
7. Start the vacuum pump and slowly increase the load to 10000 lb. Maintain the load for about 30 minutes with vacuum pump running.
8. Stop the vacuum pump and release the load.
9. Remove the pitch pellet from the mold by pushing it into a small, padded cup. The pitch pellet is now ready for testing.

10. Clean the metal discs, the piston and the every part of the pellet mold with paper towels soaked in acetone.

11. Repeat 3 to 10 to make another pellet.

12. Store the pellets in a bottle. Also store the excess pitch material.

13. Use a brass brush to clean the mortar and pestle. Perform the final cleaning using paper towels soaked in acetone.

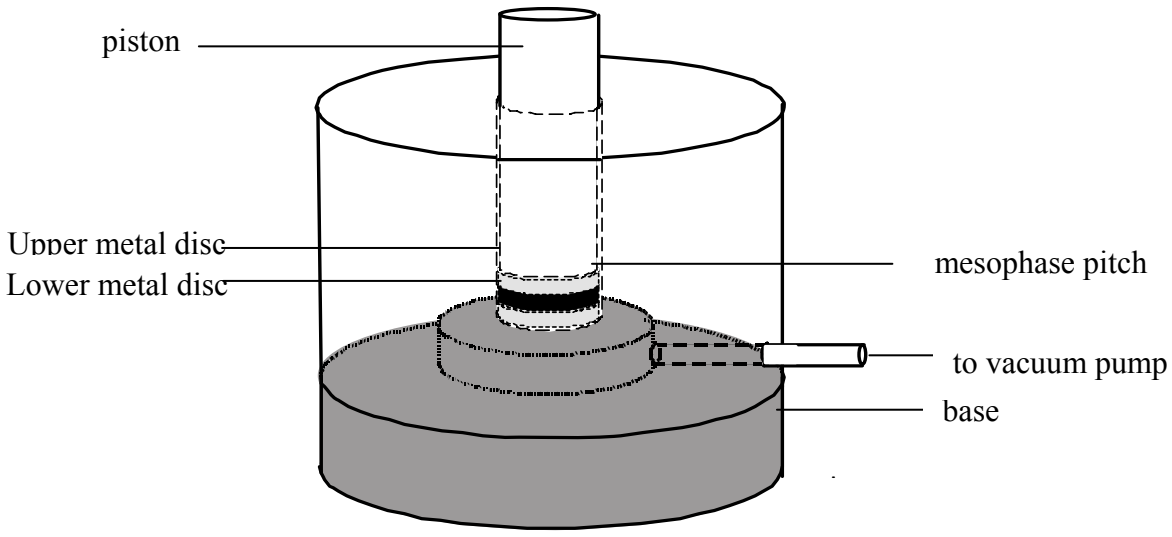

Figure A.1: Schematic of pellet mold used to make mesophase pitch pellets.

A2. Low Shear Rheometry – ARES Rotational Rheometer

A TA-Rheometrics "Advanced Rheometric Expansion System" (ARES) was used to study the low-shear rheological behavior of mesophase pitch. Most of the experiments were performed using a cone-plate fixture, displayed schematically in **Figure A.2**. ARES

is a controlled-strain instrument, in which the lower plate is rotated at a fixed angular velocity, Ω, to achieve a shear rate of $\dot{\gamma}$. The shear rate is constant at any position of the sample, provided the cone angle, ($\pi/2$- θ_0), is small. The torque and the normal force transducers are located above the cone. The measured torque, *T*, and the normal force, *F,* are used to calculate the shear stress and the primary normal stress difference (PNSD), respectively. Following relations can be used to calculate the shear rate, shear stress, and PNSD.

Shear rate: $\dot{\gamma} = -\dot{\gamma}_{\theta\phi} = \dfrac{\Omega}{\dfrac{\pi}{2} - \theta_0}$

Shear stress: $\tau_{12} = \tau_{\varphi\theta} = \dfrac{3T}{2\pi\pi^3}$

PNSD: $N_1 = \tau_{11} - \tau_{22} = \tau_{\varphi\varphi} - \tau_{\theta\theta} = -\dfrac{2F}{\pi R^2}$

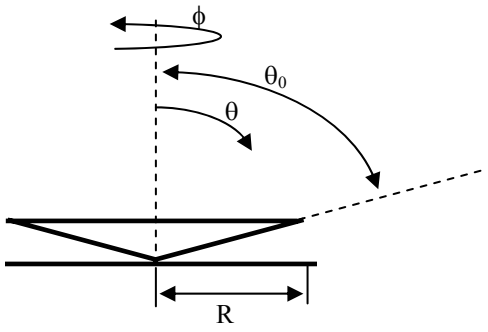

Figure A.2: Schematic of a cone and plate rheometer.

The ARES rheometer is equipped with a forced-convection oven (FCO), an air-bearing LS motor, and a force rebalance transducer (FRT). The instrument is connected to a computer and the experimental conditions can be monitored using TA Orchestrator®

software loaded on that computer. The air supported actuator enables the ARES to generate very small shear rates. The low range torque transducer can measure torque as small as 0.02 g.cm. In addition, the ARES rheometer is capable of measuring normal force in the range of 2-2000 gm_f. However, as shown in Chapter 2, at high operating temperatures, the normal force drifts with the time. Please refer to **Figures A.3** and **A.4** when following this procedure.

A2.1. Transient Shear Rheometry

The following procedure should be used to study the transient-shear behavior of mesophase pitch.

1. Before starting an experiment, ensure that sufficient air pressure is maintained to the instrument. The air pressure can be read from the gauges located to the right panel of the instrument, and if required, pressure may be adjusted to the recommended level by opening/closing of the respective valve.

2. To perform the experiments under inert environment, the instrument is connected to a nitrogen line. Open the nitrogen valve before starting an experiment.

3. Turn on the rheometer. The power switch is located on the backside (on your left side) of the instrument.

4. Open the TA Orchestrator® software on the computer connected to the instrument.

5. Click on "utilities→instrument online" in the TA Orchestrator® software to initiate the connection between the instrument and the software.

6. Insert the PRT (platinum resistance thermocouple) properly into the motor shaft with electrical connection side down. (See **Figure A.4a**).

7. Click on "utilities→service→instrument configuration" in the software. A new window named "Setup Instruments Options" will open. Set the "Temperature Loop Control" to "Sample/Tool Temp". Click Ok.

8. If the PRT is not installed properly, no temperature reading will be observed. In that case perform Step#6 again.

9. Click on "control→motor mode: steady" in the software.

10. Place the lower fixture (plate) on the motor shaft. Push the fixture slightly and tighten the knob (See **Figure A.4a**). Ensure that the fixture is aligned properly.

11. Place the upper fixture (cone) into the transducer shaft and tighten the transducer knob (See **Figure A.4b**). Ensure that the fixture is aligned properly. *(Caution: too much force can overload and damage the transducer.)*

12. Bring the fixtures closer by pressing the middle and down stage translation button simultaneously (see **Figure A.3**).

13. Leave a gap of approximately 5 mm between the fixtures and close the oven.

14. Click on "control→instrument control panel" in the software. A new window named "Instrument Control Panel" will open. Enter the experiment temperature and turn on the "Environmental Controller", and the "Motor Power". Click Ok.

15. Change the oven gas supply to nitrogen by turning a valve located at the right panel of the instrument (below the air gauges). Wait for the instrument to reach the set temperature.

16. Click on "utilities→service→transducer" in the software. A window named "Set Transducer Characteristics" will open. Select "Transducer 1" and then click Ok. If during the experiments the measured torque values reached the maximum of the transducer 1 (200 g.cm), transducer 2 will be selected automatically.

17. Click on "control→gap control panel" in the software. The "Gap/Instrument Control" window will open. Under "Gap Command", set the "Command Gap" to 0.056 mm (for 25 mm cone-plate fixture) or 0.051 mm (for 50 mm cone-plate fixture), and set the "Max Force" to 25 g. Click on the tab "zero fixture," and then wait for the gap to be zeroed. Once the zero point is detected, the top fixture will return to the Commanded Gap.

18. Under the "Torque (gm-cm)", click on the "Offset torque to zero" tab, to set the zero point of the torque transducer.

19. Under the "Force (gm)", click on the "Offset force to zero" tab, to set the zero point of the force transducer.

20. Raise the upper fixture (cone) by pressing the up and middle stage translation buttons simultaneously, until the gap reading is about 10 mm.

21. Open the oven door, and place the vacuum-pelletized sample in the center of the lower fixture (plate) with the help of tweezers. Then close the oven door.

22. Lower the top fixture by pressing the down and middle stage translation buttons simultaneously until the gap reading is approximately 5 mm. Then wait for thermal equilibrium to reach.

23. As explained in Chapter 2, we wait for different duration (as high as 150 minutes) at this stage so that sufficient devolatilization of the sample takes place.

24. In the "Gap/Instrument Control" window change the Commanded Gap to 2 mm. Then click on the "set gap" tab, and wait for the gap to reach to the Commanded Gap.

25. Repeat Step# 24 with a decreasing gap every time to a final gap of 0.056 mm (2mm→1 mm→ 0.5 mm→ 0.2 mm → 0.1 mm →0.056 mm). Click "Exit".

26. The experiment should not be started immediately because the normal force due to loading of the sample still persists in the fluid. As shown in Chapter 2, a wait time of approximately 5 minutes is sufficient for the normal force to decay almost to zero.

27. After the normal force value reach approximately zero, click on "control→edit/start test" in the software. A new window, "Edit/Start Instrument Test" will open. Enter the name of the experiment and select the folder in which the results to be saved. Enter experimental details in the "Test Notes" text box.

28. Click on "Sample Geometry →predefined geometries," and select the type of the geometry installed. Then click on the "edit geometry" tab. Another window will open, in which enter the appropriate dimensions of the fixture and click Ok.

29. Under "Test Setup", select "predefined test setups," and then choose the "Measurement Type: Transient". Select "Test setup: step rate test". Click the "Edit Test" tab.

30. A new window named "Step Rate Test" opens that allows the user to enter the temperature, the sampling mode, points per zone, the shear rates, the shearing time, and the direction of measurement. Enter the desired experimental conditions. Click Ok to close the window.

31. To start the test, on the "Edit/Start Instrument Test" window, click the "Begin Test" tab.

32. After the test is completed, the data will be saved automatically in the file and directory specified earlier.

After the transient experiments, the pitch samples were collected for microstructural analysis using a specially developed protocol. The technique is discussed in **section A.5**.

33. After sample collection, clean the surfaces of the fixtures using brass tools. Remove any remaining traces of pitch/superglue with paper towel soaked in acetone.

34. Repeat steps #10-33 to run additional transient tests.

After all experiments are completed

35. Change the oven gas supply to air from nitrogen. Close the nitrogen valve connecting to the instrument.

A2.2: Steady Shear Rheometry

The following procedure should be used to perform the steady-shear rheological experiments using the cone and plate geometry.

1. Follow steps 1 to 28 described in **section A2.1** of this chapter.

2. Under "Test Setup", select "predefined test setups," and then choose the "Measurement Type: Steady". Select "Test setup: Steady Rate Sweep Test". Click the tab "Edit Test" tab.

3. A new window named "Steady Rate Sweep Test" will open. Enter the temperature, the initial shear rate, the final shear rate, and the number of points per decade of interest. Choose "data collection mode: time based". Set the "Delay Before Measure" as 200 second and set the "Measurement Time" as 100 seconds. Choose one "Directions Per Measurement". Then click Ok to close the window.

4. To start the test, on the "Edit/Start Instrument Test" window, click "Begin Test" tab.

5. When the test is concluded, the data will be saved in the file and directory specified earlier. After the conclusion of steady-sheared experiments, the pitch samples were collected for microstructural analysis, using the technique described in **section A.5**.

6. After sample collection, clean the surfaces of the fixtures using brass tools. Remove any remaining traces of pitch/superglue with paper towel soaked in acetone.

7. Repeat steps 1-5 to conduct additional steady shear tests

8. When the testing is complete, follow step # 35 described in **section A2.1** of this chapter, to finish the experiments.

A2.3. Dynamic Oscillatory Rheometry

Dynamic experiments are performed to investigate the rheological characteristic. A small sinusoidal strain is applied by oscillating the plate with an angular velocity Ω such that $\Omega = \Omega_0 \cos(\varpi t)$, where ω is the frequency of oscillation in rad/s. The shear strain is, $\gamma = \frac{\Omega_0}{\varpi} \frac{\sin(\varpi t)}{\tan\left(\frac{\pi}{2} - \theta_0\right)}$. The ratio, $\frac{\Omega_0}{\varpi \tan\left(\frac{\pi}{2} - \theta_0\right)}$ is the strain amplitude, γ_0.

The measured shear stress, σ(t), is proportional to the amplitude of the applied strain γ_0 and itself varies sinusoidally with time. The shear stress can be represented as $\sigma(t) = \gamma_0 \left[G'(\varpi)\sin(\varpi t) + G''(\varpi)\cos(\varpi t)\right]$. The term, G', is in phase with the strain and is called the storage modulus. G" is out of phase with the strain, and is called the loss modulus. The ratio, G"/G', is called the loss tangent or tanδ. During dynamic experiments, ARES rheometer measures the torque and the phase angle difference, δ, which are then used to obtain the storage and loss moduli.

The following procedure was used to perform the dynamic experiments in ARES rheometer. Cone and plate geometry was used for most of the experiments. To check the geometric independence of the results, a limited set of experiments were performed using 25 mm parallel plate fixture.

To determine the linear viscoelastic region of mesophase pitch, strain-sweep experiments were performed initially.

1. Follow steps 1 to 28 described in **section A2.1** of this chapter. For parallel plate fixture select a final gap of 1 mm. Before bringing the cone and plate together, change the motor mode to "dynamic" by clicking "Control→Motor mode: dynamic" tab in the software.

2. Under "Test Setup", select "predefined test setups," and then choose the "Measurement Type: Dynamic". Select "Test setup: dynamic strain sweep test". Click on the "Edit Test" tab.

3. A new window named "Dynamic strain sweep test" opens that allows the user to enter the frequency, the temperature, the sweep mode, the initial strain, the final strain, and the number of points per decade of interest. Enter the desired experimental conditions. Click Ok.

4. To start the test, on the "Edit/Start Instrument Test" window, click the "Begin Test" tab.

5. After the test is completed, the data will be saved in the file and directory selected earlier.

6. Remove the fixtures carefully from the rheometer. Clean the surfaces of the fixtures using brass tools. Remove any remaining traces of pitch with paper towel soaked in acetone.

7. Repeat steps 1-6 to run additional strain-sweep tests.

Once the linear viscoelastic region is determined, a strain value within linear viscoelastic region was selected for frequency sweep experiments. The following procedure was followed to perform frequency-sweep experiments.

1. Follow step #1 of strain-sweep experiment procedure (discussed above)

2. Under "Test Setup", select "predefined test setups," and then choose the "Measurement Type: Dynamic". Select "Test setup: dynamic frequency sweep test (strain control)". Click the "Edit Test" tab.

3. A new window named "Dynamic frequency sweep test (strain control)" opens that allows the user to enter the percentage strain, the temperature, the sweep

mode, the initial frequency, the final frequency, and the number of points per decade of interest. Enter the desired experimental conditions. Click Ok.

4. To start the test, on the "Edit/Start Instrument Test" window, click the "Begin Test" tab.

5. When the test finishes, the data will be saved in the file and directory specified earlier.

8. Remove the fixtures carefully from the rheometer. Clean the surfaces of the fixtures using brass tools. Remove any remaining traces of pitch with paper towel soaked in acetone.

6. Repeat steps 1-6 to run additional frequency-sweep tests

To study the relaxation behavior of mesophase pitch sample, dynamic time-sweep experiments were performed as described in Chapter 4. In addition, as discussed in Chapter 4, high-strain time-sweep experiments were also performed to disrupt initial ordered microstructure. The following procedure was followed to perform the dynamic time-sweep experiments.

1. Follow step #1 of "strain-sweep test" procedure (discussed above).

2. Under "Test Setup", select "predefined test setups," and then choose the "Measurement Type: Dynamic". Select "Test setup: dynamic time sweep test". Click the "Edit Test" tab.

3. A new window named "Dynamic time sweep test" opens that allows the user to enter the frequency, the percentage strain, the temperature, the total time of experiment, and the time per measurement. Enter the desired experimental conditions. Click Ok.

4. To start the test, on the "Edit/Start Instrument Test" window, click the "Begin Test" tab.

5. When the test finishes, the data will be saved in the file and directory specified earlier.

After the time-sweep experiments the pitch samples were collected for microstructural analysis, using the technique described in **section A.5**.

6. After sample collection, clean the surfaces of the fixtures using brass tools. Remove any remaining traces of pitch/superglue with acetone and paper towel.

7. Repeat steps 1-5 to run additional tests

8. When the testing is complete, follow steps 33 to 35 described in **section A2.1** of this chapter, to clean and to shut down the rheometer.

During some of the experiments, liquid nitrogen cylinders, connected to a dewar was used as a source of nitrogen. For that case, instead of steps #2 and 15 of section A2.1, following procedure was followed.

1. Click on "control→instrument control panel" in software. Turn the Liquid Nitrogen Dewar on. Click Ok.

2. Open the valve on the liquid nitrogen tank.

3. Wait for about 20 minutes to fill the dewar. On the "instrument control panel" window in the software, switch the "Oven Pressure Source" from "gas" to "LN2". Click Ok.

After completion of tests, following steps were conducted to switch off the liquid nitrogen dewar.

1. Click on "control→instrument control panel" in the software. On the "instrument control panel window" switch the "Oven pressure Source" from "LN2" to "gas". Turn the "Liquid Nitrogen Dewar" off. Click Ok.

2. Using insulated gloves to close the valve on the liquid nitrogen cylinder.

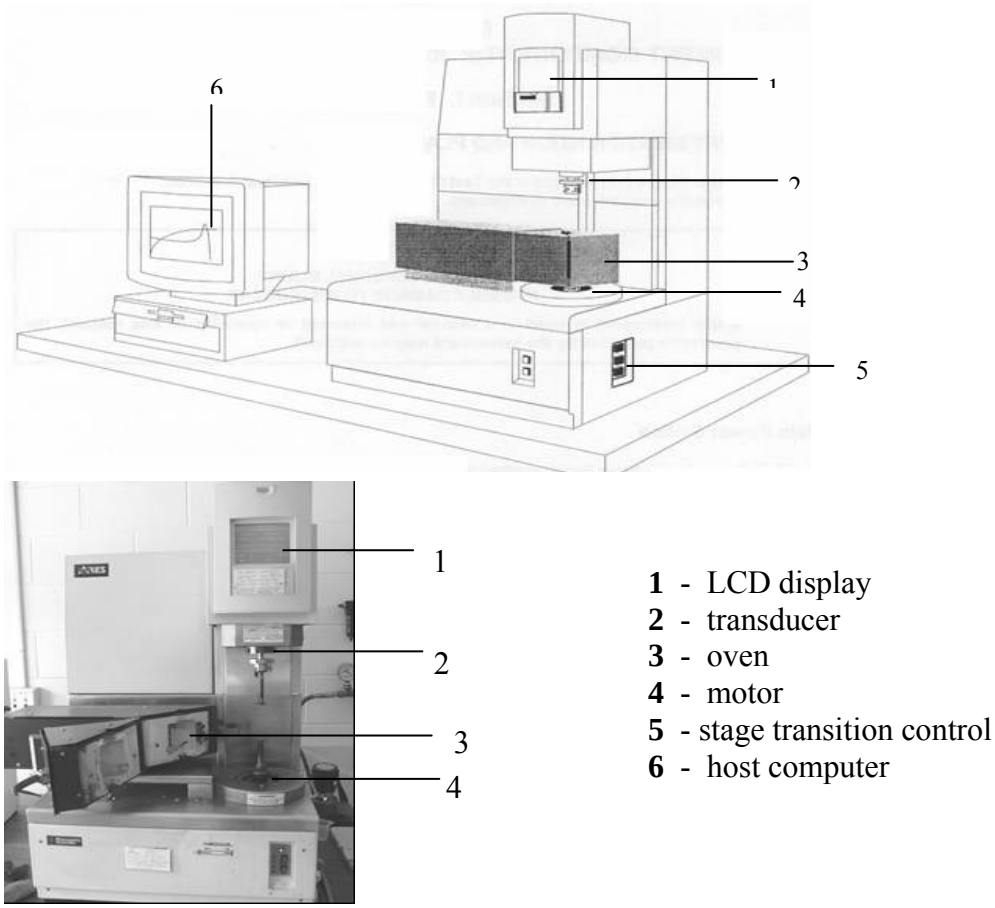

Figure A.3 Schematic and picture of the ARES controlled-strain rotational rheometer.

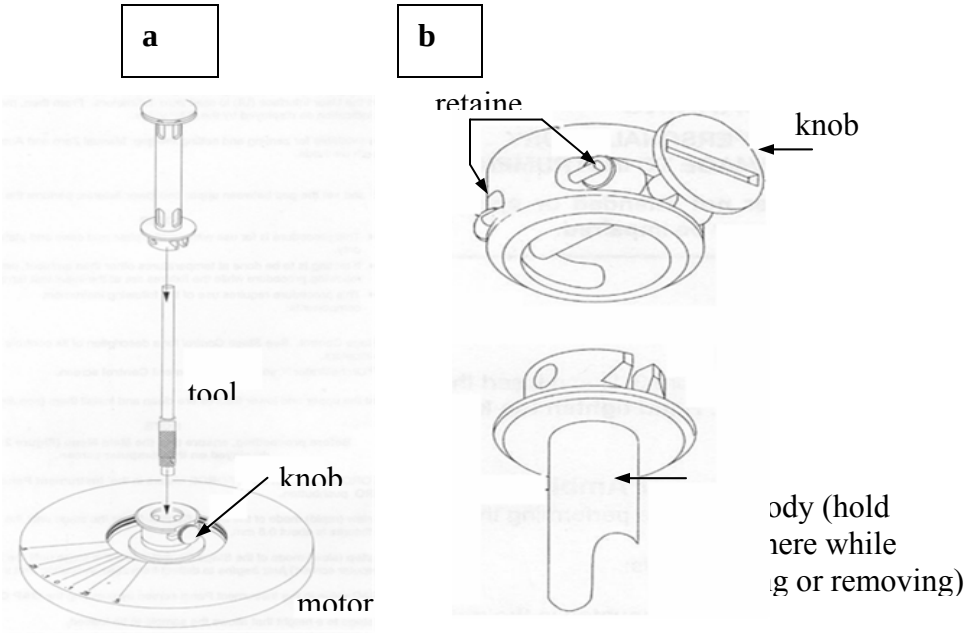

Figure A.4 (a) Tool PRT and lower fixture installation, (b) upper fixture installation

A4. Preparation of epoxy blocks

After rheological experiments, samples were collected and embedded in the epoxy blocks for microstructural study. Following procedure was used to prepare the epoxy blocks.

1. Apply Buehler release agent inside of a 32 mm diameter plastic mounting cup.
2. Pour approximately 50 ml in a disposable plastic glass of Castolite resin and add 10 drops of hardener (Leco Corporation) into it. Stir the mixture slowly until it is homogeneous.
3. Fill approximately three fourth of the mounting cup with the resin.
4. Place the cup in an oven and maintain the oven temperature at about 70°C for 12 hours.
5. Remove the cup from the oven. After the cup reached room temperature, remove the epoxy block. At this point the epoxy should be hard.

A5. Sample collection technique for microstructural analysis

Pitch samples with different rheological histories were collected for microstructural analysis. If the cone and plates are separated after rheological experiments not using any special protocol, the molten sample will be subjected to extensional flow. As a result, as shown in **Figure A.5a** the microstructure will be disrupted. To collect undisrupted samples, a special protocol was developed and is outlined below.

1. At the end of rheological tests, immediately click on "control→hold" in the software. This will enable the auto-tension mode, which maintains a constant gap in between cone and plate of the rheometer.
2. Open the oven and allow the sample to cool. Once the sample temperature reaches below the softening point of the pitch, click on the "control→hold" tab again.
3. Raise the upper fixture slightly by pressing the up and middle stage translational button. Apply a light tap on the bottom plate to separate the upper and lower fixture. (*caution*: excessive force can damage the normal force transducer).

4. Allow the fixtures to cool to room temperature.
5. Once cold, carefully remove the top fixture (cone) by loosening the knob.
6. Remove the lower fixture (plate) by loosening the knob.

This procedure enabled us to collect undisrupted samples from rheometer. Picture of one such undisrupted sample is shown in **Figure A.5b**.

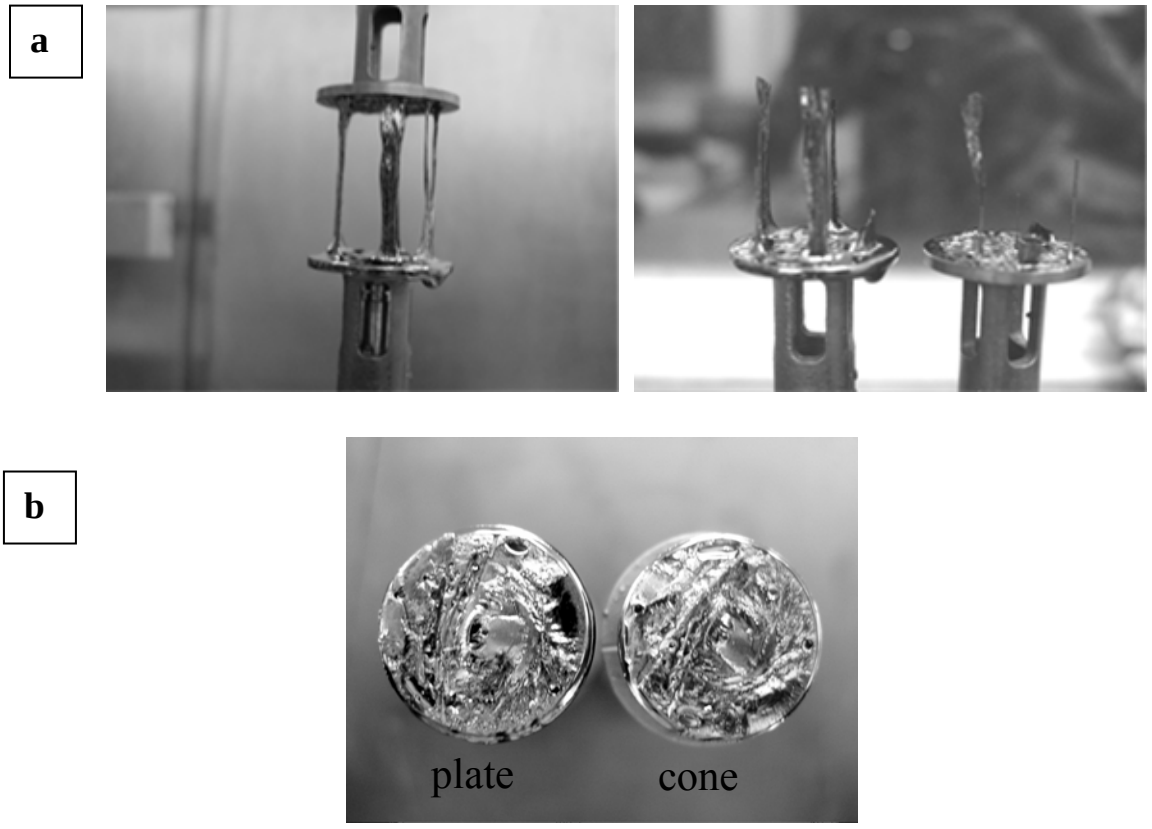

Figure A.5: Photograph of mesophase pitch sample after the cone and plate were separated: (a) using no special protocol, (b) using a special protocol (auto-tension mode).

A6. Sample preparation for microstructural analysis

After removing the lower fixture (plate) from the rheometer, sheared pitch was transferred on a solid epoxy block for microstructural analysis. The procedure is outlined

below, and this technique enables us to study the microstructure of the sample in the flow-vorticity plane. Please refer to Figure **A.6** when following this procedure.

1. Apply Buehler release agent inside of a 32 mm diameter plastic mounting cup.

2. After removing the lower fixture (lower plate) from the rheometer, flip the fixture and place it on the epoxy block such that the pitch is submerged in super glue.

3. Carefully place the epoxy block and the fixture together in an oven. Maintain the oven temperature at about 70°C. Keep the sample inside the oven for approximately 1hour 30 minutes.

4. At this stage the fixture and epoxy block should be joined. Remove the fixture and the block together and allow it to cool to the room temperature.

5. Once cold, separate the epoxy block from the fixture by applying force on the block. The pitch sample should be transferred onto the epoxy block. The sample was then polished for microstructural analysis.

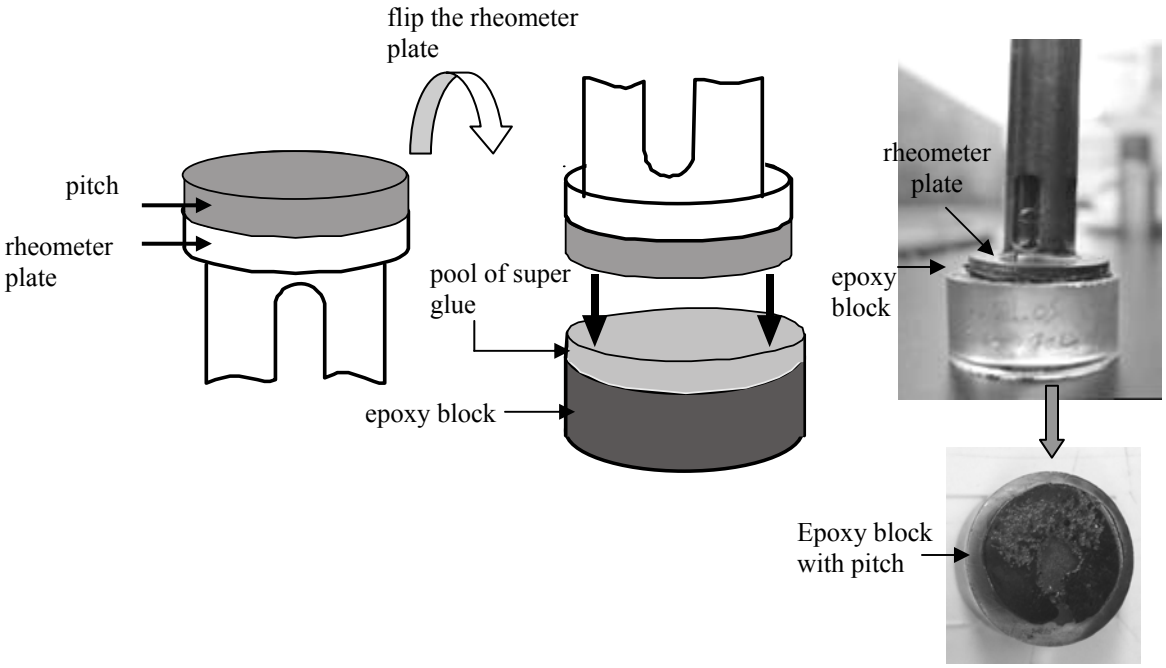

Figure A.6: Schematic and photographs of sample collection technique from rheometer plate onto an epoxy block

For microstructural in other two orthogonal planes, (i.e., flow-gradient plane, and flow-vorticity plane) and X-ray analysis, samples were also collected on Duct tape. Please refer to **Figure A.7** when following this procedure.

1. Cut about 2 inches of Duct tape from its roll.
2. Place it on the sample (rheometer plate) with sticky side touching the sample.
3. Press the tape gently so that it sticks to the surface of the sample.
4. Once the tape sticks to the sample, pull it from one corner.
5. If significant amount of sample is left on the rheometer plate, repeat steps 1 to 4.

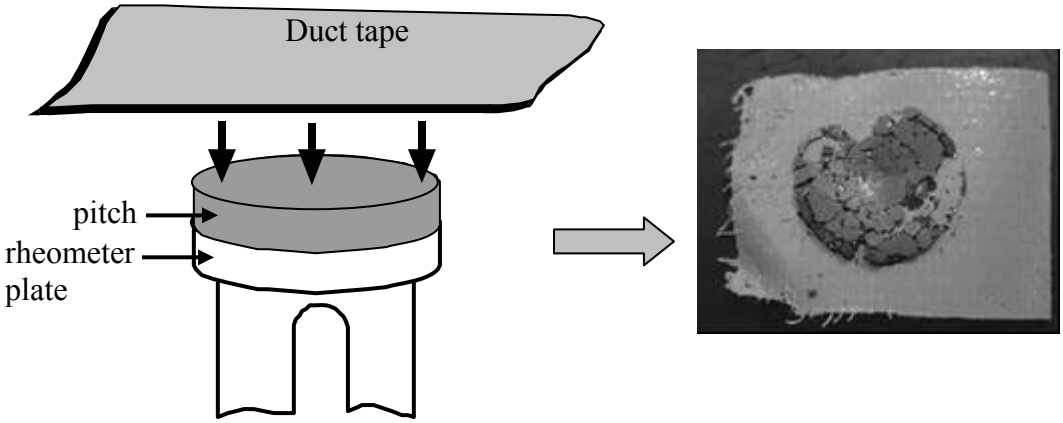

Figure A.7: Schematic and photograph of sample collection technique from rheometer plate onto a duct tape

For microstructural analysis of flow-gradient and gradient -vorticity planes, samples were embedded in epoxy using following procedure. Please refer to **Figure A.8** when following this procedure.

1. Pour Super Glue (Loclite®) on the flat side of a solid epoxy block (prepared earlier). Maintain a pool of liquid.

2. Using a hand-saw cut the previously prepared solid epoxy blocks through the cross-section into small discs that can be used as supports.

3. Place a small piece of epoxy block on the bottom plate of the mounting cup.

4. Remove a small piece of sample from the Duck tape using tweezers. Stick it on the epoxy block by Superglue. The section/plane of interest should be touching the bottom plate of the mounting cup.

5. Let the superglue dry for 15 minutes.

6. Pour approximately 50 ml of Castolite resin in a disposable plastic glass and add 10 drops of hardener (Leco Corporation) into it. Stir the mixture slowly until it is homogeneous.

7. Pour a small amount of resin into the plastic mounting cup. Fill approximately three fourth of the cup. The epoxy block supporting the sample should be covered with resin.

8. Place the cup in an oven and maintain the oven temperature at about 70°C for 12 hours.

9. Remove the cups from the oven. After the cup reached room temperature, remove the epoxy block embedded with the samples. The block should be hard and ready for polishing.

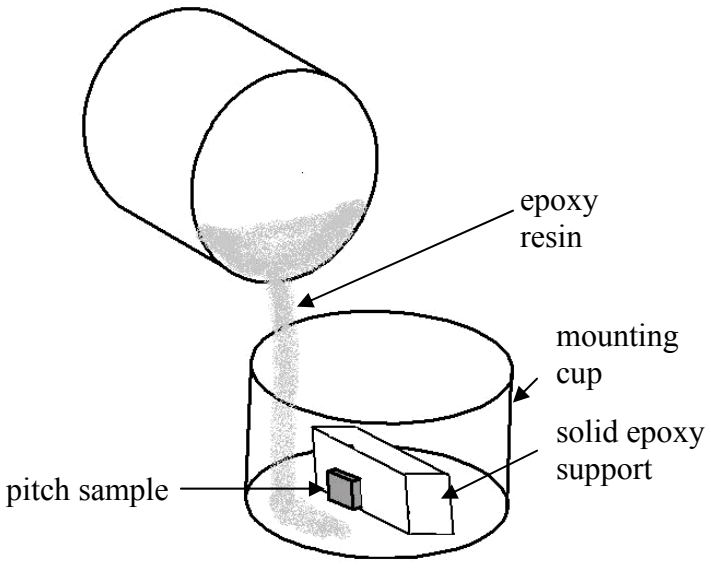

Figure A.8: Mounting of sample in epoxy for microstructural analysis

A7 Sample Polishing for Optical Microscopy

Samples embedded in the epoxy were polished using Ecomet 2 polisher-grinder and Automet 2 power head. The polishing was performed in several steps, each with increasing levels of fineness. After final polishing, microstructure was studied using optical microscopy. The following procedure was used to polish the pitch samples.

1. Switch-on the Ecomet 2 polisher-grinder and Automet 2 power head.

2. Place the epoxy embedded samples in a sample holder with the pitch sample side down (generally 3 samples are placed at the same time). Ensure that the samples are properly labeled. Fix the sample holder in the Automet 2 power head. Set the force and the time (cycle-time) as 12 lb and 3 minutes, respectively.

3. If the pitch surface is not exposed, place a 320 grit Buehler Carbimet SiC paper on the wheel of the Ecomet 2 polisher-grinder. Move the water distributor over the grit paper so that paper surface is completely covered with water.

4. Set the motor speed to 120 rpm and start the Ecomet 2 motor. Bring the sample in contact with the grid paper by pressing two green switches together. These switches are located at the left and right hand sides of the Automet 2.

5. Grind the samples until the pitch surface is exposed.

6. Detach the sample holder from the Automet 2 power head and wash the samples under running water.

7. If the pitch surface is already exposed, instead of 320-grit paper, start with 600-grit Buehler Carbimet SiC paper. Follow steps 2 to 6, however, change the polishing time to 30 seconds.

8. Remove the 600-grit paper and replace it with 1200-grit Buehler Carbimet SiC paper. After polishing for 10 minutes, wash the sample under running water. At this point, the pitch surface should be almost scratch-free. For few cases, finer polishing was also performed to get a better finish of the surface.

9. For finer polishing, remove the 1200-grit paper, and replace it with a white label paper (Allied High Tech Products, Inc). This paper is available in adhesive back and to reuse stick it on a 1200-grit SiC paper. Apply distilled water on the surface of the paper. Spray 1μm diamond suspension on the white label paper and polish the samples for 1 minute. Apply distilled water intermittently. After polishing, wash the sample surfaces with distilled water.

10. Remove the white label paper and replace it with Chem-Pol black polishing cloth (Allied High Tech Products, Inc). This cloth also has adhesive back and similar to the white label paper stick it on a 1200-grit paper. Apply distilled water on the surface of the paper. Spray 0.05 μm alumina suspension on the cloth intermittently during polishing. Continue the polishing for 2 minutes. After polishing, wash the sample surface with distilled water.

11. Inspite of cleaning with distilled water, alumina particles may remain on the surface. To remove the remaining alumina particles, soap solution must be used. Fill a plastic glass with distilled water and mix 10-15 drops of concentrated Micro Organic Soap (Allied High Tech Products, Inc). Position the sample inside the soap solution and then gently rub the surface for 2 minutes with cotton swab.

12. Take the sample out of the soap solution and dry the surface by blowing canned compressed canned air (Miller-Stephenson Allied from High Tech Products, Inc). Now the sample is ready for microstructural analysis.

The polishing times mentioned above are approximate. Depending on the sample condition, slightly different polishing time may be needed.

A8. Optical Microscopy

Polished pitch samples were studied using an Olympus BX60 microscope by cross-polarized light and first order red plate. A limited set of analyses were repeated using Aus Jena Jenapol Interphako microscope. The color calibration was performed using a standard sample described in Chapter 3.

Following procedure was used to study the microstructure of pitch samples. Refer to **Figure A.9** when following this procedure.

1. Turn on the light source of the microscope. Select the “reflected light” condition. Slowly increase the light intensity level to maximum.

2. As shown in **Figure A.9a**, place the analyzer, U-ANT on the top-slot of the “wavelength retarder plate holder” (U-TAD). Slide the first order red plate, U-TP530 into the “wavelength retarder plate holder” (shown by green arrow). Insert

the holder in a slot, above the eyepieces, as shown in **Figure A.9a**. Make sure that the other analyzer, U-AN360, is taken out of its slot.

3. Insert the polarizer (U-PO), with the engraving facing forward, into the "Polarizer slider insertion slot".

4. Place a ring of soft clay on a microscope slide and place the polished sample on top. Press the sample using the sample flattener. During pressing, the soft clay will deform and a horizontal surface will be obtained.

5. Chose an objective magnification of 5X.

6. Place the sample on the rotating microscope stage. Bring the sample in focus by adjusting the focusing knobs. *Caution: While watching the stage externally, it should be raised such that the sample surface is close to the lens but not touching it. The coarse focus knob should then be turned so that the sample moves away from the lens and the surface comes into coarse focus. The fine focus knob may next be used for clearer focus.*

7. Translate and rotate the sample to a desired position. Refocus if necessary.

8. If the magnification is not satisfactory, change the objective to increasing levels of magnification (10X, 20X, 50X) and refocus as needed.

9. At this stage the photographs of the sample need to be captured for further analysis. Connect the camera adapter (MM3XS, Martin Microscope Company) to the Sony Cyber-shot DSC-S70 camera. Remove the right eyepiece of the microscope and insert the camera adapter in its place (please see **Figure A.9b**)

10. Press the camera zoom switch to its maximum. This ensures that the pictures will be independent of camera magnification. Turn the camera flash off by pressing the flash on/off button.

11. Turn on the timer switch from the camera menu. This ensures that the captured pictures will be unaffected by the hand vibration. Press the shutter switch and wait for approximately 10 seconds for the camera to capture a picture.

12. Remove the memory stick from the camera and download the pictures on a computer using memory card reader. Now these pictures are ready for further processing.

13. Remove the camera with the adapter from the microscope and replace the right eyepiece. If required rotate the sample or focus at a different location of the sample. Follow the steps 9 to 12 for photographs.

14. Once finished, reduce the light intensity to minimum and turn off the microscope. Detach the camera from the adapter.

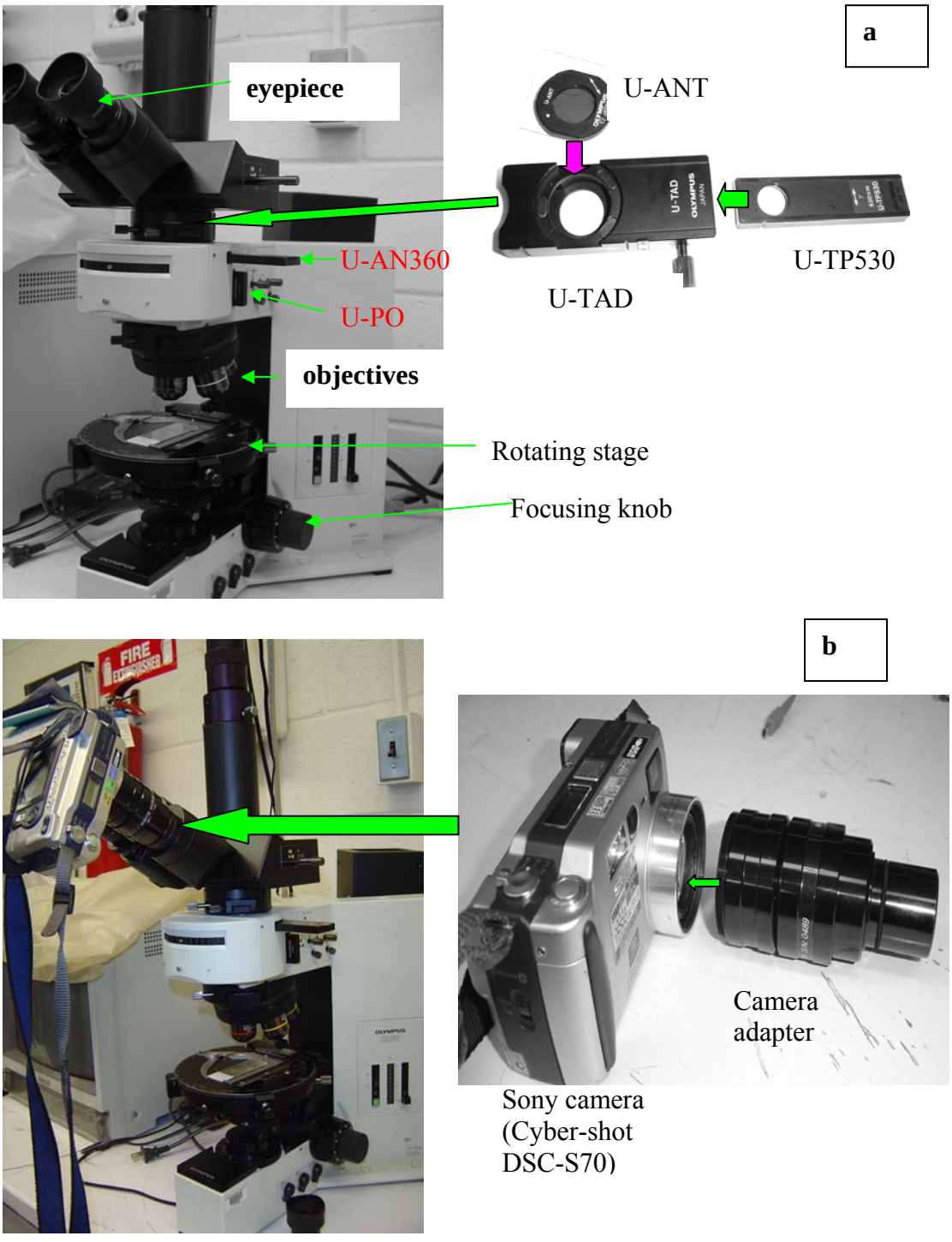

Figure A.9: (a) Arrangement of Olympus BX-60 microscope; (b) Camera arrangement for photography

A.9 Microstructural analysis

The pictures from the digital camera may be color enhanced using Photoshop and the microstructural analysis can be performed using Image Pro software. The procedure is described below.

1. Open Adobe Photoshop software. Open the picture that is to be studied. If the picture contains the regions other than pitch, use the "Polygonal lasso tool" to select the desired area. Try to avoid the voids/dark or shiny areas. One of such pictures with a selected (pitch) region is shown in **Figure A.10**.

2. Click on "Image→Adjust → Auto levels". Photoshop will enhance the picture automatically. As shown in **Figure A.10** the selected pitch region of **Figure A.10** became brighter and significant color enhancement occurred.

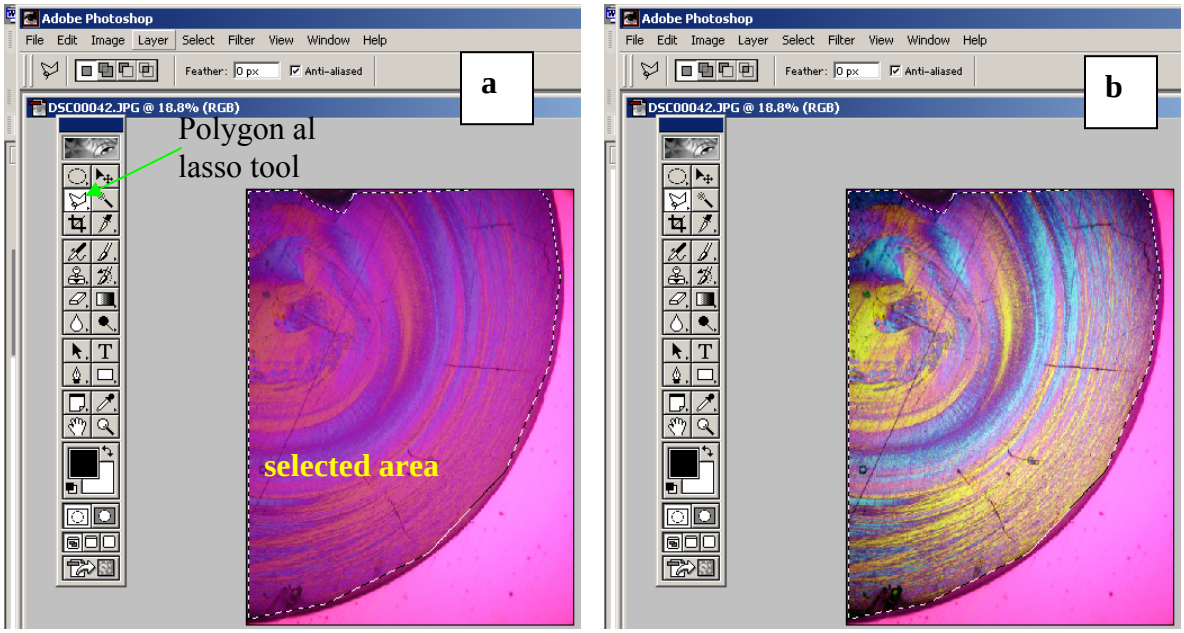

Figure A.10: (a) screenshot of the selected area of a pitch sample using polygonal lasso tool; (b) screenshot of the same region after picture enhancement.

3. Save the picture in a separate file (in *.jpg format). Select the highest image quality. The picture is now ready for analysis.

4. Start ImagePro Plus® software and open the picture to be studied.

5. Click on "Measure→ spatial calibration" from the top menu. Select the "Name" same as the objectives being used. (the calibration needs to be checked occasionally)

6. To measure the dimension (length or width) of a particular feature of the picture click on "Measure→Measurement". A new window will open, on which select "Create click and drag line feature" icon. Draw a line that covers the dimensions to be measured. Measure the dimensions of the entities. Once finished, click on the "Input/Output" tab. Under Export data, check (select) "Data to output: Measurements" and "Output data to: File". Then click on "Export Now". Paste these data in Excel.

7. To measure the area percentage of a particular color in a given picture (or in a region), select the region of interest using "irregular AOI" tool. This tool can be accessed by clicking an icon at the top menu. Selected region of a particular micrograph is shown in **Figure A.11**.

8. Click on "Measure→ Count/size" from top menu. A new window will open. Click on the "manual" tab. Then click on the "Select Colors" tab. Another window will open.

9. Click on the "Color Cube based" tab. Now use the "Eyedropper tool" (click on the icon) and click on a region of the picture with the particular color of interest. The software will select all the pixels with same color. Perform this operation multiple times at the different places of the picture to select all the regions of similar color. The selected regions appear as red (red color can be changed to any user defined color). As shown in **Figure A.11**, the yellow regions of **Figure A.11a** are selected and those selected regions appear red. Close the window once the areas are selected.

10. Now click on "Measure→ Select Measurement" on "Count/size" window. Another window will open. From the left hand list, select "Area" and "Per-Area" (ratio of area of object to total area of image or object). Click Ok.

11. Click on "Count" on "Count/size window. It will automatically calculate the area and percentage area (per-area) of the selected regions. To export the data click on "File→Data to Clipboard".

12. Import these data in Excel and perform further analysis.

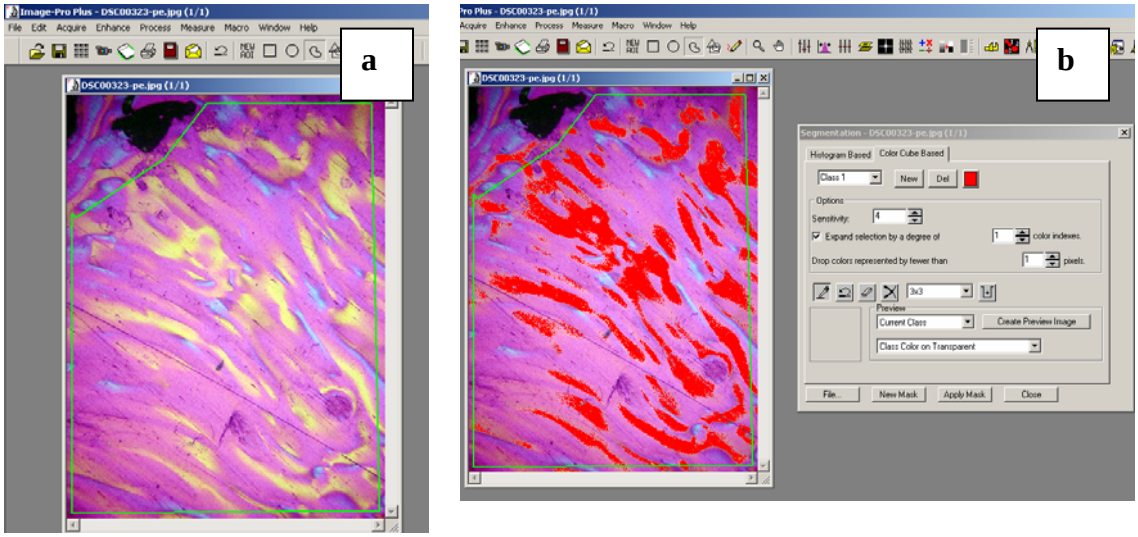

Figure A.11: (a) screenshot of a selected area of the sample using irregular AOI tool; (b) screenshot of the same picture with yellow-regions selected.

A10. Steady High shear Rheometry – ACER Capillary Rheometer

The high shear rate (300-10,000 s^{-1}) viscosity was measured using a Rheometrics ACER capillary rheometer. Capillaries with a diameter of 1 mm and of different lengths (different L/D ratios) were used. The wall shear rate for a capillary rheometer is, $\dot{\gamma} = \frac{4v_p R_p^{\ 2}}{R_c^3}$, where, v_p is the piston velocity, R_p is the radius of the piston and R_c is the radius of the capillary. For a given speed of the piston, the pressure drop, ΔP, across the capillary was measured. The wall shear stress (τ_w) is related to the pressure drop by the following equation.

$$\tau_w = \frac{\Delta P R_c}{2L_c}$$, where L_c is the length of the capillary.

The apparent viscosity (μ_a) can be estimated as $\frac{\tau_w}{\dot{\gamma}}$

The following procedure was used to measure the high-shear behavior of mesophase pitch.

1. Open the ACER software on the computer. Click on "run→online" in the ACER software to begin the communications between the computer and the rheometer.

2. Start with a clean capillary die of desired L/D ratio. Click on "setup→hardware→geometry" in the software. A new window will open. Check "capillary" and enter the length, diameter, and entry half-angle of the capillary in that window.

3. Insert the die into the bottom of the barrel and secure it in place with the die holder. Tighten the die holder with hand.

4. Select either a 20 or 70 MPa pressure transducer and connect it to the instrument control panel using the specific cable.

5. Click on "setup→hardware→transducers" in the software. Enter the maximum range of the installed pressure transducer and click Ok.

6. Close the ACER rheometer safety door. Click on "setup→control panel" in the software. A new window will open. Under Length Calibration, click on "home ram" and then "start" in the control panel window of the ACER software. This will move the piston holder to the topmost position and subsequently sets the piston position to zero.

7. On the same window, mentioned in step#6, input the desired temperatures for the three zones of the barrel. Set the same temperatures for the three zones. Click "set" and then "on" to turn on the heaters. Activate the upper and lower exhaust by checking the respective boxes.

8. Wait for the barrel to reach the set temperatures.

9. Transducer calibration is to be performed next. On the same window mentioned in step#6, under Transducer Calibration, check the "P1" tab and then click on "tare". After pressure reading in the main window became zero, click on "cal in". The pressure reading should reach 80% of the maximum transducer value. Close the control panel window to finish the calibration procedure.

10. Open the ACER rheometer safety door. Put a small amount of the sample into the barrel and pack it down with the tamping rod. Repeat this process until the barrel is filled just below the conical section of the barrel mouth.

11. Place the piston into the piston holder and tighten the locking bolt by hand.

12. Lower the piston into the mouth of the barrel by pressing the “down” tab on the manual control box.

13. Once the piston enters the barrel, move it down slowly (by half pressing the down button in manual control box) and monitor the force value. A slight positive value of force ensures that the piston is in contact with the sample. At this point, stop the movement of the piston.

14. The mesophase pitch sample is loaded at a temperature close to its softening point. However, the experiments are performed at higher temperatures. Loading the sample at lower temperature prevents the bloating of the sample during sample loading. Once the sample is loaded, increase the set temperature to the desired values. Wait for the temperatures to reach the set point. During the temperature increase, some material will ooze out of the barrel, which is unavoidable.

15. Click on “run→start” in the software. A new window will open. Under Sweep Type, select “rate” and then click the box “edit”.

16. A new window will open. Enter the individual shear rates to be tested and then click Ok.

17. In the same window mentioned in step#15, under Steady State, select the manual mode. This will let the user decide when steady state occurs and to proceed to the next rate.

18. Click on “start,” and the piston will move down at a speed corresponding to the first specified shear rate. The stress values as a function of time will be displayed on computer. Once the stress values reach a steady state, click on “start”. The piston will now move at a speed corresponding to the next specified rate. Continue this process until the barrel is empty.

19. After the test is completed, save the data by clicking on “file→save” in the software.

20. Return the piston to the top position by pressing the “up” button on the manual control box.

21. Remove the hot piston from the piston holder carefully. Allow the piston to cool down to the room temperature. Clean the piston surface with a brass brush and then with paper towels soaked in acetone.

22. Unscrew the die holder using the tool provided with the rheometer. Push the die out of the barrel by the tamping rod. Put the die holder and the die into a fluidized sand bath for cleaning.

23. Remove the pressure transducer and allow it to cool. Once cool, clean it carefully using paper towels soaked in acetone.

24. Click on "setup→control pane" in the software. Turn the heaters off by clicking the box tab "off". Allow the rheometer to cool.

25. Clean the barrel thoroughly by pushing paper towels through the barrel. Also use paper towels soaked in acetone. If the barrel still not clean, purge it with molten polystyrene. Follow the steps mentioned above and use a high shear rate.

A11. Wide-angle X-ray Diffraction

As discussed in Chapter 3, wide angle X-ray diffraction technique was used to investigate the microstructure of mesophase pitch. The fundamental of X-ray diffraction phenomenon and its use for the microstructural characterization of carbon fibers/materials is summarized below. As discussed earlier, mesophase pitch consists of poly-aromatic compounds and due to liquid crystalline nature some orientational order is present. Although the stacking of the mesophase molecules (mesogens) is not as regular as graphite planes in carbon fibers, some similarities exist. The planer aromatic molecules of mesophase pitch form a pseudo-hexagonal packing that results in several diffraction patterns.

X-rays are electromagnetic radiation with characteristic wavelength of ~1 Å, which is similar to the spacing of atoms in many periodic structures. If the wave length of the scattered wave is same as that of the incident one, it is called elastic scattering. Whereas, if the wave-length of scattered radiation changes, it is called inelastic scattering. In addition to scattering, X-rays can also be absorbed by the sample. Of these phenomena, elastic scattering can be used to probe the structural arrangements of atoms within the sample.

If the sample contains some kind of regular structure, the scattered x-rays in certain directions interfere constructively and diffraction patterns are obtained. For constructive interference, the diffracted waves must be in phase. X-ray diffraction phenomenon from two parallel planes of atoms is described next (**Figure A.12**). The distance between two planes is d and the incident rays make an angle θ to the planes. Diffracted X-rays from each plane (also called as reflecting plane) of atoms will be in

phase for an angle θ such that the additional distance ($2.d.sin\theta$) traveled by the different waves (*eg*. wave 2) is equal to an integer number of wavelengths, also known as Bragg's law,

$$2.d.sin\theta = n.\lambda$$

This condition was proposed by Bragg and known as.

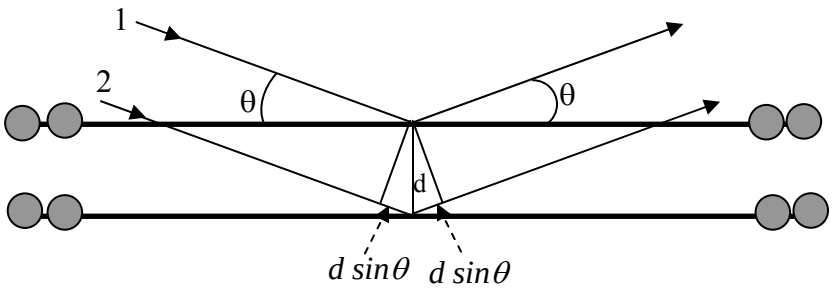

Figure A.12: Diffraction from parallel plane of atoms (not shown where the X-rays are drawn). The distance between two planes is *d*.

For a three–dimensionally arranged sample there are multiple reflecting planes and if each of these planes satisfies the Bragg's law, diffraction will occur. Correspondingly, different peaks can be observed in intensity *vs*. 2θ chart.

Figure A.13 shows the typical crystal structure of graphite [Pierson, 1993; Longo, 2006]. The carbon layers in graphite are stacked in an **ABAB** sequence, in such a way that half of the carbon atoms have atoms directly above and below them in adjacent layers. The common reflecting planes associated to graphite are (002), (100), and (110) and as a result multiple peaks in intensity vs. 2θ will be obtained.

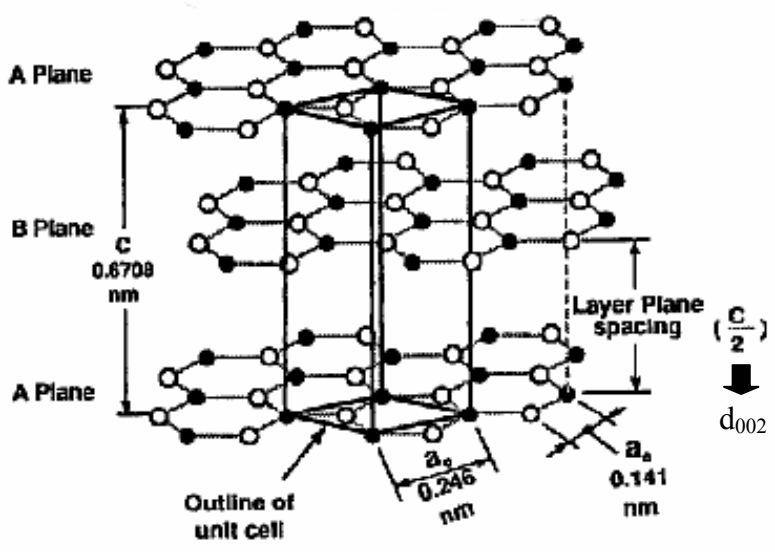

Figure A.13: (a) Crystal structure of graphite showing ABAB stacking sequence and unit cell [Pierson, 1993]

During our experiments, photographic X-ray technique was used. For the preferred orientation of the planes present in the sample, diffraction patterns were obtained at different locations (different azimuthal position) on the photographic plate. From the azimuthal position of the diffraction, the orientation of a particular layer relative to a given axis can be determined. How the different planes resulted in diffraction peaks at different azimuthal locations is described by Cullity (1956).

In mesophase pitch based carbon fibers, the arrangement of carbon layers are not regular as graphite and the corresponding structure is called turbostatic structure. The distance between layer planes is slightly higher ($d_{002} \geq 3.440$ Å) than that observed for graphite ($d_{002} = 3.354$ Å) (Cato and Edie, 2003). The carbon layers are preferentially stacked parallel to the fiber axis. Typical diffraction pattern for a mesophase pitch based

carbon based carbon fiber is shown in **Figure A.14** Here, (00l) reflection at the equator and a ring shaped (10) band was observed.

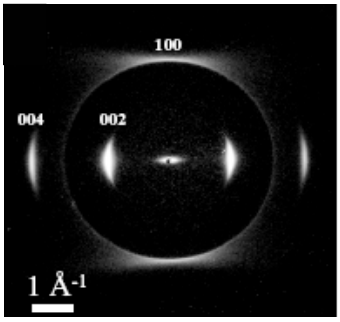

Figure A.14: X-ray diffraction pattern of a mesophase pitch based carbon fiber. (Paris et al., 2000)

Generally, the texture of carbon fibers is of two different types, radial and onion. Sketch of the geometrical situation for equatorial diffraction from carbon fibers with radial and onion textures are shown in **Figure A.15**. The orientation of carbon layers are shown by the solid lines. For the given X-ray beam direction, as shown in **Figure A.15**, the Braggs condition for the (002) reflections requires the reflecting planes to be inclined by an angle θ with respect to the X-ray beam. As seen in **Figure A.15**, only the shaded areas contributes to the (002) reflection [Paris et al., 2000]. Similarly, for mesophase pitch, as reported in Chapter 3, (002) reflection was observed at the equatorial position in the steady-state sample for the layer-planes with the director oriented in the vorticity or gradient direction.

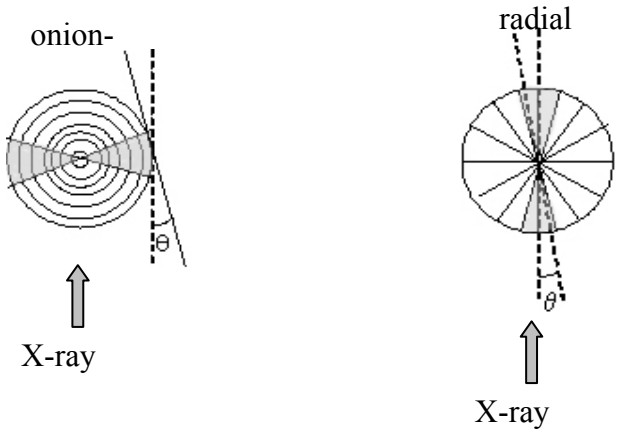

Figure A.15: Sketch of the geometrical constraints for the Bragg condition of the 002 equatorial reflections in two different types of fiber geometry. The solid lines represent the graphite layer plane orientation. Adapted from Oscar et al., 2000

A Rigaku X-ray diffraction system was used to perform the wide angle X-ray diffraction experiments on the samples with different flow histories. The X-ray source was an Osmic Micromax Cu K_α X-ray source with a collimator pinhole size of 0.3 mm. The distance from the sample to the detector was 10 cm. Diffracted patterns were captured on 2D image plates, which were scanned using a Fuji BAS 1800 scanner. The distance from the sample to the detector was 113.97 mm. An exposure time of 30 min per image was utilized throughout the study.

The samples were collected from rheometer plate on a duct tape using the procedure discussed in Appendix A6. The sample was mounted on Scotch® tape oriented properly relative to the X-ray beam direction. The Scotch® tape with the sample was then placed on a sample holder, which was then positioned in between the X-ray source and the detector (see **Figure A.16**). The WAXD diffractograms were analyzed using Polar® software. Diffractograms were also obtained for the bare tape, (i.e., no sample on it) to perform the background correction.

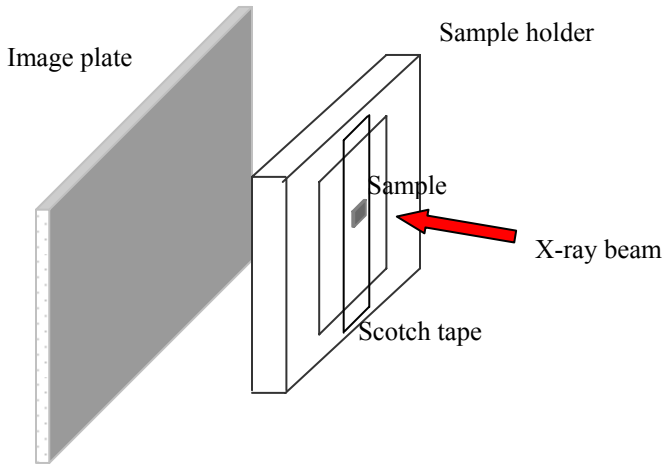

Figure A.16: Sample set-up for wide-angle X-ray diffraction.

To analyze the X-ray data, following procedure was used.

1. Open the WAXD X-ray diffraction images (with file extension *.inf) in Polar® 2.6.8 software.

2. Click on "File→Preferences". Click on the "Image" tab and set the color scheme to rainbow and the image magnification to 0.50. Click Ok.

3. Click on "Processing→Find Center→ By X-Y Profile". A window named "Profile Scan" will open. Select the "X-scan" tab and then click on "Scan". A new graph with two vertical lines and horizontal line will open. A dip of the intensity should be observed for the small angle hole. Move the vertical lines in such a way that those two lines pass through the points of intersection of the horizontal line and the intensity curve (see **Figure A.17**). Click on "Find Center" tab at the top of the graph window. A small window will open, which shows the center value. Click Ok

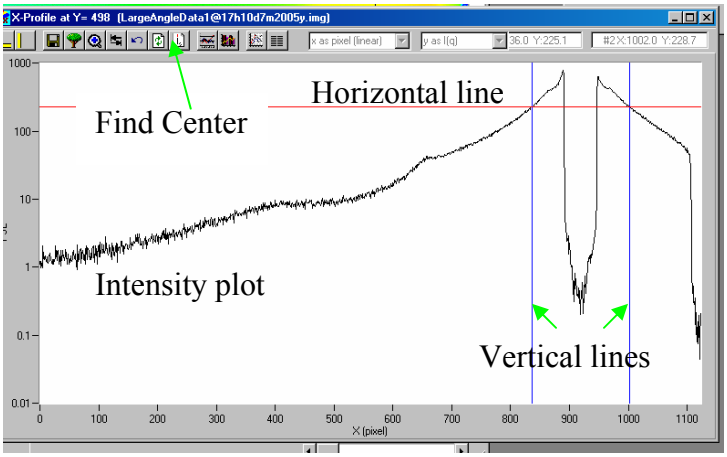

Figure A.17: Screenshot of the window showing Intensity vs. pixel

4. Click on the "y-scan" tab and follow the same procedure as step#3. The center of the image is now identified. Click on "Processing→Push Image to Stack". This will allow the user to perform further processing.

5. Background correction of the diffractogram is to be performed next. Open the background file (for Scotch® tape without pitch sample) and identify the center of the image following the steps# 3 and 4.

6. Click on "Processing→Image-Image processing". A new window will open in which click on the "Process" tab. In the drop down menu choose the sample image as "Image #1" and the background image as "Image #2". Set the operator for each image to 'X' and between the images to '-'.Input the multiplying factor for images # 1 and #2 as '1' and click on "process". A new window will open, which displays the subtracted image. If the background subtraction is not satisfactory, perform the centering operation again and change the multiplying factor for image #2. Save the centered image in *.xdp format.

7. Click on "Analysis→WAXD→Fiber-like" Fraser-correction". A new window named "Fraser Correction" will open. Enter the wavelength as 0.15406 nm, β of 0, sample to detector distance as 113.97 mm, and the set value of the converted pixel as 0.008 1/nm. Click Ok. A new window will display the Fraser corrected image (**Figure A.18**). Save the image in *.xdp format.

8. Click on "Analysis→ Integrated I(s)". Select the tab "Int.Range". Enter the start and term a angle as 90° and 270°, respectively. Click on "Set Range→ Do It".

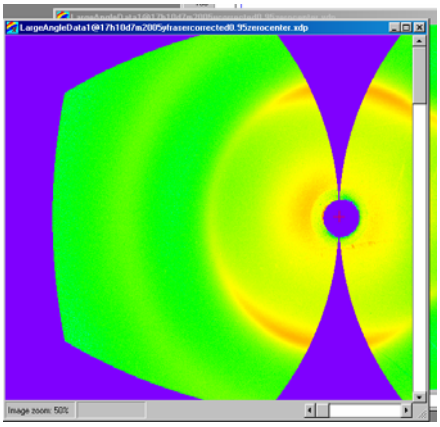

Figure A.18: Screenshot of a Fraser corrected image

9. A window with intensity as a function of pixel will open. Note the pixel values correspond to the peaks. Change the x-axis title from pixel to 2*theta(deg) from the drop down menu. Also, change the axes to linear scale by clicking on the icons on the left corner.

10. Click on the "Data List" icon. A new window will open, which shows the values of 2theta(deg) and the corresponding Intensity (user unit) in a tabular form. Click on "Select All→Copy". This will copy the data in the clipboard, which can be pasted in Excel for further processing.

11. To obtain the azimuthal intensity profile for a particular plane, click on "Analysis→Sliced I(s)" on a Fraser corrected image. A new window named "Sliced Intensity" will open. Select the "Az-Scan" tab. For a particular plane enter the pixel value noted in Step #9 as "radius". Enter the values of angle from "90°" to "270°". Click on "Scan".

12. A new window displays the Intensity as a function of kai. Follow the same procedure as Step#10 to export the data into Excel.

13. To calculate the orientation parameter, click on "Analysis→WAXD→property: Pole Orientation" on a Fraser corrected image. A new window named "Pole Orientation" will open. Change "Pole at Region" to 2nd quadrant. The 's' (scattering vector) value for a particular plane is the pixel value noted earlier (step#9). Enter the expected standard deviation (e.g. ±5), and the azimuthal angle range. Click Ok.

14. A new window displays the values of c2 ($\langle\cos^2\Phi\rangle$), and f = $(3\langle\cos^2\Phi\rangle-1)/2$, the Herman's orientation factor, for the plane considered.

A12. Single-screw extruder experiments

To study the microstructure developed during various processing conditions, experiments were performed using a single screw extruder fitted with custom made dies. Details of these custom made dies were provided in Chapter 5. These dies were screwed/unscrewed from the extruder using a custom made tool. During steady state flow through these dies, the flow was interrupted and the die was quenched. The solid pitch sample was then polished at various sections for microstructural analysis.

A detailed procedure used to run the single screw extruder and to collect the dies for microstructural analysis follows.

1. Install a die in the die-head. Use the custom made tool to tighten the die properly.
2. Install an appropriate pressure probe. A 1500 psig pressure probe was generally used, but other sizes are also available.
3. Turn on the power to the equipment.
4. Turn on the cooling water flow to extruder jacket by opening the valve on the main line.
5. Turn on the "on/off" switches for the four heating zones and set the desired temperatures. Set the temperature of first zone in vicinity of the softening point of the material. Maintain a positive temperature gradient towards the end of the extruder. Wait for the extruder to reach the thermal equilibrium.
6. When the zones reach the set temperatures, turn on the extruder motor. Slowly increase the speed to the desired value.
7. Fill the inlet hopper with pitch pellets. It will take some time before pitch comes out of the die. If the extruder was used for other materials previously, purge it until pure pitch comes out of the die.
8. A small blind hole is provided near the exit of the dies to insert an external thermocouple to measure the temperature. To obtain a desired temperature at the

die exit, change the zone temperatures accordingly. Wait for thermal equilibrium to reach. Meanwhile, continue adding pitch into the hopper.

9. Watch the pressure probe reading to ensure that the pressure does not reach the maximum limit of the probe.

10. Once the flow is steady and the pressure reaches equilibrium, submerge the tip of the die into a bowl filled with ice water. At the same time turn-off the extruder motor and the heaters. This process will quench the pitch sample inside the die.

Immediately remove the die from the die head using the custom made tool. Place the die inside the bowl filled with ice-water. Once it is cold, store the die for polishing.

A13. Polishing of dies for microstructural analysis

Following procedure was used to study the microstructure in the longitudinal mid-plane.

1. Place a die in the mounting cup and then embed it in epoxy (follow the same procedure described in Appendix A5).

2. Use Buehler polisher-grinder with 80 grits papers to grind the epoxy blocks. Continue grinding until you reach in vicinity of the longitudinal mid-plane.

3. Polish the exposed pitch surface in several steps, each with increasing level of fineness. Follow the same procedure as described in Appendix A7. During polishing, cracks and voids may be observed. Fill these voids/cracks with low viscosity Superglue.

4. The polished samples may then be studied using optical microscope. Follow the same procedure as described in Appendices A8 and A9.

To study the microstructure in various cross-sections, the dies with solid pitch sample inside was cut using a handsaw. These small pieces were then embedded in the epoxy with the section of interest touching the bottom plate of the mounting cup. Follow steps 2 to 4 for polishing and microstructural study.

Appendix B

Viscous Heating During Flow Through Capillaries

Flow through a capillary was simulated as 2D axisymmetric non-isothermal problem.

Diameter of the capillary = 1mm

Length of the capillary = 20 mm

The computation domain and the corresponding meshing is shown below (Figure B.1)

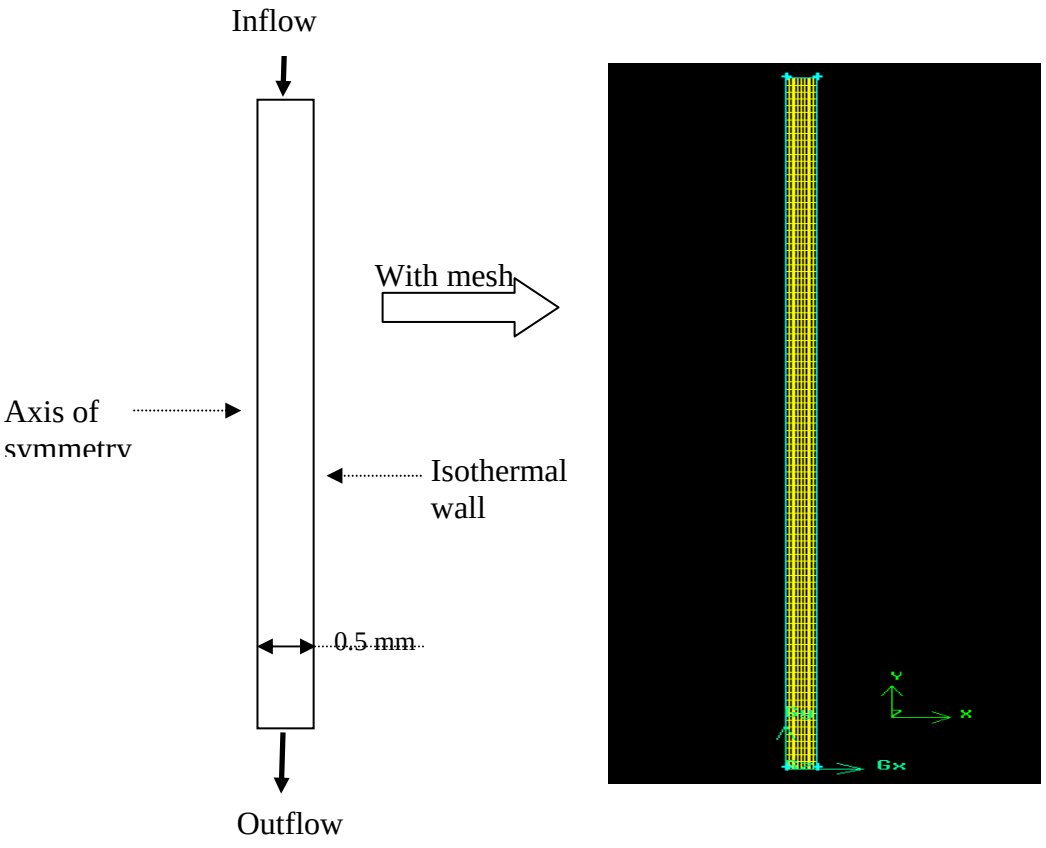

Figure B.1: Figure shows the computation domain, the boundary conditions, and the mesh file.

Fluid: Newtonian fluid with constant viscosity of 100 Pa s at 280°C.

Density: 1230 kg/m^3 (*MGC brochure*).

Heat Capacity (Cp): 2721 J/kg K (*MGC brochure*).

Thermal conductivity (k): 0.5 W/mK (similar value observed for common polymers)

Temperature dependence of viscosity: Arhenius Law

$$\eta(\dot{\gamma}, T) = F(\dot{\gamma})H(T) \qquad H(T) = \exp\left[\alpha\left(\frac{1}{T - T_0} - \frac{1}{T_\alpha - T_0}\right)\right]$$

F($\dot{\gamma}$) and H(T) are the shear-rate and temperature dependence of viscosity, respectively. For the present case F($\dot{\gamma}$) is constant and is set to 100 Pa s.

Here, E/R = α = 34321 °C, T_α = 280°C, T_0= -273°C.

Consider, shear rate ($\dot{\gamma}$): 7000 s^{-1}

The flow rate: 6.87E-07 m^3/s

Inlet temperature: 280°C

Isothermal wall temperature: 280°C

The temperature distribution across the capillary is shown in Figure B.2. The maximum temperature rise was 12°C near the exit.

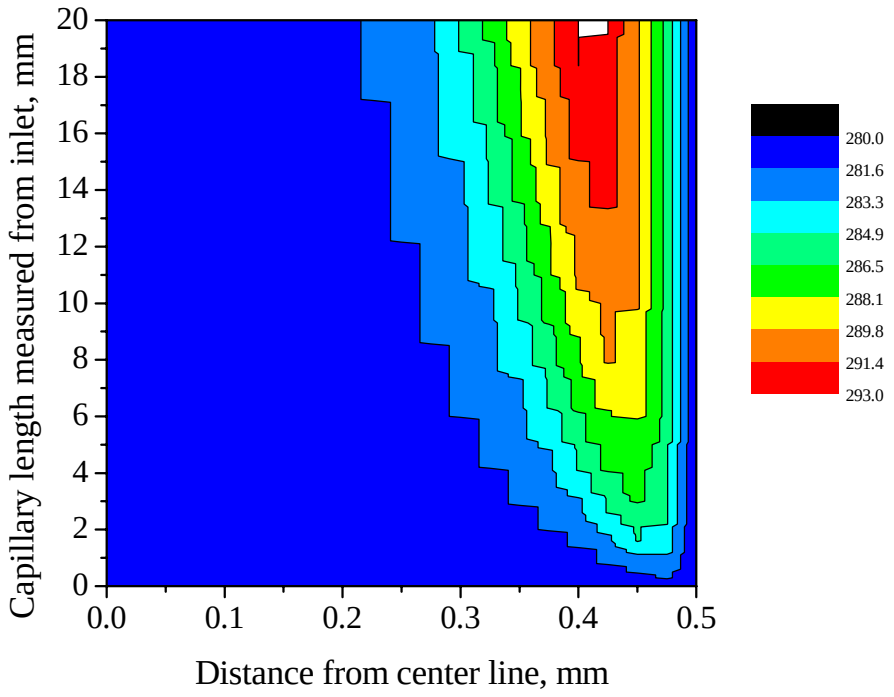

Figure B.2: Temperature distribution across the capillary.

Appendix C

Heat Loss in the Single-Screw Extruder Die

During processing flow experiments, approximately 7 mm of the die protruded out of the extruder. Polyflow® was used to simulate the temperature profile of the whole die. Similar to the capillary flow problem (Appendix B), the fluid was considered Newtonian with a viscosity of 100 Pa s at 280°C. The schematic of the computation domain is shown below.

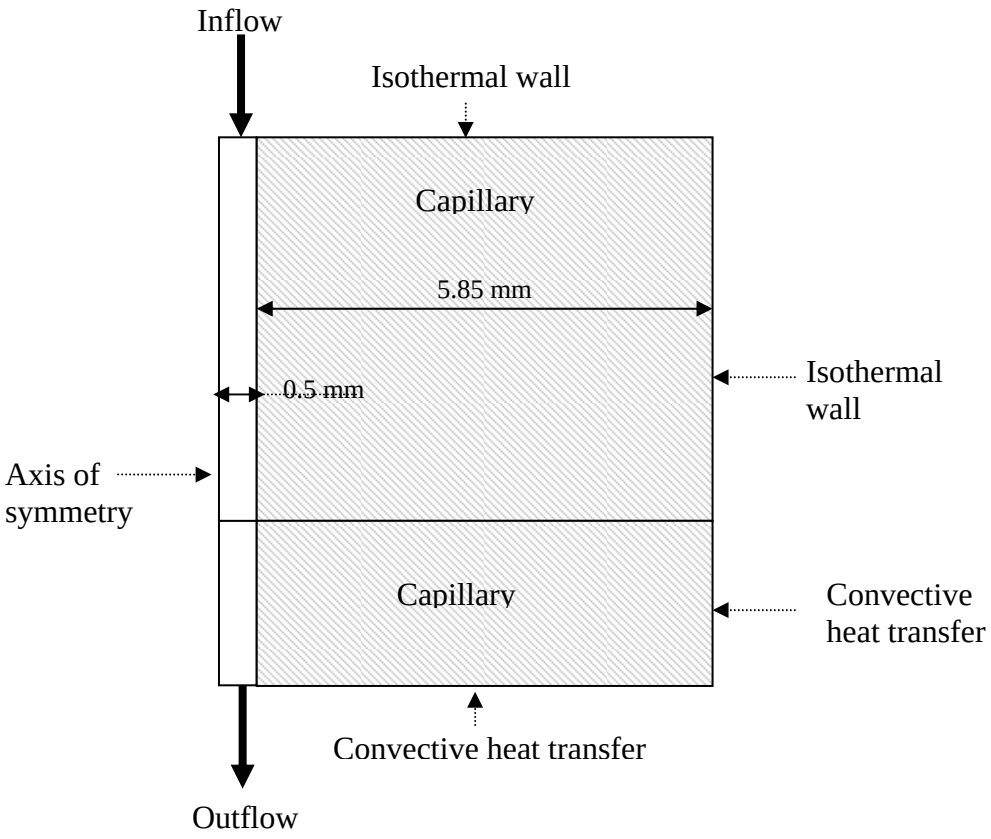

Figure C.1: Schematic of computation domain and the boundary conditions. Figure not in scale.

The fluid flow through capillary was simulated as 2D axisymmetric non-isothermal problem and the solid capillary wall (made of brass) was solved for heat-conduction problem.

Diameter of the capillary = 1mm

Length of the capillary = 20 mm

Thickness of brass wall = 5.85 mm

The length of the die, which was in contact with air = 7 mm (In this region convective heat transfer to air took place).

Fluid: Newtonian fluid with constant viscosity of 100 Pa s at 280°C.

Density of the fluid: 1230 kg/m^3 (*MGC brochure*).

Heat Capacity of the fluid (Cp): 2721 J/kg K(*MGC brochure*).

Thermal conductivity of the fluid (k): 0.5 W/mK (similar value observed for common polymers)

Temperature dependence of viscosity: Arhenius Law

$$\eta(\dot{\gamma}, T) = F(\dot{\gamma})H(T) \qquad H(T) = \exp\left[\alpha\left(\frac{1}{T - T_0} - \frac{1}{T_\alpha - T_0}\right)\right]$$

F($\dot{\gamma}$) and H(T) are the shear-rate and temperature dependence of viscosity, respectively.

For the present case F($\dot{\gamma}$) is constant and is equal to 100 Pa s.

Here, E/R = α = 34321 °C, T_α = 280°C, T0= -273°C.

Thermal conductivity of the brass (k): 109 W/m K.

Heat transfer coefficient to air (h): 20 W/m^2 K

Shear rate ($\dot{\gamma}$):~1000 s^{-1}

The flow rate: 1E-7 m^3/s

Inlet fluid temperature: 297°C

Isothermal wall temperature: 297°C

Room temperature: 25°C

The contour plot of temperature for the die and the fluid within is shown in **Figure C.2**. Also shown the temperature profile at a distance of 1 mm from the exit (**Figure C.3**). From these figure it is noted that the variation of the temperature was within 1°C. Therefore, this kind geometry can be used to measure the viscosity of mesophase pitch.

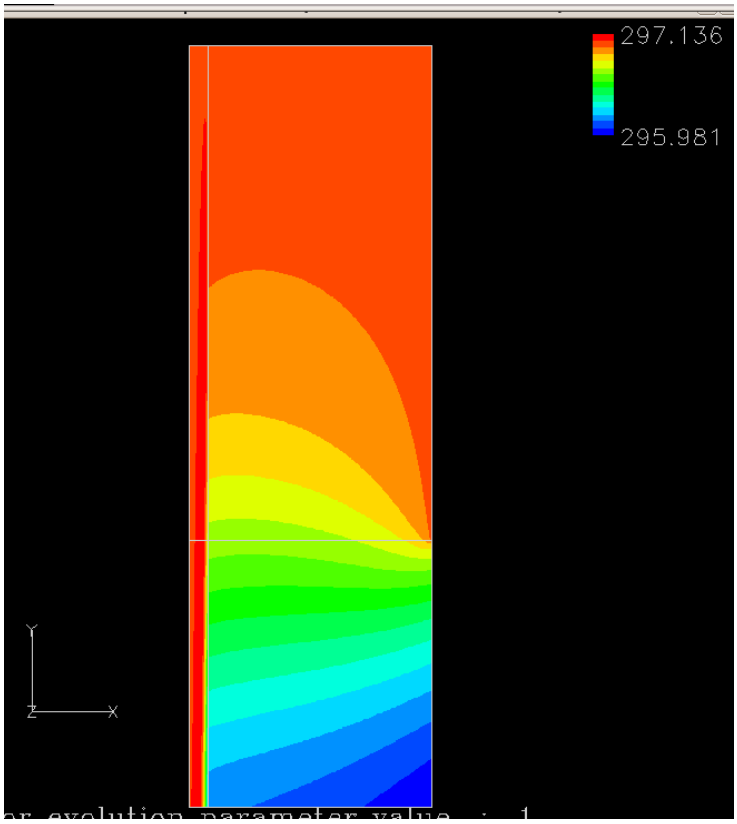

Figure C.2: The contour plot of the temperature for the die and the fluid within.

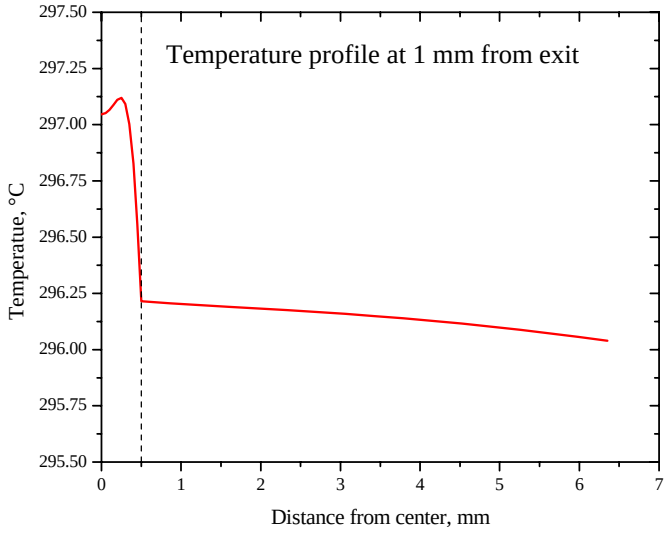

Figure C.3: Temperature profile across the die at 1 mm from the exit.

LITERATURE CITED

Balduhn R, Fitzer E. Rheological properties of pitches and bitumina up to temperatures of 500 °C. Carbon 1980; 18:155-161.

Barr JB, Chwastiak S, Didchenko R, Lewis IC, Lewis RT, Singer LS. High modulus carbon fibers from pitch precursor. Applied Polymer Symposium 1976; 29:161-173.

Barnes AB, Dauché FM, Gallego NC, Fain CC, Thies MC. As-spun orientation as an indication of graphitized properties of mesophase-based carbon fiber. Carbon 1998; 7-8(855-860).

Beris AN, Edwards BJ. Thermodynamics of flowing systems. Oxford University Press, 1986, New York.

Bolaños G, Liu GZ.; Hochgeschurtz T, Thies, M. C. Producing a carbon fiber precursor by supercritical fluid extraction. Fluid Phase Equilibria 1993; 82: 303-10.

Bright AA, Singer LS. The electronic and structural characteristics of carbon fibers from mesophase pitch. Carbon 1979; 17:59-69.

Brooks JD, Taylor GH. The formation of graphitizing carbons from the liquid phase. Carbon 1965; 3:185-193.

Burghardt WR. Oscillatory shear flow of nematic liquid crystals. J. Rheol. 1991; 35(1):49-62.

Burghardt WR. Molecular orientation and rheology in sheared lyotropic liquid crystalline polymers. Macromolecular Chemistry and Physics 1998; 199(4):471-488.

Burghardt WR, Brown EF, Auad ML, and Kornfield JA, Molecular Orientation of a Commercial Thermotropic Liquid Crystalline Polymer in Simple Shear and Complex Flow. Rheol. Acta 2005; 44: 445-456.

Cato AD. Flow and deformation behavior of mesophase pitch. Ph.D. dissertation; 2002. Clemson University, Clemson, SC.

Cato AD, Edie DD. Flow behavior of mesophase pitch. Carbon 2003; 41(7):1411–1417.

Cato AD, Edie DD, Harrison GM. Steady state and transient rheological behavior of mesophase pitch, Part I: Experiment. J. Rheol. 2005; 49(1):161-174.

Cheung T, Turpin M, Rand B. Controlled stress, oscillatory rheometry of mesophase-pitches. Carbon 1996; 34(2):265-271.

Chioujones KM, Ho W, Fathollahi B, Chau PC, Wapner PG, Hoffman WP. Microstructural analysis of in situ mesophase transformation in the fabrication of carbon–carbon composites. Carbon 2006; 44: 284-292.

Cho T, Lee YS, Rao R, Rao AM, Edie DD and Ogale AA. Structure of carbon fiber obtained from nanotube-reinforced mesophase pitch Carbon 2003; 41:1419-1424

Collett GW, Rand B. Rheological investigation of coal-tar pitch during its transformation to mesophase. Fuel 1978a; 57:162-170.

Collett GW, Rand B. Thixotropic changes occurring on reheating a coal tar pitch containing mesophase. Carbon 1978b; 16:477-479.

Dauché FM, Bolaños G, Blasig A, Thies MC. Control of mesophase pitch properties by supercritical fluid extraction. Carbon 1998; 36: 953-961.

De Andrade Lima, L.R.P., Rey A.D. Poiseuille Flow of Leslie-Ericksen Discotic Liquid Crystals: Solution Multiplicity, Multistability, and Non-Newtonian Rheology. J. Non-New. Fluid Mech. 2003; 110(2-3):103-142.

De Andrade Lima LRP, Rey AD. Linear viscoelasticity of discotic mesophases. Chem. Eng. Sci. 2004; 59:3891-3905.

De Gennes PG, Prost J. The Physics of Liquid Crystals; 1993. 2nd ed. London: Oxford University Press.

De'Nève T, Navard P, Kléman M. Shear rheology and shear-induced textures of a thermotropic copolyesteramide. J. Rheol. 1993; 37(3):515-529.

Diefendorf RJ, Riggs DM: US Patent 4208267, Forming optically anisotropic pitches, Exxon Research & Engineering Company (1980).

Doi M, Edwards BJ. The theory of polymer dynamics; 1986. Clarendon Press, Oxford.

Driscoll P, Masuda T. Rheological properties of homogeneous thermotropic liquid-crystalline polyester: dynamic viscoelastic and interrupted-flow measurements. Macromolecules 1991; 24: 1567-1574.

Dumont M, Dourges MA, Pailler R and Bourrat X. Mesophase pitches for 3D-carbon fibre preform densification: rheology and processability. Fuel 2003; 82:1523-1529.

Edie DD. The effect of processing on the structure and properties. In Delhaes P, editor. World of Carbon, 2(Fibers and Composites); CRC Press, 2003:24-46.

Edwards WF. Fractionation of carbonaceous pitches by molecular weight using dense-gas extraction. Ph.D Dissertation; 2005. Clemson University, SC.

Fathollahi B, White JL. Polarized-light observations of flow-induced microstructures in mesophase pitch. J. Rheol. 1994; 38(5):1591-1607.

Fathollahi B, Chau PC, White JL. Injection and stabilization of mesophase pitch in the fabrication of carbon–carbon composites. Part I. Injection process. Carbon 2005; 43:125-133.

Fleurot O. The viscoelastic flow behavior of pitches. Ph.D. dissertation; 1998. Clemson University, Clemson, SC.

Graziano DJ, Mackley MR. Disclinations observed during the shear of MBBA. Mol. Cryst. Liq. Cryst. 1984; 106:103-119.

Grecov D. Personal communication, 2006.

Grecov D, Rey AD. Transient rheology of discotic mesophases. Rheol Acta 2003a; 42(6):590-604.

Grecov D, Rey AD. Theoretical and computational rheology for discotic nematic liquid crystals. Mol. Cryst. Liq. Cryst. 2003b; 391:57–94.

Grecov D, Rey AD. Impact of texture on stress growth in thermotropic liquid crystalline polymers subjected to step-shear. Rheol. Acta. 2004; 44:135-149.

Grecov D, Rey AD. Steady state and transient rheological behavior of mesophase pitch, Part II: Theory. J. Rheol. 2005; 49(1):175-195.

Grizzuti N, Cavella S, Cicarelli P. Transient and steady-state rheology of a liquid crystalline hydroxypropylcellulose solution. J. Rheol. 1990; 34(8):1293-1310.

Grizzuti N, Moldenaers, Mortier PM, Mewis J. On the time-dependency of the flow-induced dynamic moduli of a liquid crystalline hydroxypropylcellulose solution. Rheol. Acta. 1993; 32(3):218-226.

Gu DF, Jamieson AM, Wang SQ. Rheological characterization of director tumbling induced in a flow-aligning nematic solvent by dissolution of a side chain liquid-crystal polymer. J. Rheol. 1993; 37(6):985-1001.

Guo T, Harrison GM, Ogale AA. Transient shear rheology and rheo-optical microstructural characterization of a thermotropic liquid crystalline polymer. Polym. Eng. Sci. 2005; 45(2):187-197.

Guo T, Harrison GM, Ogale AA. Thermal and shear flow effects on microstructure of a thermotropic liquid crystalline polymer. Polym. Eng. Sci. 2006; 46(9):1215-1222.

Guskey SM, Winter HH. Transient shear behavior of a thermotropic liquid crystalline polymer in the nematic state. J. Rheol. 1991; 35(6):1191-1207.

Hamada T, Nishida T, Sajiki Y, Matsumoto M. Structures and physical properties of carbon fibers from coal tar mesophase pitch. J. Mater. Res. 1987; 2(6):850-857.

Han CD, Kim SS. Transient rheological behavior of a thermotropic liquid crystalline polymer. II. Intermittent shear flow and evolution of dynamic moduli after cessation of shear flow. J. Rheol. 1994; 38(1):13-30.

Hurt RH, Hu Y. Thermodynamics of carbonaceous mesophase. Carbon 1999; 37: 281–292

Jian K, Shim HS, Tuhus-Dubrow D, Bernstein S, Woodward C, Pfeffer M, Steingart D, Gournay T, Sachsmann S, Crawford GP, Hurt RH. Liquid crystal surface anchoring of mesophase pitch. Carbon 2003; 41:2073-2083.

Khandare PM, Zondlo JW, Stansberry PB, Stiller AH. Rheological investigations of pitch material Part II: viscosity measurement of A240 and ARA-24 pitches using a high-temperature high-pressure rheometer. Carbon 2000; 38:889-897.

Kalika DS, Giles DW, Denn MM. Shear and time-dependent rheology of a fully nematic thermotropic liquid crystalline copolymer. J. Rheol. 1990; 34(2):139-154.

Kim SS, Han CD. Effect of Molecular Weight on the Rheological Behavior of Thermotropic Liquid-Crystalline Polymer. Macromolecules 1993; 26:6633-6642.

Kim SS, Han CD. Oscillatory shear flow behavior of a thermotropic liquid-crystalline polymer. Polymer 1994; 35(1): 93-103.

Kundu S, Ogale AA. Rheostructural studies on a synthetic mesophase pitch during transient shear flow, Carbon 2006; 44(11): 2224-2235.

Larson RG, Mead DW. Development of orientation and texture during shearing of liquid-crystalline polymers. Liquid Crystals 1992; 12(5):751-768.

Larson RG. The structure and rheology of complex fluids. Oxford University Press, 1999, New York.

Lee KM, Han CD. Effect of flexible spacer length on the rheology of side-chain liquid-crystalline polymers. Macromolecules 2003; 36:8796-8810.

Lewis IC, US Patent 4032430, Process for producing carbon fibers from mesophase pitch, Union Carbide Corporation (1977).

Lewis IC. Thermotropic mesophase pitch. Carbon 1978; 16: 503.

Longo M. Electron Diffraction and Crystal Structure. University of Michigan. Advanced Physics Laboratory. Physics 441-442 class notes. March 14, 2006. http://phys-advlab.physics.lsa.umich.edu/Phys441_442/Electron%20Diffraction/electron_diffraction2.pdf

Lu S, Blanco C, Appleyard S, Hammond C, Rand B.Texture studies of carbon and graphite tapes by XRD texture goniometry. J. Mat. Sci. 2002; 37:5283 – 5290.

Matsumoto M. Mesophase pitch and its carbon fibers. Pure & Appl Chem 1985; 57 (11): 1553-1562.

Matsumoto M, Iwashita T, Arai Y, Tomioka T. Effect of spinning conditions on structures of pitch-based carbon fiber. Carbon 1993; 31(5):715-720.

Mather PT, Jeon HG, Han CD, Chang S. Morphological and Rheological Responses to Shear Start-up and Flow Reversal of Thermotropic Liquid-Crystalline Polymers. Macromolecules 2000; 33:7594-7608.

Marrucci G. Remarks on the viscosity of polymeric liquid crystals. In Mena B, Garcia-Rejon A, Rangel-Nafaile C, editors. Advances in Rheology, Vol. 1. Universidad National Autonoma De Mexico, Mexico, 1984.

Marrucci G, Greco F. Flow behavior of liquid crystalline polymers. Adv. in Chem. Phys. 1993; 86:331-404.

McHugh JJ. The development of orientation in mesophase pitch during fiber formation. Ph.D. dissertation; 1994. Clemson University, Clemson, SC.

McHugh JJ, Edie DD. The orientation of mesophase pitch during fully developed channel flow. Carbon 1996; 34(11):1315-1322.

Meissner J. Modifications of the Weissenberg Rheogoniometer for Measurement of Transient Rheological Properties of Molten Polyethylene under Shear. Comparison with Tensile Data. J. Appl. Poly. Sci. 1972; 16:2877-2899.

Mochida I, Nakamura E, Maeda K, Takeshita K. Carbonization of aromatic hydrocarbons — III Carbonization catalyzed by alkali metals. Carbon 1975; 13: 489-493.

Mochida I, Sone Y, Korai Y. Preparation and properties of carbonaceous mesophase-II highly soluble mesophase from ethylene tar modified using aluminum chloride as a catalyst. Carbon 23: 175-178, 1985.

Mochida I, Korai Y, Ku CH, Watanabe F, Sakai Y. Chemistry of synthesis, structure, preparation and application of aromatic-derived mesophase pitch. Carbon 2000; 38:305-328.

Mochida I, Yoon S, Korai Y Mesoscopic structure and properties of liquid crystalline mesophase pitch and its transformation into carbon fiber. The Chemical Record 2002; 2:81–101.

Moldenaers P, Mewis J. Transient Behavior of Liquid Crystalline Solutions of Poly(benzylglutamate**).** J. Rheol. 1986; 30(3):567-584.

Mottram NJ, Newton C. University of Strathclyde Department of Mathematics Research Report 2004; No. 2004:10 (http://www.maths.strath.ac.uk/~aas99102/)

Murthy NS, Dantas SO, Iqbal Z, Baughman RH. X-ray diffraction evidence for the formation of a discotic phase during graphitization. Carbon 2001; 39: 809–813.

Nazem FF. Rheology of carbonaceous mesophase pitch, Fuel 1980; 59:851-858.

Nazem FF. Flow of molten mesophase pitch, Carbon 1982; 20(4):345-354.

Nielsen LE, Landel RF. Mechanical properties of polymers and composites. 2nd Edition. Marcel Dekker, NY, 1994.

Oberlin A, Bonnamy S, Lafdi K. Structure and texture of carbon fibers. In Donnet JB, Wang TK, Peng JCM, Rebouillat S editors. Carbon Fibers. Marcel Dekker, NY, 1998.

Oberlin A. Pyrocarbons. Carbon 2002; 40:7-24

Ogale AA, Lin C, Anderson DP, Kearns KM.Orientation and dimensional changes in mesophase pitch-based carbon fibers. Carbon 2002; 40:1309–1319.

Onogi S, Asada T. Rheology and rheo-optics of polymer liquid crystals. In Astarita G, Marrucci G, Nicolais G, editors. Rheology, Vol. 1, New York: Plenum, 1980:127-147.

Otani S, Oya A. Composites '86: Recent advances in Japan and the United State. In Kawata K, Umekawa S, Kobayashi A, editors. Proc. Japan4J.S. CCM-III, Jpn. Soc. Compos. Mater., Tokyo 1986a:1-10.

Otani S and Oya A. Progress of pitched-based carbon fibre in Japan. In Petroleum derived Carbons (ACS Symp. Ser. No. 303) J D Bacha, J W Newman and J L White editors. American Chemical Society, Washington, DC 1986b.

Paris O, Loidl D, Peterlik H, Müllerc M, Lichteneggera H, and Fratzl P. J. Appl. Cryst. 2000; 33:695-699

Paris O, Loidl D, Peterlik H. Texture of PAN- and pitch-based carbon fibers. Carbon 2002; 40:551–555

Paulauskas FL. DOE FY 2004 Progress Report for Automotive Lightweighting Materials. http://www1.eere.energy.gov/vehiclesandfuels/pdfs/alm_04/5d_paulauskas.pdf.

Picken SJ, Aerts J, Visser R, Northolt MG. Structure and rheology of aramid solutions: X-ray scattering measurements. Macromolecules 1990; 23:3849-3854.

Pierson HO. Handbook of Carbon, Graphite, Diamond and Fullerenes - Properties, Processing and Applications. William Andrew Publishing/Noyes, 1993. http://www.knovel.com/knovel2/Toc.jsp?BookID=242&VerticalID=0

Rand B. Carbon fibers from mesophase pitch. In Watt W, Perov BV, editors. Handbook of Composites, Vol. 1-Strong Fibers, Elsevier Science Publishers B.V., 1985:495-575.

Rey AD. Theory of non-linear viscoelasticity for single-phase nematic mixrtures. Mol. Cryst. Liq. Cryst. 1996; 281:155-170.

Rey AD, Tsuji T. Recent advances in theoretical liquid crystal rheology. Macromol. Theory Simul. 1998; 7:623-639.

Rey AD, Denn MM. Dynamical phenomena in liquid-crystalline materials. Annu. Rev. Fluid Mech. 2002; 34:233–66.

Rey AD. Personal communication.

Romo-Uribe A, Windle AH. “Log-rolling” alignment in main-chain thermotropic liquid crystalline polymer melts under shear: an *in-situ* WAXS study. Macromolecules 1996; 29:6246-6255.

Romo-Uribe A, Lemmon TJ, Windle AH. Structure and linear viscoelastic behavior of main-chain thermotropic liquid crystalline polymers. J. Rheol. 1997; 41: 1117–1145.

Ruland W. X-ray studies on preferred orientation in carbon fibers. J. Appl. Phys. 1967; 38(9): 3585-3589.

Singer LS, US Patent 4005183, High modulus high strength fibers produced from mesophase pitch, Union Carbide Corportaion (1977).

Singer LS. The mesophase in carbonaceous pitches. Faraday Discuss. Chem. Soc. 1985; 79: 265-272.

Singer LS. The mesophase and high modulus carbon fibers from pitch. Carbon 1978; 16(6):409-415.

Singh AP, Rey AD, Theory and simulation of extensional flow-induced biaxiality in discotic mesophases. J. Phys. II France. 1995; 5**:** 1321-1348.

Singh AP. Theory and simulation of flow-induced microstructure and rheology of discotic mesophases. Ph.D. dissertation; 2000. McGill University, Montreal, Canada.

Shiwaku T, Nakai A, Hasegawa H, Hashimoto T. Ordered Structure of Thermotropic Liquid-Crystal Polymers. 1. Characterization of Liquid-Crystal Domain Texture. Macromolecules 1990; 23: 1590-1599.

Sokalski K, Ruijgrok THW. Elastic constants for liquid crystals of disc-like molecules, Phys. A: Statist. Theoret. Phys. 1982; 113(1-2):126–132.

Somma E, Nobile MR.The linear viscoelastic behavior of a series of molecular weights of the thermotropic main-chain liquid crystal polymers HBA/HNA 73/27. J. Rheol. 2004; 48(6):1407-1423.

Ströbel R, Garche J, Moseley PT, Jörissen L, Wolf G. Hydrogen storage by carbon materials. J. Power Sources 2006; 159(2):781-801.

Thies MC. Personal communication.

Tseng HC, Silver DL, Finlayson BA. Application of the continuum theory to nematic liquid crystals. Phys. Fluids 1972; 15(7):1213-1222.

Tsuji T, Rey AD. Effect of long range order on sheared liquid crystalline materials. Part I. Compatibility between tumbling behavior and fixed anchoring. J. Non-Newtonian Fluid. Mech. 1997; 73:127–152.

Ugaz VM. Investigation of the Effect of Shear Flow on Molecular Orientation in Model Thermotropic Liquid Crystalline Polymers Using In Situ X-ray Scattering. Ph.D. dissertation; 1999. Northwestern University, Evanston, Illinois.

Ugaz VM, Burghardt WR, Zhou W, Kornfield JA. Transient molecular orientation and rheology in flow aligning thermotropic liquid crystalline polymers. J. Rheol. 2001; 45(5):1029-1063.

Viola GG, Baird DG. Studies on the Transient Shear Flow Behavior of Liquid Crystalline Polymers. J. Rheol. 1986; 30(3):601-628.

Von Oehsen J, Duffy E, Kundu S, Ogale AA, Cox C, Rey AD. Flow simulation of discotic liquid crystals in simple shear flow. Manuscript under preparation, 2006.

Walker LM, Wagner NJ, Larson RG, Mirau PA. The rheology of highly concentrated PBLG solutions. J. Rheol. 1995; 39(5):925-952.

Wang L, Rey AD. Pattern selection mechanism in mesophase carbon fibres. Modelling Simul. Mater. Sci. Eng.1997; 1: 67–77.

White JL, Fathollahai B, Bourrat X. Formation of microstructure in mesophase carbon fibers. In Delhaès P editor. World of Carbon, 2(Fibers and Composites); CRC Press, 2003:3-23.

Wissbrun KF, Griffin AC Rheology of a thermotropic polyester in the nematic and isotropic states. J. Poly. Sci. 1982; 20:1835-1845.

Yan J, Rey AD. Texture formation in carbonaceous mesophase fibers. Physical Review E 2002a; 65:031713-1- 031713-14.

Yan J, Rey AD. Theory and simulation of texture formation in mesophase carbon fibers. Carbon 2002b; 40: 2647–2660

Yoon SH, Korai Y, Mochida I and Kato I. The flow properties of mesophase pitches derived from methylnaphthalene and naphthalene in the temperature range of their spinning. Carbon 1994; 32(2):273-280.

Zimmer JE, White JL. Disclination structures in the carbonaceous mesophase. Adv in Liq Crystals 1982; 5:157-213.

Zhuang MS, Thies MC. Extraction of petroleum pitch with supercritical toluene: experiment and prediction. Energy Fuels 2000; 14:70–75.

Zweben C. Ultrahigh-thermal-conductivity thermal management composites for microelectronic and optoelectronic packaging. Proceedings of the American Society for Composites, Technical Conference 2005, 20th 127/1-127/13.